UNIVERSITY OF CALIFORNIA
SANTA CRUZ

INVESTIGATION INTO THE PHOTOPHYSICS AND PHASE BEHAVIOR OF CONJUGATED POLYELECTROLYTE COMPLEXES

A dissertation submitted in partial satisfaction
of the requirements for the degree of

DOCTOR OF PHILOSOPHY

in

CHEMISTRY

by

Anna Rose Johnston

September 2022

The Dissertation of Anna Rose Johnston
is approved:

_____
Professor Alexander Ayzner, Chair

_____
Professor Yat Li

_____
Professor David Kilger

_____
Peter Biehl
Vice Provost and Dean of Graduate Studies

.

CONTENTS

CHAPTER FIGURES

APPENDIX FIGURES

Abstract

Oppositely charged, water-soluble polyelectrolytes undergo a spontaneous complexation and phase separation process with applications in fields spanning food science, origin of life studies, biomedicine, underwater adhesives, and general materials science. Specifically, associative phase separation leading to complex coacervation of oppositely charged polyelectrolytes has been extensively studied to understand prebiotic organization and to inform research into synthetic cell mimics. However, the phase behavior of conjugated polyelectrolytes (CPEs), macromolecules

analogous to chromophores and light-harvesting antennae found in photosynthetic organelles, has been investigated only minimally. Many questions remain regarding controlling of CPEs phase behavior, and how the formation of dense CPE-rich phases influences the resultant photophysics of theses molecular semiconductors. The work in this thesis primarily focuses on gaining a systematic understanding of the influence of ionic strength on the phase behavior of CPEs. The main tools used in this inquiry are steady-state absorption (or optical density (OD)) and photoluminescence (PL), time-resolved photoluminescence (TRPL), time resolved photoluminescence anisotropy, fluorescence microscopy, and fluorescence lifetime imaging (FLIM). The major findings of this work are as follows: the concentration and identity of cations in solution were found to manipulate the radiative decay rate and the exciton diffusion dynamics highlighting the importance of the interactions of the CPE complex with ions differing in polarizability and size; the influence of molecular ions leads to a transition from a two-phase system to an optically clear single phase with increased lifetime and decrease depolarization rate not accessible with similar concentrations of atomic salts; the chemical structure of a CPE can be rationally designed to undergo liquid/liquid phase separation to stabilize a semiconducting coacervate microstate; the interaction between ethyleneglycol units and K+ ions is critical in forming the coacervate phase; excited state energy transfer between the donor and acceptor CPEs occurs within the highly electronically coupled complex coacervate droplet phase.

Acknowledgements

I would like to acknowledge and thank our collaborator Professor Sarah Perry for her help getting established in the technique of rheology. I would also like to acknowledge and thank Dr. Ben Abrams for his unwavering help and expertise in fluorescence microscopy methods.

I would like to thank each of the undergraduate researchers I've worked with over the years; Melanie Blum, Mia Shockley, and Eris Minckler for their awesome contributions to this work and for helping me to become a better mentor. I would like to thank my former labmates Dr. Gregory Pitch, Dr. Michael Roders, Dr. William Hollingsworth, and Dr. Carmen Segura for welcoming me into the lab and for being my mentors, each in their own unique and quirky way. Thank you also to my more recent labmates; Dr. in training Ivette Mora, Dr. in training Rachael Richards, and Dr. in training Levi Matsushima for putting up with me as their mentor and for all the support they knowingly and unknowingly provided me as friends. The lab is in extremely capable and talented hands. Each of you is going to accomplish great things.

A special shout out goes to my cohort whom which I shared every aspect of the graduate school experience. You all know who you are. Thank you for being by my side during the best moments over the last five years, and for getting me through the toughest. I wish to also thank the UCSC Chemistry and Biochemistry department at large for being an extremely supportive and hilarious community. Every coincidental hallway interaction, departmental celebration, and conference with all of you was priceless to me. I would like to thank my committee members Professor Yat

Li and Professor David Kliger for their guidance and encouragement through the PhD milestones. Knowing that you believed in my helped me to believe in myself.

And finally, I'd like to thank my advisor Professor Alexander Ayzner for helping me in countless ways to become the independent researcher, mentor, teacher, and overall scientist I am today. Alex, thank you for your patience, for sharing your extreme intelligence, for pushing yourself to be a better mentor, for pushing me when I needed it, for having confidence in me when I felt mine waiver, for supporting me in my goal to teach, for always building me up instead of putting me down, and for putting up with my poorly timed, often questioningly unprofessional, sarcasm.

Dedication

This work is dedicated to my family; Dad, Mom, Jessie, Eric, and Scott. I couldn't have done this without your love and support.

Chapter 1

Introduction

1. Introduction

The importance of investing in the research and development of alternative energy methods is of global significance. Population increase amidst the technological revolution places our energy demands at an all-time high, with no ceiling in sight. Among the many methods currently implemented, harvesting energy from sunlight shows great promise to meet our energy needs in a renewable and sustainable way. Currently, global energy consumption is estimated to be 5.8×10^{20} Joules per year.[1,2] This amount of energy is supplied to the earth's surface by the sun in just over one hour. Great effort continues to be put into harnessing that energy using inorganic and organic photovoltaics for direct conversion to electricity.[3–7] Similar efforts are being undertaken to develop technologies capable of using solar energy to drive chemical transformations and produce fuel. One notable example being the production of hydrogen gas from the photochemical water splitting reaction.[8–10] Whether the goal is to produce electricity or fuel, solar energy technology is a promising pathway when considering the design and development of new sustainable materials.

When designing new materials for light harvesting applications, it is advantageous to look to nature for inspiration. Photosynthetic cells in plants, algae, and some bacteria have evolved to efficiently use the energy from sunlight to produce fuel for the organism. Specifically, the light reactions of photosynthesis proceed via a cascade of elegant events on the molecular level within the thylakoid membrane. This complicated process can be simplified to three steps; (1) **broad visible light absorption** by conjugated light-harvesting antennae chromophores, (2) **transfer of**

energy between chromophores over a distance through space, and (3) **localization of energy** at a protein cluster reaction center where it can be used for chemical

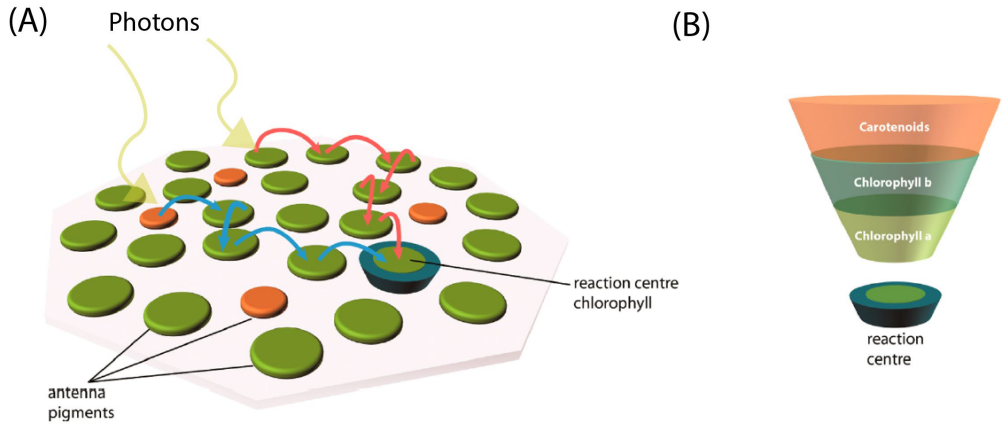

Figure 1.1: (A) Cartoon representation of photon absorption by antenna pigment molecules, energy transfer, and electron transfer at a reaction center. (B) Energy collection and transfer events represented as an energy funnel. This simplified schematic is analogous to the cascade of events that happen during the light reactions within the membrane protein photosystem II. Figure adapted from Mirkovic et. al.[11]

transformations such as oxygen evolution. These steps are represented visually in Figure 1.1.[11] In addition to these fundamental light-harvesting steps, the photosynthetic chromophores are non-covalently self-assembled and the scaffolds for these 'natural materials' are soft and deformable. It is intriguing to ask questions about how to, from a molecular level, design a new **soft** material capable of panchromatic light absorption, energy transfer, and ultimately conversion of that energy to electrical or chemical potential energy. This is the overarching idea motivating this work, creation of a dynamic, self-assembled photosystem capable of energy transfer.

The class of molecules investigated in this work are called conjugated polyelectrolytes (CPEs). Like well-known chromophores, such as chlorophyll found in photosynthetic cells, CPEs possess alternating single and double bonds (aka π-conjugation) along their backbones. This characteristic allows them to absorb and emit light in the visible to near-infrared (near-IR) region of the electromagnetic spectrum. Varying the chemical structure of the CPE backbone can change which region of visible (or near-IR) light these molecules are active in. Figure 1.2 shows the

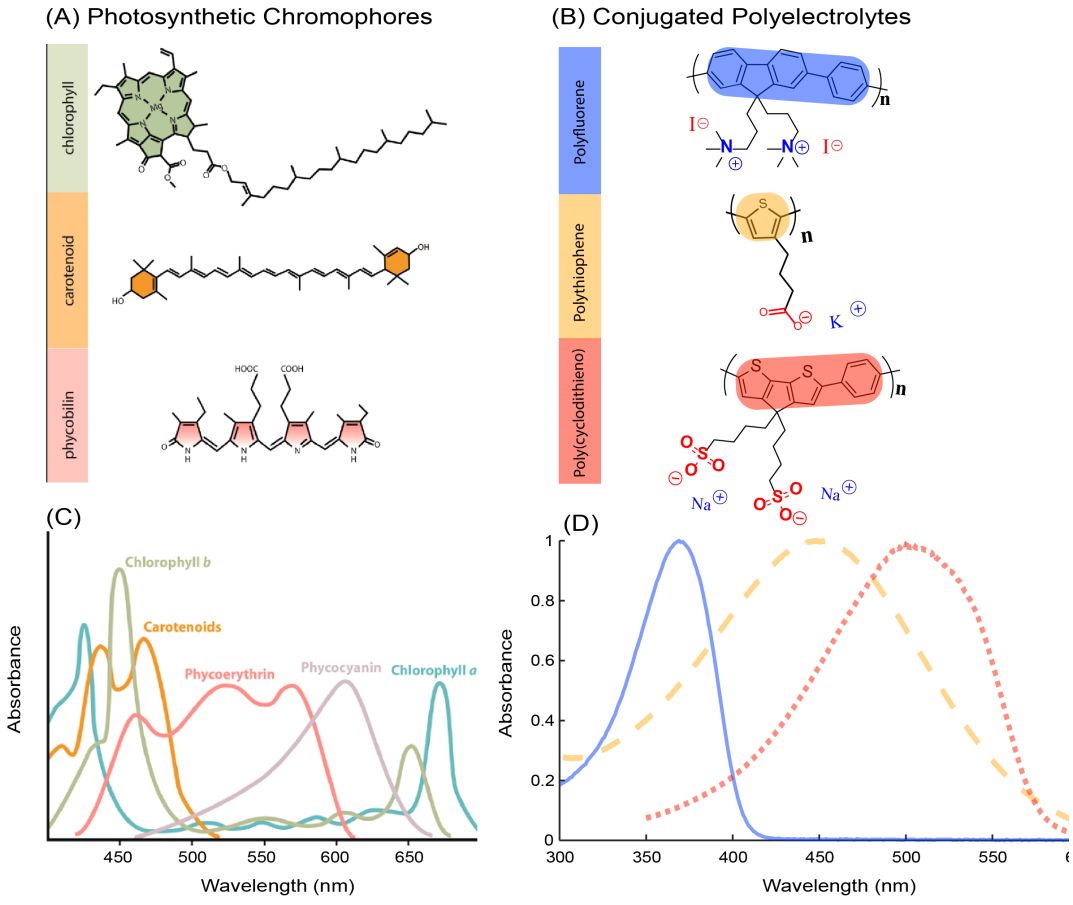

Figure 1.2: The chemical structures of common photosynthetic chromophores are shown in (A) and the wavelengths of light at which these chromophores absorb are shown in (C). Comparative CPE structures and absorbances can be seen in panel (B) and (D) respectively. Panels A and C were adapted from Mirkovic et. al.[11]

chemical structures of the CPEs used in this work, and the wavelengths at which they absorb light, alongside common photosynthetic chromophores.[11] In addition to their light active properties, CPEs possess other attractive characteristics including their charged sidechains. These sidechains can be cationic or anionic and impart water solubility to these otherwise hydrophobic polymers. This is desirable as it allows the development of these materials in an aqueous, liquid state. Liquid-state materials have many unique properties compared to solid-state materials like deformability and sensitive response to external stimuli. Modification of the sidechains can impart these molecules with varying electrostatic interaction strengths. These charged moieties also allow for electrostatic interactions of the sidechains with other charged entities in solution. These range from polar molecules to ions and oppositely charged CPEs. When two oppositely charged CPEs are combined in solution they are known to spontaneously form complexes (CPECs) as shown in Figure 1.3.[12] This spontaneous self-assembly results in a higher order structure with new photophysical implications. If the CPEs chosen for self-assembly into CPECs have light absorption and emission signatures with spectral overlap, this complexation brings them in sufficient spatial proximity to undergo electronic energy transfer (EET). When designing an artificial light-harvesting system, EET is a core process that must be optimized. The reader can find a detailed discussion of EET in section 1.1.3.

Previously, Hollingsworth et. al. showed that CPEs at stoichiometrically charged matched ratios formed CPECs capable of broad visible light absorption and ultrafast energy transfer (~240 fs). This work showed that CPEs could self-assemble into non-covalently linked artificial light-harvesting antennae, and that the timescale of energy transfer along the CPEC network was comparable to that found in natural photosynthetic systems.[13] Following these promising results in the dilute regime, a natural next step from a materials perspective is to scale up the amount of material by increasing the CPE concentration. Increasing CPE concentration in principle would also increase electronic coupling leading to more dynamic energy transfer within the material. The idea of designing a system where many CPE chains interact would allow excitons to explore a larger energetic CPEC landscape is intriguing. In principle, this could lead to a larger delocalization of the exciton throughout the CPE network with a higher probability of encountering a synthetic reaction center. Increasing CPEC concentration and introducing a reaction center molecule, such as the well-known electron acceptor

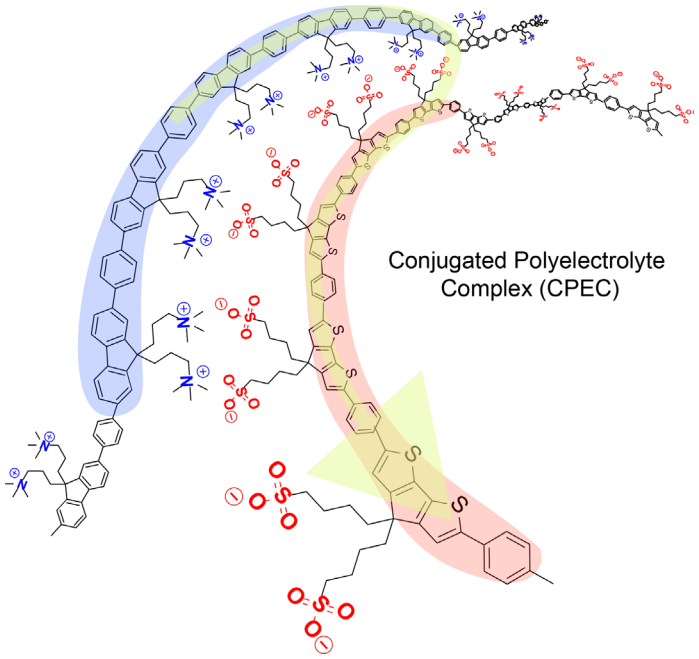

Figure 1.3: Cartoon representation of a conjugated polyelectrolyte complex (CPEC) where the yellow arrow is representing electronic energy transfer (EET) from the donor CPE to the acceptor CPE.s

C60, would allow for the formation of a more complex hierarchy of light-harvesting components.

As the complexity of an artificial light-harvesting system increases, it is advantageous to simplify the design pathway. This can be done using self-assembly to spontaneously form non-covalently linked systems. The formation of a dense liquid phase can be achieved in this way using associative phase separation of charged macromolecules, akin to CPEs. This leads to liquid-liquid phase separation termed complex coacervation and is discussed in more detail in section 1.1.4. The work presented herein is focused on the use of associative phase separation to manipulate the phase behavior and resultant photophysics of CPECs. Specifically, the use of complex coacervation to produce a light-active liquid phase capable of efficient EET has been studied only minimally. The work presented in this thesis is one step towards realizing that goal.

1.1 Background

1.1.1 Electronic Transitions in Conjugated Polyelectrolytes

The basis of this work requires an understanding of how conjugated organic molecules absorb and emit light. Unlike saturated hydrocarbons which possess only σ-orbitals for bonding, conjugated hydrocarbons have both σ and π-orbitals which results in alternating single and double bonds and a π-system delocalized over multiple nuclei. The π-electrons within these molecular orbitals are further from the positively charged nucleus and thus more loosely bound than the σ-electrons. As a result, energy of an incident photon capable of exciting these more loosely bound electrons is lower and typically falls within the visible part of the electromagnetic

spectrum (~400-700nm). The classical physical description behind the absorption of this energy involves the incident electromagnetic field of light inducing oscillations in the π-electron cloud. This input of energy allows the electrons to reorient around the molecule into a higher energy molecular orbital configuration.

Though the classical decription can help one begin thinking about light absorption, the quantum-mechanical description provides a more complete understanding. The energy levels of these π-electrons are quantized. When the energy of an incident photon matches the energy difference between the ground state (S_0) configuration and the higher lying energy levels (S_1, S_2, S_3, etc.) , absorption occurs. This is depicted by the blue lines in the Jablonski diagram found in Figure 1.5. The probability of absorption and the promotion of an electron from the initial state to the final state depends on the direction of the incident oscillating electric field. This direction can be described by the polarization vector shown in Figure 1.4A, and is particularly relevant to time-resolved fluorescence anisotropy measurements discussed in section 1.2.2. When an organic molecule undergoes an electronic transition, the redistribution of the electrons results in a change in the charge distribution within the molecule. This change will have both a magnitude and direction. This is summarized by the electronic transition dipole moment which is calculated from the wavefunctions of the initial (ψ_i) and final (ψ_f) electronic states

$$\vec{\mu}_{i\to f} = \int \psi_f(\vec{r}) e\vec{r} \psi_i(\vec{r}) dV \qquad \textbf{(1.1)}$$

where $\vec{r} = (x, y, z)$ is the position operator in 3D, with the origin of the coordinates coinciding with the center of the molecule's charge distribution, e is the charge of an electron, dV is the volume element, and the integration is over all space. A visual

example of the transition dipole moment and the transition denisty ($\psi_f\psi_i$) for the prototypical conjugated organic molecule anthrancene are shown in Figure 1.4B. The transition density describes the redistribution of charge and changes in the occupied electronic state associated with the absorption of light and transition from the initial to the final electronic state. In anthracene, this results in the clustering of electron density on a particular side of the molecule and a resultant transition dipole parallel to the conjugated π-system. The probability of light absorption depends on $\cos^2(\theta)$, where θ is the angle between the electric field and the transition dipole moment. This probability is maximized when θ =0, where Figure 1.4C shows this ideal orientation.[14] The probability of absorption increases with the square of the magnitude of the transition dipole moment as described by the following proportionality.

$$P_{i\rightarrow f} \propto \left|\vec{\mu}_{i\rightarrow f}\right|^2 \qquad \textbf{(1.2)}$$

The probability of light absorption per unit time is refered to as the transition rate (r_{if}) which can be described using Fermi's golden rule.[15,16] This rate is related to the mean lifetime ($r = 1/\tau$) of the excited state described in detail in section 1.2.1. Fermi's golden rule can be described by

$$r_{if} = \frac{2\pi}{\hbar}|M_{if}|^2\rho_f \qquad \textbf{(1.3)}$$

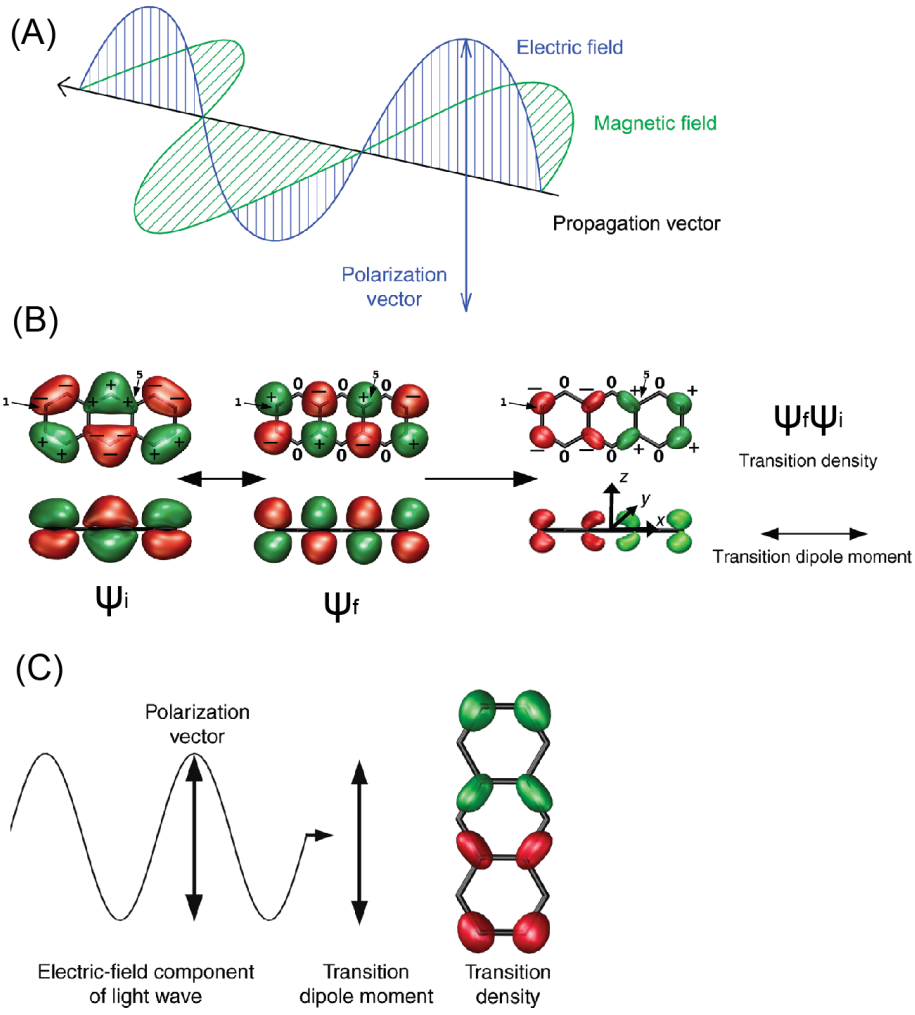

Figure 1.4: (A) Electromagnetic field of light showing the polarization vector of the electric field component. (B) Transition density and transition dipole moment example using the transition from ψ_i to ψ_f of anthracene where (C) shows the optimal alignment between the polarization of the electric field with the transition dipole moment. Figure adapted from Walla.[14]

where the transition probability from an initial to a final energy eigenstate depends on the density of final states (ρ_f), and on the coupling between the initial and final states of the system described by the matrix element of interaction (M_{if}).

$$M_{if} = \int \psi_f^* V \psi_i dv \qquad \textbf{(1.4)}$$

Here ψ_i is the wavefunction of the initial state, ψ_f is the wavefunction of the final state, and V is the operator describing the physical interaction which couples the states.

Absorption is a nearly instantaneous process, occurring in less than 10^{-15} s, in which the energy from a photon promotes an electron from S_0 to multiple vibrationally excited states within higher lying electronically excited states. Since these electronic excitations are coupled to the vibrational modes, they are thus termed 'vibronic transitions'. These transitions follow the Franck-Condon principle meaning they occur quickly enough that molecular motion can be ignored. For this reason, absorption spectra are not sensitive to molecular dynamics in the excited state. After

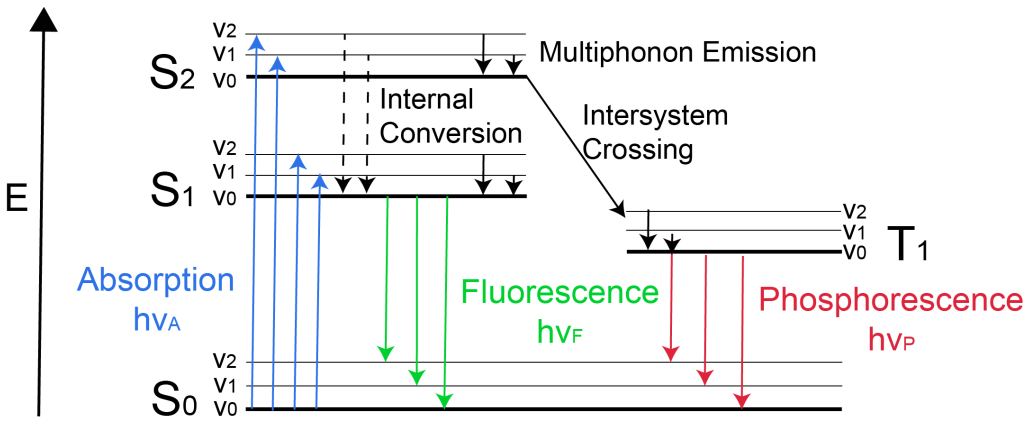

Figure 1.5: Jablonski Diagram showing vibronic transitions where absorption ($h\nu_A$) occurs within 10^{-15} s, internal conversion occurs within 10^{-12} s, intersystem crossing occurs within 10^{-8}-10^{-3} s, fluorescence ($h\nu_F$) occurs within 10^{-9}-10^{-7} s, and phosphorescence ($h\nu_P$) occurs 10^{-3}s-days.

excitation, organic molecules undergo nonradiative transitions via vibrational relaxation (aka multiphonon emission, solid black arrows in Figure 1.5) and internal conversion within 10^{-12} s (dotted arrows in Figure 1.5). These transitions relax the molecule to the ground vibrational state of the first electronically excited state (S_1-v_0) and can then return to S_0 by releasing the remaining energy as light through fluorescence ($h\nu_F$), or phosphorescence ($h\nu_P$) (Figure 1.5). This emission process happens over longer timescales than absorption. Fluorescence (10^{-9}-10^{-7} s, green arrows in Figure 1.5) occurs from spin paired electrons and phosphorescence (10^{-3}s-days, red arrows in Figure 1.5) occurs from spin unpaired electrons having undergone intersystem crossing to a lower lying triplet state. Intersystem crossing is another non-radiative transition not typically observed for CPEs. For this reason, emission through fluorescence will be the focus in the work discussed herein. The time between absorption of a photon and emission of a photon is termed the 'fluorescence lifetime'. For a detailed discussion on fluorescence lifetimes see section 1.2.1.

An idealized version of an excitation and emission spectrum are shown in Figure 1.6A where the vibronic progression is resolved, the spectra are mirror images of one another, and there is an energy offset due to internal conversion referred to as the Stokes shift. However, due to ground state thermal fluctuations leading to an ensemble of vibronic transitions, true liquid-state spectra are typically broadened. For CPEs this broadening is more significant due to an ensemble of chain conformations existing in solution. This can be seen for a common polyfluorene CPE dissolved in water in Figure 1.6B. Here, slight structuring in the emission spectrum is a result of emission occuring from a subset of lower energy CPE chromophore segments. This occurs in concert with the nonradiative transitions of the molecule preceeding emission leading to transitions solely from S_1v_0. This phenomenon is reffered to as Kasha's rule and accounts for the fact that emission spectra are typically independent of excitation wavelength.

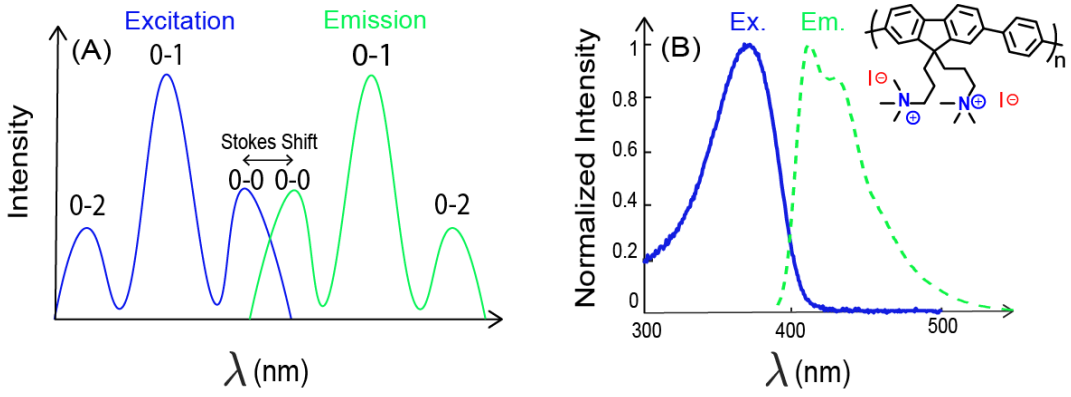

Figure 1.6: (A) Idealized excitation and emission spectra showing vibronic structuring where 0-2 is an abbreviation for S_0v_0-S_1v_2 and so on. (B) Real excitation and emission spectra of a polyfluorene CPE.

For CPEs, excitation typically occurs from the ground state bonding π-orbital to the anitbonding orbital (π^*). This π- π^* transition results in a short lived excited

state after which these molecules relax back to their ground state and emit light as fluorescence. The photophysics of CPEs are intrinsically linked to their backbones. Thus, the emission spectra of these molecules is a powerful reporter on CPE structure and orientation within the liquid state. The next section will provide a discussion regarding how the aggregation of CPEs can influence their emission characteristics.

1.1.2 Aggregation Effects on Conjugated Polyelectrolyte Emission

In both dilute and concentrated CPE solutions, intra and inter-chain interactions occur leading to the clustering of molecules (aka aggregation). Aggregation brings CPE backbone segments within sufficient spatial proximity that electronic coupling of their respective wavefunctions can occur. This coupling gives rise to new absorbing and emitting states which can often be observed as a shift of the excitation and emission spectra to higher or lower energies. The direction of the shift depends upon the relative orientation of the monomer segments, with the most simplified orientations being described as head-to-head (aka H-aggregates) and head-to-tail (aka J-aggregates). Figure 1.7 depicts these two orientations and the differences in their electronic transitions for a simplified

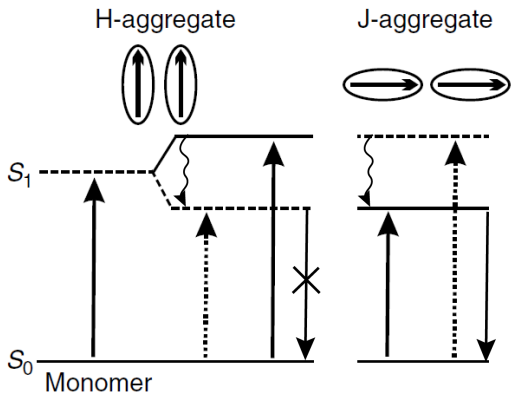

Figure 1.7: H-aggregate (left) and J-aggregate (right) excited state energy level splitting and electronic transitions relative to the monomeric case. Energy level diagram is based on Kasha's theory for aggregation of small molecule dyes.[17]

dye-monomer/dimer-aggregate model developed by Michael Kasha.[17] Kasha's theory states that excitation of H-aggregates results in transitions to higher energy states, and that the transition to lower lying states is forbidden (shown by the arrow with an X through it in Figure 1.7). This excitation is followed by a relaxation to lower energy states with vanishing transition dipole moments and low fluorescence emission probability. In contrast, excitation of J-aggregates results in allowed transitions to lower lying energetic states, and an increase in fluorescence is typically observed compared to the monomer.

The differences in the emission characteristics of these two monomer aggregates is described by Kasha as a coulombic coupling. Kasha's model assumes a tightly bound excited state electron (aka exciton) termed a Frenkel exciton, and uses a point dipole approximation described by

$$J_c = \frac{\vec{\mu}_1\vec{\mu}_2 - 3(\vec{\mu}_1 \cdot \hat{R})(\vec{\mu}_2 \cdot \hat{R})}{4\pi\varepsilon\, \hat{R}^3} \qquad \textbf{(1.5)}$$

where $\vec{\mu}_1$ and $\vec{\mu}_2$ are the transition dipole moments of the monomers 1 and 2, $\hat{R}$ is the vector representing the distance between the center of the transition dipole moments, and ε is the dielectric constant of the medium in which the monomers are contained. For identical molecules this coupling becomes

$$J_c = \frac{\vec{\mu}^2(1 - 3\cos^2\theta)}{4\pi\varepsilon\, \hat{R}^3} \qquad \textbf{(1.6)}$$

where θ is the angle between the transition dipole moment and $\hat{R}$. As this angle changes, monomer aggregates can take on more H-like ($54.7^o < \theta < \frac{\pi}{2}$ and $J_c > 0$) or J-like ($\theta < 54.7^o$ and $J_c < 0$) orientations. At 54.7^o (aka the magic angle) $J_c = 0$ and there is no coupling between the monomers.

Work by Kasha and McRae discusses this coupling between monomers into H-or J-dimer aggregates leading to the splitting of the first excited state into a symmetric and anti-symmetric linear combination of the original excited states of the monomers. The sign of J_c can give information on the relative energies of these new levels where H-aggregates ($+J_c$) have the symmetric state at higher energy and J-aggregates ($-J_c$) have the anti-symmetric state at higher energy. Due to the process of vibrational relaxation and internal conversion discussed earlier, this leads to H-aggregate emission from the lower lying anti-symmetric state and J-aggregates emitting from the lower lying symmetric state. Because only the symmetric state can couple to the ground state, this results in H-aggregates decaying non-radiatively to the ground state. J-aggregates in contrast decay from the symmetric state to the ground state radiatively. These differences in electronic transitions can be observed in absorption and emission spectra where H-aggregates will show a blue shift to higher energies and a decrease in the fluorescence intensity relative to non-aggregated monomers in solution. J-aggregates will show a red-shift to lower energies typically accompanied by an increase in fluorescence intensity.

It may already be clear that the dimer model put forth by Kasha is too simple to be applied directly to CPEs which are long chains of covalently linked monomer units. For this reason, Spano et. al have worked to extend Kasha's work by first considering higher order linear aggregates whose emergent exciton energy levels are assumed to form bands described by the wavevector k as

$$\left|k\right\rangle = \frac{1}{\sqrt{N}}\sum_n e^{ikn}\left|n\right\rangle \quad k = 0, \pm\frac{2\pi}{N}, \pm\frac{4\pi}{N}, \dots, \pm\pi \qquad \textbf{(1.7)}$$

where N is the number of monomers and $|n\rangle$ is the quantum state vector.[18]

Here, the probability of absorption and emission of a photon only applies to the $k = 0$ exciton and the energy splitting of the monomer excited state is then represented by bending of the band energy (Figure 1.8). For H-aggregates (upward band bending), vibronic transitions from the lower lying states of the excitation band to the higher lying vibrational states (i.e., v=1,2) of S_0 are allowed while the transition to v=0 of S_0 is forbidden. For J-aggregates (downward band bending) all vibronic transitions are allowed. For this reason, the 0-0 vibronic transition can vary in

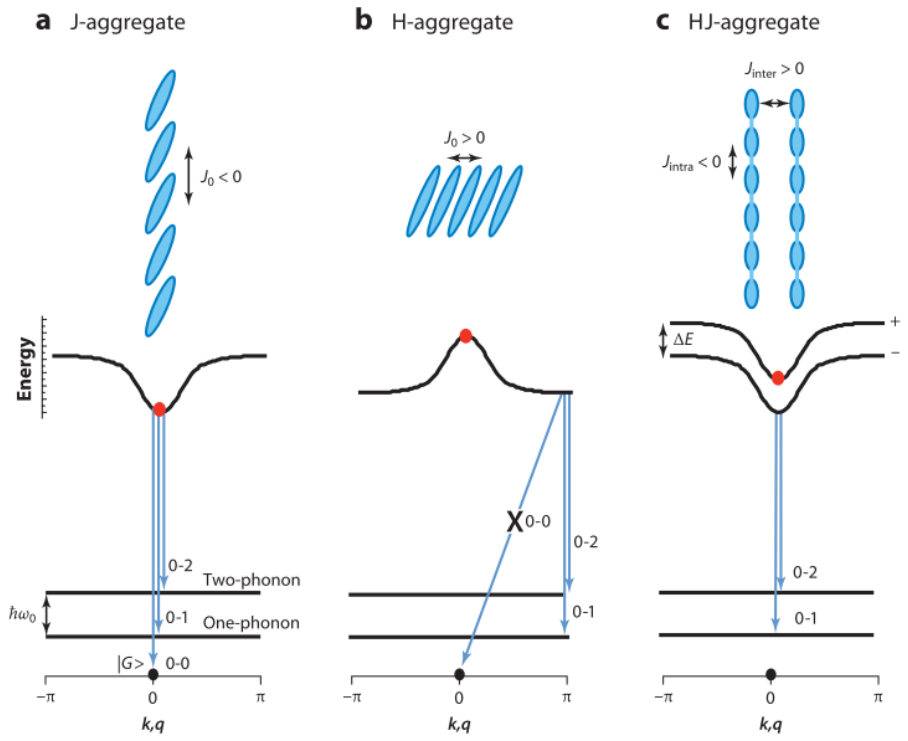

Figure 1.8: Spano's H and J aggregate molecular orientation comparison (a.b) to that of the H-J aggregate (c) all showing nearest neighbor coupling (J). The red dot indicates exciton that is optically allowed from the ground state ($|G\rangle$, black dot), arrows indicate emission, q is the phonon wave vector, and ΔE is the energy difference between the symmetric and antisymmetric bands associated with the H-J aggregate. Figure from Spano et. al.[18]

intensity depending on if a linear combination of monomers is more H-like or J-like in nature. This can be represented as

$$S_R = \frac{I_{0-0}}{I_{0-1}} \qquad \textbf{(1.8)}$$

where I_{0-0} is the intensity of the 0-0 vibronic transition, I_{0-1} is the intensity the 0-1 vibronic transition. Here, $S_R \leq 1$ is representative of H-aggregates and $S_R \geq 1$ is representative of J-aggregates. This theory for the linear combination of monomer units gives a description of spectroscopic characteristics of aggregation effects through comparison of vibronic emission intensities. Though more complex than Kasha's dimer model, it gives similar prediction of H-aggregates leading to non-emissive dark states and J-aggregates giving rise to bright emissive states.

In the case of a CPEC, H and J aggregate formation can occur within a single CPE chain (intrachain interactions) and between chains (interchain interactions). Increasing CPE concentrations in solution will result in a higher probability of both intra and interchain interactions and thus photophysical aggregation effects. Having laid the foundation for light absorption and emission of CPEs, the next section will discuss how these molecules can transfer excitation energy through space.

1.1.3 Electronic Energy Transfer

There are many systems studied in which a photon is absorbed and the resultant exciton on one chromophore can transfer through space to another chromophore. For the optimization of synthetic light-harvesting antennae, the design must allow for these excitons to transfer efficiently and quickly through space. This excited state energy can then decay radiatively or be used to fuel a photochemical

reaction. This process is called electronic energy transfer (EET) (aka resonance energy transfer or sometimes, Förster resonance energy transfer) and occurs between a donor molecule in an excited state and an acceptor molecule in its ground state. For EET to take place several conditions must be met, and these are described by the theory established by Theodor Förster.[19,20] First, there must be sufficient spectral overlap between the emission spectrum of the donor and absorption spectrum of the acceptor where the extent of spectral overlap can be described by the overlap integral $J(\lambda)$.

$$J(\lambda) = \int_0^\infty F_D(\lambda)\varepsilon_A(\lambda)\lambda^4 d\lambda \qquad \textbf{(1.9)}$$

Here, $F_D(\lambda)$ is the normalized fluorescence intensity of the donor between λ and $\lambda + \Delta\lambda$ (the change in wavelength across the emission spectrum), and $\varepsilon_A(\lambda)$ is the extinction coefficient of the acceptor at λ. Thus, $J(\lambda)$ can be determined experimentally using absorption and fluorescence spectroscopy. Figure 1.9 shows an example of spectral overlap for a donor and acceptor molecule next to spectral overlap of a real EET donor and acceptor CPEC pair.

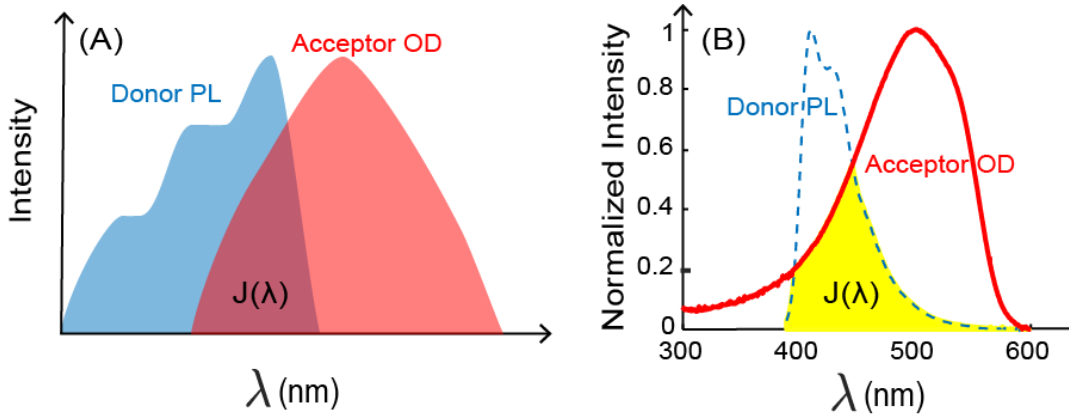

Figure 1.9: Panel (A) shows an example of spectral overlap between a generalized donor and acceptor molecule. Panel (B) shows spectral overlap between the PL of a polyfluorene donor CPE and the absorbance (aka optical density (OD)) of a

EET also depends on the relative orientation of the transition dipole moments of the donor and acceptor molecules which is describe by the orientation factor κ^2.

$$\kappa^2 = \vec{\mu}_D \vec{\mu}_A - 3(\vec{\mu}_D \cdot \hat{R})(\vec{\mu}_A \cdot \hat{R}) \qquad \textbf{(1.10)}$$

Here, κ^2 is simply the numerator found in equation 5 and contains the same physical description of relative dipole orientations. κ^2 can have values ranging from 0 to 4 with $\kappa^2 = 0$ indicating perpendicular dipoles, $\kappa^2 = 1$ indicating dipoles oriented in an H-like fashion, and $\kappa^2 = 4$ indicating a J-like orientation. The value of κ^2 can be determined experimentally using fluorescence anisotropy described in section 1.2.2. However, κ^2 is often taken to be 2/3, a value which represents donors and acceptors randomly oriented due to rotational diffusion before EET takes place. Often, the distance at which the EET efficiency is 50% (i.e., the Förster radius in nm, R_0) is of practical interest and, if κ^2 is known, can be calculated using

$$R_0^6 = \left(\frac{Q_D \kappa^2 9000(ln10)}{128\pi^5 N n^4}\right) J(\lambda) \qquad \textbf{(1.11)}$$

where Q_D is the quantum yield of the donor in the absence of the acceptor, n is the refractive index of the medium, and N is Avogadro's number. If R_0 (typically 30-60 Å) is calculated and the rate of energy transfer $k_T(r)$ is known, the distance between the donor and acceptor (r) can then determine using

$$k_T(r) = \frac{1}{\tau_D}\left(\frac{R_0}{r}\right)^6 \qquad \textbf{(1.12)}$$

where τ_D is the fluorescence lifetime (described in section 1.2.1) in the absence of the donor. Alternatively, if the distance is known it can be used to calculate $k_T(r)$.

This simplified physical picture of EET and the physical constants that result provide an excellent basis for understanding EET. The theory is often successfully

applied to biological systems in which there is one donor molecule and one acceptor molecule, whose transition dipole moments are treated as point dipoles. with a well-defined r between them that is large compared to their size. However, when it comes to modeling EET involving CPEs the assumptions required for the Förster model are violated. CPEs are large quasi-linear macromolecules with many electronically interacting monomer units. Thus, treating them as point dipoles is not an accurate representation. Additionally, the CPEs within CPEC are complexed closely together, meaning r is much smaller than the size of the emitting portions of these molecules (i.e., chromophores). Though additional models have been proposed to correct for some of the failings of the Förster model they typically assume that the photophysical characteristics of the donor and acceptor are fixed. As we have already seen in the discussion of aggregation effects, this is not true of CPEs. Aggregation effects of a single CPE chain, and large conformational changes that occur when self-assembling into CPECs, can shift the absorption and emission spectra to higher or lower wavelengths. This can in turn cause restructuring of the vibronic transition intensities. For these reasons, modelling EET in CPEs to extract rates and efficiencies is extremely challenging.

Regardless, the picture of EET laid down by Förster helps to build a foundation to understand EET. For CPEs, a more detailed discussion of what constitutes an EET donor and acceptor is necessary. After initial transfer of energy from the donor CPE to the acceptor CPE, additional migration takes place within the single acceptor CPE chain. This is due to different segments of the chain having varying lengths of conjugation due to random torsional disorder. In CPEs, and

exciton generated on a chain segment with a specific conjugation length will have a specific energy analogous to a 1-D particle in a box

$$E_n = \frac{n^2 h^2}{8mL^2} \qquad \textbf{(1.13)}$$

where n is the quantum number, h is Planck's constant, m is the mass of the particle, and L is the length of the box (i.e., chromophore unit). Thus, a chain segment with a longer conjugation length (i.e., longer chromophore) will have a lower energy than a portion with a shorter conjugation length. When discussing 'chromophores' in the context of CPEs, this is the description that the reader should refer to. Therefore, initial exciton diffusion on the acceptor CPE manifests as a 'random walk', which is then followed by a 'downhill migration' within the ensemble of acceptor chromophores until they have migrated to portions of the chain with the lowest energy conformation before emitting.

Design of a **soft** material capable of light-harvesting would need to have efficient, rapid, and directional EET. According to the Förster model, the rate of EET can be increased by increasing the spectral overlap or by increasing the amount of electronic coupling within the system. CPEs, though complicated compared to simple dyes, provide excellent exciton highways through which EET can take place. Thus, strategically increasing CPEC concentration can help to increase the electronic couplings between chains leading to more rapid EET. One avenue for increasing CPEC concentration via self-assembly in the liquid state is through associative phase separation. This is termed complex coacervation and will be discussed in detail in the next section.

1.1.4 Complex Coacervation

When two oppositely charged macromolecules are mixed at stoichiometrically charged matched ratios they are known to spontaneously complex, and to associatively phase separate. This can occur for a variety of charged molecules including proteins, surfactants, colloids, and polymers. Here, we will focus on the associative phase separation of a polycation and polyanion specifically. When this interaction leads to a separation into two liquid phases it is termed complex coacervation and an equilibrium is established between a polyelectrolyte dilute phase (supernatant) and a polyelectrolyte dense phase (coacervate) (Figure 1.10).[21] This equilibrium can be shifted using temperature, polyelectrolyte concentration, and by changing the ionic strength of the solution. These changes can aid in varying the strength of complexation and the resultant phase behavior.[22] Complex coacervation has been studied extensively in visible light inactive, non-conjugated polyelectrolytes.[21,23–41] It was not until recently that studies on conjugated polyelectrolyte complex coacervation have been undertaken.[42,43] While coacervation has been investigated for applications in drug delivery, cosmetics, food

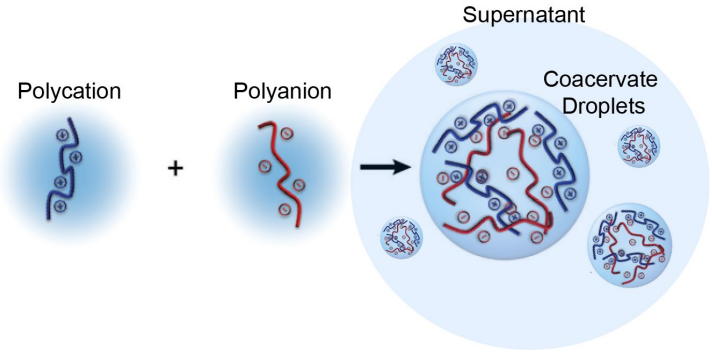

Figure 1.10: Cartoon showing spontaneous self-assembly and phase separation of two oppositely charged polyelectrolytes into a complex coacervate. Figure adapted from Sing and Perry.[21]

science, and to aid origin of life studies, the work presented in this thesis is specifically geared toward applications for light-active soft materials design.

The early theory of complex coacervation began with Voorn and Overbeek when they described coacervation as an interplay between translational entropy of counterions and the electrostatic attraction of the charged species in solution. The resultant Voorn-Overbeek model combines the Flory-Huggins theory of polymer mixing and the Debye-Hückel theory of dilute electrolytes with the specific aim of modeling polyelectrolyte systems.[21] This resulted in the following expression for free energy of mixing (F_{vo})

$$F_{vo} = Vk_bT\left(\sum_i \frac{\phi_i}{N_i} ln\,(\,\phi_i) - \alpha[\sum_i \sigma_i\phi_i]^{\frac{3}{2}} + \frac{1}{2}\sum_{ij}\chi_{ij}\phi_i\phi_j]\right) \quad \textbf{(1.14)}$$

where the first term is the mixing entropy for species i, ϕ_i is the volume fraction of monomers, and N_i is the degree of polymerization (i.e., number of monomers) and N>>1. The second term is a Debye-Hückel free energy representing the attraction between electrolytes where σ_i is a proportionality between number density and volume fraction of charges, α is the electrostatic attraction defined as $\alpha = \frac{\lambda_b}{2a}$ where a is the radius of the charge and λ_b is the distance over which the electrostatic attraction is equal to the thermal energy of the system (k_bT).

$$\lambda_b = \frac{e^2}{4\pi\varepsilon_0\varepsilon_r k_b T} \quad \textbf{(1.15)}$$

Here, e is the elementary charge, ε_0 is the vacuum permittivity, and ε_r is the dielectric constant of the medium. This is known as the Bjerrum length and for water at room temperature (T ≈ 298 K) (conditions applicable to the studies in this thesis) $\varepsilon_r \approx 80$ and $4\pi\varepsilon_0 = 1$ simplifying the expression to $\lambda_b = \frac{e^2}{\varepsilon_r k_b T}$. Thus, the second term in equation 14 accounts for the attraction between a molecular charge and the average of the distribution of surrounding opposite charges. The third term in equation 14 captures the short-range interactions. Here, χ_{ij} is the Flory parameter describing the transition from weakly repulsive monomer/solvent interactions ($0 < \chi_{ij} \lesssim \frac{1}{2}$) present in a solution of dissolved polyelectrolytes. A $\chi_{ij} > \frac{1}{2}$ represents the threshold of repulsive monomer/solvent interactions which leads to a separation of the solution into two coexisting phases, where one phase is richer in polyelectrolyte and poorer in solvent than the other. Figure 1.11 shows a representative phase diagram of [polymer] vs [salt] generated from this model.

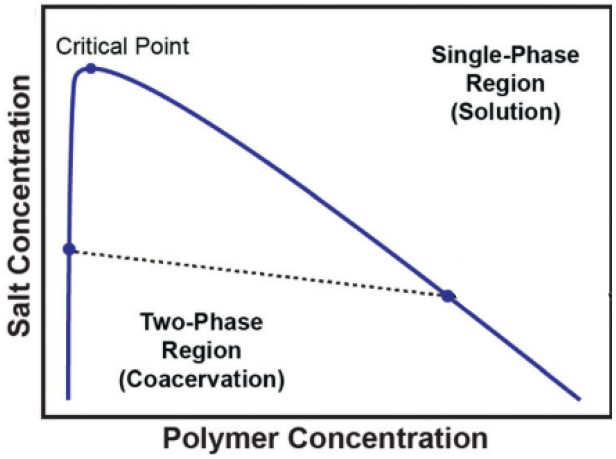

Figure 1.11: Phase diagram of [polymer] vs. [salt] giving rise to a two-phase coacervation region and a one-phase solution region. The tie-line indicates different salt partitioning behavior between the concentrated and dilute phases. Figure adapted from Sing and Perry.[21]

Though the Voorn-Overbeek model accurately captures the fact that coacervation occurs at low salt concentrations, and that high salt concentration leads to dissolving of the complex into one phase, it has several limitations. First, the Debye-Hückel theory is only applicable to weak and dilute electrolytes up to ~5 mM concentrations and assumes simple monovalent salts. Typical salt concentrations utilized in coacervate studies, including the studies discussed herein, are often much higher in the 0.5-5.0 M range. Second, the theory treats all charges as point particles with negligible volume and does not distinguish between charges on the polyelectrolytes and the salt ions in solution. This does not properly account for the fact that the polyelectrolyte charges exist on covalently linked monomer units within a chain which give rise to a distinct linear charge density. And finally, this model treats the solvent (i.e., water) as a continuum which ignores any local structuring effects of water molecules leading to coacervation.

Due to these limitations, experimental observations often directly conflict predictions made by the Voorn-Overbeek theory. It has been observed experimentally that upon phase separation salt ions preferentially partition into the phase dilute in polyelectrolyte, however, Voorn-Overbeek predicts the opposite. Additionally, recent efforts show that the driving force behind coacervation is mainly entropic gain from counterion release with minor enthalpic contributions.[12] Voorn-Overbeek theory considers coacervation to be an enthalpically driven process that comes about due to an increase in electrostatic attraction. These findings have spurred theoretical development around modeling complex coacervation using polymer field theory, scaling theory, and others to address the know limitations of Voorn-Overbeek. A

detailed discussion of these models is beyond the scope of this text. The reader can refer to the recent work by Sing and Perry for an introduction into recent developments around these models.[21]

Leading up to the work presented herein, minimal work had been done to investigate the complex coacervation of conjugated polyelectrolytes.[42,43] In fact, studies published previously show insufficient evidence for the formation of a true semiconducting liquid phase via complex coacervation. Rather, the concentrated phases reported on in these studies show characteristics of more solid-like colloidal gels than true liquid droplets.[42,43] The realization of an actual liquid semiconducting CPEC phase capable of EET is what this work builds towards.[44,45] Fine tuning of this new material has awesome implications for applications in novel soft materials.

1.2 Overview of Experimental and Analytical Methodology

The purpose of this section is to provide additional details of characterization methods used throughout the following studies. A majority of the inquiry was focused on the photophysics of highly concentrated CPEs and CPECs. Characterization methods include a combination of steady-state absorption and fluorescence (described in section 1.1.1), time-resolved photoluminescence (section 1.2.1) and time-resolved photoluminescence anisotropy (section 1.2.2), fluorescence microscopy (section 1.2.3), and fluorescence lifetime imaging (section 1.2.4). Additionally, phase behavior was characterized using rheology (section 1.2.5), the study of the flow and deformation of matter.

1.2.1 Time – Resolved Photoluminescence

Time-resolved photoluminescence (TRPL) is a crucial measurement to a more in depth understanding of CPE photophysics and their implications to light harvesting. TRPL can lend valuable insight into exciton migration and is a necessary tool for extracting EET rates and estimating exciton diffusion lengths. As outlined in section 1.1.1, when a CPE is exposed to visible light of a frequency which matches that of an electronic transition, the molecule can be promoted to an excited state. The average amount of time the CPE spends in the excited state before decaying via spontaneous emission to the ground state is termed the fluorescence lifetime (τ) and is defined as

$$\tau = \frac{1}{k_r + k_{nr}} \qquad \textbf{(1.16)}$$

where k_r and k_{nr} are the radiative and non-radiative rate constants. This lifetime can add to steady-state photoluminescence measurements by giving insight into CPE chain microstructure and resultant exciton migration either along a single CPE or within a CPEC. Additionally, exciton lifetimes of CPEs have direct implication for their applications in organic photovoltaics and organic light emitting diode technologies. Following excitation with an infinitesimally short light pulse, the number of excited fluorophores ($[F(t)^*]$) will decrease with time

$$\frac{d[F(t)^*]}{dt} = -(k_r + k_{nr})\,[F(t)^*] \qquad \textbf{(1.17)}$$

because the number of excited fluorophores is proportional to fluorescence intensity, integrating between t=0 and t gives the single exponential function in equation 18.

For molecules in which excitons decay along a single decay pathway, this decay can be described as

$$I(t) = I_0 e^{-\frac{t}{\tau}} \qquad \textbf{(1.18)}$$

where I_0 is the initial fluorescence intensity, $I(t)$ is the fluorescence intensity after some time t, and τ is the fluorescence lifetime determined by measuring the time it takes for the fluorescence intensity to reach $1/e$ of I_0. For systems in which the exciton population can decay by multiple distinct pathways, the expression becomes

$$I(t) = \sum \alpha_i e^{-\frac{t}{\tau}} \qquad \textbf{(1.19)}$$

where the preexponential factor α_i represents the portion of the excited state population decaying along pathway i and $\alpha_1 + \alpha_2 + \alpha_3 + \cdots \alpha_i = 1$. In the case of a multiexponential decay the average lifetime ($< \tau >$) can be calculated according to

$$< \tau > = \sum \frac{a_i \tau_i^2}{a_i \tau_i} \qquad \textbf{(1.20)}$$

Fluorescence lifetimes are often measured using the technique of time-correlated single photon counting (TSCPC).[46] The basic premise of the experiment involves exciting a sample with a vertically polarized pulsed laser and measuring the time between the laser pulse and detection of an emitted photon at a polarization of 54.7º (the magic angle). Detection at the magic angle is necessary to avoid polarization effects on the fluorescence decay curve of the emitted light. These photon events are then binned into time channels used to create a histogram of total photon counts vs. time. This can then be used to generate the fluorescence decay curve of the fluorophore. This is process is represented pictorially in Figure 1.12.

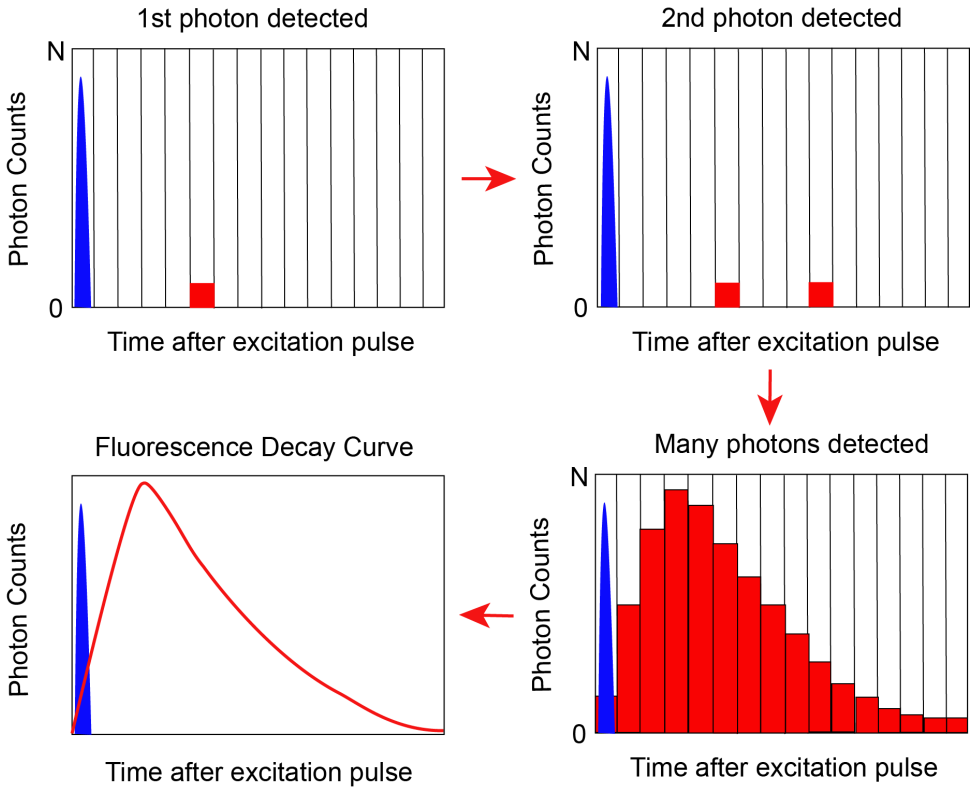

Figure 1.12: Cartoon representation of TCSPC photon binning to generate a fluorescence decay curve where the blue curve represents the excitation pulse of the laser.

In an ideal experiment, the sample would be excited by a δ-pulse of light and the system electronics would be able to detect an emitted photon instantaneously. In this case the TRPL decay curve would be the true decay curve associated with the sample being measured. However, in a real experiment, the laser pulse has a defined temporal width and the instrument's electronic components (i.e., the monochromator, photomultiplier tube, etc.) have temporal lags intrinsic to their operation. For this reason, the collected decay curve is a convolution of the excitation pulse and the electronic instrument response with the true TRPL decay curve. The convolved decay curve takes the form

$$N(t) = \int_0^t L(t')I(t-t')dt' \qquad \textbf{(1.21)}$$

Here, $N(t)$ is the measured intensity at time t, $L(t')$ is the measured instrument response function (IRF), and $I(t-t')$ is the fluorescence intensity from the sample at some time t which originates as a response to a delta-excitation pulse at time t' with amplitude $L(t)$. To obtain $I(t)$, model functions must be iteratively convolved with the measured IRF (typically measured from a purely scattering solution) until a suitable fit between $N(t)$ and $L(t)$ is found. This is typically done using iterative reconvolution with a least squares minimization analysis method.[47]

$$\chi^2_{LS} = \frac{1}{n}\left[\sum_{i=1}^{n} \frac{(N(t_k)-N_c(t_k))^2}{N(t_k)}\right] \qquad \textbf{(1.22)}$$

where $N(t_k)$ is the measured photon counts at time t_k, $N_c(t_k)$ is the modeled number of photon counts at time t_k, and n is the number of data points. A good fit in this method yields a χ^2_{LS} close to 1.

1.2.2 Time – Resolved Fluorescence Anisotropy

Characterization of the time-resolved fluorescence anisotropy has a similar experimental set up to TRPL measurements in which TCSPC is still utilized. However, where TRPL helps to answer questions regarding the fluorescence lifetime of samples, TR-anisotropy is used to answer questions about exciton dynamics through polarization of the emission. The key difference in the experiment involves exciting with vertically polarized light and detecting fluorescence in the vertical (I_{vv}) and horizontal (I_{vh}) planes (Figure 1.13). In the liquid state, absorbing chromophores will be randomly oriented in solution meaning and there will be a distribution of transition dipole moments. For this case I_{vv} is proportional to $< cos^2(\theta) >$ and I_{vh} is proportional to $< sin^2(\theta) >$ and the steady state anisotropy (r) takes the form

$$r = \frac{3<cos^2(\theta)>-1}{2} \qquad \textbf{(1.23)}$$

where all transition dipole moments oriented in the vertical plane gives $r = 1$, and transition dipole moments oriented in the horizontal plane would not be excited by the vertical polarized light giving $r = 0$. Realistically, the fundamental anisotropy (r_0) will reflect the distribution of transitional dipole moment orientations and should have a value between 0 and 1.

$$r_0 = \frac{2}{5}\left(\frac{3cos^2(\beta)-1}{2}\right) \qquad \textbf{(1.24)}$$

Here β is the angle between the absorption and emission dipoles. The two-fifths factor represents the initial selection of the randomly oriented chromophore population and restricts the fundamental anisotropy to $0 < r_0 < 0.4$.

Though steady state anisotropy provides useful information about the initial structural state of absorbing chromophores, it is more interesting from a light-harvesting perspective to understand how excitons travel through the CPEC matrix. After excitation, excitons created on the chromophores with their transition dipole moments vertically aligned will quickly migrate through EET. This motion effectively scrambles the initial polarization, and the excitons find themselves on portions of the CPE chain with a lower energy configuration (i.e., longer chromophores). This happens within a single CPE chain or on an acceptor CPE chain in a CPEC after EET occurs. Thus, the emitted light will show a decay of the fundamental anisotropy with time as this depolarization event takes place. This time-dependent anisotropy can be described as

$$r(t) = \frac{I_{vv}(t) - (G)I_{vh}(t)}{I_{vv}(t) + (2G)I_{vh}(t)} \qquad \textbf{(1.25)}$$

and is represented in Figure 1.13. The numerator is accounting for the differences in photon count intensity for each polarization of the emission. The denominator is the

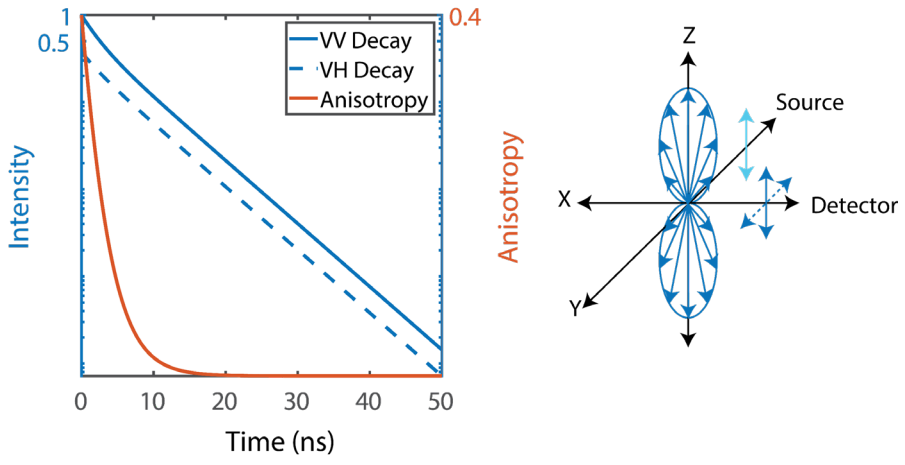

Figure 1.13: Representative time-resolved anisotropy decays (left) in blue, with the calculated anisotropy decay in orange. The ensemble of transition dipoles excited in solution is shown on the right.

total counts where I_{vv} is emission along the z-axis, and the factor of 2 in front of I_{vh} accounts for emission along the x and y-axis relative to the laser table. G is the G-factor that accounts for components of the experimental set up such as optics or the monochromator interacting differently with light polarized in different planes. The G-factor can be measured using

$$G = \frac{\int I_{hv}(t)dt}{\int I_{hh}(t)dt} \qquad \textbf{(1.26)}$$

where the excitation light is horizontally polarized, and the emission is collected in the vertical (I_{hv}) and horizontal directions (I_{hh}).

It is important to note that traditionally, anisotropy has been utilized for small molecule dyes either free in solution or as fluorescent tags attached to biochemical macromolecules of interest. In these experiments, anisotropy can be used to determine rotational diffusion of a dye free in solution or bound where the motion of the chromophore is the main pathway of depolarization. Anisotropy decaying in these types of experiments can be fit using an exponential model

$$r(t) = \sum_j r_0 e^{-\frac{t}{\theta_j}} \qquad \textbf{(1.27)}$$

where θ_j is the rotational correlation time. This model assumes spherical chromophores and the fitting procedure is immediately complicated with a simple deviation from that shape. Not only is it completely inappropriate to assuming chromophores in a CPE to be spherical, but depolarization over time will also be due to a combination of rotational motions of chain segments AND exciton motion via EET. Thus, modeling such a decay becomes increasingly complicated. We have found the use of models proposed by Ludescher et. al. to be a good basis for

interpreting TR-anisotropy of CPEs.[48] For a detailed discussion of these models applied to our CPE systems see Chapter 2.

1.2.3 Fluorescence Microscopy

Fluorescence microscopy has long been utilized as a powerful tool for research into spatial and temporal information regarding cell biology. This often involves the use of fluorescent labeling with small dye molecules such as 4′,6-diamidino-2-phenylindole (aka DAPI). Depending on experimental design and choice of microscope, fluorescent microscopy can help answer a variety of questions regarding microscale morphology, spatial distributions of fluorophores, energy transfer, and even fluorescence lifetimes. Investigating CPEs and CPECs using fluorescence microscopy has the unique advantage of the samples being intrinsically fluorescent. This negates the need for labeling with fluorescent tags that may have undesirable intermolecular interactions within your sample.

Widefield epifluorescence microscopy involves illumination and imaging of light from the entire sample which helps to speed up the imaging process. This can make the use of widefield microscope advantageous for collecting data from large amounts of samples, and for observing samples in real time. The simplicity of wide-field microscopy means it's more accessible and cheaper to use making it an attractive choice for learning the technique of fluorescence microscopy. However, the design of widefield microscopes makes it impossible to exclude out-of-focus or scattered light. For this reason, images taken using widefield microscopes tend to

have lower resolution and are prone to shadow artifacts due to uneven illumination of the sample.

This drawback motivated the development and implementation of confocal microscopes. The main design difference of confocal microscopes is a pinhole aperture introduced to the system that only allows light from a thin focal plane to reach the photomultiplier tube (PMT) detector. When shooting for higher resolution images, the use of laser scanning confocal microscopy is a superior choice of techniques. A comparison of a simplified widefield and confocal microscope design are shown in Figure 1.14.[46] Because of loss of signal due to the smaller sampling volume of confocal scopes, the laser is scanned across the sample, intensity is measured at each position using a PMT, and the image is created pixel-by-pixel.

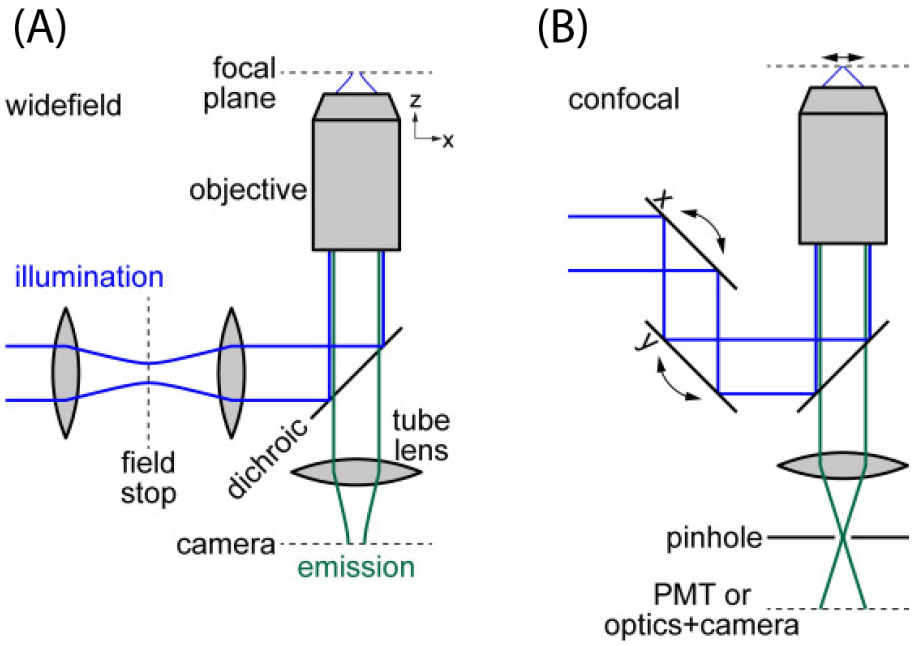

Figure 1.14: Comparison of (A) widefield and (B) confocal microscope designs. Image adapted from Wang et. al.[48]

1.2.4 Fluorescence Lifetime Imaging

Though independently powerful, the combination of TRPL and confocal laser scanning microscopy allows inquiry into fluorescence lifetime distributions at the micron scale. This fluorescence lifetime imaging (FLIM) technique uses TSCPC principles and a high repetition pulsed laser to excite the sample and measures the time between excitation and the detection of a single photon. The key difference of FLIM is that the photon distribution is collected not only over a time interval (t) but also over spatial coordinates (x,y) by tracking the position of the scanning laser beam of the confocal microscope. This produces a collection of lifetimes over a microscopy image area and is represented in Figure 1.15.[46] This lifetime distribution can then be fit using maximum likelihood analysis and raw data can be converted to color coded pixels representing different decay times (Figure 1.16). FLIM results used to characterize the photophysics of CPE simple coacervate

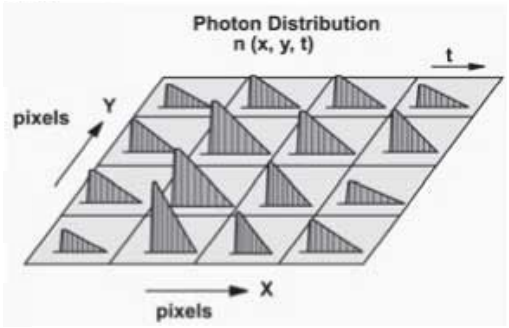

Figure 1.15: Representation of TRPL decay curves collected for individual pixel to create a FLIM image.[46]

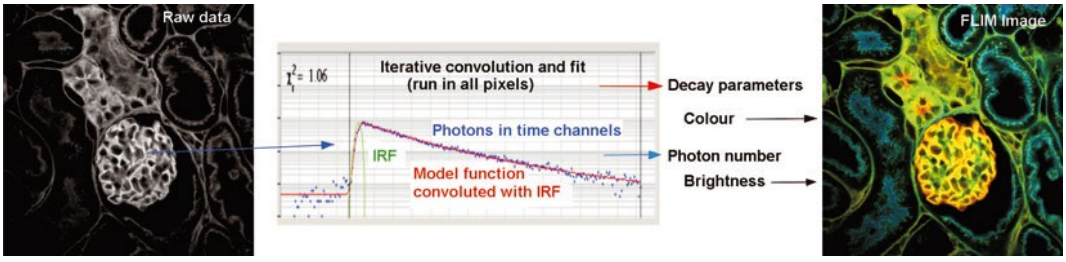

Figure 1.16: Left show the raw FLIM image. In the center is a global decay curve generated using all pixels within the FLIM image and the fit for that data. Right shows the calculated fluorescence decays for each pixel, where specific colors are chosen to represent lifetime ranges.

droplets will be discussed in detail in Chapter 4, and CPE complex coacervates droplets in Chapter 5.

1.2.5 Rheology

Rheology is defined as the science behind the flow and deformation of matter. It is an important technique for the investigation of molecular structure of a material and for evaluating a materials performance under conditions it may experience in its application.[49–53] The relationship between stress (applied force per unit area) and physical deformation (strain) is an intrinsic property of a material that comes about due to short- and long-range intermolecular interactions. Depending on the strength of these interactions your material can take on more solid or liquid properties. For ideal solids, one of the materials properties of interest is the elasticity. This can be determined using the relationship between stress and strain via Hooke's Law

$$\sigma = G \cdot \gamma \qquad \textbf{(1.28)}$$

where σ is stress, G is the elastic modulus of the material, and γ is the strain. For ideal liquids, the equivalent property is the viscosity η which can be calculated using the relationship between stress and shear rate γ_{sr} via Newton's Law.

$$\sigma = \eta \cdot \gamma_{sr} \qquad \textbf{(1.29)}$$

Most materials do not behave as ideal solids or liquids, but rather exhibit materials properties of both solids and liquids. These are termed viscoelastic materials and the stress they experience is related to the combination of the strain and strain shear rate.

$$\sigma = G * \gamma + \eta * \frac{d\gamma}{dt} \qquad \textbf{(1.30)}$$

Thus, investigating this relationship allows for the calculation of the modulus and viscosity of a viscoelastic material. This investigation can be done using a rheometer. Specifically, a strain controlled dual head rheometer with separated motor and transducer was used in this work and is shown in Figure 1.17.[53] Here, a sample is loaded between two plates, the bottom plate rotates with a chosen angular displacement and velocity which are used to calculate the strain and strain shear rate

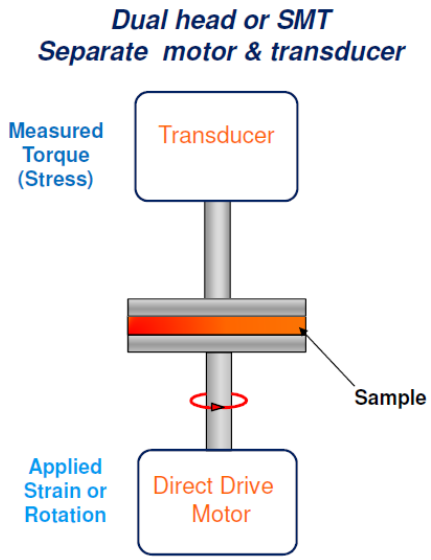

Figure 1.17: Simplified representation of rheomter used for SAOS measurments.[53]

$$\gamma = \theta \cdot K_\gamma \qquad \textbf{(1.31)}$$

$$\gamma_{sr} = \Omega \cdot K_\gamma \qquad \textbf{(1.32)}$$

where θ is the displacement angle equal to the arc length s and the radius of the plate r ($\theta = s/r$), Ω is the angular velocity ($\Omega = \Delta\theta/\Delta t$), and K_γ is the strain constant which depends on the geometry of the chosen plates. This physically deforms the sample, and the mechanical energy is either conserved in an elastic response or dissipated and lost as heat. The torque experienced by the sample is picked up by a transducer at the top plate and is used to calculate the stress

$$\sigma = M \cdot K_\sigma \qquad \textbf{(1.33)}$$

where M is the torque related to the radius of the plate and the force acting at a 90º ($M = r \cdot F$) and K_σ is the stress constant dependent on the geometry of the chosen plates.

Using a rheometer gives access to a variety of flow test, transient test, and oscillatory experiments that can help characterize a material. Because the work herein is focused on the development of **soft** light harvesting materials, we are interested in characterizing the contributions of solid-like and liquid-like behaviors of our samples. To do this we utilize small amplitude oscillatory shear (SAOS) measurements which applies a sinusoidal strain to the sample at a specific angular displacement and amplitude. The sample is then monitored for the resultant stress response and the shift between the strain and stress is the phase angle (δ) (Figure 1.18). The elastic response is an in-phase response (δ=0º), the viscous response is out of phase (δ=90º), and a viscoelastic response would be between the two extremes (0º < δ < 90º). The collective stress of a viscoelastic material is termed the complex stress, which in turn defines the complex modulus, the materials overall resistance to deformation, as

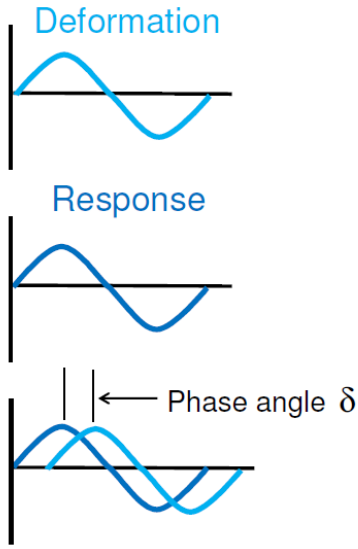

Figure 1.18: Strain (top) and stress (middle) of a SAOS measurement are shown as sign waves where their offset (bottom) is referred to as the phase angle δ.[53]

$$G^* = G' + iG'' \qquad \textbf{(1.34)}$$

where G' is the elastic modulus and is a measure of a materials ability to store mechanical energy, and G'' is the loss modulus and is a measure of the materials ability to dissipate mechanical energy as heat. The relationship between these moduli can be described geometrically using the following relationships: $G' = \cos\delta$, $G'' =$

$\sin\delta$, $G^* = \sqrt{G'^2 + G''^2}$, and $\tan(\delta) = \frac{G''}{G'}$. This last relationship is referred to as the loss tangent and is an excellent metric for how liquid-like a sample is where $\tan(\delta) < 1$ describes a more solid-like sample where the magnitude of the elastic modulus dominates, $\tan(\delta) > 1$ describes a more liquid-like sample where the loss modulus dominates, and $\tan(\delta) = 1$ describes the gelation point of the material. In this work, the relationship between the moduli is investigated in detail for several unique systems in which the molecular interaction of CPEs with various ions is characterized.

1.3 Description of Chapters to Follow

The focus of the following chapters is on investigating the fundamental phase behavior and resultant photophysics of CPEs and CPECs. Chapter 2 presents published work involving a conjugated/non-conjugated polyelectrolyte complex and an atomic salt series. This work led to the formation of a light-active colloidal gel phase with interesting photophysical properties. Chapter 3 discusses published work involving a fully conjugated CPEC complex fluid capable of highly efficient EET. A molecular salt series was used to tune phase behavior of this dense fluid phase. Chapter 4 presents a recently submitted manuscript of a study during which we believe the first true example of liquid, simple coacervate droplets were formed and characterized. This was made possible due to the synthesis of a novel copolymer in our lab by Dr. Gregory Pitch. Chapter 5 discusses the follow up study to the simple coacervate work involving the CPEC complex coacervates formed with a series of these novel copolymers.

1.4 References

(1) Goel, M.; Verma, V. S.; Goel Tripathi, N. Solar Energy: Made Simple for a Sustainbale Future; Springer, 2022.

(2) Lee, N. A.; Gilligan, G. E.; Rochford, J. Solar Energy Conversion. Green Chem. An Incl. Approach **2018**, 309 (September), 881–918. https://doi.org/10.1016/B978-0-12-809270-5.00030-3.

(3) Holmes, A.; Deniau, E.; Lartigau-Dagron, C.; Bousquet, A.; Chambon, S.; Holmes, N. P. Review of Waterborne Organic Semiconductor Colloids for Photovoltaics. ACS Nano **2021**, 15 (3), 3927–3959. https://doi.org/10.1021/acsnano.0c10161.

(4) Xie, L.; Song, W.; Ge, J.; Tang, B.; Zhang, X.; Wu, T.; Ge, Z. Recent Progress of Organic Photovoltaics for Indoor Energy Harvesting. Nano Energy **2021**, 82 (2021), 105770. https://doi.org/10.1016/j.nanoen.2021.105770.

(5) Wang, X.; Sun, Q.; Gao, J.; Wang, J.; Xu, C.; Ma, X.; Zhang, F. Recent Progress of Organic Photovoltaics with Efficiency over 17%. Energies **2021**, 14 (14), 4200. https://doi.org/10.3390/en14144200.

(6) Wang, T.; Kupgan, G.; Brédas, J. L. Organic Photovoltaics: Relating Chemical Structure, Local Morphology, and Electronic Properties. Trends Chem. **2020**, 2 (6), 535–554. https://doi.org/10.1016/j.trechm.2020.03.006.

(7) Sutherland, L. J.; Weerasinghe, H. C.; Simon, G. P. A Review on Emerging Barrier Materials and Encapsulation Strategies for Flexible Perovskite and Organic Photovoltaics. Adv. Energy Mater. **2021**, 11 (34), 2101383. https://doi.org/10.1002/aenm.202101383.

(8) Frischmann, P. D.; Mahata, K.; Würthner, F. Powering the Future of Molecular Artificial Photosynthesis with Light-Harvesting Metallosupramolecular Dye Assemblies. Chem. Soc. Rev. **2013**, 42 (4), 1847–1870. https://doi.org/10.1039/c2cs35223k.

(9) Concepcion, J. J.; House, R. L.; Papanikolas, J. M.; Meyer, T. J. Chemical Approaches to Artificial Photosynthesis. https://doi.org/10.1073/pnas.1212254109.

(10) Tahir, M.; Pan, L.; Idrees, F.; Zhang, X.; Wang, L.; Zou, J. Electrocatalytic Oxygen Evolution Reaction for Energy Conversion and Storage : A Comprehensive Review Nano Energy Electrocatalytic Oxygen Evolution Reaction for Energy Conversion and Storage : A Comprehensive Review. Nano Energy **2017**, 37 (October), 136–157. https://doi.org/10.1016/j.nanoen.2017.05.022.

(11) Mirkovic, T.; Ostroumov, E. E.; Anna, J. M.; Van Grondelle, R.; Govindjee; Scholes, G. D. Light Absorption and Energy Transfer in the Antenna Complexes of Photosynthetic Organisms. Chem. Rev. **2017**, 117 (2), 249–293. https://doi.org/10.1021/acs.chemrev.6b00002.

(12) Fu, J.; Schlenoff, J. B. Driving Forces for Oppositely Charged Polyion Association in Aqueous Solutions: Enthalpic, Entropic, but Not Electrostatic. J. Am. Chem. Soc **2016**, 138, 980–990. https://doi.org/10.1021/jacs.5b11878.

(13) Hollingsworth, W. R.; Magnanelli, T. J.; Segura, C.; Young, J. D.; Bragg, A. E.; Ayzner, A. L. Polyion Charge Ratio Determines Transition between Bright and Dark Excitons in Donor/Acceptor-Conjugated Polyelectrolyte Complexes.

J. Phys. Chem. C **2018**, 122 (39), 22280–22293. https://doi.org/10.1021/acs.jpcc.8b06195.

(14) Walla, P. J. Modern Biophysical Chemistry: Detection and Analysis of Biomolecules, Second Edition; Wiley-VCH Verlag GmbH & Co. KGaA, 2014.

(15) Dirac, P. A. M. The Quantum Theory of the Emission and Absorption of Radiation. R. Soc. Proc. A **1927**, 243–265.

(16) Zhang, J. M.; Liu, Y. Fermi ' s Golden Rule : Its Derivation and Breakdown by an Ideal Model Fermi ' s Golden Rule : Its Derivation and Breakdown by an Ideal Model. Eur. J. Phys. **2016**, 37 (065406), 1–14.

(17) Kasha, M.; Rawls, H. R.; El-Bayoumi, M. A. The Exciton Model In Molecular Spectroscopy. Pure Appl. Chem. **1965**, 11 (3–4), 371–392. https://doi.org/10.1351/pac196511030371.

(18) Spano, F. C.; Silva, C. H- and J-Aggregate Behavior in Polymeric Semiconductors. Annu. Rev. Phys. Chem. **2014**, 65, 477–500. https://doi.org/10.1146/annurev-physchem-040513-103639.

(19) Olaya-Castro, A.; Scholes, G. D. Energy Transfer from Förster-Dexter Theory to Quantum Coherent Light-Harvesting. Int. Rev. Phys. Chem. **2011**, 30 (1), 49–77. https://doi.org/10.1080/0144235X.2010.537060.

(20) Sahoo, H. Förster Resonance Energy Transfer - A Spectroscopic Nanoruler: Principle and Applications. J. Photochem. Photobiol. C Photochem. Rev. **2011**, 12 (1), 20–30. https://doi.org/10.1016/j.jphotochemrev.2011.05.001.

(21) Sing, C. E.; Perry, S. L. Recent Progress in the Science of Complex Coacervation. Soft Matter **2020**, 16 (12), 2885–2914.

https://doi.org/10.1039/d0sm00001a.

(22) Fu, J.; Fares, H. M.; Schlenoff, J. B. Ion-Pairing Strength in Polyelectrolyte Complexes. Macromolecules **2017**, 50, 1066–1074. https://doi.org/10.1021/acs.macromol.6b02445.

(23) Black, K. A.; Priftis, D.; Perry, S. L.; Yip, J.; Byun, W. Y.; Tirrell, M. Protein Encapsulation via Polypeptide Complex Coacervation. ACS Macro Lett. **2014**, 3 (10). https://doi.org/10.1021/mz500529v.

(24) Mountain, G. A.; Keating, C. D. Formation of Multiphase Complex Coacervates and Partitioning of Biomolecules within Them. Biomacromolecules **2020**, 21 (2), 630–640. https://doi.org/10.1021/acs.biomac.9b01354.

(25) Veis, A.; Bodor, E.; Mussell, S. Molecular Weight Fractionation and the Self-suppression of Complex Coacervation. Biopolymers **1967**, 5 (1), 37–59. https://doi.org/10.1002/bip.1967.360050106.

(26) Drobot, B.; Iglesias-Artola, J. M.; Le Vay, K.; Mayr, V.; Kar, M.; Kreysing, M.; Mutschler, H.; Tang, T. Y. D. Compartmentalised RNA Catalysis in Membrane-Free Coacervate Protocells. Nat. Commun. **2018**, 9 (1), 3643. https://doi.org/10.1038/s41467-018-06072-w.

(27) Kaur, S.; Weerasekare, G. M.; Stewart, R. J. Multiphase Adhesive Coacervates Inspired by the Sandcastle Worm. ACS Appl. Mater. Interfaces **2011**, 3 (4), 941–944. https://doi.org/10.1021/am200082v.

(28) Last, M. G. F.; Deshpande, S.; Dekker, C. PH-Controlled Coacervate-Membrane Interactions within Liposomes. ACS Nano **2020**, 14 (4), 4487–

4498. https://doi.org/10.1021/acsnano.9b10167.

(29) Deshpande, S.; Dekker, C. Studying Phase Separation in Confinement. Curr. Opin. Colloid Interface Sci. **2021**, 52, 101419. https://doi.org/10.1016/j.cocis.2021.101419.

(30) Li, L.; Rumyantsev, A. M.; Srivastava, S.; Meng, S.; De Pablo, J. J.; Tirrell, M. V. Effect of Solvent Quality on the Phase Behavior of Polyelectrolyte Complexes. Macromolecules **2021**, 54 (1), 105–114. https://doi.org/10.1021/acs.macromol.0c01000.

(31) Li, L.; Srivastava, S.; Meng, S.; Ting, J. M.; Tirrell, M. V. Effects of Non-Electrostatic Intermolecular Interactions on the Phase Behavior of PH-Sensitive Polyelectrolyte Complexes. Macromolecules **2020**, 53 (18), 7835–7844. https://doi.org/10.1021/acs.macromol.0c00999.

(32) Johnson, N. R.; Wang, Y. Coacervate Delivery Systems for Proteins and Small Molecule Drugs. Expert Opin. Drug Deliv. **2014**, 11 (12), 1829–1832. https://doi.org/10.1517/17425247.2014.941355.

(33) Meng, S.; Ting, J. M.; Wu, H.; Tirrell, M. V. Solid-to-Liquid Phase Transition in Polyelectrolyte Complexes. Macromolecules **2020**, 53 (18), 7944–7953. https://doi.org/10.1021/acs.macromol.0c00930.

(34) Adhikari, S.; Leaf, M. A.; Muthukumar, M. Polyelectrolyte Complex Coacervation: Effects of Concentration Asymmetry. J. Chem. Phys. **2018**, 149, 163308. https://doi.org/10.1063/1.5029268.

(35) Stewart, R. J.; Wang, C. S.; Song, I. T.; Jones, J. P. The Role of Coacervation and Phase Transitions in the Sandcastle Worm Adhesive System. Adv. Colloid

Interface Sci. **2017**, 239 (1), 88–96. https://doi.org/10.1016/j.cis.2016.06.008.

(36) Adhikari, S.; Leaf, M. A.; Muthukumar, M. Polyelectrolyte Complex Coacervation by Electrostatic Dipolar Interactions. J. Chem. Phys. **2018**, 149 (16). https://doi.org/10.1063/1.5029268.

(37) Messaoud, G. Ben; Promeneur, L.; Brennich, M.; Roelants, S. L. K. W.; Le Griel, P.; Baccile, N. Complex Coacervation of Natural Sophorolipid Bolaamphiphile Micelles with Cationic Polyelectrolytes †. Green Chem. **2018**, 20, Complex coacervation of polyelectrolytes with surf. https://doi.org/10.1039/c8gc01531g.

(38) Veis, A. A Review of the Early Development of the Thermodynamics of the Complex Coacervation Phase Separation. Adv. Colloid Interface Sci. **2011**, 167 (1–2), 2–11. https://doi.org/10.1016/j.cis.2011.01.007.

(39) Black, K. A.; Priftis, D.; Perry, S. L.; Yip, J.; Byun, W. Y.; Tirrell, M. Protein Encapsulation via Polypeptide Complex Coacervation. ACS Macro Lett. **2014**, 3, 1088–1091. https://doi.org/10.1021/mz500529v.

(40) Priftis, D.; Xia, X.; Margossian, K. O.; Perry, S. L.; Leon, L.; Qin, J.; De Pablo, J. J.; Tirrell, M. Ternary, Tunable Polyelectrolyte Complex Fluids Driven by Complex Coacervation. **2014**. https://doi.org/10.1021/ma500245j.

(41) Huang, J.; Morin, F. J.; Laaser, J. E. Charge-Density-Dominated Phase Behavior and Viscoelasticity of Polyelectrolyte Complex Coacervates. Macromolecules **2019**, 52 (13), 4957–4967. https://doi.org/10.1021/acs.macromol.9b00036.

(42) Le, M. L.; Rawlings, D.; Danielsen, S. P. O.; Kennard, R. M.; Chabinyc, M.

L.; Segalman, R. A. Aqueous Formulation of Concentrated Semiconductive Fluid Using Polyelectrolyte Coacervation. ACS Macro Lett. **2021**, 10 (8), 1008–1014. https://doi.org/10.1021/acsmacrolett.1c00354.

(43) Danielsen, S. P. O.; Nguyen, T.-Q.; Fredrickson, G. H.; Segalman, R. A. Complexation of a Conjugated Polyelectrolyte and Impact on Optoelectronic Properties. ACS Macro Lett. **2019**, 8 (1), 88–94. https://doi.org/10.1021/acsmacrolett.8b00924.

(44) Johnston, A. R.; Perry, S. L.; Ayzner, A. L. Associative Phase Separation of Aqueous π-Conjugated Polyelectrolytes Couples Photophysical and Mechanical Properties. Chem. Mater. **2021**, 33 (4), 1116–1129. https://doi.org/10.1021/acs.chemmater.0c02424.

(45) Johnston, A. R.; Minckler, E. D.; Shockley, M. C. J.; Matsushima, L. N.; Perry, S. L.; Ayzner, A. Conjugated Polyeelctrolyte-Based Complex Fluids as Aqueous Exciton Transport Networks. Angew. Chemie - Int. Ed. **2022**, 134 (20), 1–12. https://doi.org/10.1002/anie.202117759.

(46) Wang, Y. L.; Grooms, N. W. F.; Civale, S. C.; Chung, S. H. Confocal Imaging Capacity on a Widefield Microscope Using a Spatial Light Modulator. PLoS One **2021**, 16 (2 February), 1–17. https://doi.org/10.1371/journal.pone.0244034.

(47) Santra, K.; Zhan, J.; Song, X.; Smith, E.; Vaswani, N.; Petrich, J. W. What Is the Best Method to Fit Time-Resolved Data? A Comparison of the Residual Minimization and the Maximum Likelihood Techniques As Applied to Experimental Time-Correlated, Single- Photon Counting Data. Phys. Chem. B

2016, 120, 2484–2490. https://doi.org/10.1021/acs.jpcb.6b00154.

(48) Ludescher, R. D.; Peting, L.; Hudson, S.; Hudson, B. Time-Resolved Fluorescence Anisotropy for Systems with Lifetime and Dynamic Heterogeneity. Biophys. Chem. **1987**, 28 (1), 59–75. https://doi.org/10.1016/0301-4622(87)80075-3.

(49) Srivastava, S. S.; Tirrell, M. V. Structure and Rheology of Polyelectrolyte Complex Coacervates †. Soft Matter **2018**, 14, 2454. https://doi.org/10.1039/c7sm02041d.

(50) Worldwide, M. I. WHITEPAPER A Basic Introduction to Rheology. **2016**.

(51) De, P. R.; Mendes, S.; Alicke, A. A.; Zurich, E.; Thompson, R. L. Parallel-Plate Geometry Correction for Transient Rheometric Experiments Machine Learning Techniques for Accuracy Improvement of RANS Simulations View Project Transient Aspects of the Polymer Induced Drag Reduction Phenomenon View Project. Artic. Appl. Rheol. **2014**. https://doi.org/10.3933/ApplRheol-24-52721.

(52) Liu, Y.; Momani, B.; Henning Winter, H.; Perry, S. L. Rheological Characterization of Liquid-to-Solid Transitions in Bulk Polyelectrolyte Complexes †. | Soft Matter **2017**, 13, 7332. https://doi.org/10.1039/c7sm01285c.

(53) Krishna, S. Rheology Theory and Applications https://people.clarkson.edu/~skrishna/DHR_Rheology_Theory.pdf.

Chapter 2

Associative Phase Separation of Aqueous π-Conjugated Polyelectrolytes Couples Photophysical and Mechanical Properties

---

Acknowledgements: This chapter was originally published in Chemistry of Materials with the following authorship: Anna R. Johnston, Sarah L. Perry, and Alexander L. Ayzner. Anna Johnston carried out all experimental work, data analysis, and originally crafted the manuscript. Sarah Perry provided valuable insight and interpretation of the rheology data and edited the manuscript. Alexander Ayzner edited the manuscript and oversaw the project. I would like to extend a big thank you to both Alex and Sarah for their help.

This material is based upon work supported by the National Science Foundation under grant no. 1848069 and the ACS Petroleum Research Fund New Directions (grant no. 60244- ND7). This material is also based upon work supported by the National Science Foundation Graduate Research Fellowship under grant no. DGE-1842400. Part of this work was performed at the Stanford Nano Shared Facilities (SNSF), supported by the National Science Foundation under award ECCS-1542152. We would also like to thank Dr. Carmen Segura and Dr. Brian Dreyer for their helpful discussions regarding this work.

Abstract: The associative phase separation of water-soluble polyelectrolytes is important across many different fields including food science, biomedicine, materials science, and prebiotic organization. Specifically, associative phase separation leading to complex coacervation of oppositely charged polyelectrolytes has been extensively studied to inform research into synthetic cell mimics. However, the phase behavior of conjugated polyelectrolytes (CPEs), macromolecules analogous to chromophores found in light harvesting organelles, has been investigated only minimally. A

systematic understanding of the influence of ionic strength on the phase behavior of CPEs could provide insights into the potential for these systems to form complex coacervates and improve control over the photophysical properties of these materials. In this study, the influence of increasing ionic strength (0−5.0 M) of three simple salts (LiBr, KBr, and CsBr) on the phase behavior of a cationic CPE [poly(fluorene-alt-phenylene)] and an anionic non-conjugated polyelectrolyte [poly(4-styrenesulfonate)] complex is interrogated. Associative phase separation into diluted and concentrated polyelectrolyte phases was found to occur regardless of salt type. We report on the phase composition and influence of the ion type on the photophysical properties of the concentrated phase, where the nature of the counter cation was found to manipulate the radiative decay rate and the exciton diffusion dynamics. Additionally, we demonstrate the ability of the polymer-rich phase to recruit a nonpolar, fullerene-based electron acceptor PC[70]BM, resulting in photoluminescence quenching likely due to photoinduced electron transfer. Our findings show promise for the formation of CPE-based coacervate-like phases and highlight the importance of the interactions of the complex with ions differing in polarizability and size. Additionally, the potential for these systems to form liquid electron donor/acceptor bulk heterojunctions has great implications for their use in optoelectronics.

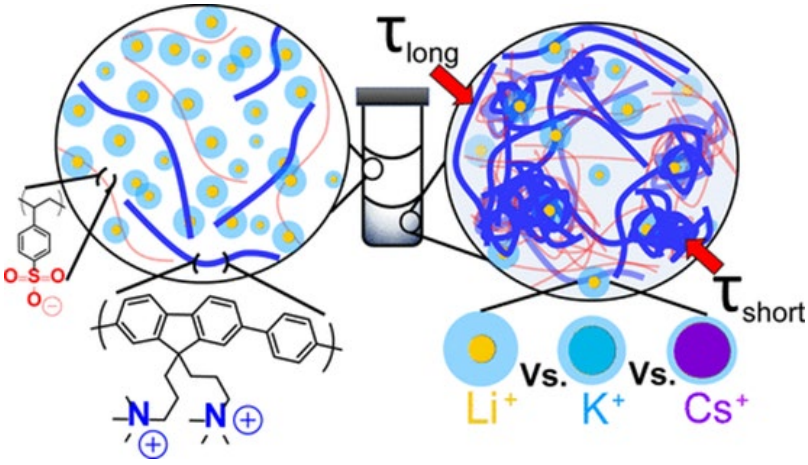

2.1 Introduction

Due to their aqueous solubility and sensitivity to ionic strength, polyelectrolytes have found use in a number of materials and biomedical applications. A remarkable and highly useful property of this class of polymeric materials is their rich phase behavior, which usually depends strongly on salt concentration. When oppositely charged polyelectrolytes are combined in aqueous solution, they can readily ion-pair to form complexes.[1-7] This can lead to associative phase separation, thereby forming a dilute solution with a low total polyelectrolyte concentration coexisting with a concentrated phase that is highly enriched in polyelectrolyte complexes. When the concentrated phase is liquid, it is referred to as a polyelectrolyte complex coacervate.

Complex coacervates have been utilized heavily in food science and the personal care industry; more recently they have been investigated for drug delivery applications, underwater adhesives, and printable electronics.[1,8-15] Notably, this phenomenon has also gained interest due to the hypothesis that coacervation may have contributed to early cell development.[8,10,16,17] This hypothesis states that phase separation of charged biological macromolecules led to the formation of membraneless organelles that later became encapsulated by lipid membranes and thus effectively compartmentalized. Coacervation in synthetic systems is currently being studied to better understand early cell development and to inform efforts into the design of synthetic cell mimics.

Unlike most polyelectrolytes under investigation, conjugated polyelectrolytes (CPEs) stand apart due to the presence of polarizable π-electrons, which lead to electronic states that are delocalized along the polymer backbone. This results in a strong dependence of optoelectronic properties such as light absorption, light emission, and excited-state energy migration on the conformation of the CPE chain. We have previously shown that oppositely charged CPEs can be assembled into aqueous complexes in dilute solution, leading to the emergence of new electronic states. The CPEs within the complex were chosen to act as an electronic energy donor/acceptor pair and were shown to support extremely rapid electronic energy transfer on a timescale commensurate with natural chromophore-based antennae found in light-harvesting organelles.[18]

It is intriguing to wonder whether the associative phase separation of CPEs can be used to form concentrated phases that are analogous to non-conjugated polyelectrolyte systems. Doing so would result in a strongly coupled many-body system, where polymer excited states (excitons) would be able to migrate rapidly between CPE chains within the dense phase. The ionic atmosphere could then be used to judiciously manipulate exciton dynamics, in principle leading to tunable optoelectronic properties in a fluid aqueous system. Realization of such a system is of interest as a membraneless, photophysically active component of an overarching artificial light-harvesting system that mimics a set of core functions of a light-harvesting organelle.

Though complex coacervation using non-conjugated polyelectrolytes continues to be an active area of research, phase behavior in conjugated systems has been studied to a much lesser degree. Danielsen, Segalman*, et al.* studied the associative phase separation of polythiophene-based CPE with a non-conjugated oppositely charged polyelectrolyte in water/THF mixtures.[15] Depending on the mixture composition, they reported formation of both coacervate phases and what they referred to as coacervate-precipitates, i.e., phases with properties that appear to be intermediate between liquids and solids. However, to the best of our knowledge, aqueous associative phase separation of CPEs in the presence of substantial amounts of excess salt has not been studied to date.

In this report, we interrogate associative phase separation between a model cationic CPE based on a poly(fluorene-*alt*-phenylene) backbone and a model oppositely charged non-conjugated polyelectrolyte (Figure 2.1). With increasing ionic strength, we find evidence for the formation of a coacervate-like phase with a microstructure that resembles a colloidal gel. To keep the investigation tractable, we focus on the influence of simple cations (Li^+, K^+, Cs^+) with a fixed bromide counterion. We then interrogate the phase composition and photophysical properties of the CPE within both the dilute and concentrated phases. Using time-resolved photoluminescence (PL) and time-resolved PL anisotropy measurements, we show that the small ion nature and concentration exerts a strong influence on the photophysical properties of the dense phase. PL anisotropy dynamics of the dense phase show nonclassical, heterogeneous decay behavior indicative of distinct sub-ensembles of fluorophore environments with differing characteristic PL

depolarization times. We find evidence that the desolvation free energy and the polarizability of the cation influence phase behavior of the complex via the cation interaction with the polarizable π-electrons of the CPE backbone. Furthermore, we show that the conjugated backbone of the CPE can help recruit nonpolar organic electron acceptors with vanishing aqueous solubilities into the dense phase, leading to PL quenching likely due to photoinduced electron transfer. Our results imply that salt-mediated phase separation in CPE-based systems holds substantial promise for the construction of tunable optically active systems in aqueous environments. The systems also serve as a testbed to interrogate fundamental many-body interactions between ions and highly delocalized π-electrons.

2.2 Results

To prepare polyelectrolyte complex solutions, we fixed the total polymer concentration and the stoichiometric polyion charge ratio, while varying the amount and type of simple salt ions. The polyanion was poly(4-styrenesulfonate) (NaPSS), while the polycation was a CPE containing a derivative of poly(fluorene-*alt*-phenylene) (PFPI). The chemical structures of the polyelectrolytes

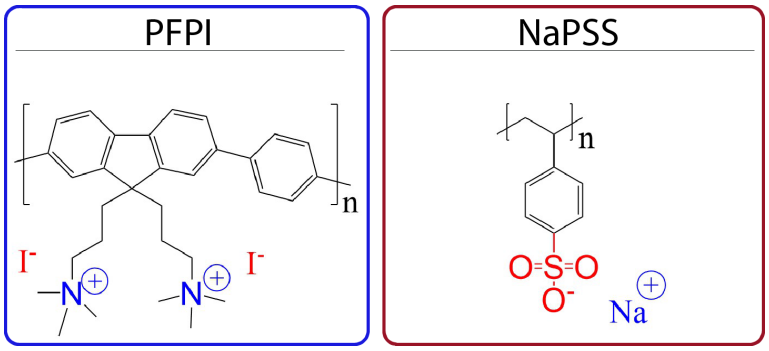

Figure 2.1: Chemical structures of the conjugated cationic polyelectrolyte, poly([fluorene]-*alt*-[phenylene]) (PFPI), and the nonconjugated anionic polyelectrolyte, poly(4-styrenesulfonate) (NaPSS).

are shown in Figure 2.1. CPEs may readily interact with salt ions via, e.g., ion-π interactions, which depend on the ion charge density and thus the ionic radius. Given the highly polarizable nature of extended π-electrons along the CPE backbone, we anticipate that the latter may also couple to the polarizability of the small ions, particularly in the high-ionic-strength limit of interest to this work. Our specific choice of the salt series was made to partially ascertain the influence of cation-π interactions on the phase behavior and optical properties of our half-conjugated polyelectrolyte complex solutions. To keep this investigation tractable, we chose to use bromide salts with three alkali metal cations arranged in order of decreasing charge density and increasing polarizability: Li^+, K^+ and Cs^+. Table 1 lists the relevant aqueous ionic radii, mean ion-water distance, charge densities, dipolar polarizabilities, and Gibbs free energies of aqueous solvation for the ions used in this work.[20,21,48]

Table 2.1: Characteristics of the monovalent cation series.[20,21,48,50,51]

Ion	HydrationRadius (Å)	Charge Density ($Å^{-3}$)	Dipolar Polarization ($Å^3$)	ΔG_{solv} (kcal/mol)
Li^+	3.82	0.54	0.032	-97.8
K^+	3.31	0.09	0.8-1.2	-54.9
Cs^+	3.29	0.05	2.4-3.1	-46.7

2.2.1 Phase Behavior

Figure 2.2 shows photographs of the aqueous polyelectrolyte complex samples before centrifugation for the three salt types after a waiting period of 24

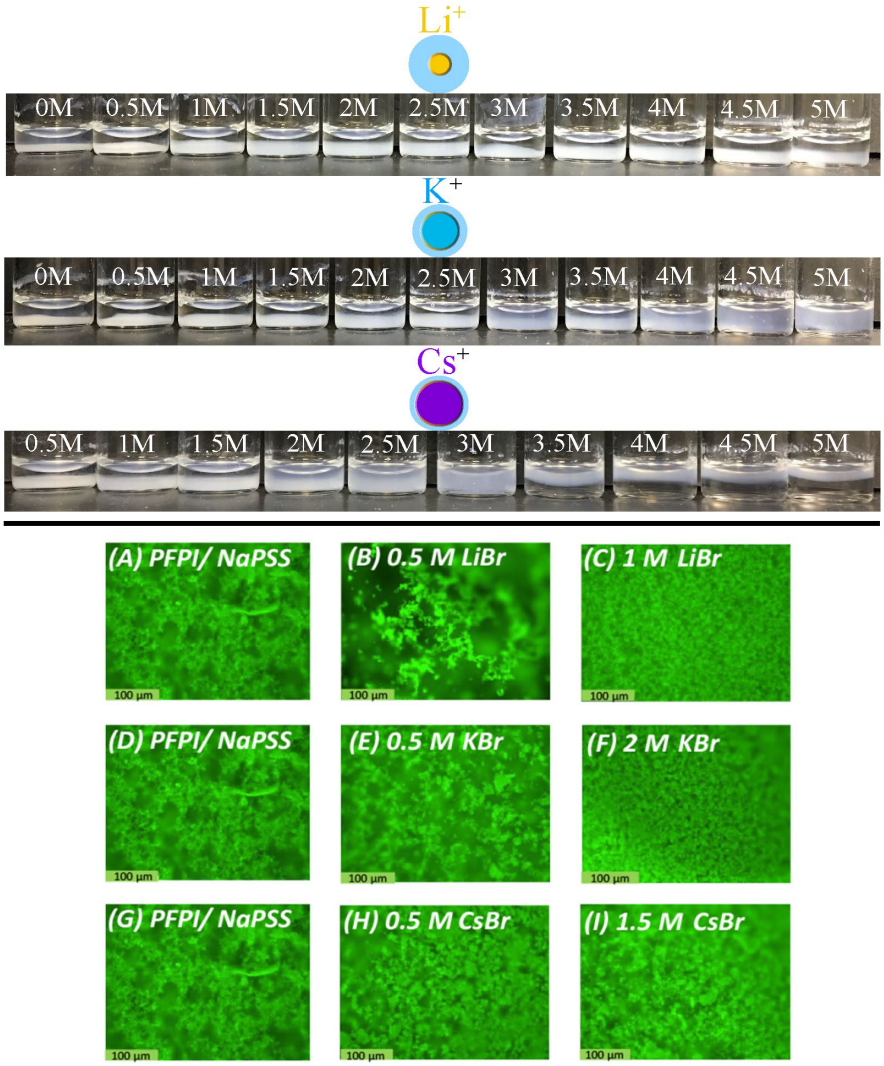

Figure 2.2: Top: Pictures of PFPI/NaPSS complex solutions exposed to increasing LiBr, KBr, CsBr concentrations. Cartoons representing ionic and hydration radii of cations are drawn to relative scale using values from Table 2.1. Bottom: Fluorescent micrographs of PFPI/NaPSS complex solution with added LiBr (A-C), KBr (D-F), and CsBr (G-I) at salt concentrations before and after the nominal 'solid-like' to 'liquid-like' transition determined via rheology.

hours that allowed the solutions to settle. Visual inspection confirmed that most solutions exhibit phase separation, herein one of the phases appears to be a dilute solution. We observe that the concentrated phase was denser than the corresponding polymer-poor supernatant for both LiBr and KBr. Surprisingly, the density of the CsBr concentrated phase appeared to be smaller than that of the supernatant at high

ionic strength (< 3 M). We used optical microscopy to ascertain whether the liquid droplet formation commonly associated with liquid-liquid phase separation was readily apparent (Figure 2.2A-I). We did not observe liquid droplets but rather a structure that resembled a colloidal gel with a morphology that changed with increasing salt concentration. The gel structure appears to densify as ionic strength is increased, with the particle size gradually decreasing.

We collected similar images of samples containing PFPI at the same concentration but in the absence of NaPSS (Figure AI.1). Visual inspection of PFPI in the absence of NaPSS also shows phase separation, albeit with a much smaller concentrated phase. We observe a clear transition from precipitant (0.5 M of each salt) to a concentrated phase that is less opaque and exhibits lower interfacial tension between the layers at higher ionic strength. Microscopy reveals aggregate formation comparable to the low ionic strength (i.e. 0.5 M) solutions of the complex (Figure 2.2B, E, and H). A similar phase reversal as the high ionic strength CsBr samples was seen for the concentrated phase with PFPI alone in the presence of CsBr (2.5 M, 5 M) and KBr (5 M). However, in the high-salt-concentration limit, the morphology of PFPI/NaPSS differs substantially from that of PFPI alone. Whereas the former resembles a closely packed colloidal gel, the latter appears like a collection of largely small, disconnected fractal particles. Interestingly, the concentrated phase of pure PFPI samples at high ionic strength (Figure AI.1C, D) are notable exceptions, with images showing what appears to be the onset of a colloidal gel.

To quantify the phase separation and the partitioning of the CPE between the two phases in PFPI/NaPSS complex solutions, we first took advantage of the large extinction coefficient of PFPI to characterize the dilute phase following centrifugation. Light absorption measurements of the dilute phase of each sample indicate the presence of PFPI, which we converted to concentration using the molar extinction coefficient of aqueous PFPI in isolation. We find an increase in PFPI concentration with increasing salt concentration across all three salt types, shown in Figure 2.3A . While this trend could generally be expected for complex coacervate-type materials,[7,22-24] we note that KBr leads to a larger increase in PFPI concentration

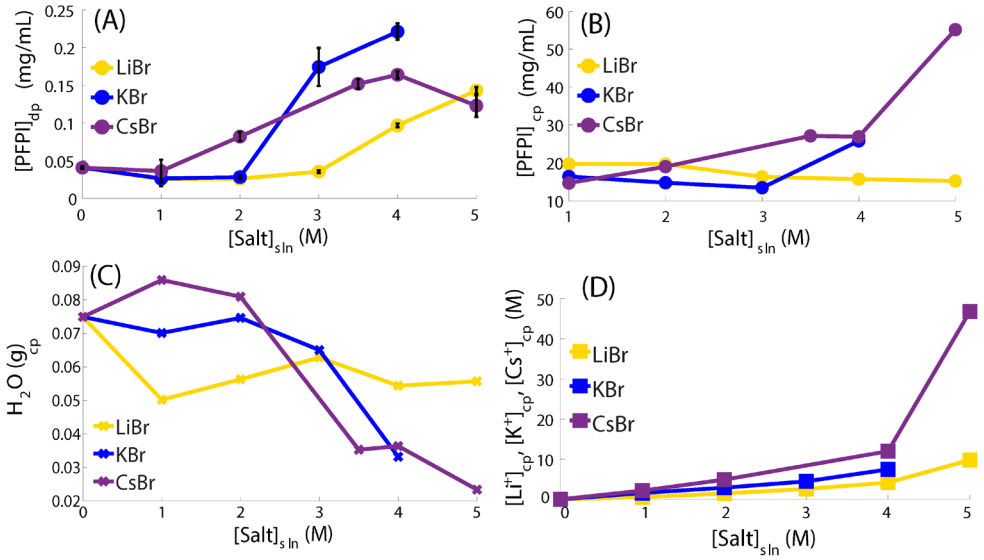

Figure 2.3: Phase composition. (A) Concentration of PFPI in the dilute phase ($[PFPI]_{dp}$) at each salt concentration for each salt type, as determined via UV-Vis. (B) Concentration of PFPI in the concentrated phase ($[PFPI]_{cp}$) determined from $[PFPI]_{dp}$ and phase volumes. (C) Amount of water in concentrated phase determined via lyophilization. (D) Cation concentration in the concentrated phase determined using ICP-OES dilute phase concentrations and phase volumes.

in the dilute phase relative to the other salts. For most salt concentrations, both KBr and CsBr lead to significantly more PFPI in the dilute phase relative to LiBr.

We also find a nonmonotonic ~5-10 nm spectral redshift of the PFPI absorption spectrum in the dilute phase, as well as subtle changes in the spectrum shape with increasing salt concentration (Figure AI.2A-C). To collectively quantify these effects, in Figure AI.2D we have plotted the first moment of the absorption spectrum in energy space as a function of salt concentration. This first moment decreases slightly upon addition of 0.5 M salt for all salt types, which is largely due to a redshift. For CsBr, the first moment then increases slowly but monotonically with increasing salt concentration, whereas for LiBr the change is nonmonotonic. For KBr, the moment is largely unchanged after the initial drop and subsequent rise at 1 M. Together, the data imply that the ensemble of PFPI chromophores in the dilute phase depends relatively weakly on the cation nature.

Using the calculated concentration of PFPI in the dilute phase ($[PFPI]_{dp}$) and the estimated phase volumes following centrifugation (Table AI.1), the concentration of PFPI in the concentrated phase ($[PFPI]_{cp}$) of each sample was determined. Figure 2.3B shows that is ~20 mg/mL $[PFPI]_{cp}$ at [LiBr] = 1 M, and $[PFPI]_{cp}$ is comparable for all three salts up to 2 M. $[PFPI]_{cp}$ decreases slightly as [LiBr] is increased past 1 M, while $[PFPI]_{cp}$ undergoes a substantial increase with increasing [KBr] and [CsBr] over the same salt concentration range. Interestingly, $[PFPI]_{cp}$ is well above 10

mg/mL, which is the concentration at which pure PFPI forms a hydrogel in an aqueous solution with no excess salt.

Further phase composition analysis was carried out to determine water and cation content. Using gravimetric analysis and lyophilization, we estimate that the water content in the concentrated phase is quite small. Using our estimated phase volumes, we find a water concentration of order 0.1 mM. Figure 2.3C shows that the water mass decreases with increasing ionic strength. This suggests that as more salt is available in solution, more ions enter the complex and displace water. This is supported by the cation concentration increase in the concentrated phase shown in Figure 2.3D. These values were obtained using the dilute phase ion concentration via ICP-OES analysis (Figure AI.3B) and phase volumes (Table AI.1). The particularly large $[PFPI]_{cp}$ and Cs^+ concentration in the concentrated phase at 5 M total [CsBr] is a direct consequence of the drop in phase volume.

2.2.2 Rheology

Having characterized the PFPI composition of the dilute phase, the nature of the concentrated phase was then interrogated. The question to be answered is, can a π-conjugated polyelectrolyte complex coacervate (πPCC) be formed using salt-induced phase separation in aqueous solution? Here, we turned to rheology to characterize the viscoelastic properties of the concentrated phase of each sample. Specifically, we preformed small-amplitude oscillatory shear (SAOS) measurements, in which a specified sinusoidal strain is applied at an angular frequency ω, and the resultant

stress is measured. Phase-separated samples were centrifuged before carefully extracting the concentrated phase prior to measurements.

The mechanical response of a viscoelastic material is conveniently described in terms of the complex frequency-dependent modulus. The time-dependent ratio of the applied stress (σ) to the material strain (γ) in a SAOS measurement is given by a combination of an in-phase and an out-of-phase component as

$$\frac{\sigma(\omega,t)}{\gamma} = G' \sin(\omega t) + G'' \cos(\omega t) \qquad \textbf{(2.1)}$$

This expression includes the real part of the complex modulus, or the elastic modulus (G'), which is related to the stored elastic energy upon deformation. The purely imaginary loss modulus (G'') describes energy dissipation. Under sinusoidal shear, the dissipative term lags the elastic term by a phase angle δ, the (loss) tangent of which is given by

$$\tan(\delta) = \frac{G''}{G'} \qquad \textbf{(2.2)}$$

A $\tan(\delta) < 1$ is indicative of a primarily solid-like, elastic response where G'' dominates over G', whereas the opposite is true for samples with predominantly viscous, liquid-like response. Figures 2.4A, 4B and 4C show the storage and loss moduli at select ion concentrations as a function of ω in the presence of LiBr, KBr and CsBr, respectively.

The frequency sweep data show a trend of decreasing modulus with increasing salt concentration, as is expected for polyelectrolyte complex materials (Figure 2.4).[24-28] The viscoelastic response of the complexes prepared in the absence of added salt is dominated by G' over the entire range of frequencies sampled, indicating that it behaves largely as an elastic solid. However, with increasing salt concentration we observe a change in the viscoelastic response, with samples

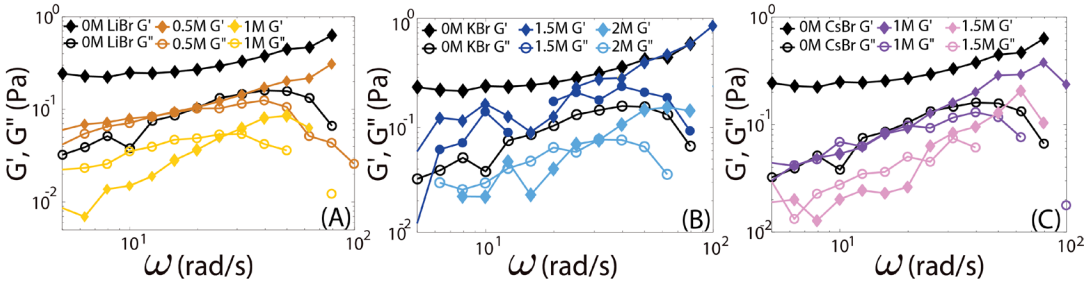

Figure 2.4: SOAS frequency sweeps showing select storage (G') and loss (G") moduli for PFPI/NaPSS complex with added (A) LiBr, (B) KBr, and (C) CsBr.

prepared at higher salt concentrations showing behavior that is dominated by G'' at low frequency and G' at higher frequency. These trends can also be observed by plotting the loss tangent as a function of ω (Figures 2.5A-C), with more viscous, liquid-like behavior emerging at salt concentrations around 1 M LiBr, 2.0 M KBr, and 1.5 M CsBr. It is worth mentioning that the low viscosity of the high-ionic-strength samples (i.e., 2 - 3 M KBr, 1.5 - 3.5 M CsBr) introduced more noise in low-frequency measurements as the measured stress approaches the instrumental limit. This suggests that the strength and/or number of interaction regions in the complex decreases with increasing ionic strength, likely due to the large increase in ion content of the complex that can competing with the electrostatic interactions between the polyelectrolytes themselves. Overall, the viscoelastic response of these materials

appears similar to that of a polymer melt or colloidal gel, which has been reported previously for a range of polymeric complex coacervates.[24,25,26,28]

While the trends in the frequency-dependent viscoelastic response are similar to those reported for other polyelectrolyte complex materials, it is worth noting the extremely low magnitude of the modulus overall. For example, the modulus of solid-like NaPSS in complex with poly(diallyldimethylammonium chloride) (PDADMAC) in the presence of low concentrations of KBr was in the range of 10^4-10^5 Pa.[24] However, for PFPI/NaPSS complexes, the highest value of the modulus is on the order of 1 Pa. This dramatic difference in the modulus could be explained by the very low water content and the colloidal gel-like morphology of the complex solution.

Defining the liquid- or solid-like character of a viscoelastic material can be challenging as this response is generally a function of frequency. However, polyelectrolyte complex coacervates have been shown to undergo salt dependent solidification that can be described as a physical gelation.[24] The critical gel point can be identified based on the presence of a frequency invariant response in the material. This transition can be more clearly observed by plotting the loss tangent as a function of salt concentration at different ω (Figures 2.5D-F). We break down the response of the material into three regions. In Figures 2.5D-F, the area left of the black dotted line on each plot roughly corresponds to salt concentrations which exhibit a solid-like material response. Interestingly, the addition of salt does not appear to have a significant effect on the loss tangent of the solid material, which is different from previous reports.[24] The area between the black and blue dotted lines corresponds to

the region where a solid-to-liquid transition occurs, and the area right of the blue dotted line corresponds to concentrations which exhibit a more viscous, liquid-like response. The regions which show evidence of a liquid-like response for each salt type were found to be: 1 - 5 M for LiBr; 2 - 4 M for KBr; and 1.5 - 5 M for CsBr, excluding 3 M CsBr, for which no phase separation was observed on the timescale

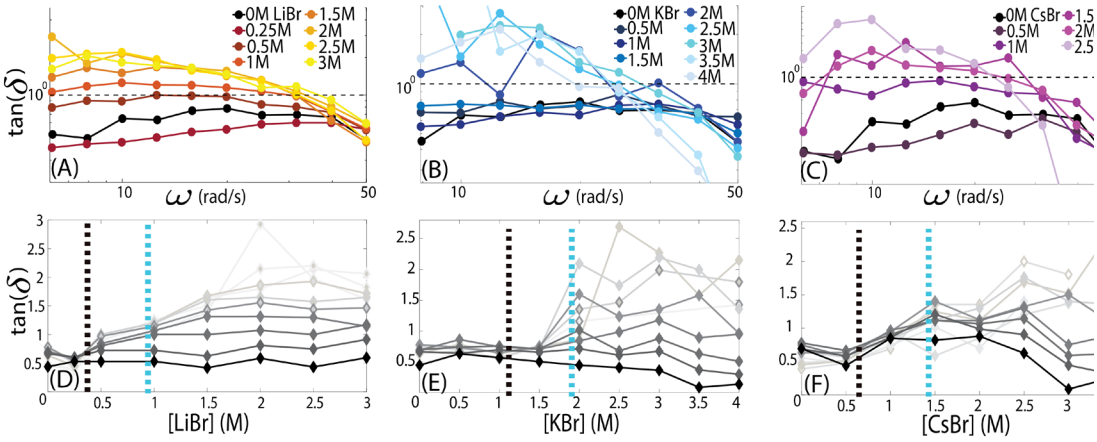

Figure 2.5: Frequency sweep results. tan(δ) vs frequency (5-50 rad/s) for PFPI/NaPSS complex with added (A) LiBr, (B) KBr, and (C) CsBr. tan(δ)) vs [Salt] (grey scale represents frequency range: 5 (light-grey)-50 (black) rad/s) for (D) LiBr series, (E) KBr series, and (F) CsBr series where solid-like (left of dotted black line), gel-like (left of dotted blue line), and liquid-like (right of dotted blue line) regions are highlighted.

between sample preparation and measurements, or upon centrifugation. These data provide evidence for the salt-driven formation of a liquid πPCC phase, albeit one that appears to differ from a classical coacervate phase in its morphology.

2.2.3 Time-Resolved Photoluminescence with No Excess Salt

Having characterized the rheological properties of the concentrated phase, we studied whether increasing salt concentration had an influence on the photophysical properties of the CPE within the concentrated phase. The delocalized electronic states of a CPE are sensitive to the microstructure of the chain, which leads to photophysical properties that closely track the ensemble of chain conformations. Thus, spectroscopic techniques can be used to probe the structure of the complexes without the need for secondary reporters. Time-resolved photoluminescence (TRPL) is a convenient and informative spectroscopic probe because it is highly sensitive to intra- and inter-chain excited-state delocalization. Different TRPL decay components can, in principle, be related to radiative relaxation due to

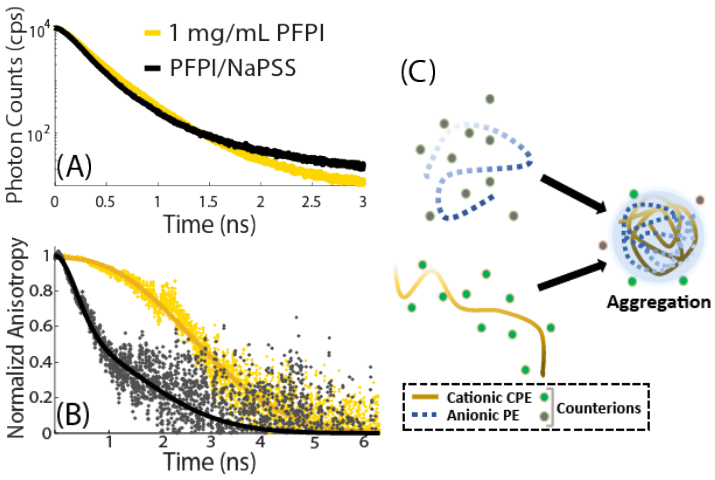

Figure 2.6: Time-resolved spectroscopy. (A) Time-resolved photoluminescence, and (B) time-resolved photoluminescence anisotropy comparing a dilute solution of PFPI (1 mg/mL) to complexes of PFPI/NaPSS (1 mg/mL:0.6 mg/mL) with no added salt. (C) Complexation cartoon, showing tight coiling of PFPI, which leads to rapid exciton hopping and thus a fast PL depolarization decay time.

different microstructural states or environments.

Figure 2.6A shows the TRPL decay from both isolated aqueous PFPI solution with no excess salt and the concentrated phase of the PFPI/NaPSS complex solution, similarly with no added salt. We used a front-face geometry to collect TRPL measurements on concentrated samples following centrifugation. All decays were successfully deconvolved from the instrument response function using a biexponential model, which was the minimal model necessary to capture the functional form of the decays. The lifetimes from deconvolved decays are listed in Table 2.2. Pure PFPI shows a distinct biexponential decay with short (150 ps) and long (360 ps) lifetime components. Upon addition of NaPSS, there is a subtle increase in the short component (230 ps) accompanied by a significant increase in the long component (1.08 ns). This suggests a shift in the photophysical properties of PFPI due to a change in the microstructure of the conjugated backbone upon complexation (Figure 2.6C).

Additional insight into the change in CPE microstructure upon complexation can be obtained by performing a polarization-sensitive time-resolved PL anisotropy measurement. In this experiment, the sample is excited with a vertically polarized light pulse, and the time-resolved fractional difference between emission parallel and perpendicular to the excitation is tracked. If the ensemble-average transition dipole moment of the emitting state changes orientation with time, emission will become depolarized, acquiring a horizontal component. Thus, this technique is sensitive to exciton migration and physical motion of CPE chains.

The normalized PL anisotropy dynamics for the isolated PFPI solution and the concentrated phase of the salt-free PFPI/NaPSS complex are shown in Figure 2.6B. The anisotropy of PFPI in isolated aqueous solution depends weakly on time over a period longer than the average PL lifetime. This indicates that the PFPI backbone contains regions that are significantly extended. An extended chain with a limited number of inter-chain interactions has few ways to scramble the orientation of the transition dipole moment of the emitting exciton state. At longer times, rotation of chromophores along the chain or overall chain rotation will nevertheless depolarize the emission, which leads to a complete decay of the anisotropy. Comparing the normalized anisotropy of pure PFPI to that of the concentrated phase of the salt-free complex solution shows that the rate of depolarization is increased significantly upon complexation with NaPSS. Such an observation is consistent with significantly more collapsed chains within the complex, as this allows for facile exciton hopping between chromophores either along the same chain or between different chains. This scrambles the memory of the initial orientation of the average transition dipole moment and thus leads to anisotropy decay.

2.2.4 Time-Resolved Photoluminescence with Excess Salt. Figure 2.7A, B and C show TRPL decays of the concentrated phase for select salt concentrations, which capture the observed trend for each salt type. Table 2.2 lists the deconvolved lifetimes and their ampltudes for the concentrated phase. Table 2.3 shows the comparison between the concentrated-phase PFPI lifetime with the corresponding dilute phase at select salt concentrations. Upon exposure of the complex to increasing LiBr (Figure 2.7A), we observe little variation in emission dynamics, which are dominated by the short lifetime component. The average PFPI lifetime for the LiBr series was found to fluctuate around ~241 ps. An intriguing difference is seen upon exposing the complex to increasing KBr. We find a monotonic increase in the average PL lifetime, which corresponds to an approximately 50 % increase at 3.5 M KBr compared to the complex on its own (230 ps vs. 440 ps). Increasing CsBr gives qualitatively similar results to KBr. In the high-salt concentration limit, the

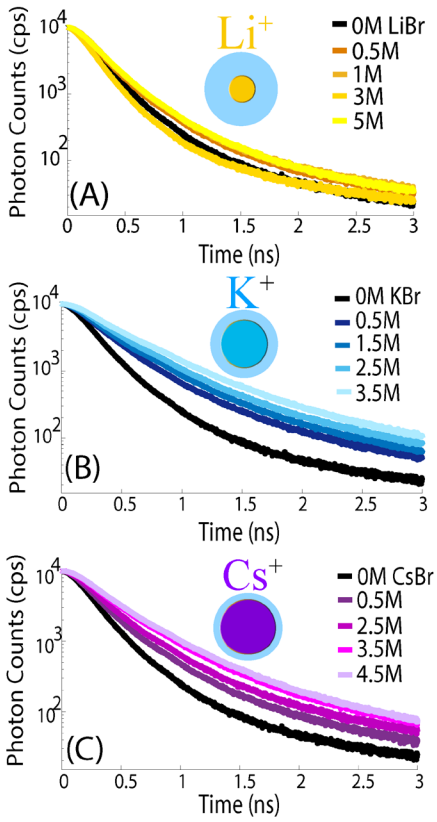

Figure 2.7: Time-resolved photoluminescence decay curves of the concentrated phase upon increasing (A) LiBr, (B) KBr, and (C) CsBr.

concentrated phases of both KBr and CsBr also show similar PL lifetimes. This suggests that, on average, PFPI chains within the complex adopt a similar microstructure, a result that is in agreement with trends from rheology. A comparison of lifetimes collected for the concentrated phase of PFPI in the absence of NaPSS at select LiBr, KBr, and CsBr concentrations can be found in Table AI.2. Although increasing ionic strength does lead to an increase in the PL lifetime in the concentrated phase of PFPI on its own, for most samples the PFPI lifetime in the concentrated phase of PFPI/NaPSS is larger than PFPI alone. We observe the largest relative increase for KBr, with the PFPI/NaPSS complex having a lifetime that is 46% longer than the corresponding concentrated phase without NaPSS.

To better compare the change in PL lifetime with salt concentration for each salt type, Figure 2.8A shows plots of the short and long lifetime components, respectively, as a function of salt concentration for the three salts. Figure 2.8C shows the fractional contribution of the short component, $F_1 = a_1\tau_1/(a_1\tau_1 + a_2\tau_2)$, where a_1 is the amplitude of the short component, a_2 is the amplitude of the long component, τ_1 is the lifetime of the short component, and τ_2 is the lifetime of the long component. The short component for LiBr shows no obvious trend with increasing salt concentration, with the lifetime remaining largely unchanged compared to the salt-free complex. In contrast, increasing both KBr and CsBr leads to a monotonic increase in the short component. It is interesting to note that the rate at which this lifetime evidently reaches saturation at high salt is larger for KBr than CsBr suggesting a more gradual change in PFPI chain microstructure for CsBr.

Relatively minor, but readily measurable changes in F_1 are found to accompany changes in emission lifetimes. Figure 2.8B shows that most of the exciton population emits over the short decay lifetime. Upon increasing KBr and CsBr, a small decrease is observed in the short component fraction with increasing ionic strength. Interestingly, we observe no significant changes in the long component lifetime, which fluctuates about ~1.1 ns regardless of simple salt type.

It is well-known that conjugated polymers can support excitons that are delocalized over a single chain or shared between two or more chromophores located either along a single coiled chain or between proximal chains. When excitons are largely delocalized along the CPE backbone, the PL lifetime is expected to be relatively long, corresponding to J-like excitons.[29,30] In contrast, when the exciton center-of-mass wavefunction is shared between multiple chromophores, the PL lifetime becomes relatively small, which corresponds to H-like excitons. With this simplified model in mind, we interpret the short PFPI lifetime component in the concentrated phase as arising from regions with substantial inter-chromophore (monomer-monomer) interactions. The long component should then be associated with PFPI chains with relatively few inter-chromophore interactions.

Table 2.2: Deconvolved PL lifeftimes and component amplitudes.

Sample	a_1	τ_1 (ns)	a_2	τ_2(ns)	$\langle\tau\rangle$ (ns)
1mg/mL PFPI	0.997	0.15	0.003	0.36	0.15
PFPI/NaPSS	0.999	0.23	0.001	1.08	0.23
0.5 M LiBr	0.999	0.26	0.001	1.25	0.26
1.0 M LiBr	0.999	0.26	0.001	1.18	0.26
1.5 M LiBr	0.999	0.23	0.001	1.13	0.24
2.0 M LiBr	0.999	0.24	0.001	1.20	0.25
2.5 M LiBr	0.999	0.25	0.001	1.15	0.25
3.0 M LiBr	0.999	0.21	0.001	1.26	0.21

3.5 M LiBr	0.999	0.22	0.001	1.15	0.22
4.0 M LiBr	0.999	0.23	0.001	1.20	0.23
4.5 M LiBr	0.999	0.22	0.001	1.12	0.22
5.0 M LiBr	0.998	0.26	0.002	1.13	0.27
Sample	**a_1**	**τ_1 (ns)**	**a_2**	**τ_2(ns)**	**<τ> (ns)**
0.5 M KBr	0.995	0.29	0.005	1.04	0.30
1.0 M KBr	0.992	0.34	0.008	1.12	0.36
1.5 M KBr	0.991	0.34	0.009	1.10	0.36
2.0 M KBr	0.987	0.36	0.013	1.08	0.38
2.5 M KBr	0.989	0.35	0.012	1.10	0.38
3.0 M KBr	0.987	0.35	0.013	1.07	0.38
3.5 M KBr	0.979	0.40	0.021	1.12	0.44
4.0 M KBr	0.991	0.33	0.009	1.08	0.35
4.5 M KBr	0.987	0.35	0.013	1.08	0.38
5.0 M KBr	0.990	0.34	0.010	1.08	0.36
Sample	**a_1**	**τ_1 (ns)**	**a_2**	**τ_2(ns)**	**<τ> (ns)**
0.5 M CsBr	0.997	0.28	0.003	1.10	0.28
1.0 M CsBr	0.998	0.28	0.003	1.16	0.29
1.5 M CsBr	0.996	0.29	0.004	1.14	0.31
2.0 M CsBr	0.995	0.32	0.005	1.19	0.33
2.5 M CsBr	0.996	0.30	0.004	1.17	0.31
3.0 M CsBr	0.995	0.32	0.005	1.14	0.33
3.5 M CsBr	0.992	0.34	0.008	1.14	0.36
4.0 M CsBr	0.990	0.34	0.010	1.13	0.37
4.5 M CsBr	0.992	0.34	0.009	1.10	0.36
5.0 M CsBr	0.991	0.34	0.009	1.11	0.37

Table 2.3: Average PL lifetime comparison for dilute and concentrated phases.

Dilute Phase	<τ> (ns)	Concentrated Phase	<τ> (ns)
2M LiBr	0.16	***2M LiBr***	0.25
4M LiBr	0.21	***4M LiBr***	0.23
2M KBr	0.22	***2M KBr***	0.38
4M KBr	0.27	***4M KBr***	0.35
2M CsBr	0.22	***2M CsBr***	0.33
4M CsBr	0.26	***4M CsBr***	0.37

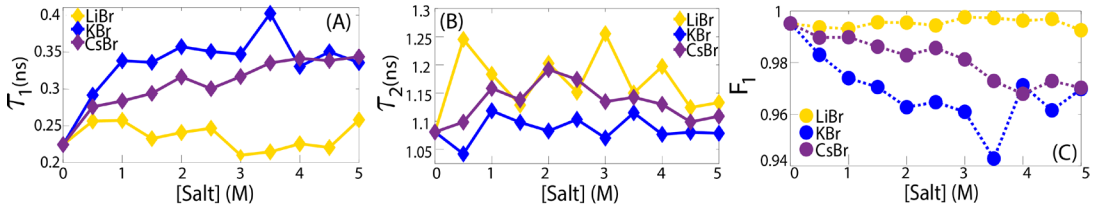

Figure 2.8: PL lifetimes and decay component amplitudes in the concentrated phase as a function of salt concentration. (A) Short and (B) long lifetimes (τ_1 and τ_2, respectively) vs. [Salt] for each salt type. (C) Factional contribution to the short decay lifetime vs. [Salt] for each salt type.

2.2.5 Salt-Dependent PL Anisotropy Dynamics.

We preformed time-resolved PL anisotropy measurements on the concentrated phase at select salt concentrations for each salt type within the region that showed rheological evidence for formation of liquid coacervate-like states (2.5 M and 5 M LiBr, KBr, and CsBr). We found that transferring the concentrated phase into the optical cuvette resulted in a slow change of the measured anisotropy over the first ~5 hrs of the sample re-settling. For this reason, results shown below are from samples that were allowed to mechanically settle for a minimum of 24 hrs before measurements were taken. Additional decays collected immediately upon transfer to the cuvette and 5 hrs after loading of the cuvette can be found in Figure AI.10 and Table AI.4. We find that all anisotropy curves at the above-mentioned salt concentrations display a fast-initial decay. However, the anisotropy does not decay to zero on the timescale of the experiment, and for certain samples the shape of the anisotropy decay at intermediate times is complex, displaying a local maximum.

Such nontraditional anisotropy decay shapes have previously been reported in the biophysical literature, where time-resolved anisotropy had been used to probe

small-molecule fluorophores either free in solution or bound to large particles such as proteins or membranes.[31] In a system which contains a population of both bound and unbound fluorophores, i.e., one that displays spatial heterogeneity, the anisotropy can increase in time instead of monotonically decaying to zero.[19,31,32] In such systems, the decay rate of PL depolarization had previously been attributed to the rotational motion of the fluorophore. Such complex anisotropy behavior has also been observed in time-resolved vibrational anisotropy experiments on water in inverse micelles with interfacial and bulk-like liquid states.[33] Analogous interpretation in the case of

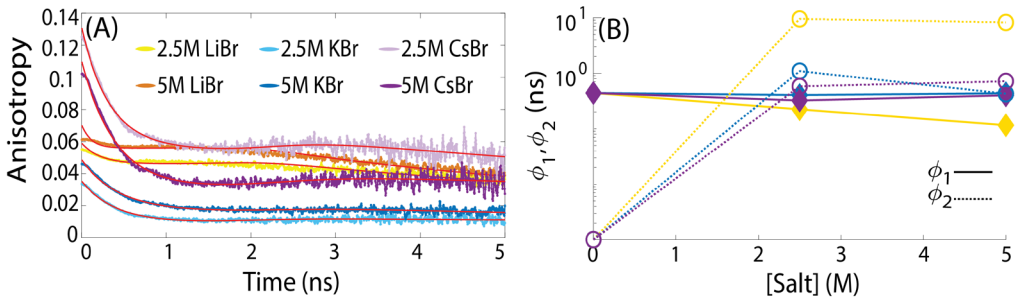

Figure 2.9: PL depolarization dynamics in the concentrated phase. (A) Time-resolved PL anisotropy decays of PFPI/NaPSS with 2.5 M and 5 M LiBr (yellow), KBr (blue), and CsBr (purple) where red lines indicate fits. (B) Fast (φ_1, solid lines with diamond markers) and slow (φ_2, dotted lined with open circle markers) correlation times vs. [Salt] for PFPI/NaPSS complex with 2.5 M and 5 M LiBr, KBr, and CsBr.

conjugated polymers in condensed phases is more complicated. This is because PL can be depolarized both by exciton hopping via electronic energy transfer between chromophores and by rotational motion of the chain.

To extract quantitative information, we have applied two simple physically motivated models. These models were previously simulated by Ludcher *et al.* to elucidate how differences in PL lifetime components coupled with spatial heterogeneity influence the observed time-resolved anisotropy decay curves.[19]

Modeling anisotropy decays allows us to extract PL depolarization times. These can then be compared to gain insight into the differences in local environments experienced by the CPE chain in the presence of different salts. In both models, the short and long PL lifetime components (Figure 2.8A and B) are associated with their own distinct anisotropy decay laws. In model 1, for a given PL lifetime component, the anisotropy decay is comprised of two terms, the first of which is a single exponential and the second is a constant. The constant term accounts for the fact that in relatively large macromolecular assemblies, the anisotropy may not decay to zero on the timescale of the experiment. The anisotropy, $r(t)$, then takes the following functional form:

$$r(t) \propto f_1(t)\left[\alpha_1 \exp\left(-\frac{t}{\varphi_1}\right) + (1-\alpha_1)\right] + f_2(t)\left[\alpha_2 \exp\left(-\frac{t}{\varphi_2}\right) + (1-\alpha_2)\right] \quad \textbf{(2.3)}$$

where α_i is the fraction of the anisotropy decay with depolarization time φ_i, *associated with given lifetime component* (a_i, τ_i). Here φ_1 is associated with the shorter PL lifetime (τ_1), while φ_2 is associated with the longer lifetime (τ_2). The α_i were not constrained to sum to unity to allow for a relative difference in the fundamental anisotropies (i.e., limiting anisotropy as time goes to zero) of the two components. The time-dependent weights $f_i(t)$ that determine the contribution of each anisotropy decay law in square brackets are constrained by the fractional *PL lifetime* decay (describing the time dependence of the exciton population) as

$$f_i(t) = a_i \exp\left(-\frac{t}{\tau_i}\right) \Big/ \sum_{j=1}^{2} a_j \exp\left(-\frac{t}{\tau_j}\right) \quad \textbf{(2.4)}$$

where τ_i is the PL lifetime and a_i is the amplitude of the excited-state population characterized by that lifetime (Table 2.2). The time-dependence of the f_i gives rise to the complexity of the anisotropy decay form.

When model 1 was insufficient to capture the functional form of the anisotropy satisfactorily, we used a slightly modified model. Model 2 differs from model 1 via an additional multiplicative term, which describes the timescale for the overall depolarization of a generalized "large particle", φ_p, to which sub-populations with φ_1 and φ_2 are bound:

$$r(t) \propto \left\{ f_1(t) \left[\alpha_1 \exp\left(-\frac{t}{\varphi_1}\right) + (1-\alpha_1) \right] + f_2(t) \left[\alpha_2 \exp\left(-\frac{t}{\varphi_2}\right) + (1-\alpha_2) \right] \right\} \exp\left(-\frac{t}{\varphi_p}\right) \quad \textbf{(2.5)}$$

Solid red lines in Figure 2.9A indicate fits to the above models. Although the models are simple given the complexity of our system, they do a reasonably good job of qualitatively capturing the entirety of the data set. Nevertheless, the fits are not perfect and some caution is warranted in interpretation.

Anisotropy fitting parameters are listed in Table 2.4. Figure 2.9B shows a plot of φ_1 and φ_2 for two concentrations from each salt type. For the complex with no excess salt, the primary contribution to the anisotropy decay comes from $\varphi_1 \sim 0.44$ ns. A similar φ_1 is found for samples in the presence of both KBr and CsBr, whereas it is nominally smaller for LiBr by nearly a factor of two (< 0.23 ns), though the fits at short time for LiBr are noticably worse. Evidently adding salt introduces a significant contribution from an additional depolarization time φ_2 which falls

between ~ 0.4 ns and ~ 1 ns for KBr and CsBr depending on the sample. Interestingly, φ_2 is significantly larger for LiBr (~ 9 ns).

Table 2.4: Time resolved PL anisotropy fitting parameters.

Sample	$\varphi_{1\ (ns)}$	α_1	$\varphi_{2\ (ns)}$	α_2	$\varphi_{p\ (ns)}$
PFPI/NaPSS ($t_{24\ hrs}$)	0.44	0.77	0.001	0.50	--
2.5 M LiBr ($t_{24\ hrs}$)	0.22	0.22	9.45	1.00	--
5.0 M LiBr ($t_{24\ hrs}$)	0.12	0.21	8.21	1.00	--
2.5 M KBr ($t_{24\ hrs}$)	0.40	0.76	1.09	0.69	--
5.0 M KBr ($t_{24\ hrs}$)	0.44	0.63	0.43	0.52	12.6
2.5 M CsBr ($t_{24\ hrs}$)	0.32	0.55	0.58	0.43	12.4
5.0 M CsBr ($t_{24\ hrs}$)	0.40	0.71	0.56	0.60	22.4

2.3 Discussion

In this work we first set out to characterize the nature of aqueous phase separation in oppositely charged complexes containing a CPE. Second, we aimed to determine what the influence of phase separation was on the photophysical properties of the CPE, if any, both within the dilute and concentrated phases. Our final objective was to uncover whether the nature of the monovalent cation influenced the phase behavior and the photophysical properties of our system.

Using rheological measurements, we found evidence for formation of a viscoelastic liquid coacervate phase for all three simple bromide salts that were investigated. However, microscopy measurements showed that PFPI/NaPSS samples resembled a colloidal gel whose morphology changed with increasing salt concentration. Thus, although rheological measurements suggest formation of a viscoelastic liquid phase, we believe the phase behavior is more complex. Danielsen and Segalman, *et al.* found that in water/THF mixtures at a certain solvent mixture

composition, the phase behavior was indicative of what they referred to as coacervate-precipitates.[15] Based on our observations, we believe it is likely that the concentrated phase in our samples also exhibits a coexistence of liquid-like and solid-like domains, which give rise to the colloidal gel-like microstructure. The salt concentration at which liquid-like behavior was observed was higher than what was previously observed with non-conjugated polyelectrolyte complexes. We speculate that such phase behavior is related to increased hydrophobic and/or monomer-monomer interactions of CPEs compared to most non-conjugated polyelectrolytes.

Our supposition that the microstructure of the concentrated phase resembles a colloidal gel is consistent with the observation of two PL lifetime components, suggesting two distinct local environments: a primary sub-population associated with the short PL lifetime and a minor one associated with the long lifetime. Previous work on simulations of colloidal gels showed that such a system is likely to be dynamically heterogeneous, displaying particle populations with two distinct relaxation times (slow and fast).[49] We propose that the short PL component is associated with relatively closely packed "slow" particles with substantial inter-chromophore PFPI interactions. Exciton hopping between chromophores within these populations ought to be relatively rapid, potentially leading to the short anisotropy

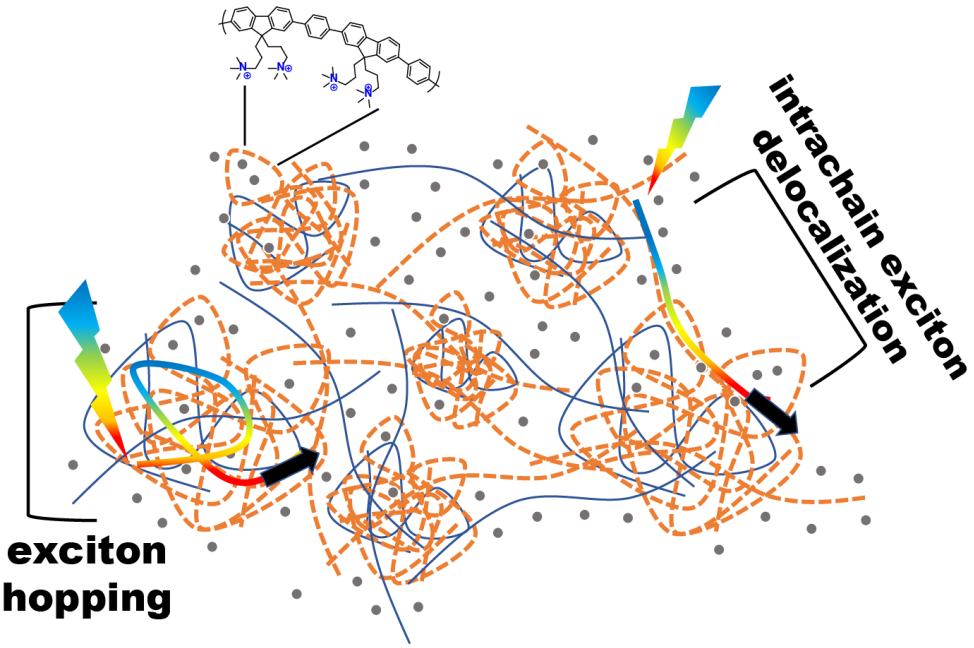

Figure 2.10: Cartoon showing a coexistence between domains within the colloidal gel where the chain is coiled and excitons hop rapidly between chromophores, as well as regions where the chain is relatively extended.

depolarization time. The longer PL lifetime should then be associated with a minor population of "fast" gel particles, where PFPI chains exist in a relatively extended conformation and perhaps form connecting tie-chains between the slower particles. The long depolarization time of such particles would be consistent with the relatively large chain extension, leading to intrachain exciton delocalization and a relatively long memory of the initial transition dipole moment orientation. A cartoon of such a coexistence is shown in Figure 2.10. The PL lifetime of PFPI in the dilute solution (Table 2.3) was smaller than that of PFPI within the complex and effectively possessed only one decay component. It is clear that the local environment experienced by PFPI is qualitatively different in the two phases, presumably with more intra-chain π-stacking interactions between isolated chains occurring in the dilute phase.

It is interesting that the PFPI PL lifetimes within the concentrated phase changed markedly with increasing KBr and CsBr but remained relatively unchanged with LiBr. This is despite the fact that, based on the rheological characterization, differences between the concentrated phases at a given salt concentration across the salt series were not drastic. Although the role of the bromide anion cannot be ignored, we focus on the cation-π interaction under the simplifying assumption that anion-induced interactions are approximately unchanged as the cation is varied.[34,35]

The cation-π interaction will contain contributions from the screened coulomb interactions of the ion primarily with the quadrupole moment of the aromatic CPE backbone, as well as the coupling between the polarizability of the ion and π-electrons.[36] The Li^+ charge density is largest across the cation series, which leads to the strongest coulombic cation-π interaction in the gas phase compared to K^+ and Cs^+. However, the cation-π interaction is significantly modified by hydration of both the ion and the aromatic backbone in the aqueous medium, resulting in substantial differences in desolvation free energy (Table 2.1). In fact, motivated by understanding biological ion-conducting channels, prior work has shown that the strength of the cation-π interaction can undergo a relative reversal compared to its gas-phase value.[37] Relative to Li^+, it was observed that the aqueous cation-π interaction with K^+ could be stronger and could be competitive with the water-K^+ interaction. This reversal from the gas phase to the aqueous phase was largely attributed to the larger desolvation penalty for Li^+ relative to K^+.[20,38] Measurements of cation concentration in the dilute phase indicate that the dilute phase in the presence of LiBr has a slightly larger Li^+ concentration (Figure AI.3B) compared to the other

cations, which is consistent with the larger desolvation cost. There is further evidence from vibrational predissociation spectroscopy that K^+ may act as a bridge between aromatic regions.[39]

Recent molecular dynamics simulations have shed substantial light on the nature of the cation-π interaction at extended aromatic surfaces of relevance to this work. Simulations by Pham, *et al.* using first-principles calculations of aqueous carbon nanotube-ion interactions show that K^+ has a larger binding energy with the nanotube surface than either Na^+ or Cl^-.[52] This leads to preferential K^+ adsorption at the aromatic surface relative to the middle of the tube. The reasons for this were (i) significant nanotube-ion wavefunction hybridization, and (ii) a "softer" solvation shell with significant water reorganization. These factors result in the K^+ becoming partially desolvated when near the surface. In contrast, the Na^+ ion remained fully solvated and displayed substantially less wavefunction hybridization with the carbon nanotube. These authors used a 1 M ion concentration commensurate with this work. It is also intriguing that the authors do not find a static K^+-nanotube interaction. Instead, it is seen that K^+ readily diffuses along the nanotube surface. Additionally, Williams, *et al.* used parameterized polarizable force fields to study graphene-ion interactions and converged on a similar result: aqueous K^+ interacts quite strongly with graphene.[53] The first (global) minimum of the potential of mean force was larger than that of Li^+, once again showing partial dehydration of K^+ at the graphene surface. In contrast, Li^+ retained its hydration shell even in proximity of the extended aromatic surface. It is worth noting that there was some disagreement between the

two studies regarding the degree of Na^+ dehydration. This was attributed to differences in the curvature of the aromatic surface.

In addition to differences in desolvation free energies, the dipolar polarizability increases by a factor of ~31 from Li^+ to K^+ and by ~2.75 in going from K^+ to Cs^+. The difference between K^+ and Cs^+ is significant, yet the relative photophysical changes seen as a function of salt concentration are similar. However, it is notable that the concentrated phase at high ionic strength appears to be significantly more enriched in Cs^+ than K^+ and Li^+. We believe the increase in the Cs^+ polarizability leads to a stronger interaction with the conjugated CPE backbone and thus a better "solvation" environment for the CPE backbone in the concentrated phase compared to the other cations, particularly when the water content is low. Interestingly, we found that K^+ led to a faster jump in PL lifetime with increasing salt concentration compared to Cs^+, although the two ions converge on the same lifetime at the highest concentrations. Motivated by the work of Pham, *et al.*, we speculate that this may be due to a larger K^+ diffusion coefficient along the aromatic surface compared to Cs^+.[52] Thus, more Cs^+ may be required to observe the same overall influence on the CPE backbone. This possibility raises intriguing questions about how one might vary the nature of the cation to manipulate the cation-backbone interaction.

It is reasonable to suggest that similar cation-π interactions may be operative in the concentrated phase of PFPI samples in the absence of NaPSS, which should lead to a similar ordering of the average PL lifetime across the cation series. We

evaluated this for a few select salt concentrations in the high salt concentration limit (Table AI.2). We find that for most samples, lifetimes in the presence of KBr and CsBr are longer than those with LiBr. However, this is not universally true, as the 5-M LiBr sample shows the longest PL lifetime. Interestingly, this sample distinguishes itself based on the visual appearance of the concentrated phase, which looks more liquid. This is also borne out in the corresponding microscopy image (Figure AI.1D). Thus, although there are similarities in PL lifetime trends between the concentrated phases of PFPI alone and in the complex with NaPSS, there are some compelling differences. A deeper investigation into CPE behavior in the absence of an oppositely charged polyelectrolyte and at large [LiBr] will be the subject of future work.

In addition to polarizability, differences in hydration radius also need to be considered as a possible factor in TRPL differences of the PFPI/NaPSS complex in the presence of LiBr relative to both KBr and CsBr. The hydration radius could play a direct role in the ability of a cation to enter, swell, and disrupt complexation. It is possible that the small radius of Li^+ ion could allow it to infiltrate the complex to a comparable extent as K^+ and Cs^+ but without a comparable disruption in the CPE π-π interactions. However, the hydration radius is in fact the largest for Li^+ at ~3.8 Å, and comparable for K^+ and Cs^+ at ~3.3 Å. This idea is consistent with K^+ and Cs^+ leading to similar results, particularly when compared to Li^+. Thus, differences in hydrated ion radii are unlikely to explain our TRPL trends, further bolstering the primary role of the cation-π interaction in these observations.

Putting it all together, we attribute the increase in PL lifetime for KBr and CsBr relative to LiBr as a resulting from a partial break-up of H-like exciton states associated with inter-chromophore interactions. This is due to the increase in relative proximity of K^+ and Cs^+ to the CPE backbone and increased cation-π interaction. The combination of rheological and TRPL results leads us to propose that the larger size of hydrated Li^+ ions may also partially hinder infiltration of the polyelectrolyte complex leading to a significantly smaller disruption of π-stacking interactions, in contrast to the K^+ and Cs^+ ions.

These specific ion interactions and variations of solvation energy between ion types play a major role in the ordering of ions in the well-known Hoffmeister series involving protein solubility, leading to 'salting-in' and 'salting-out' phenomena. However, it is well-established that different macroions lead to different ion orderings along the Hoffmeister series. Because of this and the additional complexity that a CPE presents, our focus in this work was instead on a limited series of simple cations, deliberately avoiding more complex molecular ions. In the future it will be of fundamental interest to expand the scope of the phase behavior and photophysics investigation across the entirety of an effective Hoffmeister ion series.

An aqueous, coacervate-like CPE-based concentrated phase has intriguing light-harvesting implications. We hypothesized that the delocalized π-electrons of a CPE backbone could in principle recruit other nonpolar π-conjugated organic semiconductors into the concentrated phase. Such molecules would otherwise have a vanishing propensity to infiltrate the polyelectrolyte-rich aqueous phase unless the

molecules were polar or ionically charged. As a proof of principle, we used a quintessential fullerene derivative, PC[70]BM, to test our hypothesis. This fullerene derivative is part of a family of the most well-studied photoinduced electron acceptors. This molecule has been used to efficiently convert excitons on conjugated polymers to spatially separated electron/hole pairs in thin film organic solar cells.[44-47] PC[70]BM is highly soluble in organic solvents, such as chloroform or chlorobenzene, used to cast solar cell thin films; it has near-zero solubility in water. If PFPI can in fact recruit PC[70]BM to be in the vicinity of the CPE backbone, we expect that PL from PFPI excitons will become partially quenched primarily via photoinduced electron transfer to PC[70]BM. This should give rise to a decrease in the average PL lifetime of PFPI.

The effects of exposing the PFPI/NaPSS concentrated phase to PC[70]BM were analyzed by calculating the PL quenching ratio, Q, for each sample, defined by

$$Q = 1 - \int_0^\infty I_q(t)dt \,/\, \int_0^\infty I_{nq}(t)dt \qquad \textbf{(2.6)}$$

where $I_q(t)$ is the deconvolved PFPI PL decay after exposure to organic PC[70]BM solutions, and $I_{nq}(t)$ is the corresponding decay of the control (non-quenched) sample not exposed to PC[70]BM solution. Figure AI.9A shows a bar graph of Q for the different conditions that we explored. A plot of the decays, fits, and deconvolution parameters are reported in Figure AI.8 and Table AI.3. We observe a notable color change of the concentrated phase to a light opaque brown. Compared to corresponding controls, the CPE PL is quenched in all samples exposed to PC[70]BM (Figure AI.8A and B).

When compared to the unheated 3.5 M KBr control, the most significant quenching was found to occur for the $CHCl_3$ sample with a $Q \sim 39\%$. Though a more thorough investigation is warranted, this result is interesting for two reasons. First, it appears that the organic solvent used to dissolve PC[70]BM had a measurable influence on the probability of PC[70]BM transfer into the coacervate. Second, given that the fullerene derivative does not contain functional groups expected to promote aqueous solubility, the maximal quenching that we observe is quite substantial. A judicious choice of functionalization pattern of the photoinduced electron acceptor will very likely lead to a significant further increase in quenching. Thus, we believe that the fullerene-infiltrated CPE-based coacervate can be manipulated to produce photoinduced electron/hole pairs at the CPE/fullerene interface with impressive rates. A cartoon of the fullerene-infiltrated system is shown in Figure AI.9B. Future work will systematically investigate the fullerene/CPE interaction in detail, including the role of the nonconjugated polyelectrolyte component.

2.2.4 Conclusion

We have shown that conjugated polyelectrolytes can undergo salt-induced aqueous associative phase separation into a dilute and concentrated phase, which shows evidence of complex coacervation. However, we have also shown that the phase behavior is more complex than pure liquid/liquid phase separation and likely corresponds to formation of a colloidal gel. We found that the photophysical properties of the concentrated phase depended on the nature of the excess salt ions, allowing us to manipulate the radiative relaxation and exciton diffusion dynamics. Using time-resolved PL anisotropy measurements, we showed that the concentrated

phase is spatially heterogeneous with depolarization times that depend on the ion type. Our work raises interesting questions about the possibility of using the nature of the ion to tune the coupling between phase behavior and photophysical properties of complex fluids. It is particularly intriguing to ask whether the presence of molecular ions can both lead to the formation of pure liquid-liquid phase separation, as well further tune the optical properties of the fluid.

The ability to form a coacervate-like CPE state also has interesting implications for light-harvesting applications. Specifically, we showed that a model nonpolar, fullerene-based electron acceptor can be infiltrated into the concentrated phase, leading to photoluminescence quenching likely by photoinduced electron transfer. Our work suggests that liquid electron donor/acceptor bulk heterojunctions may be formed in aqueous solution, which may serve as photochemical reaction media or sensing platforms for high ionic-strength environments.

2.2.5 References

(1) Dubin, P.; Stewart, R. J. Complex Coacervation. *Soft Matter* **2018**, 14, 329–330, DOI: 10.1039/c7sm90206a.

(2) Fu, J.; Schlenoff, J. B. Driving Forces for Oppositely Charged Polyion Association in Aqueous Solutions: Enthalpic, Entropic, but Not Electrostatic. *J. Am. Chem. Soc* **2016**, 138, 980–990, DOI: 10.1021/jacs.5b11878.

(3) Fu, J.; Fares, H. M.; Schlenoff, J. B. Ion-Pairing Strength in Polyelectrolyte Complexes. *Macromolecules* **2017**, 50, 1066–1074, DOI: 10.1021/acs.macromol.6b02445.

(4) Schlenoff, J. B. Non-Equilibrium Phenomena and Kinetic Pathways in Self-Assembled Polyelectrolyte Complexes. *J. Chem. Phys.* **2018**, 149, 163314, DOI: 10.1063/1.5039621.

(5) Tirrell, M. Polyelectrolyte Complexes: Fluid or Solid? *ACS Cent. Sci.* **2018**, 4, 532–533, DOI: 10.1021/acscentsci.8b00284.

(6) Srivastava, S. S.; Tirrell, M. V. Structure and Rheology of Polyelectrolyte Complex Coacervates †. *Soft Matter* **2018**, 14, 2454, DOI: 10.1039/c7sm02041d.

(7) Sing, C. E.; Perry, S. L. Recent Progress in the Science of Complex Coacervation. *Soft Matter* **2020**, 16, 2885–2914, DOI: 10.1039/d0sm00001a.

(8) Keating, C. D. Aqueous Phase Separation as a Possible Route to Compartmentalization of Biological Molecules. *Acc. Chem. Res.* **2011**, 45 (12), DOI: 10.1021/ar200294y.

(9) Alberti, S.; Gladfelter, A.; Mittag, T. Considerations and Challenges in Studying Liquid-Liquid Phase Separation and Biomolecular Condensates. *Cell*. **2019**, 176, 419–434, DOI: 10.1016/j.cell.2018.12.035.

(10) Martin, N. Dynamic Synthetic Cells Based on Liquid–Liquid Phase Separation. *ChemBioChem* **2019**, 20, 1–17, DOI: 10.1002/cbic.201900183.

(11) Black, K. A.; Priftis, D.; Perry, S. L.; Yip, J.; Byun, W. Y.; Tirrell, M. Protein Encapsulation via Polypeptide Complex Coacervation. *ACS Macro Lett.* **2014**, 3, 1088-1091, DOI: 10.1021/mz500529v.

(12) Rumyantsev, A. M.; Zhulina, E. B.; Borisov, O. V; Petersburg, S. Complex Coacervate of Weakly Charged Polyelectrolytes: Diagram of States. *Macromolecules* **2018**, 51, 3788–3801, DOI: 10.1021/acs.macromol.8b00342.

(13) Messaoud, G. Ben; Promeneur, L.; Brennich, M.; Roelants, S. L. K. W.; Le Griel, P.; Baccile, N. Complex Coacervation of Natural Sophorolipid Bolaamphiphile Micelles with Cationic Polyelectrolytes †. *Green Chem.* **2018**, 20, 3371-3385, DOI: 10.1039/c8gc01531g.

(14) Krogstad, D. V.; Lynd, N. A.; Choi, S.-H.; Spruell, J. M.; Hawker, C. J.; Kramer, E. J.; Tirrell, M. V. Effects of Polymer and Salt Concentration on the Structure and Properties of Triblock Copolymer Coacervate Hydrogels. *Macromolecules* **2013**, 46, 1512–1518, DOI: 10.1021/ma302299r.

(15) Danielsen, S. P. O.; Nguyen, T.-Q.; Fredrickson, G. H.; Segalman, R. A. Complexation of a Conjugated Polyelectrolyte and Impact on Optoelectronic Properties. *ACS Macro Lett.* **2019**, 8, 88–94, DOI: 10.1021/acsmacrolett.8b00924.

(16) Nakashima, K. K.; Vibhute, M. A.; Spruijt, E. Biomolecular Chemistry in Liquid Phase Separated Compartments. *Front. Mol. Biosci.* **2019**, 6, 1-9, DOI: 10.3389/fmicb.2019.00021.

(17) Aumiller, W. M.; Cakmak, F. P.; Davis, B. W.; Keating, C. D. RNA-Based Coacervates as a Model for Membraneless Organelles: Formation, Properties, and Interfacial Liposome Assembly. *Langmuir* **2016**, 32, 10042–10053, DOI:

10.1021/acs.langmuir.6b02499.

(18) Hollingsworth, W. R.; Magnanelli, T. J.; Segura, C.; Young, J. D.; Bragg, A. E.; Ayzner, A. L. Polyion Charge Ratio Determines Transition between Bright and Dark Excitons in Donor/Acceptor-Conjugated Polyelectrolyte Complexes. *J. Phys. Chem. C* **2018**, 122, 22280–22293, DOI: 10.1021/acs.jpcc.8b06195.

(19) Ludescher, R. D.; Peting, L.; Hudson, S.; Hudson, B. Time-Resolved Fluorescence Anisotropy for Systems with Lifetime and Dynamic Heterogeneity. *Biophys. Chem.* **1987**, 28, 59–75, DOI: 10.1016/0301-4622(87)80075-3.

(20) Addison, C. Inorganic Chemistry of the Main-Group Elements Volume 4. *R. Soc. Chem.* **1997**, DOI: 10.1039/9781847556387.

(21) Sternheimer, R. M. Electronic Polarizabilities of Ions from the Hartree-Fock Wave Functions. *Phys. Rev.* **1954**, 96, 951-968, DOI: 10.1103/PhysRev.96.951.

(22) Spruijt, E.; Westphal, A. H.; Borst, J. W.; Cohen Stuart, M. A.; Van Der Gucht, J. Binodal Compositions of Polyelectrolyte Complexes. *Macromolecules* **2010**, 43, 6476–6484, DOI: 10.1021/ma101031t.

(23) Li, L.; Srivastava, S.; Andreev, M.; Marciel, A. B.; De Pablo, J. J.; Tirrell, M. V. Phase Behavior and Salt Partitioning in Polyelectrolyte Complex Coacervates. *Macromolecules* **2018**, 51, 2988–2995, DOI: 10.1021/acs.macromol.8b00238.

(24) Liu, Y.; Momani, B.; Henning Winter, H.; Perry, S. L. Rheological Characterization of Liquid-to-Solid Transitions in Bulk Polyelectrolyte Complexes †. | *Soft Matter* **2017**, 13, 7332, DOI: 10.1039/c7sm01285c.

(25) Spruijt, E.; Sprakel, J.; Lemmers, M.; Cohen Stuart, M. A.; Van Der Gucht, J. Relaxation Dynamics at Different Time Scales in Electrostatic Complexes: Time-Salt Superposition. *Phys. Rev. Lett.* **2010**, 105, 1–4, DOI: 10.1103/PhysRevLett.105.208301.

(26) Liu, Y.; Winter, H. H.; Perry, S. L. Linear Viscoelasticity of Complex Coacervates. *Adv. Colloid Interface Sci.* **2017**, 239, 46–60, DOI: 10.1016/j.cis.2016.08.010.

(27) Wang, Q.; Schlenoff, J. B. The Polyelectrolyte Complex/Coacervate Continuum. *Macromolecules* **2014**, 47, 3108-3116, DOI: 10.1021/ma500500q.

(28) Spruijt, E.; Stuart, M. A. C.; Van Der Gucht, J. Linear Viscoelasticity of Polyelectrolyte Complex Coacervates. *Macromolecules* **2013**, 46, 1663–1641, DOI: 10.1021/ma301730n.

(29) Manas, E. S.; Spano, F. C. Absorption and Spontaneous Emission in Aggregates of Conjugated Polymers. *J. Chem. Phys.* **1998**, 109, 8087–8101, DOI: 10.1063/1.477457.

(30) Manas, E. S.; Spano, F. C. Modeling Disorder in Polymer Aggregates: The Optical Spectroscopy of Regioregular Poly(3-Hexylthiophene) Thin Films. *Cit. J. Chem. Phys.* **1998**, 109, 234701, DOI: 10.1063/1.1914768.

(31) Lakowicz, J. R. Principles of Fluorescence Spectroscopy Joseph R. Lakowicz, Editor. *Princ. Fluoresc. Spectrosc. Springer, New York, USA, 3rd edn,* **2006**, DOI: 10.1007/978-0-387-46312-4.

(32) Smith, T. A.; Ghiggino, K. P. A Review of the Analysis of Complex Time-Resolved Fluorescence Anisotropy Data. *Methods Appl. Fluoresc.* **2015**, 3, 1-15, DOI: 10.1088/2050-6120/3/2/022001.

(33) Fayer, M. D.; Levinger, N. E. Analysis of Water in Confined Geometries and at Interfaces. *Annu. Rev. Anal. Chem* **2010**, 3, 89–107, DOI: 10.1146/annurev-anchem-070109-103410.

(34) Ma, J. C.; Dougherty, D. A. The Cation-π Interaction. *Chem. Rev.* **1997**, 97, 1303–1324, DOI: 10.1021/cr9603744.

(35) Mahadevi, A. S.; Sastry, G. N. Cation−π Interaction: Its Role and Relevance in Chemistry, Biology, and Material Science. *Chem. Rev.* **2012**, 113, 2100–2138, DOI: 10.1021/cr300222d.

(36) Schyman, P.; Jorgensen, W. L. Exploring Adsorption of Water and Ions on Carbon Surfaces Using a Polarizable Force Field. *J. Phys. Chem. Lett* **2013**, 4, 468-474, DOI: 10.1021/jz302085c.

(37) Kumpf, R. A.; Dougherty, D. A. A Mechanism for Ion Selectivity in Potassium Channels: Computational Studies of Cation-π. *Science* **1993**, 261, 1708-1710, DOI: 10.1126/science.8378771.

(38) Salomon, M. The Thermodynamics of Ion Solvation in Water and Propylene

Carbonate. *J. Phys. Chem.* **1970**, 74, 2519-2524, DOI: 10.1021/j100706a019.

(39) Cabarcos, O. M.; Weinheimer, C. J.; Lisy, J. M. Competitive Solvation of by Benzene and Water: Cation-π Interactions and π-Hydrogen Bonds. *J. Chem. Phys* **1998**, 108, 5151, DOI: 10.1063/1.476310.

(40) Barford, W.; Tozer, O. R. Theory of Exciton Transfer and Diffusion in Conjugated Polymers. *J. Chem. Phys.* **2014**, 141, 164103, DOI: 10.1063/1.4897986.

(41) Barford, W.; Marcus, M. Theory of Optical Transitions in Conjugated Polymers. I. Ideal Systems. *J. Chem. Phys.* **2014**, 141, 164101, DOI: 10.1063/1.4897984.

(42) Marcus, M.; Tozer, O. R.; Barford, W. Theory of Optical Transitions in Conjugated Polymers. II. Real Systems. *J. Chem. Phys.* **2014**, 141, 164102, DOI: 10.1063/1.4897985.

(43) Tozer, O. R.; Barford, W. Intrachain Exciton Dynamics in Conjugated Polymer Chains in Solution. *J. Chem. Phys.* **2015**, 143, 84102, DOI: 10.1063/1.4929378.

(44) Liu, T.; Troisi, A. What Makes Fullerene Acceptors Special as Electron Acceptors in Organic Solar Cells and How to Replace Them. *Adv. Mater.* **2013**, 25, 1038–1041, DOI: 10.1002/adma.201203486.

(45) Loi, M. A.; Toffanin, S.; Muccini, M.; Forster, M.; Scherf, U.; Scharber, M. Charge Transfer Excitons in Bulk Heterojunctions of a Polyfluorene

Copolymer and a Fullerene Derivative. *Adv. Funct. Mater.* **2007**, 17, 2111–2116, DOI: 10.1002/adfm.200601098.

(46) Hwan Kim, D.; Ayzner, A. L.; Appleton, A. L.; Schmidt, K.; Mei, J.; Toney, M. F.; Bao, Z. Comparison of the Photovoltaic Characteristics and Nanostructure of Fullerenes Blended with Conjugated Polymers with Siloxane-Terminated and Branched Aliphatic Side Chains. *Chem. Mater.* **2013**, 25, 431-440, DOI: 10.1021/cm303572d.

(47) Wei, G.; Wang, S.; Sun, K.; Thompson, M. E.; Forrest, S. R. Solvent-Annealed Crystalline Squaraine: PC70BM (1:6) Solar Cells. *Adv. Energy Mater.* **2011**, 1, 184–187, DOI: 10.1002/aenm.201100045.

(48) Marcus, Y. Ionic Radii in Aqueous Solutions. *Chem. Rev.* **1988**, 88, 8, 1475-1498, DOI: 10.1021/cr00090a003.

(49) Puertas, A. M. Dynamical Heterogeneities Close to a Collodial Gel. *J. Chem. Phys.* **2004**, 121, 28, DOI: 10.1063/1.1768936.

(50) Nightingale Jr., E. R. Phenominological Theory of Ion Solvation. *J. Phy. Chem.* **1959**, 63, 9, 1381-1387, DOI: 10.1021/j150579a011.

(51) Israelachvili, J. N. Intermolecular and Surface Forces 3rd Edition. *Academic Press Elsevier Inc.*, **2011**.

(52) Pham, T. A., Mortuza, S. M.G., Wood, B. C., Lau, E. Y., Ogitsu, T., Buchsbaum, S. F., Siwy, Z. S., Fornasiero, F., Schwegler, E., Salt Solutions in Carbon Nanotubes: The Role of Cation-π Interactions. *J. Phys. Chem. C* **2016**, 120,

13, 7332–7338, DOI: 10.1021/acs.jpcc.5b12245

(53) Williams, C. D., Dix, J., Troisi A., Carbone, P. Effective Polarization in Pairwise Potentials at the Graphene-Electrolyte Interface. *J. Phys. Chem. Lett.* 2017, 8, 3, 703–708, DOI: 10.1021/acs.jpclett.6b027

Appendix I

Supporting Information for

Associative Phase Separation of Aqueous π-Conjugated Polyelectrolytes Couples Photophysical and Mechanical Properties

I.1 Experimental

Sample Preparation. The cationic conjugated polyelectrolyte, poly([fluorene]-alt-phenylene) derivative (PFPI) (MW=21,000 Da, PDI=1.2), was obtained from Solaris Chem Incorporated. The anionic non-conjugated polyelectrolyte, poly(4-styrenesulfonate) (NaPSS) (MW=~1,000,000 Da), was obtained from Sigma-Aldrich. Phenyl-C71-butyric acid methyl ester (PC[70]BM) was obtained from Ossila. Lithium bromide (LiBr, > 99.0 % purity) was obtained from Tokyo Chemical Industries (TCI), potassium bromide (KBr, 99.99 % purity) was obtained from Sigma-Aldrich, and cesium bromide (CsBr, 99.9 % purity) was obtained from Alfa Aesar. Chlorobenzene (spectrometric grade, 99.9 % purity) was obtained from Alfa Aesar. Chloroform (HPLC grade, ≥ 99.8 % purity) was obtained from Sigma-Aldrich. All chemicals were used as received.

Stock solutions of 10 mg/mL NaPSS, 5 mg/mL PFPI, 5 M and 7 M of each salt type were prepared using HPLC grade water (Sigma-Aldrich). The NaPSS stock was stirred at 70 °C for 10 min, the PFPI stock was stirred at 85 °C for 24 hrs. Both stocks were then cooled to room temperature and filtered using a 0.45 μm nylon syringe filter (Fischer Scientific) before use. All salt stocks were heated to 70 °C for 10 min to ensure salt crystals were fully dissolved. High molarity (7 M KBr, and 7 M

CsBr) salt stocks were supersaturated solutions and were transferred hot for this reason, rather than being allowed to cool to room temperature before preparation of the high concentration salt samples in either series.

Samples containing 0-5 M LiBr, KBr, and CsBr (in 0.5 M increments) were prepared with a 50:50 molar-charge ratio of PFPI:NaPSS (1 mg/mL: 0.6 mg/mL). The order of addition was as follows: HPLC water, salt (LiBr/KBr/CsBr), simultaneous addition of PFPI and NaPSS. Samples were stirred at room temperature for a minimum of 8 hrs before any analysis was performed. Samples in photos were allowed to separate by gravity for ~ 8 hrs before photos were taken. Samples were gently centrifuged (Minispin Plus, Eppendorf) at 3,000 rpm (252 x g) for 15 min in order to adequately separate the two phases for further characterization.

Samples containing PC[70]BM were prepared as follows. The dilute phase of the 3.5 M KBr solution was carefully separated from the concentrated phase. Next, 1 mL of an organic layer (either C_6H_5Cl or $CHCl_3$) containing 30 mg/mL dissolved PC[70]BM was added to the concentrated phase. The C_6H_5Cl/ PC[70]BM layer was found to be less dense than the aqueous concentrated phase and thus remained suspended above it, whereas the $CHCl_3$ layer containing PC[70]BM was found to be more dense than the concentrated phase and settled to the bottom of the vial (Figure AI.8B). These samples were then compared and characterized against the concentrated phase of a 3.5 M KBr PFPI/NaPSS standard after stirring at 650 rpm at room temp for 2 hrs, and again after stirring at 1150 rpm and heating to 70 °C for 43 hrs.

I.2.2 Microscopy. Images were collected with a Leica DM5500 B widefield microscope available in the UCSC Life Sciences Microscopy Center (Figures 1 and AI.1). 6 μL of each sample was loaded onto a glass microscope slide and covered with a glass coverslip in order to arrest evaporation during imaging. Samples were excited using a 360 ± 40 nm excitation filterand imaged with a Leica DFC450 color camera using a 20x objective and a 470 ± 40 nm fluorescent filter.

UV-Vis Spectroscopy. Dilute phase characterization was carried out for each sample after lightly centrifuging at 3000 rpm (252 x g) for 15 min. The dilute phase was carefully separated from the concentrated phase for optical density measurements taken using a Shimadzu UV-2700 spectrophotometer over the range of 300−800 nm in 1.0 nm increments in a quartz cuvette with a 1 mm pathlength (Figure AI.2).

Rheometry. Small-amplitude oscillatory shear (SAOS) measurements were performed on the concentrated phase of each sample at the Stanford Nano Shared Facility (SNSF): Soft and Hybrid Materials Facility (SMF) using an ARES-G2 strain-controlled rheometer from TA Instruments in strain-controlled oscillatory mode. A 40 mm cone-and-plate geometry with an angle of 2° and a truncation gap of 0.047 mm was used for all rheological experiments. The temperature was set at 20 °C via a Peltier controller, and a solvent trap was utilized to minimize evaporation of the sample during measurement.

After centrifugation and careful extraction of the concentrated phase, samples were loaded and oscillated at a low frequency and strain % (1 Hz, 5 %) for 2 min prior to measurement in order to homogenize the sample. Amplitude sweeps were

carried out from 0.1-1000 % strain at an angular frequency of 31.4159 rad/s (5 Hz) in order to determine the linear viscoelastic region for each sample (Figure AI.4). Frequency sweeps (Figure 4 and AI.5) were then carried out for each sample from 0.1-100 rad/s and a strain % determined to fall within the linear viscoelastic region (ranging from 1-20 strain % depending on sample type). All SAOS measurements were performed in triplicate to ensure the reliability of the data. Due to the inherently low viscosities of the samples, only data that fell well above the lower instrumental torque limit of 0.05 μN•m is reported.

Time-Resolved Photoluminescence. Time-resolved photoluminescence measurements were performed via time-correlated single photon counting (TCSPC) using a home-built apparatus. Samples were excited with a pulsed supercontinuum picosecond laser (Super K EXTREME, NKT Photonics) coupled to an acousto-optic filter and an external RF driver (Super K SELECT, NKT Photonics). Measurements were carried out at a 78 MHz pulse repetition rate. The primarily horizontally polarized excitation pulse was first rotated by 90° by an achromatic ½ λ plate (Thorlabs) before being linearly polarized by a Glan-Thompson polarizer (Thorlabs) mounted on an automated rotation stage. Polarization of the emitted light was also varied using a Glan-Thompson polarizer. Samples were excited with vertically polarized light (400 nm), and emission was collected in a front-face geometry at a polarization of the magic angle (54.7°), with the emission wavelength centered about 440 nm. Emitted light was collimated and focused by a set of achromatic doublets (Thorlabs) onto a monochromator slit. A 420 nm long-pass filter was used to minimize any influence of the reflected excitation beam. Emission wavelengths were

selected by an Acton Spectra Pro SP-2300 monochromator (Princeton Instruments). A hybrid PMT with minimal after-pulsing (Becker and Hickl) was used to record the time-resolved fluorescence decay. An SPC-130 photon counting module (Becker and Hickl) coupled to a Simple-Tau 130 table-top TCSPC system was used for photon counting. For magic-angle measurements, collection was carried out until approximately 10,000 photon counts were reached in the main channel. After collection, magic angle data was baselined by subtracting the average of the first 30 collected data points (prior to the rise onset). Fluorescence lifetimes were determined via forward convolution with the measured instrument response function (obtained using a scattering Ludox sample) and a sum-of-exponentials model. This was done using the DecayFit (Fluorescence Decay Analysis Software 1.3, FluorTools, www.fluortools.com) MATLAB package developed by Dr. Soren Preus, using non-linear least squares fitting minimization. Goodness of fit was determined by chi-squared parameter and by visual inspection of the plotted residuals.

Time-Resolved Photoluminescence Anisotropy. Anisotropy measurements were carried out on the set up described above. For anisotropy experiments, samples were excited with vertically polarized light (420 nm) and emission (480 nm) was collected at vertical (VV-component) and horizontal (VH-component) polarizations. Collection was carried out until approximately 20,000 counts were reached for the VH-component in the main channel. The VV-component measurement was then carried out for the same amount of time. Anisotropy data were time-shifted such that the max photon count of respective VV and VH signals were the same. G factor measurements were carried out in order to correct for instrumental differences in

detection of the different polarization components. This was done using horizontal excitation and collection of horizontal (HH-component) and vertical (HV-component) emission. Depolarization times were determined by fitting to two simple models simulated by Ludescher et al.[19]

Dilute Phase Ion Concentration Determination. Li^+, K^+, and Cs^+ ion concentration of the dilute phase for each sample exhibiting phase separation were measured using a Thermo iCAP 7400 Inductively Coupled Plasma Optical Emission Spectrometer (ICP-OES). Calibration curves for each cation were established using LiBr, KBr, and CsBr standards ranging from 100-1000 ppm. Samples were diluted in order to reduce all salt concentrations to below the instrumental limit of 1000 ppm. Use of the ICP-OES was possible through the UCSC Earth and Marine Sciences Plasma Analytical Facility.

I.2 Supporting Information

Widefield Microscopy Images.

Figure AI.1 shows photographs and fluorescence micrographs of the conjugated polyelectrolyte PFPI with increasing LiBr, KBr, and CsBr. Photographs show phase separation occurs for PFPI on its own with increasing ionic strength. LiBr samples exhibit an off-yellow coloring similar to the yellow of a concentrated PFPI stock solution. The solutions are also found to become more optically clear with increasing ionic strength. KBr and CsBr photos show a similar decrease in opaqueness of the off-white concentrated phase, with phase reversal occurring for 2.5 M CsBr, and 5 M solutions of both salt types. The slight apparent swirling of the 5 M KBr solution is due to agitation of the sample before the photo was taken and

represents the low surface tension between the two phases.

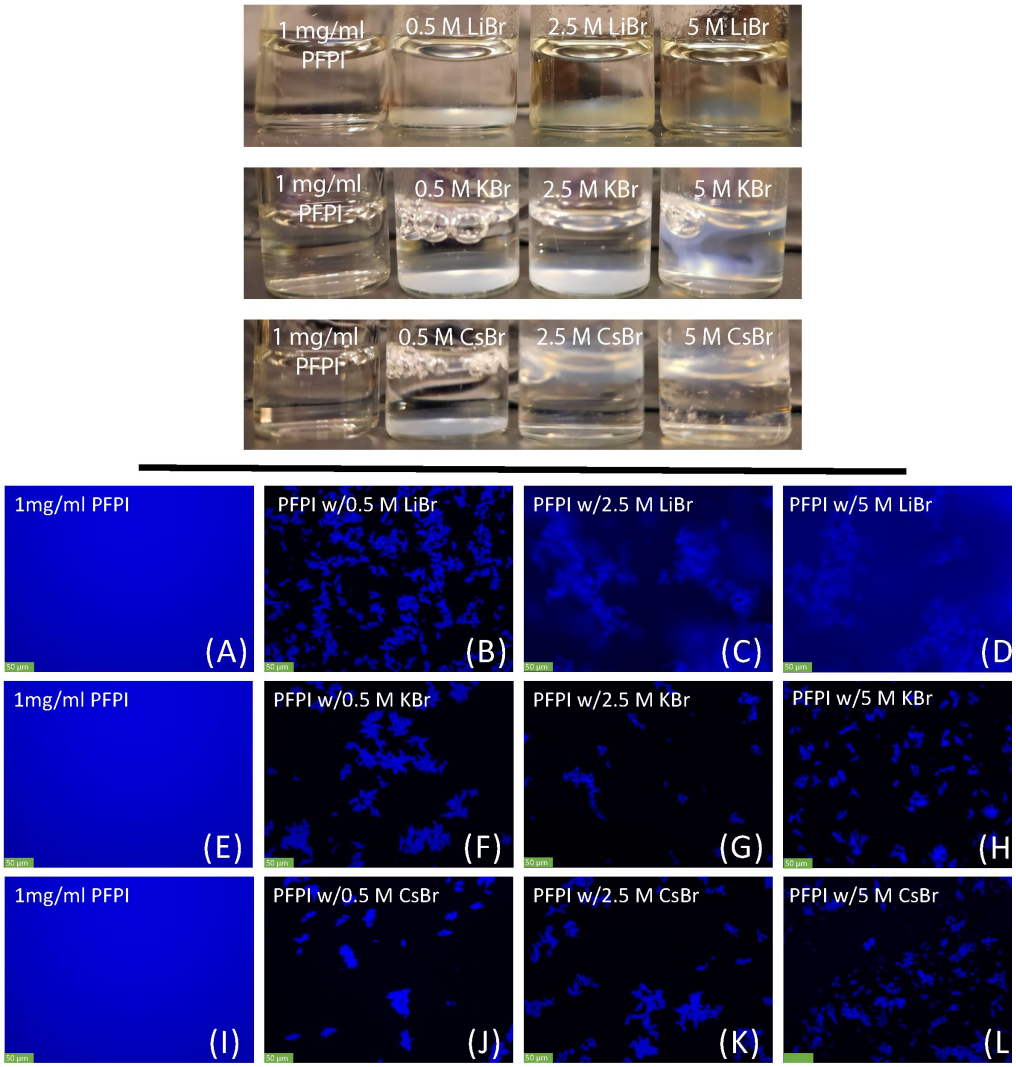

Figure AI.1: Top: Photos of control samples of 1 mg/mL PFPI with increasing LiBr, KBr, and CsBr. Bottom: Fluorescent micrographs of 1 mg/mL PFPI (A, E, and I) with increasing concentrations of LiBr (B-D), KBr (F-H), and CsBr (J-L).

UV-Vis Spectroscopy.

Peak normalized spectra in Figure AI.2 A-C show 5-10 nm redshifts for all samples upon increasing salt concentration. This shift was captured by calculating the first moment of the OD probability distribution (Figure AI.2D) using the absolute OD spectra.

Absolute OD spectra show an increase in absorbance intensity with increasing salt across all three salt types indicating more PFPI enters the dilute phase. The maximum absorbance value (~ 380 nm) was converted to [PFPI] using the Beer-Lambert Law and the molar extinction coefficient of isolated PFPI solution (5.6885 $(mg/mL)^{-1}$ mm^{-1}). The concentration of PFPI in the dilute phase and concentrated phase as a function of increasing salt are shown in Figure 2.3A and 2.3B of the main text, respectively.

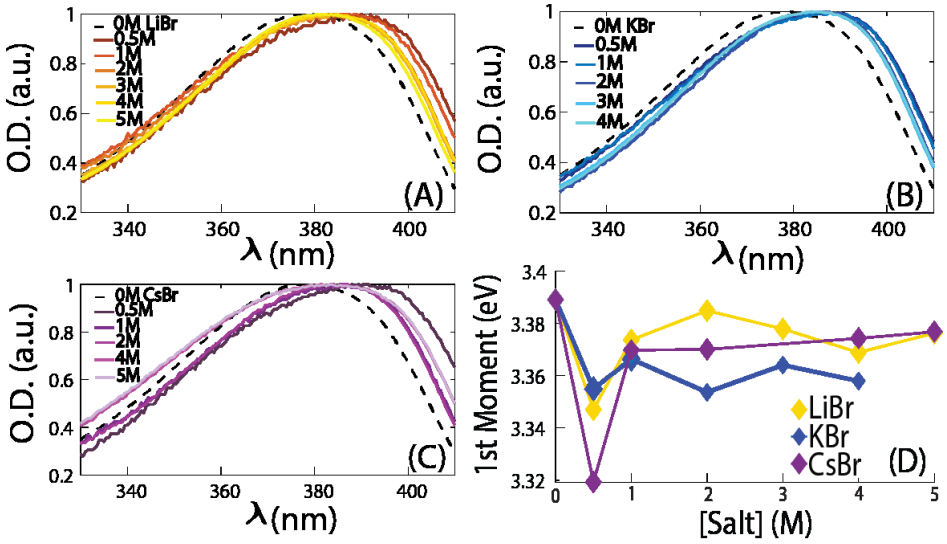

Figure AI.2: Normalized OD spectra of the dilute phase of PFPI/NaPSS samples with 0-5 M (A) LiBr, (B) KBr, and (C) CsBr. (D) 1st moment of spectral distribution for each salt type.

Inductively Coupled Plasma Optical Emission Spectroscopy and Water Content.

Ion concentrations in the dilute phase of each sample were measured using a Thermo iCAP 7400 Inductively Coupled Plasma Optical Emission Spectrometer and are shown in Figure AI.3B. The LiBr samples were found to have larger concentrations of cation

(i.e., Li^+) present in the dilute phase whereas the KBr and CsBr sample set had slightly less counter cation present. The data shows that the salt in solution preferentially partitions in the dilute phase, with more salt entering the concentrated phase as ionic strength increases. This accompanied by a general decrease in the concentration of water (Figure AI.3A) within the concentrated phase and subtle changes in the phase volume ratio (Table AI.1).

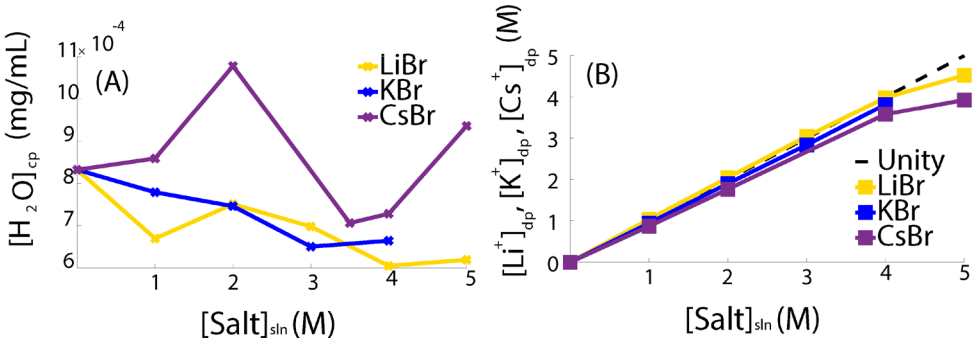

Figure AI.3: (A) Concentration of water in the concentrated phase for each sample, as determined via lyophilization. (B) Concentration of the cations $[Li^+]$ (yellow), $[K^+]$ (blue), and $[Cs^+]$ (purple) in the dilute phase of each sample showing phase separation determined by ICP-OES. Dotted black x=y trend line is shown for reference.

Table AI.1: Estimated Phase Volumes

Sample	$Volume_{dp}$ (µL)	$Volume_{cp}$ (µL)
PFPI/NaPSS	910	90
1M LiBr	925	75
2M LiBr	925	75
3M LiBr	910	90
4M LiBr	910	90
5M LiBr	910	90
1M KBr	910	90
2M KBr	900	100
3M KBr	900	100
4M KBr	950	50
1M CsBr	900	100

2M CsBr	925	75
3.5M CsBr	950	50
4M CsBr	950	50
5M CsBr	975	25

Rheology.

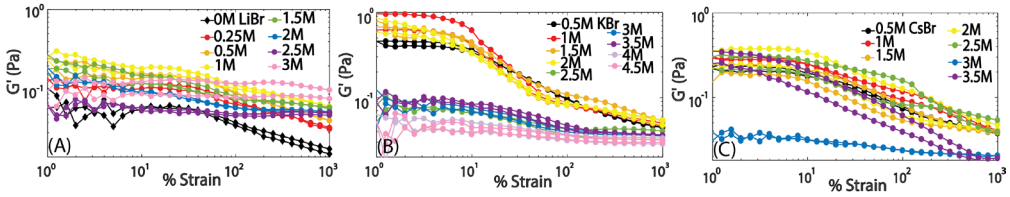

Figure AI.4: Amplitude sweeps of PFPI/NaPSS concentrated phase exposed to increasing salt. $G^{'}$ vs % Strain is shown for two trials of each sample in (A) LiBr, (B) KBr, and (C) CsBr.

Amplitude sweep and frequency sweep data were collected on an ARES-G2 strain-controlled rheometer from TA Instruments in strain-controlled oscillatory mode using 40 mm cone-and-plate geometry (2° angle, 0.047 mm truncation gap, 20 °C and solvent trap). Amplitudes sweeps shown in Figure AI.4 were carried out to select a % strain within the linear viscoelastic region, which was then set as a constant during frequency sweep experiments.[1] The extent of the linear viscoelastic region was found to increase upon increasing salt for each salt type. Results from frequency sweep experiments for multiple trials are shown in Figure AI.5. G′was found to dominate over G″for PFPI/NaPSS dense phase without added salt (Figure AI.5A), as well as for the complex exposed to lower salt concentrations of 0.5 M

LiBr, 1.5 M KBr, and 1 M CsBr (Figure AI.5B, D, F). G″was found to dominate over G′ when exposed to higher salt concentrations of 1 M LiBr, 2 M KBr, and 1.5 CsBr (Figure AI.5C, E, G). tan(δ), calculated using equation 2.2, are shown in Figure AI.6. For each salt type, the transition from tan(δ) < 1 to a tan(δ) > 1 is seen with increasing salt, as expected given the change in G′ and G″.

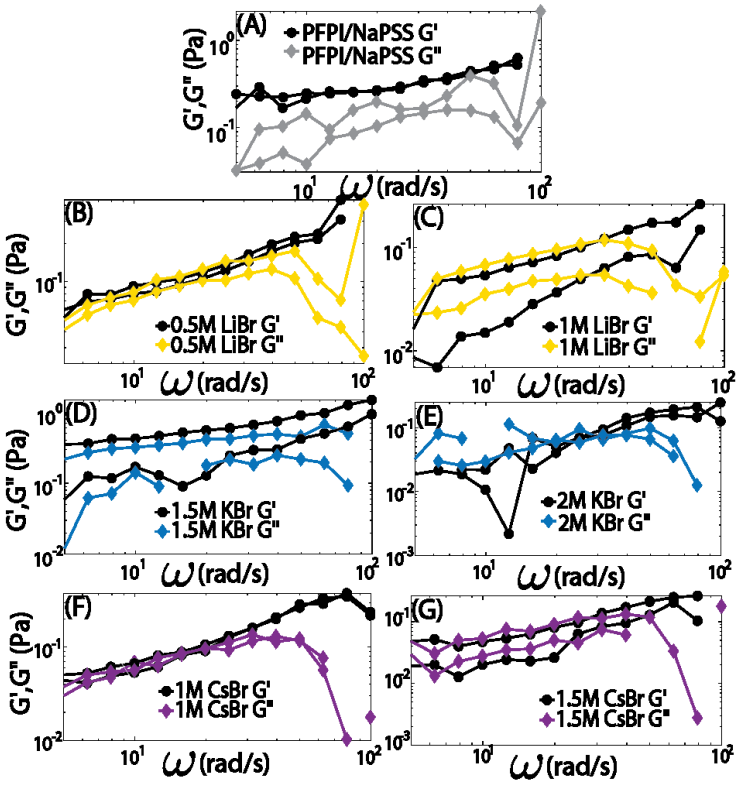

Figure AI.5: Frequency sweeps of the PFPI/NaPSS concentrated phase (A) with no additional salt and (B-G) exposed to increasing salt concentrations as labeled in each panel. G' and G''vs. frequency (ω) is shown for two trials of select samples in (B & C) LiBr, (D & E) KBr, and (F & G) CsBr.

Time-Resolved Photoluminescence

Time resolved photoluminescence (TRPL) of the concentrated phase was collected (λ_{ex} = 400 nm, λ_{em} = 440 nm) using time-correlated single photon counting carried out on a homebuilt system described in the main text and previously.[2-4] Fluorescence lifetimes were determined using forward convolution with the instrument response function and non-linear least-squares minimization with goodness of fit determined by the chi-squared parameter. Figure AI.7 shows decay

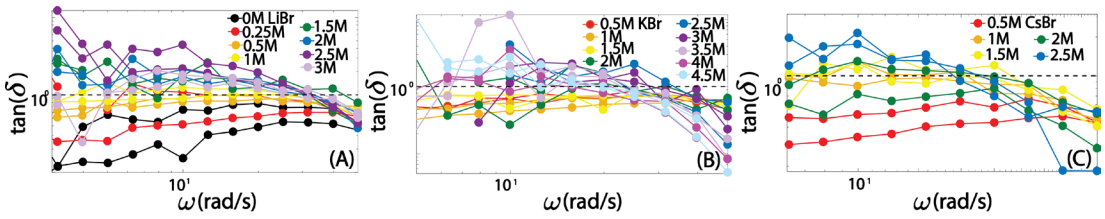

Figure AI.6: Plots of tan(δ) vs. frequency for the PFPI/NaPSS concentrated phase exposed to increasing salt for (A) LiBr, (B) KBr, and (C) CsBr. Data from two trials is shown.

curves with fits. All decays were found to be biexponential. The average lifetime $< \tau >$ for each sample was calculated using equation AI.1. All lifetimes are reported in Table 2 of the main text. All curves were found to decay completely by ~ 6 ns. Additional TRPL was collected for the concentrated phase of solutions containing 1 mg/mL PFPI and select salt concentrations as a control. Average fluorescent lifetimes are listed in Table AI.2. Fits were found to be biexponential with the short lifetime component amplitude dominating and the second lifetime component of ~1 ns exhibiting a vanishing amplitude. The average lifetime of PFPI is generally found to increase with increasing ionic strength with the highest ionic strength across each salt type exhibiting a lifetime of ~0.3 ns. Additionally, a longer average lifetime is generally seen for PFPI when complexed with NaPSS at these same salt concentrations.

$$< \tau >= \frac{\Sigma \alpha_i \tau_i^2}{\Sigma \alpha_i \tau_i} \qquad \textbf{(AI.1)}$$

Figure AI.8A shows TRPL and fits for the concentrated phase of the 3.5 M KBr sample before heating and after heating, with and without the addition of PC[70]BM. This comparison is shown for two different organic solvents, chloroform and chlorobenzene (photos shown in Figure AI.8B). Table AI.3 lists the extracted

lifetimes and the quenching coefficient (Q) calculated using equation 2.6 in the main text. Figure AI.9A shows a comparison of Q across solvent type and prep methods and S9B shows a cartoon involving quenching due to PC[70]BM intercalation.

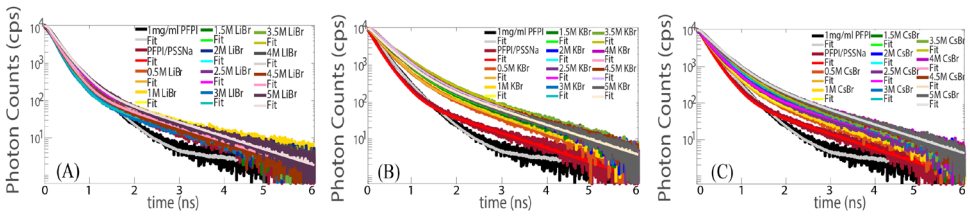

Figure AI.7: TR-PL of PFPI/NaPSS samples with 0-5 M (A) LiBr, (B) KBr, and (C) CsBr with biexponential fits convolved with the instrument response function.

Table AI.2: Time-resolved PL lifetimes for concentrated phase of 1 mg/mL PFPI with varying salt concentrations compared to lifetimes of PFPI/NaPSS concentrated phase.

Sample: PFPI only	<τ>(ns)	Sample: Complex	<τ> (ns)
1mg/mL PFPI	0.15	**PFPI/NaPSS**	0.23
0.5 M LiBr	0.20	**0.5 M LiBr**	0.26
2.5 M LiBr	0.20	**2.5 M LiBr**	0.25
5 M LiBr	0.33	**5.0 M LiBr**	0.27
0.5 M KBr	0.23	**0.5 M KBr**	0.30
2.5 M KBr	0.26	**2.5 M KBr**	0.38
5 M KBr	0.28	**5.0 M KBr**	0.36
0.5 M CsBr	0.25	**0.5 M CsBr**	0.28
2.5 M CsBr	0.24	**2.5 M CsBr**	0.31
5 M CsBr	0.30	**5.0 M CsBr**	0.37

I.2.6 Time-Resolved Photoluminescence of Concentrated Phase with Quencher

TRPL of the concentrated phase of 3.5 M KBr with the nonpolar quencher PC[70]BM was collected (λ_{ex} = 400 nm, λ_{em} = 440 nm) by the same method described above. Interestingly, the use of heat to promote transfer of PC[70]BM into the concentrated phase results in less quenching than the unheated case. Though Danielsen and Segalman, et al. (ref. 15 in main text) highlight the possibility of coacervate exchange into the organic solvent, we believe that the high ionic-strength environment used in this study makes exchange unlikely. It is possible that the increase in thermal energy results in a partial expulsion of ions from the complex, leading to an increase in inter-chain interactions and a lowering of the PL lifetime of the heated control sample. However, currently this is a mere speculation.

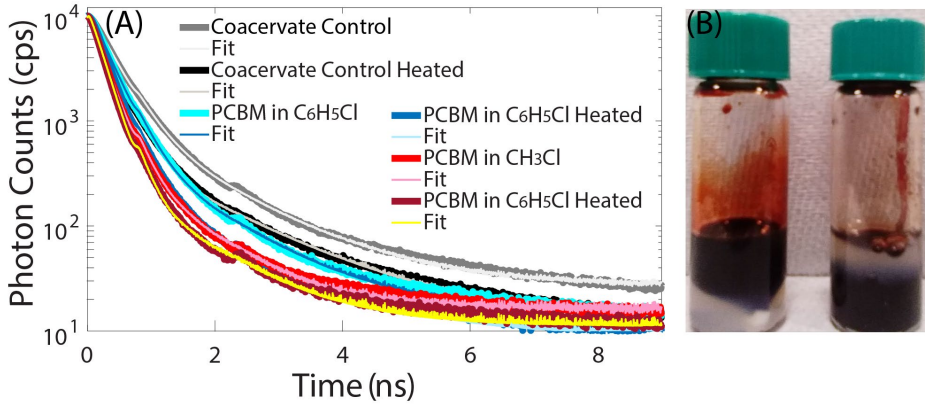

Figure AI.8: (A) TRPL of concentrated phase of the PFPI/NaPSS /3.5 M KBr sample when exposed to PC[70]BM dissolved in C_6H_5Cl, and PCBM dissolved in CH_3Cl before and after heating with fits. Decays for the appropriate controls are also shown. (B) Photos of concentrated phase (opaque light brown) and organic phase (dark brown, left-C_6H_5Cl, right-CH_3Cl) containing PC[70]BM.

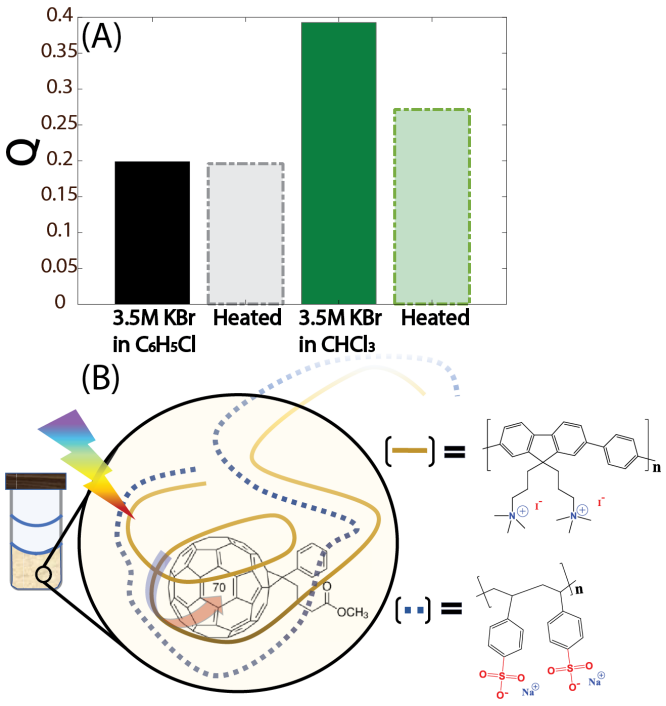

Figure AI.9: A comparison of the efficacy of two organic solvents (C_6H_5Cl and $CHCl_3$) on the intercalation of PC[70]BM and subsequent quenching is presented. (A) Quenching Coefficient (Q) of 3.5M KBr PFPI/NaPSS concentrated phase fluorescence before and after heating for samples containing PC[70]BM. (B) Cartoon of intercalation and quenching.

Table AI.3: Time-Resolved Photoluminescence Fit Parameters for Concentrated Phase of PFPI/NaPSS/3.5 M KBr Sample Exposed to PC[70]BM Under Various Conditions.

Sample	α_1	τ_1 (ns)	α_2	τ_2(ns)	$\langle\tau\rangle$ (ns)	Q
PFPI/NaPSS/3.5 M KBr	0.9997	0.33	3E-04	1.27	0.33	--
" " Heated	0.9999	0.28	1E-04	1.49	0.28	0.23
PC[70]BM in C_6H_5Cl	0.9999	0.28	1E-04	1.18	0.28	0.20
" " Heated	1.0000	0.25	8.42E-06	1.30	0.25	0.20
PC[70]BM in $CHCl_3$	1.0000	0.23	0	0.92	0.23	0.39
" " Heated	1.0000	0.19	0	1.09	0.19	0.27

I.2.7 Time-Resolved Photoluminescence Anisotropy

Time-resolved photoluminescence anisotropy measurements of the concentrated phase were carried out (λ_{ex} = 420 nm, λ_{em} = 480 nm) using TCSPC until 20,000 counts were reached for the VH-component in the main channel. Calculation of the time-dependent anisotropy $r(t)$ was carried out according to

$$r(t) = \frac{I_{VV}(t) - G I_{VH}(t)}{I_{VV}(t) + 2G I_{VH}(t)} \qquad \textbf{(AI.2)}$$

where I_{VV} and I_{VH} are the vertical-vertical and vertical-horizontal emission components, and G corrects for differences in detection of the two polarized components:

$$G = \frac{\int I_{HV}(t)dt}{\int I_{HH}(t)dt} \qquad \textbf{(AI.3)}$$

where the sample is excited with horizontally polarized light, and I_{HV} and I_{HH} are the horizontal-vertical and horizontal-horizontal emission components. Figure AI.10 shows $r(t)$ for each salt type taken at three time points. T0 refers to direct measurement upon loading of the sample into the cuvette, T1 refers to measurement after the sample has been sitting for 5 hrs, and T2 to a measurement after the sample has been sitting for 24 hrs. Fitted depolarization times are listed in Table AI.4.

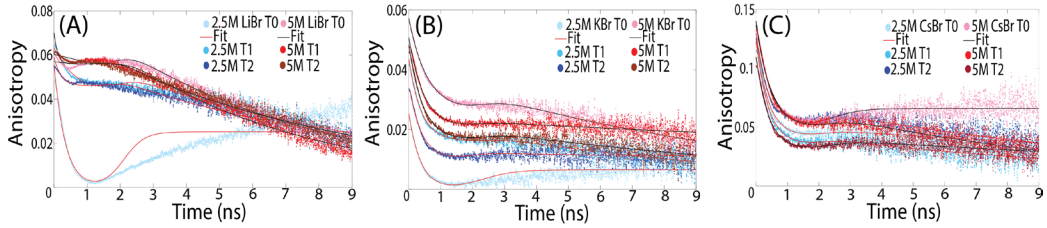

Figure AI.10: Time-resolved PL anisotropy of PFPI/NaPSS with 2.5 M and 5 M (A) LiBr, (B) KBr, and (C) CsBr directly after samples is loaded into the cuvette (T0), after 5 hrs of settling (T1), and after 24 hrs of settling (T2).

Table AI.4: Time-Resolved Photoluminescence Anisotropy Fit Parameters.

Sample	φ_1	α_1	φ_2	α_2	φ_p
PFPI/NaPSS (t_0)	**0.86**(0.75, 0.99)	**1**(fixed at bound)	**0.09**(-140, 140)	**0.16**(0.04, 0.27)	**100**(43.5, 156.5)
PFPI/NaPSS ($t_{5\ hrs}$)	**0.30** (0.27, 0.33)	**0.54** (0.53, 0.56)	**1.20**(1.07, 1.33)	**0.65** (0.63, 0.68)	**47.56**(25.53, 69.59)
PFPI/NaPSS ($t_{24\ hrs}$)	**0.44**(0.37, 0.51)	**0.77**(0.74, 0.80)	**0.001**(-3.96, 3.97)	**0.50**(0.47, 0.52)	~
2.5 M LiBr (t_0)	**0.34**(-0.84, 1.52)	**1.00**(0.97, 1.03)	**0.16**(-412, 412)	**0.55**(0.53, 0.58)	~
2.5 M LiBr ($t_{5\ hrs}$)	**0.64**(0.59, 0.70)	**0.33**(0.32, 0.34)	**9.51**(8.71, 10.3)	**1**(0.95, 1.05)	~
2.5 M LiBr ($t_{24\ hrs}$)	**0.22**(0.20, 0.25)	**0.22**(0.21, 0.24)	**9.49**(8.52, 10.5)	**1**(0.94, 1.06)	~
5 M LiBr (t_0)	**0.002**(0.001, 0.003)	**0.33**(0.33, 0.34)	**7.88**(7.54, 8.23)	**1**(fixed at bound)	**41.7**(31.4, 51.9)
5 M LiBr ($t_{5\ hrs}$)	**0.001**(0, 0.002)	**0.29**(0.28, 0.29)	**9.28**(8.84, 9.72)	**1**(fixed at bound)	**15.2**(13.9, 16.5)
5 M LiBr ($t_{24\ hrs}$)	**0.12**(0.10, 0.13)	**0.21**(0.20, 0.21)	**8.21**(8.13, 8.29)	**1**(fixed at bound)	~
2.5 M KBr (t_0)	**0.37**(0.3, 0.40)	**1**(0.98, 1.02)	**0.10**(-1.34, 1.55)	**0.73**(0.71, 0.75)	**100**(14.0, 186)
2.5 M KBr ($t_{5\ hrs}$)	**0.37**(0.28, 0.47)	**0.59**(0.41, 0.80)	**0.42**(-6.53, 7.37)	**0.48**(0.46, 0.49)	**9.88**(9.56, 10.2)
2.5 M KBr ($t_{24\ hrs}$)	**0.40**(0.38, 0.43)	**0.76**(0.74, 0.77)	**1.09**(1.01, 1.17)	**0.69**(0.68, 0.70)	~

5 M KBr (t_0)	**0.53**(0.49, 0.57)	**0.47**(0.38, 0.56)	**0.37**(-7.18, 7.91)	**0.30**(0.29, 0.32)	**10.1**(9.82, 10.3)
5 M KBr ($t_{5\ hrs}$)	**0.47**(0.44, 0.50)	**0.59**(0.58, 0.61)	**0.79**(0.63, 0.95)	**0.54**(0.52, 0.55)	**41.5**(36.5, 46.4)
5 M KBr ($t_{24\ hrs}$)	**0.43**(0.36, 0.51)	**0.63**(0.51, 0.75)	**0.43**(-3.45, 4.31)	**0.52**(0.51, 0.53)	**12.6**(12.1, 13.2)
2.5 M CsBr (t_0)	**0.38**(0.35, 0.40)	**0.65**(0.64, 0.67)	**0.67**(0.45, 0.89)	**0.59**(0.58, 0.61)	**26.3**(23.3, 29.4)
2.5 M CsBr ($t_{5\ hrs}$)	**0.39**(0.36, 0.41)	**0.69**(0.68, 0.70)	**0.80**(0.63, 0.96)	**0.62**(0.60, 0.64)	**12.8**(11.8, 13.8)
2.5 M CsBr ($t_{24\ hrs}$)	**0.32**(0.30, 0.35)	**0.54**(0.53, 0.56)	**0.58**(0.19, 0.96)	**0.43**(0.41, 0.44)	**12.4**(11.9, 12.9)
5 M CsBr (t_0)	**0.50**(0.48, 0.53)	**0.66**(0.65, 0.67)	**0.001**(-0.12, 0.12)	**0.52**(0.51, 0.53)	~
5 M CsBr ($t_{5\ hrs}$)	**0.43**(0.38, 0.48)	**0.60**(0.56, 0.64)	**0.48**(-1.00, 1.96)	**0.45**(0.44, 0.47)	**9.66**(9.33, 9.99)
5 M CsBr ($t_{24\ hrs}$)	**0.40**(0.37, 0.43)	**0.71**(0.69, 0.74)	**0.56**(0.12, 1.01)	**0.60**(0.59, 0.61)	**22.4**(20.4, 24.4)

Chapter 3

Conjugated Polyelectrolyte-Based Complex Fluids as Aqueous Exciton Transport Networks

---

Acknowledgements: This chapter was originally published in Angewandte Chemie International Edition with the following authorship: Anna R. Johnston, Eris D. Minckler, Mia C. J. Shockley, Levi N. Matsushima, Sarah L. Perry, Alexander L. Ayzner. Anna Johnston carried out the steady-state and time resolved spectroscopy experiments, rheology work, data analysis, and originally crafted the manuscript. Eris Minckler carried out steady-state spectroscopy experiments and data analysis on control samples for the CPE PFPI. Mia Shockley carried out the steady-state spectroscopy experiments and data analysis on control samples for the CPE NaPCPT. Levi Matsushima carried out the small-angle x-ray scattering (SAXS) experiments. Sarah Perry provided valuable insight and interpretation of the rheology data and edited the manuscript. Alexander Ayzner did the data analysis for the SAXS experiments, edited the manuscript, and oversaw the project. A big thank you to each one of them for their help.

This material is based upon work supported by the National Science Foundation under grant no. 1848069 and by the National Science Foundation Graduate Research Fellowship under grant no. DGE-1842400. Part of this work was performed at the Stanford Nano Shared Facilities (SNSF), supported by the National Science Foundation under award ECCS-1542152 and at the UCSC Life Sciences Microscopy Center (RRID:SCR_021135). And finally, use of the Stanford Synchrotron Radiation Lightsource, SLAC National Accelerator Laboratory, is supported by the U.S. Department of Energy, Office of Science, Office of Basic Energy Sciences under Contract No. DE-AC02-76SF00515.

Abstract: The ability to assemble artificial systems that mimic aspects of natural light-harvesting functions is fascinating and attractive for materials design. Given the complexity of such a system, a simple design pathway is desirable. Here, we argue that associative phase separation of oppositely charged conjugated polyelectrolytes (CPEs) can provide such a path in an environmentally benign medium: water. We find that complexation between an exciton–donor and acceptor CPE leads to formation of a complex fluid. We interrogate exciton transfer from the donor to the acceptor CPE within the complex fluid and find that transfer is highly efficient. We also find that excess molecular ions can tune the modulus of the inter-CPE complex fluid. Even at high ion concentrations, CPEs remain complexed with significantly delocalized electronic wavefunctions. Our work lays the rational foundation for complex, tunable aqueous light-harvesting systems via the intrinsic thermodynamics of associative phase separation.

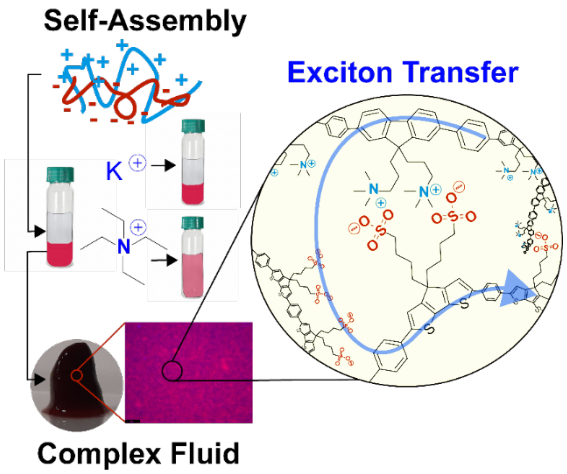

3.1 Introduction

There is a major need to construct artificial light-harvesting systems capable of efficiently converting solar energy to electrical or chemical potential energy. Such a system should mimic the natural photosynthetic process by effectively capturing, transferring, and storing photon energy. Among the materials synthesized for such efforts, organic semiconductors possess the advantages of being light-weight, highly tunable, and inexpensive to process. Major efforts have been undertaken to make new materials for organic photovoltaic devices.[1–5,6–9] Recently, much work has gone into the use of self-assembly to form components of light-harvesting systems, like electronic energy-transfer antennae.[10–15,16,17] Here the self-assembled components are arranged through non-covalent interactions to directionally guide the transport of electronic excited states (excitons) mimicking exciton transport in photosynthetic organisms.

Organic semiconductor materials are often processed in organic solvents, whether to form a thin film or a solvated assembly. In contrast, self-assembly of light-harvesting systems in water allows for the construction and processing of these materials in an environmentally benign way. Forming an aqueous system capable of multiple critical light-harvesting functions is a grand challenge. Such a system must incorporate efficient light absorption, directional exciton transfer, formation of an artificial electron/hole transport chain, and eventually the capacity to perform chemical transformations. This demanding list of requirements suggests that simplicity of assembly should be pursued to keep the overall complexity tractable.

We advance the idea that associative phase separation of polyelectrolytes holds promise to meet the above requirement of simplicity of assembly, while retaining significant potential to incorporate multiple light-harvesting functions into the overarching aqueous system. There is revived interest in aqueous associative phase separation of polyelectrolytes. Specifically, liquid- liquid phase separation of inter-polyelectrolyte complexes, in which oppositely charged polyelectrolytes electrostatically self-assemble and partition into polyelectrolyte-rich and dilute phases, has been studied thoroughly to aid understanding in early cell development, drug delivery, catalysis, and underwater adhesives.[18–25] Research efforts have largely centered on polyelectrolytes with saturated, or non-conjugated, backbones. However, associative phase separation of conjugated polyelectrolytes (CPEs) capable of visible light absorption has received significantly less attention. We have recently shown that complexation of a CPE with an oppositely charged non-conjugated polyelectrolyte led to aqueous associative phase separation and formation of concentrated, CPE-rich phases.[26] The photophysics within the polymer-rich phase were found to be strongly coupled to the ionic atmosphere. The Segalman and Chabinyc groups have also shown that oppositely charged systems with one conjugated and one non- conjugated polyelectrolyte can be used to form semiconducting and conducting fluids.[27,28]

In this work, we have used aqueous associative phase separation to form complex fluids composed of two oppositely charged CPEs which function as an exciton donor/acceptor pair. We find spectrally broad light absorption and highly efficient exciton transfer from the donor to the acceptor CPE. Additionally, the phase behavior of these complex fluids in the limit of high ionic strength depends strongly

on whether the atomic cation K^+ or small molecular cations are present. Using a chemical series of molecular ions, we demonstrate that the phase behavior is largely insensitive to the chemical structure of such ions. By probing the CPE photophysics, we can directly elucidate how the delocalized electronic wavefunction of the CPE evolves across the transition from the two-phase to the one-phase region of the phase diagram. To the best of our knowledge, our work is the first to demonstrate the formation of an aqueous complex fluid composed of an exciton donor/acceptor network capable of efficient EET.[27,28,29]

3.2 Results

To prepare complexes between oppositely charged exciton-donor and exciton-acceptor CPEs, the total polymer concentration was fixed, and the stoichiometric polyion charge ratio was held at 1:1. The salt concentration and type were then varied. The chemical structures of the cationic donor (PFPI), the anionic acceptor (NaPCPT) CPEs, and the salts used in this study are shown in Figure 3.1. The color coding indicated by the circles will be used to distinguish between the salts in subsequent figures. Our choice of the CPEs was based on the following: (1) The photophysical properties of these CPEs allow them to function as an exciton donor/acceptor pair shown by their spectral overlap in Figure 3.1. We show in the Supporting Information that these optical properties change relatively little in different environments (Figures AII.14, AII.19, and AII.20). (2) They have similar linear charge densities: ~0.017 eÅ-1 for PFPI, and ~0.019 eÅ-1 for NaPCPT (e is the electronic charge). (3) Given the similar charge densities and the chemical structures of the repeat units, we expect good alignment between oppositely charged sidechain termini

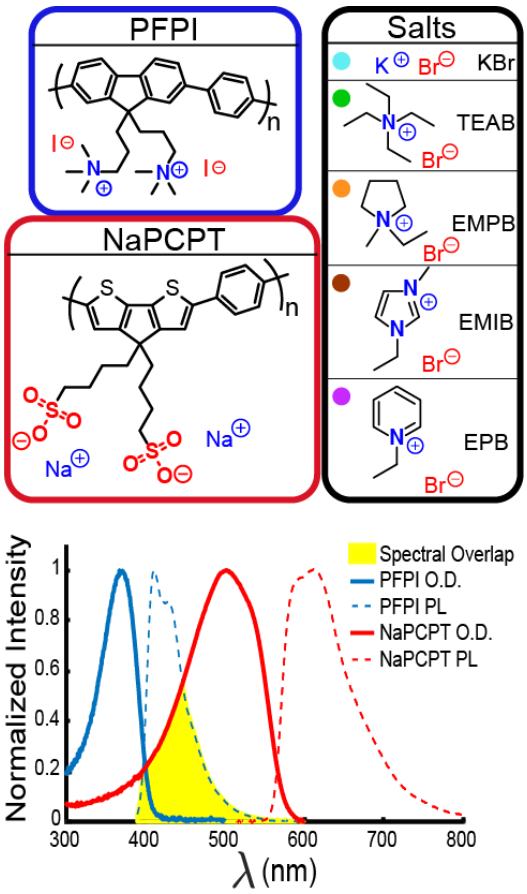

Figure 3.1: Top: Chemical structures of CPEs and salts: tetraethylammonium bromide (TEAB), 1-ethyl-1-methylpyrrolidinium bromide (EMPB), 1-ethyl-3-methylimidazolium bromide (EMIB), and 1-ethylpyridinium bromide (EPB). Bottom: normalized optical density (O.D.) and photoluminescence (PL) spectra of the CPEs (both 0.05 mg/ml in HPLC grade H2O). The yellow area indicates the spectral overlap between donor emission and acceptor absorption.

of the two CPEs. Using a chemical series of molecular ions was motivated by the fact that a CPE complex (CPEC) is quite hydrophobic. Thus, it is reasonable to suppose that when two CPEs complex at ionic charge equivalence a precipitate will likely form. Guided by our recent work with a polyelectrolyte complex between PFPI and an anionic non-conjugated polyelectrolyte with simple ions, we hypothesized that molecular ions could (i) stabilize a more fluid morphology of a CPEC concentrated phase, and (ii) lead to enhanced CPE-ion interactions that could manipulate the CPE electronic structure. The molecular ions used here are similar in size but possess varying geometries and degrees of unsaturation. These ions have also been investigated in stabilizing a liquid 'fused-salt' phase associated with hydrogen bromine redox flow batteries.[31] By including both saturated and unsaturated ions, we aimed to elucidate whether π-stacking interactions between ions and CPE backbones are an important factor in the phase behavior and photophysics of CPEC solutions.

We find that upon complexation the exciton-donor and acceptor CPEs self-assemble and associatively phase-separate, forming a dilute solution phase in coexistence with a concentrated polymer-rich phase. Cartoons in Figure 3.2 indicate subtle changes in phase volume and phase transitions as a function of salt type and concentration. Photographs of the separated concentrated phase are also included, showing this material has the visual appearance of a complex fluid that retains its shape but is easily deformable.[32]

The advantage of two optically active polyelectrolytes is that each has its own spectroscopic signature, allowing us to separately interrogate the CPEs by varying the

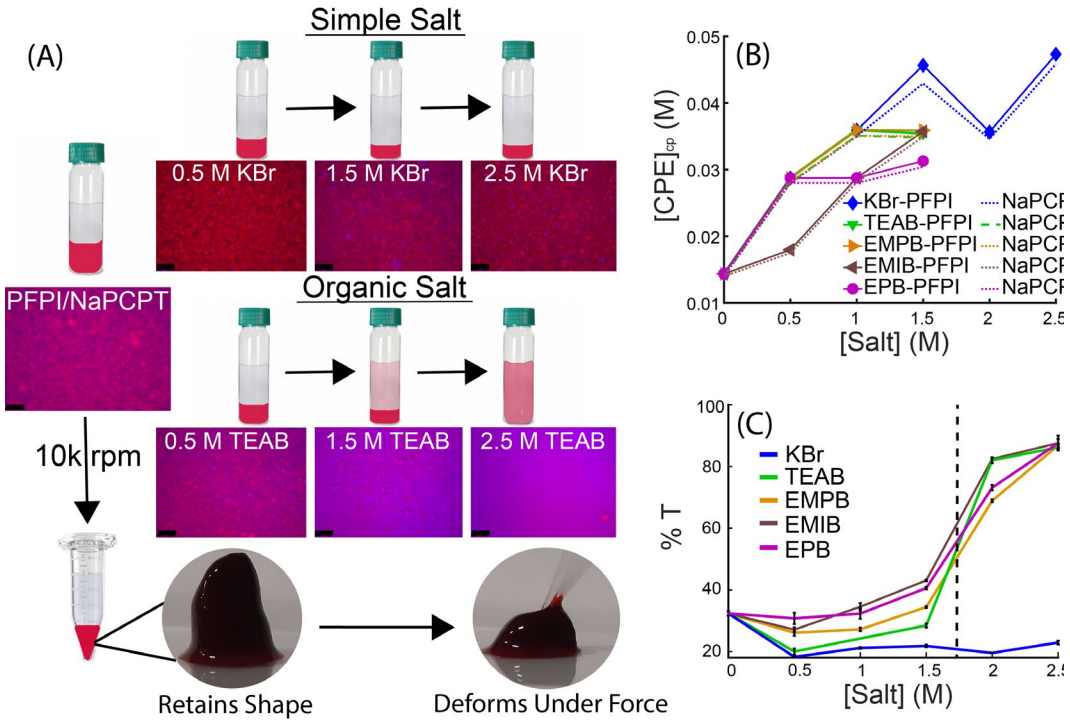

Figure 3.2: (A) Cartoon representation of observed phase separation along with PL microscopy images (50 μm scale bars) of the CPEC with no excess salt (left) and with increasing KBr and organic salts. (B) concentration of each CPE in the concentrated phase of phase-separated samples where the abscissa is the as-prepared salt concentrations of the overall solutions. (C) %T of PFPI/NaPCPT with increasing as-prepared concentrations of KBr, TEAB, EMPB, EMIB, and EPB. The salt concentration corresponding to the transition from phase-separated to dissolved solution is indicated by the black dashed lined. The figure shows that, unlike KBr, all organic salts lead to a similar transition point.

excitation and emission wavelengths. We took advantage of the dilute phase absorption to measure the CPE concentration in the concentrated phase. We first measured extinction coefficients for each CPE (Figure AII.16) and, together with estimated phase volumes and dilute-phase concentrations (Figure AII.15), calculated the amounts of both CPEs in the concentrated phase. These results are shown in

Figure 3.2B. The molar monomer concentrations for both CPEs are nearly equal, showing that the concentrated phase contains oppositely charged CPEs at near charge equivalence. The total CPE concentration increases with increasing [salt] and eventually reaches an effective plateau.[33] The highest total molar monomer concentration in the concentrated phase was found for 2.5 M KBr and corresponds to ~100 mM in total monomer (~33 mg/mL PFPI, ~27 mg/mL NaPCPT), compared to the total monomer concentration of 6 mM (2 mg/mL PFPI, 1.6 mg/mL NaPCPT) in the initial solution before phase separation. Thus, the concentrated phase is highly enriched (~17x) in both CPEs compared to the hypothetical dissolved solution.

The observed trend of increasing CPE concentration with increasing [salt] is somewhat unexpected. Most experimental and computational reports on liquid complex coacervates describe a decrease in polymer concentration with increasing [salt]. This "self suppression" phenomenon is typically associated with increased electrostatic screening at high ionic strength and higher water content in the dense phase.[33–36] However, this trend of increasing polymer concentration with increasing [salt] has been reported for solid complexes formed from hydrophobic polyelectrolytes, and was attributed to Donnan effects associated with the osmotic pressure of the salt ions.[32] It is unclear from our data whether the observed plateau in the polymer concentration is indicative of a so-called open phase boundary reported for more hydrophobic polymers, where no critical point exists, or if the more traditional self-suppression regime of coacervation was merely not observed in our experiments.[37]

Next, we collected photoluminescence (PL) microscopy images to visualize the phase microstructure. Figure 3.2A shows wide-field PL microscope images of bulk solutions for varying [salt]. Phase-separated samples were mechanically homogenized prior to acquiring the images for each salt type and concentration. We note that following homogenization, the complex fluid naturally separates from the dilute phase while retaining its original morphology. Images collected across the salt series are shown in Figures AII.1-AII.6. Blue regions correspond to PFPI PL signal, while red regions correspond to that of NaPCPT (Figure AII.1). Overlaid PL images with pink/purple tones are indicative of PL coming from both CPEs in that area. Exposure times for the excitation wavelengths corresponding to each polymer were chosen to maximize image contrast.

For all [KBr], the microscale morphology resembles a colloidal gel (Figure AII.2). At low salt concentrations, the CPEC morphology with KBr vs. TEAB is qualitatively similar. In stark contrast to KBr, in the presence of TEAB at 2.0 M, well-defined particles begin to disappear as the solution becomes more homogeneous (Figure AII.3). At 2.5 M TEAB, the solution becomes homogeneous and optically clear. This transition indicates that the state of the system on the [salt] – [CPE] phase diagram crosses from the two-phase region into the one-phase region. Similar phase behavior was observed for all organic ions regardless of chemical structure (Figures AII.3-AII.6).

We can quantify this salt-induced dissolution transition by measuring the solution turbidity via % transmittance (%T) at a nonabsorptive photon wavelength. Figure 3.2C shows a comparison of %T for each salt type as a function of salt

concentration. We found a low %T of ~20-40 for samples in which phase separation occurs. This indicates formation of scattering particles with dimensions on the order of the wavelength of visible light, consistent with microscopy images. We find that this dissolution occurs between 1.5 – 2.0 M for each organic salt, eventually forming optically clear solutions at 2.5 M salt with %T ~ 90. It is intriguing that this phase transition is not observed with increasing [KBr]. The turbidity curves are remarkably similar for all organic ions used, showing approximately the same phase transition point. This observation suggests that the general hydrophobic nature of the ions is the dominant factor in the macroscopic phase behavior difference relative to KBr, not specific chemical interactions.

Although images in Figure 3.2 cannot be used to quantitatively compare PL intensities, we can do so by averaging the PL signal of each image while keeping the exposure and gain fixed for each filter setting. This analysis shows that the total PFPI PL signal in CPEC samples was strongly quenched (see Figure AII.12C): < 0.14 (arbitrary units) mean intensity for the CPEC compared to > 70 for the no-salt PFPI control and ~20 for isolated PFPI in the presence of organic salts (Figure AII.12A). Quenching of CPE PL could proceed via two mechanisms: (i) collapse of CPE chains into tight coils, forming non-emissive exciton trap states, or (ii) EET between donor and acceptor CPEs in the CPEC. In the phase-separated control PFPI solutions (Figure AII.12A), quenching of PFPI PL must occur due to aggregation effects and the formation of non-emissive interchain states as these samples lack NaPCPT as a possible EET acceptor. This is consistent with microscopy images of these control solutions shown in Figures AII.7-AII.11. However, the PFPI PL signal in the CPEC

for all salt types is smaller by a factor of > 143 compared to that of the PFPI control at the same salt concentration (Figure AII.12C). Therefore, the strong quenching of PFPI PL within phase separated CPEC solutions together with the increase in PL from NaPCPT (Figure AII.12D) is much more likely due to EET from the exciton donor PFPI to the acceptor NaPCPT.

To understand the effects of increasing non-covalent interactions (i.e., electrostatic, hydrophobic, and π-π) across the salt series on the rheological properties of the concentrated phase, we performed small-amplitude oscillatory shear (SAOS) measurements. Rheology experiments were carried out on the concentrated phase of the CPEC both with no excess salt and with 1.0 M salt at a strain amplitude within the linear viscoelastic region. All samples displayed shear thinning and an approximately frequency-independent response in which the storage modulus (G') dominated over the loss modulus (G'') (Figures AII.17A and AII.17C). Similar yield strains of ~5% were found for each sample (Figure AII.17D) when conducting amplitude sweeps. The properties of the concentrated phase are consistent with known properties of yield stress fluids.[38,39] The flow point, which we define as the crossover frequency after which G'' dominates, was found to decrease from 50% for the no-salt CPEC (Figure 3.3A and AII.17B) to 31% in the presence of all salts.[40] This suggests a weakening of the total interchain interaction strength within the CPEC with increasing [salt] regardless of salt type.

To quantify the relative magnitudes of the two moduli, we calculated the loss tangent according to $\tan\delta = G''/G'$, where δ is the phase angle. This provides a measure of sample deformability, with larger $\tan\delta$ values indicating samples more easily deformed under an applied force. Figure 3.3B shows the trend of the concentrated phase of the CPEC from least to most deformable is: no excess salt < KBr = TEAB < EMPB = EMIB < EPB.

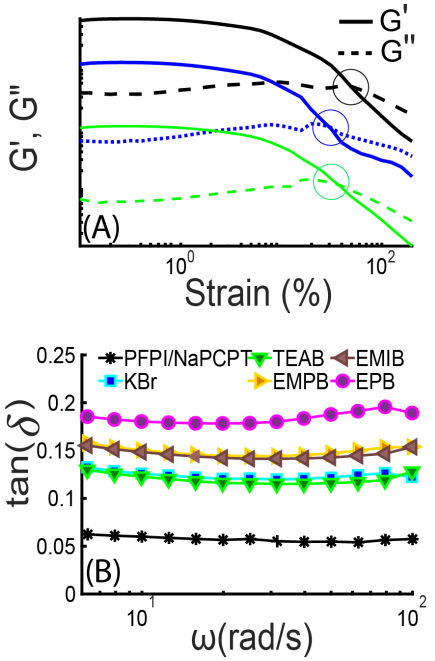

Figure 3.3: Rheological response of the concentrated phase of PFPI/NaPCPT alone, and with 1.0 M of each salt type. (A) shows the crossover of G′ and G″ vs. strain for PFPI/NaPCPT alone and for samples containing KBr/TEAB. Magnitudes of the moduli have been shifted for clarity, the colors match the key in panel B, and the circles indicate flow points. (B) tan(δ) vs. angular frequency indicating sample deformability.

We now use the distinct PL signatures of the donor and the acceptor to interrogate the photophysics of the concentrated phase. Two questions are of direct light-harvesting relevance: (i) How efficient is EET between donor and acceptor CPEs? (ii) How does the ion type and concentration influence exciton motion along the acceptor CPE network following initial transfer of donor excitons? We set out to answer these questions by isolating the concentrated phase and performing combined steady- state and time-resolved PL measurements.

Figure 3.4A and 3.4B show steady-state PL spectra of the CPEC concentrated phase with added KBr and TEAB following excitation of PFPI. Within the complex, PFPI light emission (~ 400-600 nm) is completely quenched and remains so regardless of salt type or concentration. This drastic quenching cannot simply be ascribed to formation of PFPI aggregates within the solid state. Pure aqueous PFPI solutions in the absence of salt readily form hydrogels at [PFPI] ~ 10 mg/mL, a concentration in line with that reported for poly(fluorene-alt-thiophene) gels.[41] We find that PFPI hydrogels are emissive and not self- quenched, as shown by the dashed curve in Figure 3.4A and 3.4B. These observations imply that the EET efficiency from the donor to the acceptor in the concentrated CPEC phase is nearly 100%. We also observe substantial emission from the acceptor CPE when exciting at the wavelength corresponding to maximal donor OD and minimal acceptor OD, which is also consistent with EET. Similar quenching is observed for the rest of the organic salts in the series (Figure AII.19).

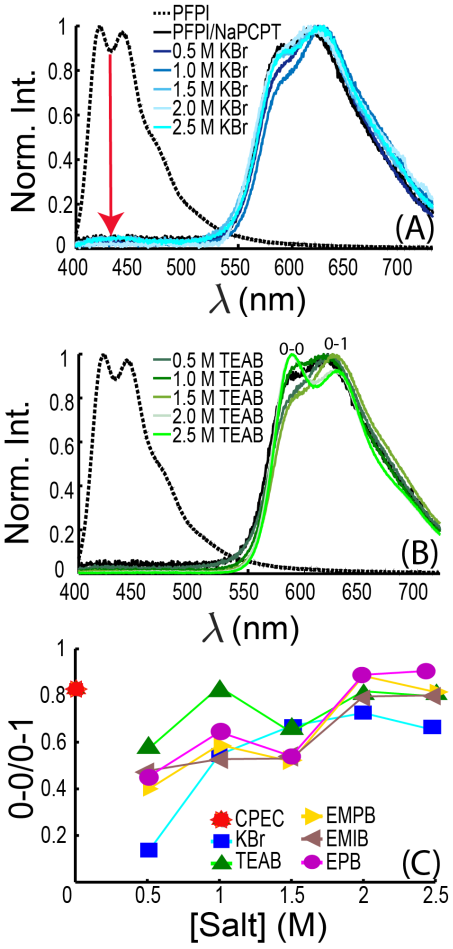

Figure 3.4: Steady-state PL spectra (excitation 375 nm) of 10 mg/mL PFPI hydrogel control and PFPI/NaPCPT complexes with increasing (A) [KBr] or (B) [TEAB]. (C) Vibronic ratio vs. [salt] for each salt type.

Interestingly, the PFPI PL intensity remains completely quenched even in bulk solution beyond the dissolution phase transition at high organic salt concentrations.

With evidence of efficient EET occurring in the concentrated phase and in the high-salt dissolved state, we wanted to understand how changes in ionic environment affected emission from the acceptor CPE across the dissolution phase transition. Once the initial PFPI exciton transfers to NaPCPT, that exciton will diffuse along the NaPCPT network, the structure of which is encoded in the acceptor PL spectrum. The ensemble of acceptor chromophores will influence this exciton motion via both the microstructure of single acceptor chains as well as excitonic couplings between proximal chains. Thus, the measured emission spectrum will directly reflect these factors. Figure 3.4A and 3.4B show that the shape of the NaPCPT emission spectrum (~ 550- 750 nm) changes as a function of salt concentration. The primary change occurs in the ratio of the 0-0 (lowest energy) peak relative to the 0-1 vibronic peak, where the final state is electronically relaxed but remains vibrationally excited. The 0-0/0-1 PL intensity ratio carries particular significance for conjugated polymers, as it reflects the interplay between intrachain (through-bond) and interchain (through-space) electronic couplings.

Specifically, it is the ratio of the square of the transition dipole moments for the 0-0 and 0-1 transitions that encodes information about such couplings.[42,43] For further analysis, we first transformed PL spectra to energy space.[44] We then divided out the ν^3 (ν – photon frequency) dependence of the emission intensity to obtain the quantity that is proportional to the square of the transition dipole moment, assuming a

frequency-independent refractive index over the emission energy range. Finally, the baseline-corrected vibronic progression was fit using a sum of Gaussians:

$$I(E) \propto \sum_{v=0}^{3} a_v e^{-(E-E_0+v\hbar\omega)^2/\sigma_v^2} \qquad \textbf{(3.1)}$$

where I is the modified intensity, E is the photon energy, E_0 is the origin of the purely electronic (0-0) transition, the a_v are Gaussian amplitudes, v is the vibrational quantum number, ω is the angular frequency of the aromatic stretching mode that predominantly couples to the electronic transition, and the σ_v are Gaussian widths. Fits for all salt types and concentrations were of excellent quality. The 0-0/0-1 peak amplitude ratios, I_{00}/I_{01}, extracted from the fits as a function of salt concentration are shown in Figure 3.4C. For three of the four organic salts (EMPB, EMIB, EPB), the ratio depends weakly on salt concentration between 0.5 and 1.5 M. At salt concentrations ≥ 2.0 M, I_{00}/I_{01} increases by ~60%. At 2.5 M the ratio is approximately the same for the four organic salts. In contrast, KBr did not give rise to the large change at 2.0 M, instead showing a slow rise with concentration above 0.5 M.

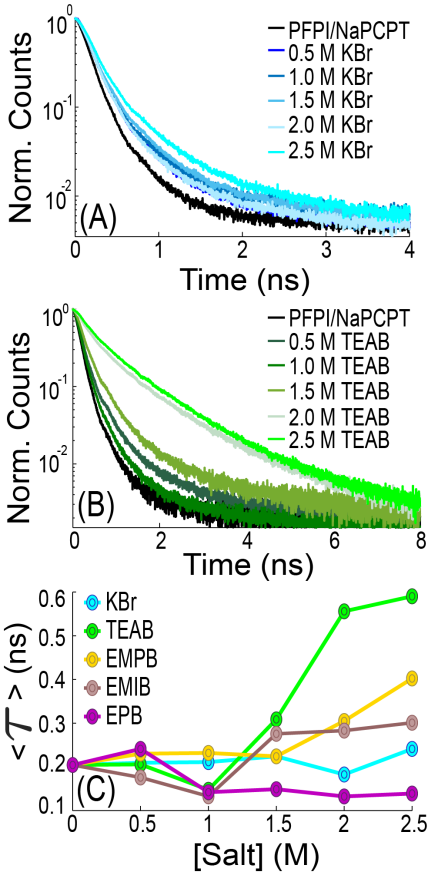

Figure 3.5: Time-resolved PL decay curves (λ_{ex} = 375 nm, λ_{em} = 600 nm) of PFPI/PCPT complex with increasing (A) [KBr], (B) [TEAB]. (C) average excited-state lifetimes (<τ>) vs. salt concentration for each salt type.

The dynamics of light emission can reveal additional information about the acceptor chain microstructure and its evolution with salt. We thus measured time-resolved PL (TRPL) decays of the concentrated complex fluid phase and dissolved solutions. We excited samples at λex = 375 nm at the peak of the PFPI absorption band and detected emission from the acceptor CPE at λem = 600 nm. Figure 3.5A shows NaPCPT TRPL decays as a function of [KBr]. Decays are biexponential, are dominated by the short lifetime component τ_1, and become slightly longer with increasing salt concentration. Figure 3.5B show the corresponding decays as a function of [TEAB]. A similarly mild lengthening of the decay is seen for TEAB as for KBr up to 1.5 M. However, at [TEAB] > 1.5 M, which is the onset of the dissolution transition, the decay is seen to lengthen substantially in strong contrast to KBr.

We find the same qualitative trend holds for most organic ions, as captured by plotting the average PL lifetime $\langle\tau\rangle$ as a function of salt type and concentration in Figure 3.5C. Decays for other salts are shown in the Supporting Information (Figure AII.21). The average lifetime of the NaPCPT within the CPEC without added salt was found to lengthen compared to the acceptor at the same concentration (1.6 mg/mL) in its native state in aqueous solution (0.14 ns). Average lifetimes associated with the concentrated phase for each [KBr] are comparable to that of the PFPI/NaPCPT complex without added salt and remain sub-0.25 ns regardless of [KBr]. Lifetimes for TEAB, EMPB, and EMIB at low salt concentrations were found to be comparable to the PFPI/NaPCPT control. In contrast to KBr, this was followed by a significant increase in lifetime for the high-salt samples (1.5 – 2.5 M). The

largest increase was seen for 2.5 M TEAB with an average lifetime of ~0.6 ns – a 200% increase from the mean concentrated-phase lifetime of the PFPI/NaPCPT control. This large increase in $\langle\tau\rangle$ is largely associated with an increase in the amplitude of the long-lifetime component τ_2, which falls in the range between ~1 and ~1.5 ns depending on the salt (Figure AII.24). The amplitude for the long-lifetime component, though relatively small, increases by approximately two orders of magnitude for most organic ions between 1.5 and 2.5 M. Samples containing EPB are notable outliers from the other organic salts by exhibiting on-average shorter lifetimes than the complex without added salt. This ~40% decrease in $\langle\tau\rangle$ is consistent with the decrease in PL intensity of the bulk solution shown in Figure AII.12. Similar trends are seen for TRPL measurements where the acceptor CPE is excited near its OD peak (λex = 500 nm, λem = 600 nm), shown in Figure AII.22.

Time-dependent PL anisotropy can inform on the nature of the emitting state(s). We excited the acceptor CPE with vertically polarized light (λ_{ex} = 500 nm) and measured the time-dependent emission intensity in the vertical (I_{VV}) and horizontal (I_{VH}) planes (λ_{em} = 600 nm) to probe the exciton dynamics of the emitting states and to probe the exciton dynamics of the emitting states and to calculate the anisotropy function (Equation AII.1). Figure 3.6A shows normalized anisotropy decays for the concentrated phase prepared at 0.5 M salt for each salt type compared to the no-salt control. The anisotropy of the CPEC without any added salt was found to decay completely by 4 ns, with a majority of the exciton polarization decaying by 2 ns. Similar results were found for all salt types at 0.5 M. This finding is consistent with little to no change in the exciton lifetime and overall PL intensity found for these samples when compared to the complex on its own. In contrast, 2.5-M salt samples (Figure 3.6B) containing TEAB, EMPB, and EMIB give rise to a relatively long-lived anisotropy compared to 0.5-M samples. Concentrated phases prepared with 2.5 M KBr and 2.5 M EPB gave decays that were qualitatively similar to their 0.5 M counterparts.

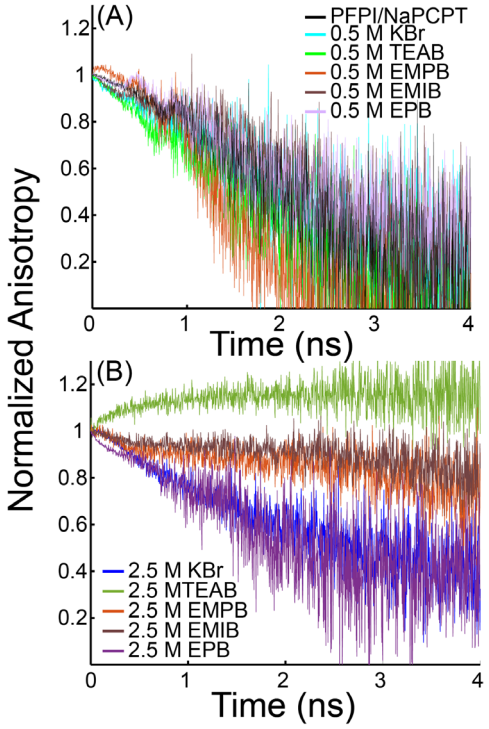

Figure 3.6: TR-PL Anisotropy as a function of time of (A) 0.5 M samples and (B) 2.5 M samples containing each salt

The fact that PFPI PL remains quenched in the one-phase region at organic salt concentrations > 2.0 M suggests the two CPEs dissolve as a complex. If the two CPEs are spatially separated, it is unlikely that collisions in the highly screened solution would occur at a sufficiently large rate to quench all donor PL. If the two CPEs instead dissolve as a bound complex, one would expect to be able to observe nanoscale microstructural features consistent with such a complex. To test this hypothesis, we performed solution small-angle X-ray scattering (SAXS) measurements in the high-salt limit for all organic salts. Figure 3.7A shows reduced SAXS intensities as a function of the scattering vector length Q. It is clear from the appearance of two Guinier-like plateau regions that the solution displays hierarchical structure on the nanoscale. SAXS curves for all organic salts are qualitatively similar. This implies that the solution nanostructure is largely independent of the molecular structure of the small ions.

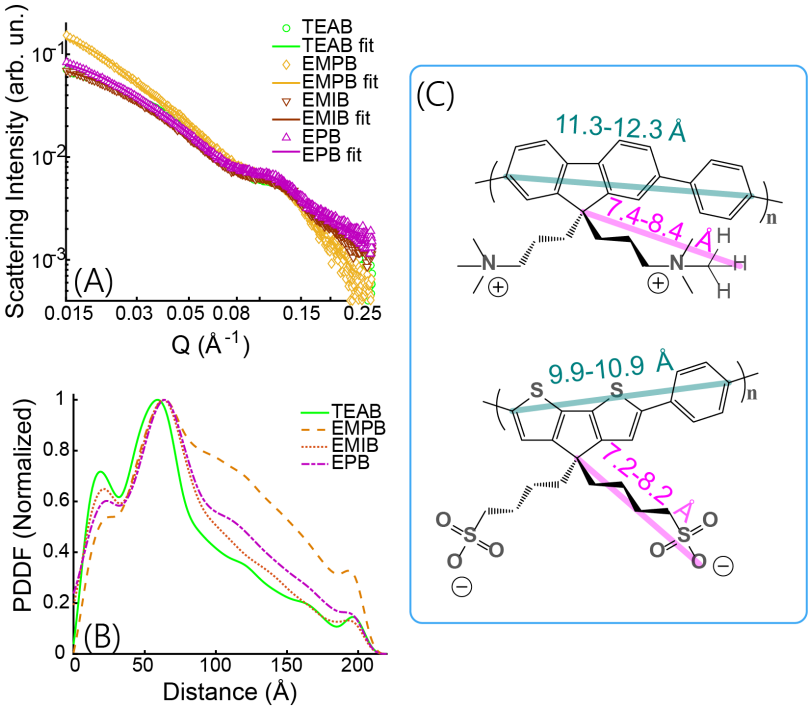

Figure 3.7: SAXS data for fully dissolved 2.5-M samples with molecular ions. (A) Reduced scattering intensity vs. scattering vector length Q. (B) Pair distance distribution functions (PDDF) obtained via the indirect Fourier transform. (C) Chemical structures of CPE repeat units with two highlighted length scales along the backbone and sidechain directions.

To determine the correlation lengths present in the dissolved solutions, we fit the scattering curves using the indirect Fourier transform. This allows determination of the particle form factor and calculation of the pair-distance distribution functions (PDDFs) of the scattering inhomogeneities in a model-independent manner. Fits are displayed in Figure 3.7A as solid lines, showing that all fits are of excellent quality. Figure 3.7B shows PDDFs for all one-phase solutions at 2.5 M salt. There are two primary peaks that stand out at ~2.5 nm and ~6 nm.

Are these correlation distances consistent with what may be expected for a dissolved CPEC? We attempted to answer this question by calculating a few relevant distances for the two CPEs in question, which are shown in Figure 3.7C. In the CPEC, we expect that on average the two CPEs are separated through a distance roughly equal to the sum of the sidechain lengths. We find the calculated distance corresponding to the sum of the sidechains is in good agreement with the lower correlation distance of 2.5 nm. The 6-nm correlation length is significantly larger than the length of the repeat unit for either CPE. In fact, this length corresponds to approximately 6 repeat units. Thus, we propose that the 6-nm correlation length corresponds to a region over which the average CPE chain is relatively straight, corresponding to a local ladder-like conformation.[45] Taken together, we believe the PDDFs are consistent with a physical picture of dissolved CPECs with on-average locally straight conformations. Such a conformation is in turn consistent with the relatively large vibronic ratio seen in NaPCPT PL spectra and the increase in $\langle\tau\rangle$ at this salt concentration.

It is helpful to distinguish our CPEC SAXS results in the one-phase region with that of a complex between nonconjugated hydrophobic polyelectrolytes. We believe the best basis for this comparison is through the recent work by Meng, et al.,[32] which used polycations and polyanions with sidechains terminated with trimethylammonium styrene or sulfonate styrene groups, respectively. Therein it was also concluded that ladder-like polyelectrolyte complexes were dissolved in high-salt NaBr solutions. Interestingly, their SAXS curves did not display such two pronounced Guiner-like plateaus. It is likely that the structure of our dissolved CPECs at high ionic strengths differ significantly from that of the styrene-based hydrophobic polyelectrolytes reported by Meng, et al.

3.3 Discussion

We first summarize our primary results: (1) CPEC dissolution was observed with all organic salts at a similar phase-transition point. This transition was not observed with KBr over the same concentration range. (2) Mechanical properties of the concentrated complex fluid phase are dependent on the geometry of molecular ions present but display similarities within a given geometric class. (3) We find strong evidence of efficient EET between the exciton donor and acceptor CPEs in both the concentrated complex-fluid phase and in the one-phase fully dissolved solution. (4) The backbone of the acceptor CPE becomes more extended as the dissolution phase transition is approached and crossed, and the microstructure of the dissolved state is a locally extended ladder-like complex.

The fact that the concentrated phase is a shear-thinning complex fluid capable of highly efficient EET has light-harvesting implications. This implies that such a

phase may be easily deposited on, e.g., an electrode surface as a paste, or 3D-printed into a desired form, for incorporation into an overarching light-harvesting system. The efficient EET provides a direct pathway towards panchromatic light absorption. While EET from the donor to the acceptor remains efficient for all concentrated phases, the change in the radiative relaxation of the acceptor with increasing salt concentration is also intriguing. First, the increasing 0-0/0-1 PL intensity ratio of the acceptor is correlated with an increase in the exciton coherence number or, consistently, the inverse participation ratio of the excitonic wavefunction.[42,43,46] In conjunction, we observe an increase in the average PL lifetime and the decay time of the TRPL anisotropy. Therefore, we conclude that the spatial extent of the electronic wavefunction along the acceptor CPE backbone lengthens with increasing salt. This consideration is also important for light harvesting implications as such lengthening leads to more rapid intrachain exciton transport. The net effect is more efficient sampling of the underlying excitonic network during the excited-state lifetime. When supplied with a photoinduced electron acceptor, CPE excitons that efficiently sample the underlying network will be able to find an interface to dissociate into spatially separated electron-hole pairs, thus storing photon energy as electrochemical energy. To this end, we previously showed that the quintessential electron acceptor, a C70 derivative, with negligible aqueous solubility may be readily incorporated into the aqueous CPE-based concentrated phase.[26] Therefore, we hypothesize that the yield of electron/hole pairs in such a complex fluid system could be tuned by varying the excess salt concentration.

The facts that (i) the dissolution phase-transition was observed for all molecular ions but not KBr, and (ii) that the concentration corresponding to this transition was independent of molecular ion structure are compelling. These are correlated with the observations that the average PL lifetime of the acceptor CPE depended relatively weakly on molecular ion type, and that the CPEC structure in the dissolved solution was largely independent of ion type. Thus, there is a kind of universality to the microstructural state of the CPEC in the presence of molecular ions chosen in this study. This is interesting because the chemical structures of the molecular ions are quite different. We propose this is due to the van der Waals and hydrophobic interactions of the molecular ions with the hydrophobic region of the CPE sidechains within the CPEC. Such interactions are much weaker with the potassium cation, which is consistent with the inability of this ion to access the dissolution phase transition over the observed salt concentration range. We conclude that, from a light-harvesting perspective, ions capable of a combination of electrostatic, van der Waals, and hydrophobic interactions are preferred agents for manipulating the structure of the CPEC state.

Though the universal influence of the molecular ions on the photophysics of the CPEC is evident, subtle changes in molecular ion structure can be used to finely tune the mechanical properties of the condensed complex-fluid phase. We found that the ordering of the loss tangent for the different salts reflected this fact. Close inspection of the molecular structures of these cations indicates the following trend: the largest, most unsaturated and highly polarizable ion EPB led to the largest plasticization of the concentrated phase. EMIB and EMPB are less effective

plasticizers than EPB, but they have equal effectiveness at disrupting CPEC chain interactions. This is likely because they are similar in structure, largely differing in the degree of unsaturation of the five-membered ring. TEAB and KBr have smaller loss tangents, but the two values are nearly identical. Though surprising, on the length scale of a chromophore (~5-10 repeat units) K^+ is spherically symmetric and so is TEAB. Additionally, the radius of TEA^+ (with very few hydrating water molecules) is approximately equal to the hydration radius of K^+.[47] Thus, one interpretation of the loss tangent ordering is that anisotropic molecular ions are more effective at increasing the loss modulus relative to the storage modulus than spherical or quasi-spherical ions. But why then was EPB not grouped together with EMIB and EMPB? We speculate that the relatively large size and the six-membered ring of EPB allow it to interact with each CPE through the largest extent of van der Waals and hydrophobic interactions possible within this salt series. However, we are unable to rule out higher-order effects such as specific arrangements conducive to cation-π or cation-backbone interactions, which may be enhanced with the pyridinium core.[48]

Interestingly, the CPEC photophysics in the presence of EPB contrasts all other molecular ions due to the significantly quenched NaPCPT PL. This was the case for both isolated control NaPCPT measurements and within the CPEC, but not for isolated PFPI solutions. We believe that EPB is acting as a photoinduced electron acceptor with respect to NaPCPT. This view is consistent with prior investigations of pyridinium-based ions.[49,50] In Table AII.1 we have listed the available energy levels obtained with a combination of cyclic voltammetry and photoemission measurements along with density functional theory calculations for polymers with identical

backbones to PFPI and NaPCPT, as well as the pyridinium cation. The totality of the data shows that EPB cannot act as a photoinduced hole acceptor given the large energy barrier for hole transfer from either CPE to EPB. On the other hand, the LUMO energies of the two polymers are relatively close to EPB. It is thus quite likely that the local energy levels of either CPE or EPB may fluctuate under the influence of local electric fluctuations due to the motion of the ionic atmosphere. We speculate that the preferrential quenching of NaPCPT excitons by EPB is due to the attraction between the anionic polymer sidechains and the molecular cation.

The broader implication of the obove observation is significant: that the same small ions thatmanipulate the mechanical properties of the concentrated phase can also electronically interact with CPEC excitons. Thus, one can imagine judiciously choosing small ions to both dictate the phase behavior and to act as charge shuttles in an overarching light-harvesting system based on a CPEC complex fluid. Within this interpretation, the following question arises. Why did $\langle\tau\rangle$ for NaPCPT remain effectively unchanged as [EPB] increased from 1 to 2.5 M? If we assume random collisional quenching, a 250% increase in [EPB] should correlate with a further decrease in $\langle\tau\rangle$. We speculate that the reason for this apparent discrepancy is that the CPEC periphery is enveloped in a kind of shell composed of condensed EPB ions. The structure of this ionic shell remains approximately constant even as more EPB is dissolved in solution, leading to a nearly constant rate of photoinduced electron (or hole) transfer from NaPCPT to EPB. It is possible that such CPEC-EPB interactions are related to the fact that EPB led to the largest plasticization of the complex fluid.

3.4 Conclusion

For the first time, we have shown that CPECs are capable of associatively phase separating into a dense complex fluid phase capable of highly efficient EET. We have also shown that molecular ions capable of electrostatic and hydrophobic interactions are a superior choice when manipulating the phase behavior of CPECs through increased sidechain solubility. This was evident by the fact that molecular ions at high ionic strength led to a phase transition to a fully dissolved solution that was not observed at high concentrations of KBr. We showed that this phase transition led to an extension of the CPEC into a ladder-like conformation, leading to an increase in exciton lifetime of the acceptor CPE. We also found that judicious choice of ion geometry can help to mechanically tune the moduli of complex CPEC fluid. We believe that a better understanding of the specific influence of ion geometry on the phase behavior will be achieved with molecular dynamics simulations. However, there will likely be a need to account for explicit solvent as well as the many-body hydrophobic, π-π, and cation-π interactions.

We believe this work has laid the rational foundation for using associative phase separation of CPEs as a relatively simple pathway towards complex, aqueous light-harvesting systems with substantial excitonic connectivity. With further manipulation of CPE sidechains and ion structure, as well as incorporation of photoinduced electron acceptors, we believe a truly panchromatic light-harvesting system capable of forming long-lived electron-hole pairs is possible. Such a system could function as a compartment of a larger meso- or micro-scale system, or as a

standalone modular light-harvesting platform with the ability to sustain diffusion of molecular species through its interior.

3.5 References

(1) Wang, X.; Sun, Q.; Gao, J.; Wang, J.; Xu, C.; Ma, X.; Zhang, F. Recent Progress of Organic Photovoltaics with Efficiency over 17%. *Energies* **2021**, *14* (14), 4200. https://doi.org/10.3390/en14144200.

(2) Xie, L.; Song, W.; Ge, J.; Tang, B.; Zhang, X.; Wu, T.; Ge, Z. Recent Progress of Organic Photovoltaics for Indoor Energy Harvesting. *Nano Energy* **2021**, *82* (2021), 105770. https://doi.org/10.1016/j.nanoen.2021.105770.

(3) Holmes, A.; Deniau, E.; Lartigau-Dagron, C.; Bousquet, A.; Chambon, S.; Holmes, N. P. Review of Waterborne Organic Semiconductor Colloids for Photovoltaics. *ACS Nano* **2021**, *15* (3), 3927–3959. https://doi.org/10.1021/acsnano.0c10161.

(4) Wang, T.; Kupgan, G.; Brédas, J. L. Organic Photovoltaics: Relating Chemical Structure, Local Morphology, and Electronic Properties. *Trends Chem.* **2020**, *2* (6), 535–554. https://doi.org/10.1016/j.trechm.2020.03.006.

(5) Sutherland, L. J.; Weerasinghe, H. C.; Simon, G. P. A Review on Emerging Barrier Materials and Encapsulation Strategies for Flexible Perovskite and Organic Photovoltaics. *Adv. Energy Mater.* **2021**, *11* (34), 2101383. https://doi.org/10.1002/aenm.202101383.

(6) Shi, Y.; Lu, X.; Zhang, Y.; Xi, J. Efficient Polymer Solar Cells That Use

Conjugated Polyelectrolyte with a Tetravalent Amine-End Side Chain. *Org. Electron.* **2020**, *77* (August 2019), 105542. https://doi.org/10.1016/j.orgel.2019.105542.

(7) Xu, Y.; Yuan, J.; Zhou, S.; Seifrid, M.; Ying, L.; Li, B.; Huang, F.; Bazan, G. C.; Ma, W. Ambient Processable and Stable All-Polymer Organic Solar Cells. *Adv. Funct. Mater.* **2019**, *29* (8), 1806747. https://doi.org/10.1002/adfm.201806747.

(8) Shi, Y.; Yu, Z.; Li, Z.; Zhao, X.; Li, X.; Xu, M.; Zhang, X.; Zhang, Q. Efficient Polymer Solar Cells Utilizing Solution-Processed Interlayer Based on Different Conjugated Backbones. *J. Appl. Polym. Sci.* **2020**, *137* (46), 49527. https://doi.org/10.1002/app.49527.

(9) Shi, Y.; Yu, Z.; Li, Z.; Zhao, X.; Yuan, Y. In-Situ Synthesis of Tio2 @go Nanosheets for Polymers Degradation in a Natural Environment. *Polymers (Basel).* **2021**, *13* (13), 2158. https://doi.org/10.3390/polym13132158.

(10) Kundu, S.; Patra, A. Nanoscale Strategies for Light Harvesting. *Chem. Rev.* **2017**, *117* (2), 712–757. https://doi.org/10.1021/acs.chemrev.6b00036.

(11) Proppe, A. H.; Li, Y. C.; Aspuru-Guzik, A.; Berlinguette, C. P.; Chang, C. J.; Cogdell, R.; Doyle, A. G.; Flick, J.; Gabor, N. M.; van Grondelle, R.; Hammes-Schiffer, S.; Jaffer, S. A.; Kelley, S. O.; Leclerc, M.; Leo, K.; Mallouk, T. E.; Narang, P.; Schlau-Cohen, G. S.; Scholes, G. D.; Vojvodic, A.; Yam, V. W. W.; Yang, J. Y.; Sargent, E. H. Bioinspiration in Light Harvesting

and Catalysis. *Nat. Rev. Mater.* **2020**, *5* (11), 828–846. https://doi.org/10.1038/s41578-020-0222-0.

(12) Hao, M.; Sun, G.; Zuo, M.; Xu, Z.; Chen, Y.; Hu, X. Y.; Wang, L. A Supramolecular Artificial Light-Harvesting System with Two-Step Sequential Energy Transfer for Photochemical Catalysis. *Angew. Chemie - Int. Ed.* **2020**, *59* (25), 10095–10100. https://doi.org/10.1002/anie.201912654.

(13) Reddy, N. R.; Aubin, M.; Kushima, A.; Fang, J. Fluorescent H-Aggregate Vesicles and Tubes of a Cyanine Dye and Their Potential as Light-Harvesting Antennae. *J. Phys. Chem. B* **2021**, *125* (28), 7911–7918. https://doi.org/10.1021/acs.jpcb.1c04262.

(14) Frischmann, P. D.; Mahata, K.; Würthner, F. Powering the Future of Molecular Artificial Photosynthesis with Light-Harvesting Metallosupramolecular Dye Assemblies. *Chem. Soc. Rev.* **2013**, *42* (4), 1847–1870. https://doi.org/10.1039/c2cs35223k.

(15) Hollingsworth, W. R.; Magnanelli, T. J.; Segura, C.; Young, J. D.; Bragg, A. E.; Ayzner, A. L. Polyion Charge Ratio Determines Transition between Bright and Dark Excitons in Donor/Acceptor-Conjugated Polyelectrolyte Complexes. *J. Phys. Chem. C* **2018**, *122* (39), 22280–22293. https://doi.org/10.1021/acs.jpcc.8b06195.

(16) Zhou, X.; Zeng, Y.; Lv, F.; Bai, H.; Wang, S. Organic Semiconductor-Organism Interfaces for Augmenting Natural and Artificial Photosynthesis.

Acc. Chem. Res. **2022**, *55* (2), 156–170. https://doi.org/10.1021/acs.accounts.1c00580.

(17) Gai, P.; Yu, W.; Zhao, H.; Qi, R.; Li, F.; Liu, L.; Lv, F.; Wang, S. Solar-Powered Organic Semiconductor–Bacteria Biohybrids for CO2 Reduction into Acetic Acid. *Angew. Chemie - Int. Ed.* **2020**, *59* (18), 7224–7229. https://doi.org/10.1002/anie.202001047.

(18) Johnson, N. R.; Wang, Y. Coacervate Delivery Systems for Proteins and Small Molecule Drugs. *Expert Opin. Drug Deliv.* **2014**, *11* (12), 1829–1832. https://doi.org/10.1517/17425247.2014.941355.

(19) Saini, B.; Singh, S.; Mukherjee, T. K. Nanocatalysis under Nanoconfinement: A Metal-Free Hybrid Coacervate Nanodroplet as a Catalytic Nanoreactor for Efficient Redox and Photocatalytic Reactions. *ACS Appl. Mater. Interfaces* **2021**, *13* (43), 51117–51131. https://doi.org/10.1021/acsami.1c17106.

(20) Drobot, B.; Iglesias-Artola, J. M.; Le Vay, K.; Mayr, V.; Kar, M.; Kreysing, M.; Mutschler, H.; Tang, T. Y. D. Compartmentalised RNA Catalysis in Membrane-Free Coacervate Protocells. *Nat. Commun.* **2018**, *9* (1), 3643. https://doi.org/10.1038/s41467-018-06072-w.

(21) Stewart, R. J.; Wang, C. S.; Song, I. T.; Jones, J. P. The Role of Coacervation and Phase Transitions in the Sandcastle Worm Adhesive System. *Adv. Colloid Interface Sci.* **2017**, *239* (1), 88–96. https://doi.org/10.1016/j.cis.2016.06.008.

(22) Lu, T.; Spruijt, E. Multiphase Complex Coacervate Droplets. *J. Am. Chem.*

Soc. **2020**, *142* (6), 2905–2914. https://doi.org/10.1021/jacs.9b11468.

(23) Chen, Y.; Yuan, M.; Zhang, Y.; Liu, S.; Yang, X.; Wang, K.; Liu, J. Construction of Coacervate-in-Coacervate Multi-Compartment Protocells for Spatial Organization of Enzymatic Reactions. *Chem. Sci.* **2020**, *11* (32), 8617–8625. https://doi.org/10.1039/d0sc03849k.

(24) Kaur, S.; Weerasekare, G. M.; Stewart, R. J. Multiphase Adhesive Coacervates Inspired by the Sandcastle Worm. *ACS Appl. Mater. Interfaces* **2011**, *3* (4), 941–944. https://doi.org/10.1021/am200082v.

(25) Sing, C. E.; Perry, S. L. Recent Progress in the Science of Complex Coacervation. *Soft Matter* **2020**, *16* (12), 2885–2914. https://doi.org/10.1039/d0sm00001a.

(26) Johnston, A. R.; Perry, S. L.; Ayzner, A. L. Associative Phase Separation of Aqueous π-Conjugated Polyelectrolytes Couples Photophysical and Mechanical Properties. *Chem. Mater.* **2021**, *33* (4), 1116–1129. https://doi.org/10.1021/acs.chemmater.0c02424.

(27) Danielsen, S. P. O.; Nguyen, T.-Q.; Fredrickson, G. H.; Segalman, R. A. Complexation of a Conjugated Polyelectrolyte and Impact on Optoelectronic Properties. **2019**, *8* (1), 88–94. https://doi.org/10.1021/acsmacrolett.8b00924.

(28) Le, M. L.; Rawlings, D.; Danielsen, S. P. O.; Kennard, R. M.; Chabinyc, M. L.; Segalman, R. A. Aqueous Formulation of Concentrated Semiconductive Fluid Using Polyelectrolyte Coacervation. *ACS Macro Lett.* **2021**, *10* (8),

1008–1014. https://doi.org/10.1021/acsmacrolett.1c00354.

(29) Shinohara, A.; Pan, C.; Guo, Z.; Zhou, L.; Liu, Z.; Du, L.; Yan, Z.; Stadler, F. J.; Wang, L.; Nakanishi, T. Viscoelastic Conjugated Polymer Fluids. *Angew. Chemie - Int. Ed.* **2019**, *58* (28), 9581–9585. https://doi.org/10.1002/anie.201903148.

(30) Hollingsworth, W. R.; Williams, V.; Ayzner, A. L. Semiconducting Eggs and Ladders: Understanding Exciton Landscape Formation in Aqueous π-Conjugated Inter-Polyelectrolyte Complexes. *Macromolecules* **2020**, *53* (7), 2724–2734. https://doi.org/10.1021/acs.macromol.0c00029.

(31) Küttinger, M.; Loichet Torres, P. A.; Meyer, E.; Fischer, P.; Tübke, J. Systematic Study of Quaternary Ammonium Cations for Bromine Sequestering Application in High Energy Density Electrolytes for Hydrogen Bromine Redox Flow Batteries. *Molecules* **2021**, *26* (9), 2721. https://doi.org/10.3390/molecules26092721.

(32) Meng, S.; Ting, J. M.; Wu, H.; Tirrell, M. V. Solid-to-Liquid Phase Transition in Polyelectrolyte Complexes. *Macromolecules* **2020**, *53* (18), 7944–7953. https://doi.org/10.1021/acs.macromol.0c00930.

(33) Li, L.; Srivastava, S.; Meng, S.; Ting, J. M.; Tirrell, M. V. Effects of Non-Electrostatic Intermolecular Interactions on the Phase Behavior of PH-Sensitive Polyelectrolyte Complexes. *Macromolecules* **2020**, *53* (18), 7835–7844. https://doi.org/10.1021/acs.macromol.0c00999.

(34) Li, L.; Srivastava, S.; Andreev, M.; Marciel, A. B.; De Pablo, J. J.; Tirrell, M. V. Phase Behavior and Salt Partitioning in Polyelectrolyte Complex Coacervates. *Macromolecules* **2018**, *51* (8), 2988–2995. https://doi.org/10.1021/acs.macromol.8b00238.

(35) Veis, A.; Bodor, E.; Mussell, S. Molecular Weight Fractionation and the Self-suppression of Complex Coacervation. *Biopolymers* **1967**, *5* (1), 37–59. https://doi.org/10.1002/bip.1967.360050106.

(36) Lawley, K. P. *Advances in Chemical Physics*; Rice, S. A., Ed.; John Wiley and Sons, 2016; Vol. 161. https://doi.org/10.1002/9780470142615.

(37) Li, L.; Rumyantsev, A. M.; Srivastava, S.; Meng, S.; De Pablo, J. J.; Tirrell, M. V. Effect of Solvent Quality on the Phase Behavior of Polyelectrolyte Complexes. *Macromolecules* **2021**, *54* (1), 105–114. https://doi.org/10.1021/acs.macromol.0c01000.

(38) Møller, P. C. F.; Fall, A.; Bonn, D. Origin of Apparent Viscosity in Yield Stress Fluids below Yielding. *Epl* **2009**, *87* (3), 38004. https://doi.org/10.1209/0295-5075/87/38004.

(39) Coussot, P. Yield Stress Fluid Flows: A Review of Experimental Data. *J. Nonnewton. Fluid Mech.* **2014**, *211* (1), 31–49. https://doi.org/10.1016/j.jnnfm.2014.05.006.

(40) TA Instruments. Rheological Techniques for Yield Stress Analysis. *TA Instruments Tech. notes - RH025* **2000**, *RH025* (1), 1–6.

(41) Huber, R. C.; Ferreira, A. S.; Aguirre, J. C.; Kilbride, D.; Toso, D. B.; Mayoral, K.; Zhou, Z. H.; Kopidakis, N.; Rubin, Y.; Schwartz, B. J.; Mason, T. G.; Tolbert, S. H. Structure and Conductivity of Semiconducting Polymer Hydrogels. *J. Phys. Chem. B* **2016**, *120* (26), 6215–6224. https://doi.org/10.1021/acs.jpcb.6b02202.

(42) Barford, W.; Marcus, M. Theory of Optical Transitions in Conjugated Polymers. I. Ideal Systems. *J. Chem. Phys.* **2014**, *141* (16), 164101. https://doi.org/10.1063/1.4897984.

(43) Marcus, M.; Tozer, O. R.; Barford, W. Theory of Optical Transitions in Conjugated Polymers. II. Real Systems. *J. Chem. Phys.* **2014**, *141* (16), 164102. https://doi.org/10.1063/1.4897985.

(44) Mooney, J.; Kambhampati, P. Get the Basics Right: Jacobian Conversion of Wavelength and Energy Scales for Quantitative Analysis of Emission Spectra. *J. Phys. Chem. Lett.* **2013**, *4* (19), 3316–3318. https://doi.org/10.1021/jz401508t.

(45) Lazutin, A. A.; Semenov, A. N.; Vasilevskaya, V. V. Polyelectrolyte Complexes Consisting of Macromolecules with Varied Stiffness: Computer Simulation. *Macromol. Theory Simulations* **2012**, *21* (5), 328–339. https://doi.org/10.1002/mats.201100097.

(46) Spano, F. C.; Clark, J.; Silva, C.; Friend, R. H. Determining Exciton Coherence from the Photoluminescence Spectral Line Shape in Poly(3-

Hexylthiophene) Thin Films. *J. Chem. Phys.* **2009**, *130* (7), 074904. https://doi.org/10.1063/1.3076079.

(47) Armstrong, C. M. Interaction of Tetraethylammonium Ion Derivatives with the Potassium Channels of Giant Axons. *J. Gen. Physiol.* **1971**, *58* (4), 413–437. https://doi.org/10.1085/jgp.58.4.413.

(48) Xiao, F.; Pignatello, J. J. Π+-π Interactions between (Hetero)Aromatic Amine Cations and the Graphitic Surfaces of Pyrogenic Carbonaceous Materials. *Environ. Sci. Technol.* **2015**, *49* (2), 906–914. https://doi.org/10.1021/es5043029.

(49) Davis, G. A. Quenching of Aromatic Hydrocarbon Fluorescence by Alkylpyridinium Halides. *J. Chem. Soc. Chem. Commun.* **1973**, *384* (19), 728–729. https://doi.org/10.1039/C39730000728.

(50) Winnik, F. M. From Pyrene-Labeled PolyUV-Isopropylacrylamide) Solutions. *Macromolecules* **1990**, *23* (6), 1647–1649.

Appendix II

Supporting Information for

Conjugated Polyelectrolyte-Based Complex Fluids as Aqueous Exciton Transport Networks

II.1 Experimental

Sample Preparation. The cationic energy donor CPE, an iodide salt of poly(ditrimethylammoniumpropyl fluorene-alt-phenylene) (PFPI) (MW = 21,000 Da, PDI = 1.2), was obtained from Solaris Chem Incorporated. The anionic energy acceptor CPE, a sodium salt of poly(dibutylsulfonate cyclopentadithiophene-alt-phenylene) (NaPCPT) (MW = 40,000 Da, PDI = 3), was obtained from 1-Material. Potassium bromide (KBr, 99.99 % purity) was obtained from Sigma-Aldrich. Tetraethylammonium bromide (> 98.0 % purity) (TEAB), 1-ethyl-1methylpyrrolydinium bromide (> 97.0 % purity) (EMPB), and 1-ethyl-3-methylimidazolium bromide (> 98.0 % purity) (EMIB) were received from TCI Chemicals. 1-ethylpyridinium bromide (99.0 % purity) (EPB) was received from Alfa Aesar. All chemicals were used as received.

Stock solutions of 20 mg/mL NaPCPT, 8 mg/mL PFPI, and 5.0 M of each salt type were prepared using HPLC-grade water (Sigma-Aldrich). The NaPCPT stock was stirred at 70 °C for 24 hours, the PFPI stock was stirred at 80 °C for 72 hours. Both stocks were then cooled to room temperature and filtered using a 0.45 μm nylon syringe filter (Fisher Scientific) before use. All salt stocks were heated to 70 °C for 20 min to ensure that salt crystals were fully dissolved.

Samples containing 0 – 2.5 M concentrations of each salt (in 0.5-M increments) were prepared with a 1:1 molar-charge ratio of PFPI:NaPCPT (2 mg/mL:1.6 mg/mL or 3 mM in each repeat unit). The order of addition was as follows: HPLC-grade water, salt, followed by simultaneous addition of PFPI and NaPCPT. Samples were stirred at 650 rpm at 80°C for 14 hrs. and allowed to cool to room temperature before any analysis was performed. Samples were centrifuged (Minispin Plus, Eppendorf) at 10,000 rpm (840 × g) for 15 min to adequately separate the two phases for further characterization.

Microscopy. Images of bulk samples were collected with a Leica DM5500 B widefield microscope equipped with a Leica DCF360 monochrome camera using a ∞/0.17/o, HCX PL FLUORTAR 20x/0.5 objective (Figures 3.1 and AII.1-AII.10). Samples were first thoroughly agitated to homogenize the dilute and concentrated phases. 20 μL of each sample was then loaded onto a glass microscope slide and covered with a glass coverslip to arrest evaporation during imaging. Samples were excited using a DAPI filter (360/40 nm excitation, 470/40 nm emission) to preferentially select for PFPI emission. A Texas Red filter (560/40 nm excitation, 570/75nm emission) was used to select for NaPCPT emission to produce two separate images which were then overlaid. Photoluminescence (PL) intensities were measured for three different sample locations and averaged using the ImageJ based software Fiji. The exposure and gain were held constant for each filter (DAPI: 20.14 ms/gain of 1, Texas Red: 3.26 ms/gain of 1) to compare PL intensities across the sample set.

Spectroscopy. Dilute-phase characterization was carried out for each sample after centrifugation (Figure AII.15). The dilute phase was carefully separated from the concentrated phase for optical density (OD) measurements. OD spectra were collected using a Shimadzu UV-2700 spectrophotometer over the range of 300 − 800 nm in 1.0-nm increments, 1 nm bandpass, and a quartz cuvette with a 1-mm pathlength. For concentrated-phase measurements (Figure AII.14), a small amount of concentrated phase from samples prepared at 0.5 M of each salt type was sandwiched between a microscope slide and cover slip and measured using the same method as the dilute phase measurements. For turbidity experiments, % transmittance (%T) measurements were collected in triplicate on the same instrument (Figure AII.13). Samples were first thoroughly agitated to homogenize the dilute and concentrated phases, loaded into a 1-mm-pathlength quartz cuvette, and the %T at the non-absorptive wavelength of 750 nm was then measured.

Rheometry. Small-amplitude oscillatory shear (SAOS) measurements were performed on the concentrated phase of PFPI/NaPCPT without additional salt and on 1.0M samples across the salt series. All measurements were taken using an ARES-G2 strain-controlled rheometer (TA Instruments) in strain-controlled oscillatory mode. A 25-mm cone-and-plate geometry with an angle of 0.1 rad and a truncation gap of 0.05 mm was used for all rheological experiments. The temperature was set to 20 °C via a Peltier controller, and a solvent trap was utilized to minimize solvent evaporation of during measurement.

After centrifugation and careful extraction of the concentrated phase, samples were loaded and oscillated at a low frequency and strain % (1 Hz, 5 %) for 2 min to homogenize the sample prior to measurement. Amplitude sweeps were carried out from 0.1 – 300 % strain at an angular frequency of 31.4rad/s (5 Hz) to determine the linear viscoelastic region for each sample. Frequency sweeps were then carried out for each sample from 0.1-100 rad/s and a strain % determined to fall within the linear viscoelastic region.

Steady-State and Time-Resolved Photoluminescence. Given the large OD of the concentrated phase, PL spectra were collected for the donor (375 nm excitation) and acceptor (500 nm excitation) separately using front-face detection and a PIXIS 100 CCD (Princeton Instruments). Time-resolved photoluminescence (TR-PL) measurements were performed via time-correlated single photon counting using a home-built system. The details of the laser system and experimental set up were described previously.[1] A pulsed picosecond diode laser (BDS-SM Series, Becker & Hickl GmbH) was used to excite samples at 375 nm, and a supercontinuum laser (NKT Photonics) was used to excite above 400 nm. Samples were excited with vertically polarized light at either 375 nm or 500 nm, and emission at 600 nm was collected in a front-face geometry with the emission polarizer set at the magic angle. A 500-nm long-pass filter was used on the emission arm of the setup when using 500-nm excitation. PL lifetimes were determined via forward convolution with the measured instrument response function (obtained using a scattering Ludox sample) and a sum-of-exponentials model. This was done using least-squares minimization

via the DecayFit MATLAB package developed by Soren Preus (Fluorescence Decay Analysis Software 1.3, FluorTools, www.fluortools.com).

Time-Resolved Photoluminescence Anisotropy. For anisotropy experiments, samples were excited with vertically polarized light (500 nm) and emission (600 nm) was collected at vertical (I_{VV}) and horizontal (I_{VH}) polarizations. Collection was carried out until approximately 20,000 counts were reached for the I_{VH} in the main channel. The I_{VV} measurement was then carried out for the same amount of time. Details of data analysis have been described previously.[1]

Small-Angle X-ray Scattering. Small-angle X-ray scattering (SAXS) measurements were conducted at beamline 4-2 of the Stanford Synchrotron Radiation Lightsource (SLAC National Accelerator Laboratory). This beamline is equipped with a Pilatus 3X detector and a robotic autosampler that feeds samples from a 96-well plate to a thin-walled quartz capillary cell. To avoid degradation, each sample was oscillated during beam exposure. 16 consecutive images were collected using 1-s exposure, 11 keV photon energy, and a sample-to-detector distance of 1.7 m. This yielded an effective scattering vector length (q) range of 0.0068 – 0.67 $Å^{-1}$. Each image was reduced to a 1D curve, and the solvent background scattering was then subtracted from each curve before averaging and performing subsequent analysis. The background for each sample was the respective organic salt (2.5 M) in HPLC-grade water. Background-corrected curves were then fitted using the indirect Fourier transform via Otto Glatter's PCG software suite. The correct fitting function was

chosen to be the one that simultaneously minimized the mean least-squares fitting error and had a Lagrange multiplier that did not introduce spurious

oscillations into the functional form of the pair-distance distribution function (PDDF). Prior to performing the indirect Fourier transform, measured SAXS curves were smoothed to reduce noise on the high-q side. Failure to do so resulted in artificial features in the PDDF at small distances. Care was taken to use the smallest amount of smoothing necessary to not distort relevant structural features.

II.2 Supporting Information

Widefield Microscopy Images. Figure AII.2-AII.6 show fluorescence microscopy images of the PFPI/NaPCPT complex without additional salt compared to increasing concentrations of salt across the series where individual fluorescence channels used for imaging have been merged. Figure AII.1 shows images of PFPI/NaPCPT representing with the individual fluorescence filters used. Images show phase separated samples resembling colloidal gel morphology. The phase boundary existing between 1.5 and 2.0 M of each organic salt is shown as the concentrated phase combines with the dilute phase to form a homogenized, optically clear solution with little to no micron sized particles. As a control study, Figure AII.7-AII.11 show fluorescence microscopy images of the donor CPE, PFPI, with increase salt concentration across the salt series. In contrast to the phase behavior of the CPEC, large aggregates indicative of precipitation is seen at low molarities, with aggregate size appearing to decrease with in increasing [salt]. Similar control solutions were

prepared for the acceptor CPE, NaPCPT, where all solutions were dissolved by eye and thus no microscopy was performed.

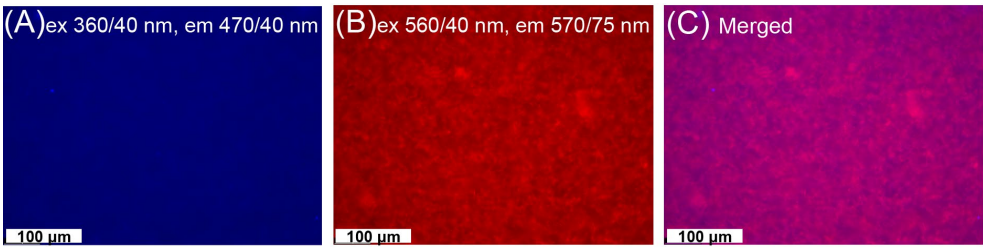

Figure AII.1: Fluorescence microscopy images of PFPI/NaPCPT with no added salt. (A) 360/40 nm excitation filter and 470/40 nm emission filter. (B) 560/40 nm excitation filter and 570/75 nm emission filter. Merged images are shown in (C).

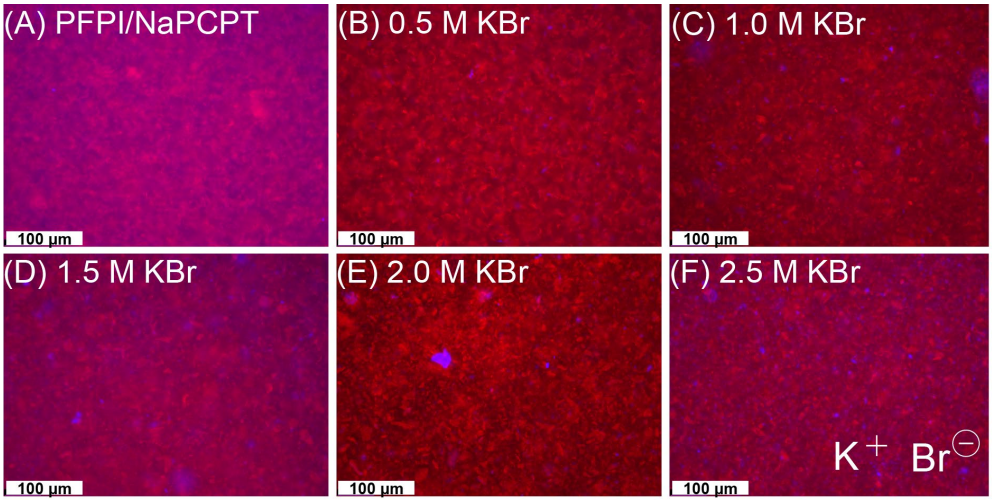

Figure AII.2: Fluorescence microscopy images of (A) PFPI/NaPCPT with increasing [KBr] (B-F).

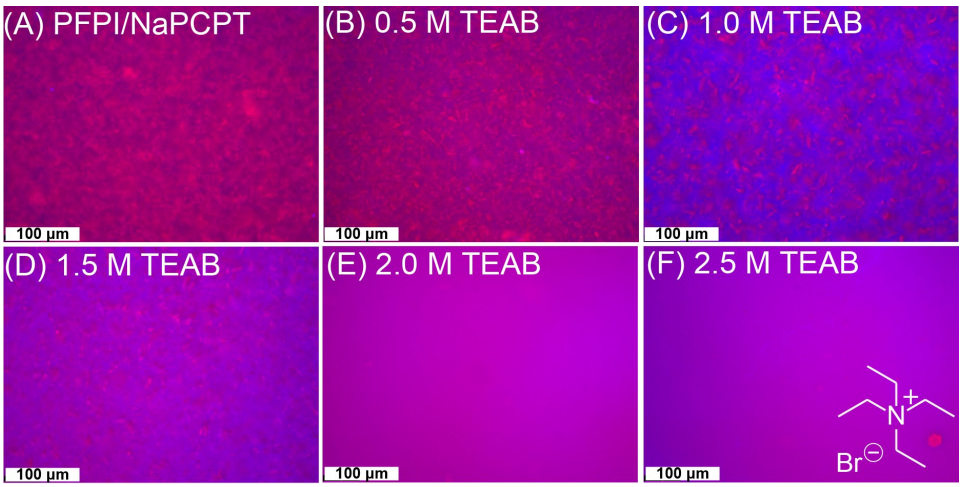

Figure AII.3: Fluorescence microscopy images of (A) PFPI/NaPCPT with increasing [TEAB] (B-F).

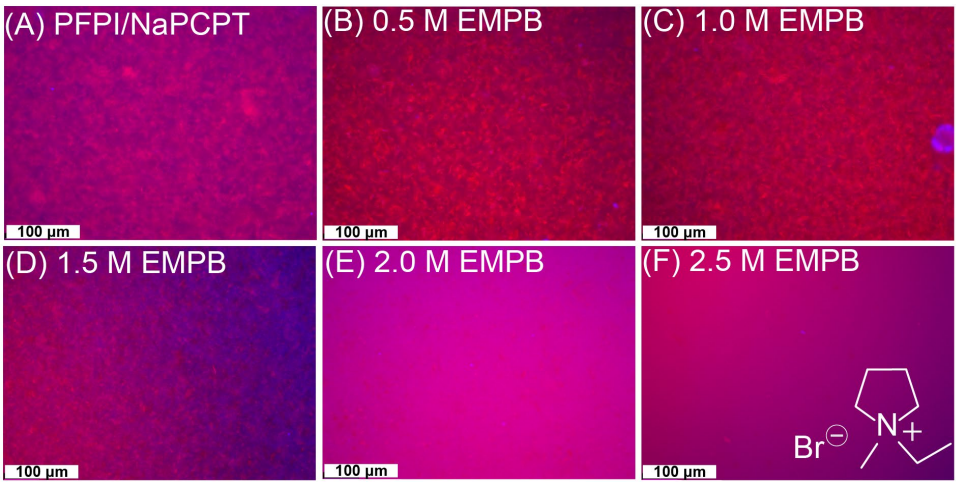

Figure AII.4: Fluorescence microscopy images of (A) PFPI/NaPCPT with increasing [EMPB] (B-F).

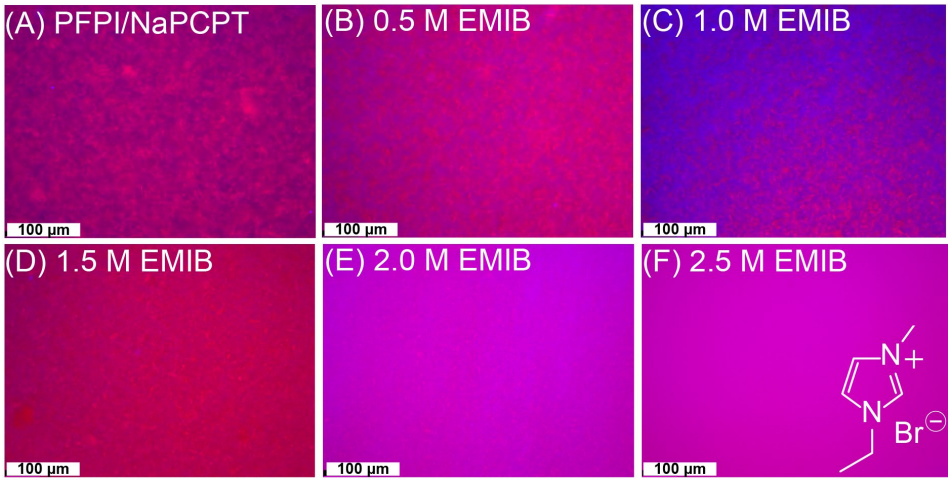

Figure AII.5: Fluorescence microscopy images of (A) PFPI/NaPCPT with increasing [EMIB] (B-F).

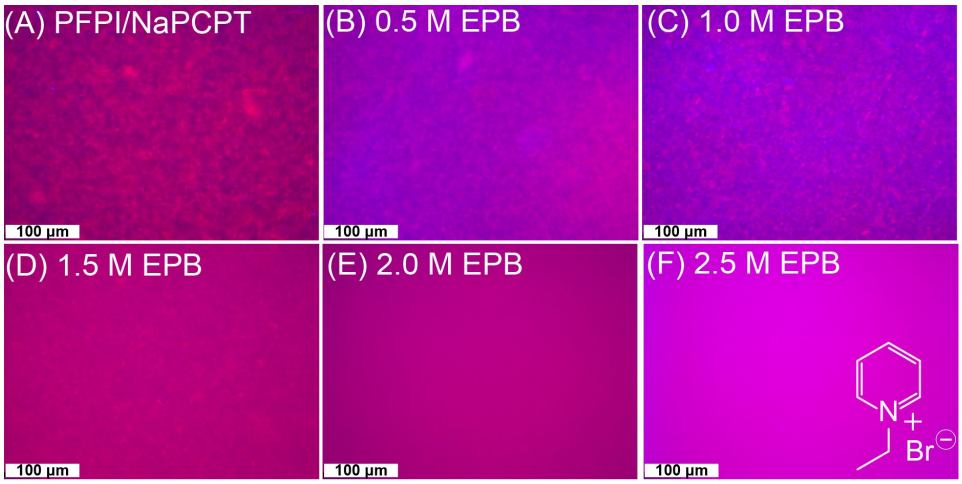

Figure AII.6: Fluorescence microscopy images of (A) PFPI/NaPCPT with increasing [EPB] (B-F).

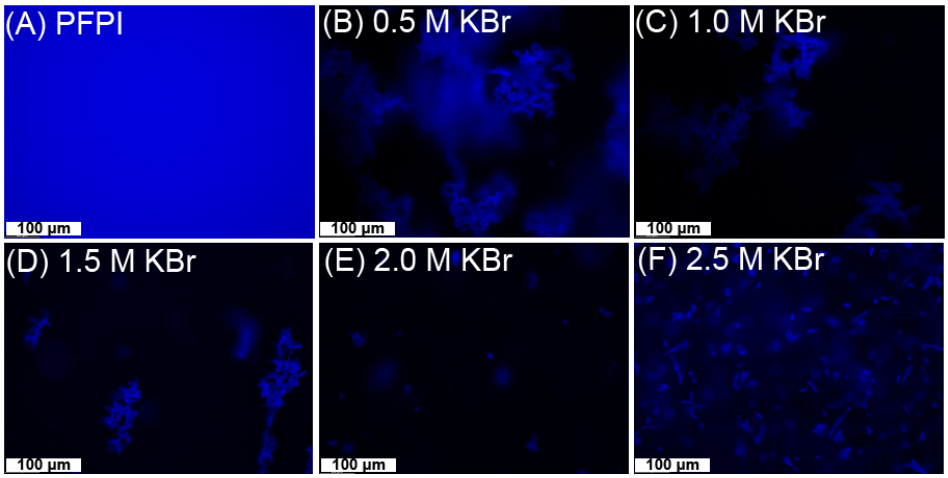

Figure AII.7: Fluorescence microscopy images of (A) PFPI with increasing [KBr] (B-F).

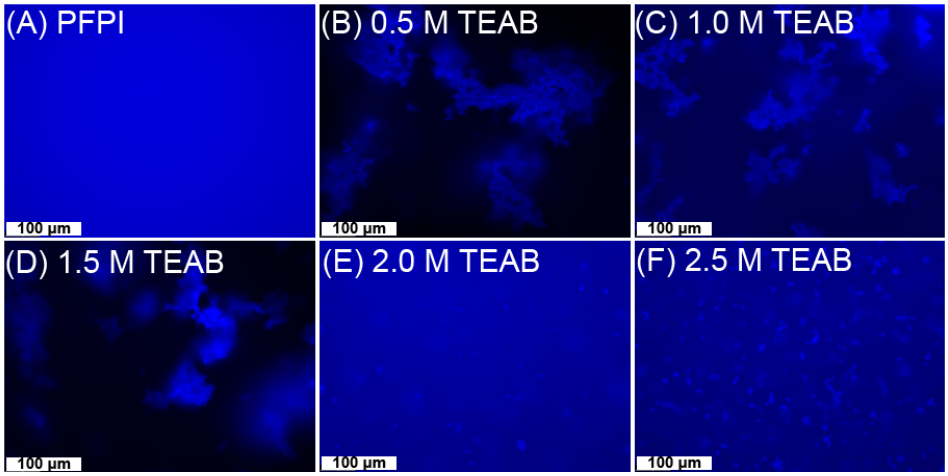

Figure AII.8: Fluorescence microscopy images of (A) PFPI with increasing [TEAB] (B-F).

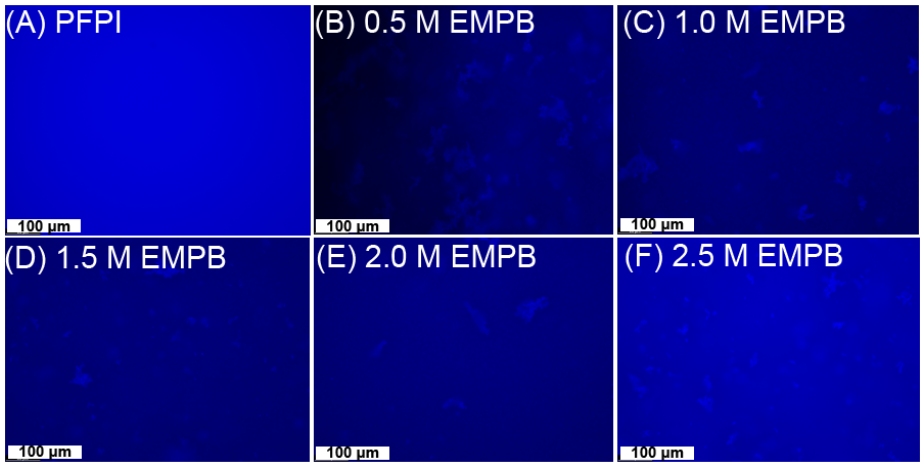

Figure AII.9: Fluorescence microscopy images of (A) PFPI with increasing [EMPB] (B-F).

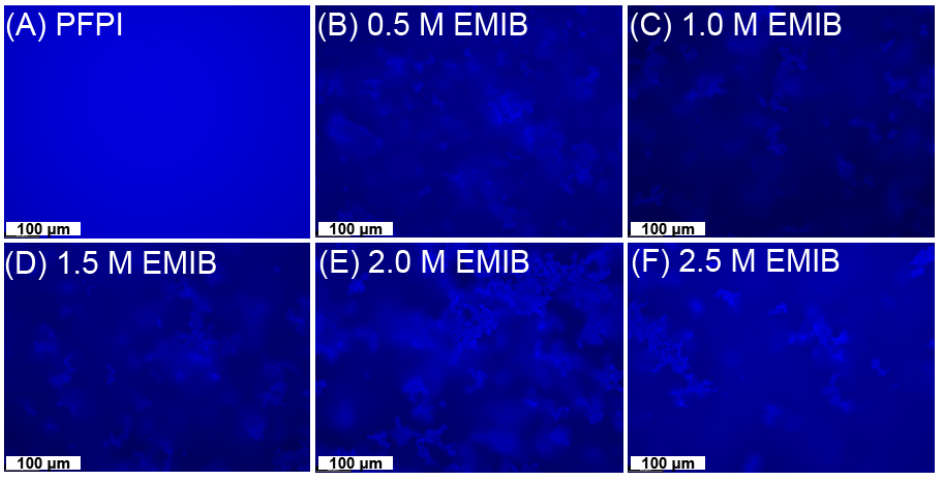

Figure AII.10: Fluorescence microscopy images of (A) PFPI with increasing [EMIB] (B-F).

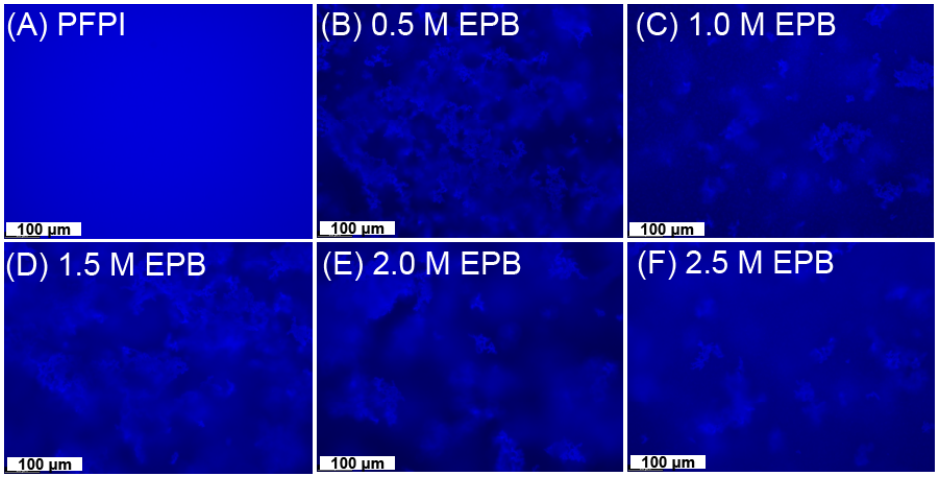

Figure AII.11: Fluorescence microscopy images of (A) PFPI with increasing [EPB] (B-F).

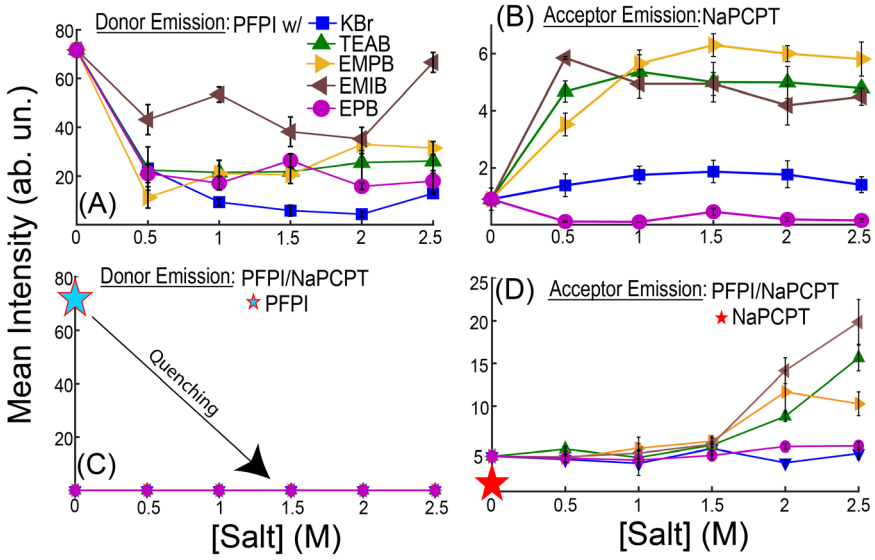

Figure AII.12: Mean fluorescence intensity determined via fluorescence microscopy of (A) 2 mg/mL PFPI control solutions, (B) 1.6 mg/mL NaPCPT control solutions, and (C & D) PFPI/NaPCPT complex with increasing concentration of each salt type. Panels A and C show results which selectively probe donor emission (λ_{ex} = 360 ± 40 nm, λ_{em} = 460 ± 40 nm, 20.14 ms exposure time) while panels B and D show results which selectively probe acceptor emission (λ_{ex} = 560 ± 40 nm, λ_{em} =570 ± 75 nm, 3.26 ms exposure time).

To set the context for evaluating changes in CPEC PL, we elucidated the dependence of PL on [salt] for control single-CPE solutions. Figure AII.12A shows

the PL signal from PFPI solutions, that gave rise to phase separation in the presence all salts for all nonzero salt concentrations. The data show that for most salts, the PL intensity – averaged over both dilute and concentrated phases – drops substantially in phase-separated solutions by approximately a factor of 4 relative to the no-salt control. Interestingly, EMIB, which contains a conjugated cation, showed a significantly smaller drop and a nearly complete recovery at 2.5 M. Figure AII.12B shows similar control measurements for NaPCPT solutions, where we observed the opposite behavior for most organic salts where the PL signal rose at [salt] ≥ 0.5 M. This was not the case with pyridinium derivative EPB, which led to PL quenching. Interestingly, KBr stood apart for both PFPI and NaPCPT controls compared to most organic ions, leading to a larger intensity drop for PFPI and a smaller rise for NaPCPT.

Figure AII.12D shows that quenching of PFPI PL in the CPEC was accompanied by an increase in NaPCPT mean PL intensity relative to the molecularly dissolved control at no salt (red star). A noticeable increase in overall intensity is clear for three of the organic salts: TEAB, EMPB, and EMIB near the onset of dissolution transition region indicated (1.5-2 M). In contrast, KBr and EPB samples give a relatively constant, lower mean PL intensity regardless of [salt].

Percent Transmittance. Percent transmittance (%T) measurements for control samples are shown in Figure AII.13 to quantify turbidity of samples. PFPI in the presence of 0.5 M KBr was found to produce the most turbid solution (Figure AII.13A), in line with the large aggregates found during microscopy analysis (Figure AII.2B). In contrast, high concentrations of KBr resulted in the reduction of aggregate formation, a higher %T, and a lower overall turbidity. All organic salts were found to induce aggregation of PFPI and showed a trend of increasing turbidity with increasing [salt]. Figure AII.13B shows similar %T vs. [salt] for NaPCPT controls. A high %T indicates NaPCPT remained dissolved in solution in the presence of the organic salts regardless of salt type or concentration. However, in the presence of KBr, the %T of samples was found to decrease indicating an increase in turbidity due to scattering of light by particles not visible to the naked eye, as these samples appeared dissolved.

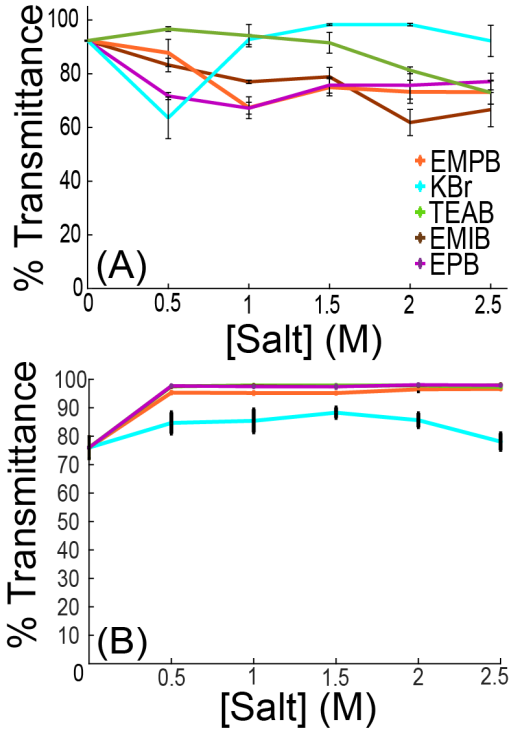

Figure AII.13: % Transmittance vs. [salt] for (A) 2 mg/mL PFPI with each salt type, and (B) 1.6 mg/mL NaPCPT with each salt

Content Analysis. Figure AII.14A shows evidence of the presence of both CPEs in the concentrated phase of all 0.5 M samples across the salt series via UV-Vis absorption measurements. Additionally Figure AII.14B and C show that the absorbance signature of both CPEs shows no dramatic shifting between salt types and conditions, and remains qualitatively similar to the dilute phase photophysics shown in Figure 3.1 of the main text. To quantify the amount of CPE in the concentrated phase via the Beer-Lambert Law, O.D. absorbance values of the dilute phase were

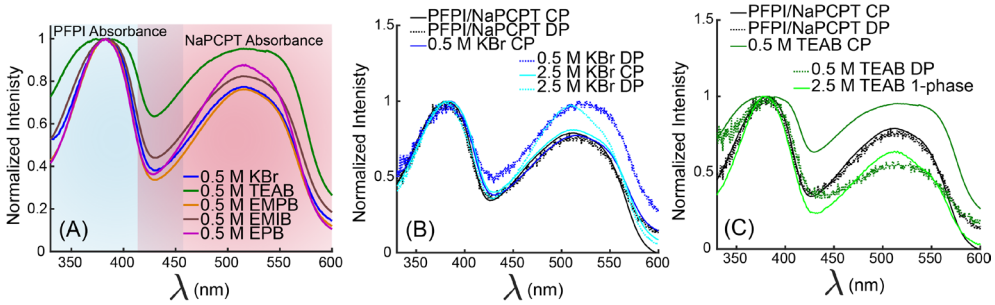

Figure AII.14: Absorbance measurements of (A) the CP of 0.5 M samples for each salt type showing both CPEs are present. (B) shows a comparison of OD measurements between the dilute phase (DP) and concentrated phase (CP) with no additional salt and at varying salt concentration. (C) shows a similar comparison for the representational organic ion TEAB.

measured (Figure AII.15) and used in conjunction with the molar extinction coefficients of each CPE and the cuvette pathlength. Due to absorbance spectra overlap of the donor and acceptor, the acceptor portion of the spectra where first fit to a sum of gaussians, and that fit was subtracted from the overall O.D. of the CPEC to determine the correct PFPI absorbance. An example of this fitting process is shown in Figure AII.15F. The molar extinction coefficients in pure water were found to be 4154 $M^{-1}cm^{-1}$ for PFPI and 32988 $M^{-1}cm^{-1}$ for NaPCPT. The molar extinction coefficients for NaPCPT in the presence of 1.0 M of each salt type were also

determined and can be found in Figure AII.16. Due to PFPI aggregating at these concentrations a similar study was unable to be performed on the molar extinction coefficient of the donor CPE.

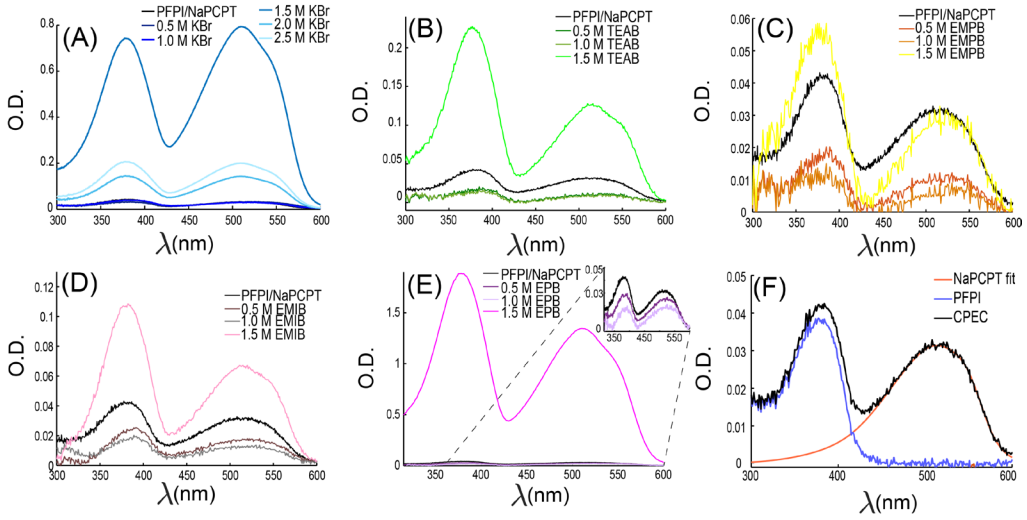

Figure AII.15: UV-Vis of dilute phase of phase separated samples for (A) KBr, (B) TEAB, (C) EMPB, (D) EMIB, and (E) EPB. (F) Fitting of CPEC O.D. is shown where absorbance of the acceptor was subtracted from that of the donor to find an accurate absorbance value.

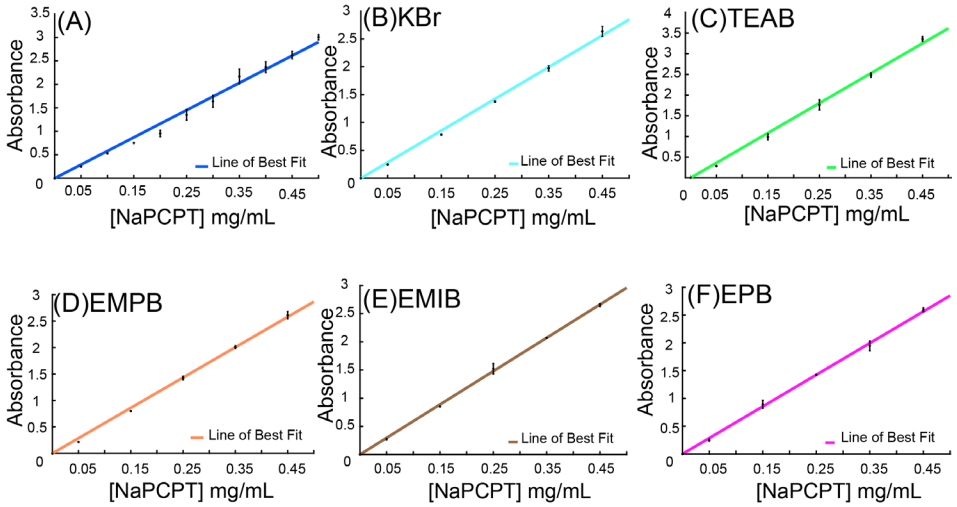

Figure AII.16: Absorbance vs. [PCPT] for (A) pure NaPCPT, and NaPCPT in the presence of 1.0 M (B) KBr, (C) TEAB, (D) EMPB, (E) EMIB, and (F) EPB. Lines of best fit were determined and used in conjunction with absorbance values found from Figure AII.15 to calculate concentrations of each CPE in each phase using the Beer-Lambert Law.

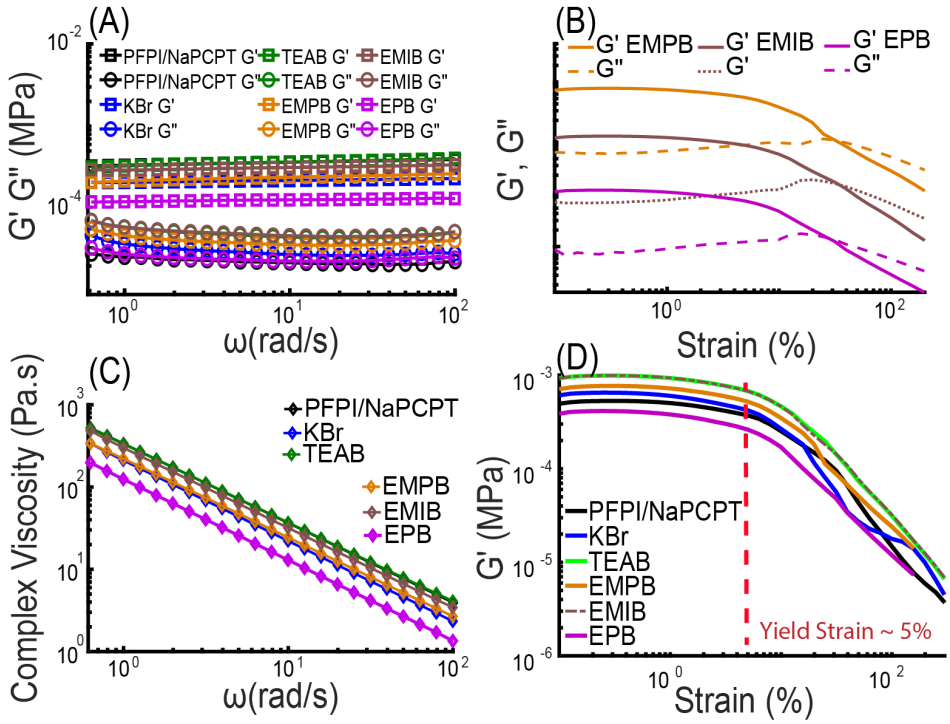

Figure AII.17: Rheological properties based on SAOS measurements. (A) Storage (G′, squares) and loss (G″, circles) moduli vs. frequency of the concentrated phase for each salt type at 1.0 M. (B) Moduli crossover and flow points for 1.0 M EMPB, EMIB, and EPB samples. (C) Complex viscosity and shear thinning with increasing frequency for each salt type at 1.0 M. (D) Loss moduli of all 1.0 M salt samples with the yield strain indicated with red line.

Rheology. Storage and loss moduli of the concentrated phase of the pure CPEC and the CPEC in the presence of 1.0 M salt are shown in Figure AII.17A as a function of frequency. The mostly frequency independent response shows the storage moduli dominating over the loss moduli regardless of sample type with a shear thinning response (Figure AII.17C). Figure AII.17B shows the flow point for EMPB, EMIB, and EPB samples while panel S16D shows a similar yield strain exists for all samples.

Steady-State Fluorescence Spectroscopy. We used the distinct PL signatures of the donor and the acceptor to ascertain the relative spatial proximity of the dissolved CPEs in the dilute phase.. If the two CPEs were dissolved as isolated chains, we would expect to find significant PL signal from both polymers. However, if the two CPEs dissolved as a bound complex we would expect efficient EET from PFPI to NaPCPT and the quenching of PFPI PL.

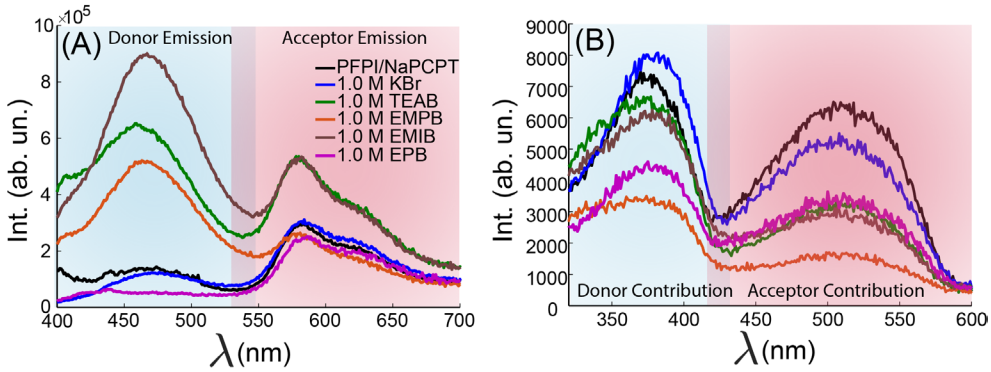

Figure AII.18: PL spectroscopy of the CPEC dilute phase at 1.0 M of each salt type. (A) PL emission spectra from excitation at 370 nm (i.e., PFPI excitation). (B) PLE spectra taken at an emission wavelength of 615 nm, corresponding primarily to PCPT emission.

PL spectra of the dilute phase at 1.0 M of each salt and the PFPI/NaPCPT sample without added salt are shown in Figure AII.18. Upon excitation of PFPI at 370 nm (Figure AII.18A), we observed emission from both PFPI (~ 400-550 nm) and NaPCPT (~ 550-700 nm) for TEAB, EMPB and EMIB salts. This observation implies that a fraction of the dilute-phase solution is composed of isolated CPE chains. We found the PFPI PL intensity was low for the dilute solution with no salt, as well as in the presence of 1.0 M KBr and EPB. For the no-salt solution, this observation likely merely reflects the fact that the PFPI concentration is low (Figure AII.15). However,

at 1.0 M KBr the low donor PL intensity suggests that the two CPEs dissolve primarily as a complex, leading to efficient EET from PFPI to NaPCPT.

To confirm that EET takes place in the dilute phase, we measured the PL excitation (PLE) spectrum of NaPCPT. In this experiment, the PL wavelength was fixed at 615 nm – within the NaPCPT emission band – and PL signal was detected as the excitation wavelength was swept over the full absorption window of the CPEC. PLE spectra for the dilute-phase solutions are shown in Figure AII.18B. Contributions to emission at 615 nm are found to occur from excitations associated with both the donor PFPI (absorption ~ 325-425 nm) and the acceptor NaPCPT (absorption ~ 425-600 nm). Because PFPI PL was strongly quenched in the dilute-phase solutions with no salt, with KBr, and with EPB, the only way the PLE spectrum of NaPCPT can show a contribution from the donor OD region is due to EET from PFPI to NaPCPT. This is confirmation that in the dilute phase of these solutions the CPEs exist primarily as an associated yet soluble complex, which is also observed in more conventional polyelectrolyte systems.[2] Though a similar contribution to the NaPCPT PLE from the PFPI OD region is seen for the other salts, it cannot be unambiguously stated that this is due to EET. The reason is that for those samples the PL spectrum of NaPCPT (Figure AII.18A) sits on a substantial PFPI PL background, as PFPI emission was not fully quenched. Thus, even though it is likely that in these solutions a fraction of the donor and acceptor CPE chains do exist as a complex, this cannot be concluded definitively.

Figure AII.19 shows steady-state fluorescence spectra of the concentrated phase of EMPB, EMIB, and EPB samples excited at 375 nm (i.e., donor excitation) compared to 10 mg/mL PFPI gel phase. The fluorescence of the donor was found to be quenched within the complex and remained so regardless of salt type or concentration. Similar data is shown in Figure AII.20 for the concentrated phase excited at 500 nm (i.e., acceptor excitation).

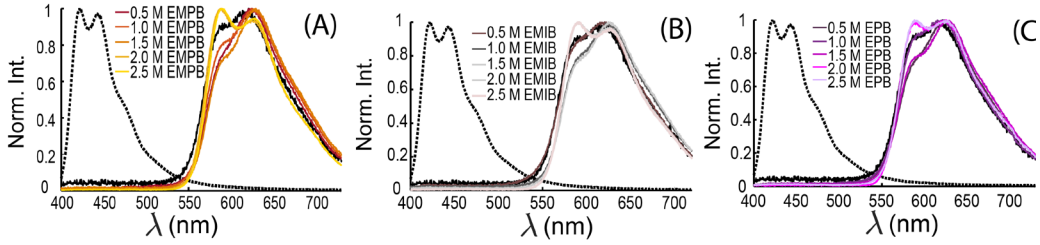

Figure AII.19: Steady state photoluminescence emission spectra (excitation 375 nm) of 10.0 mg/mL PFPI control and PFPI/PCPT complex with increasing (A) [EMPB], (B) [EMIB], and (C) [EPB].

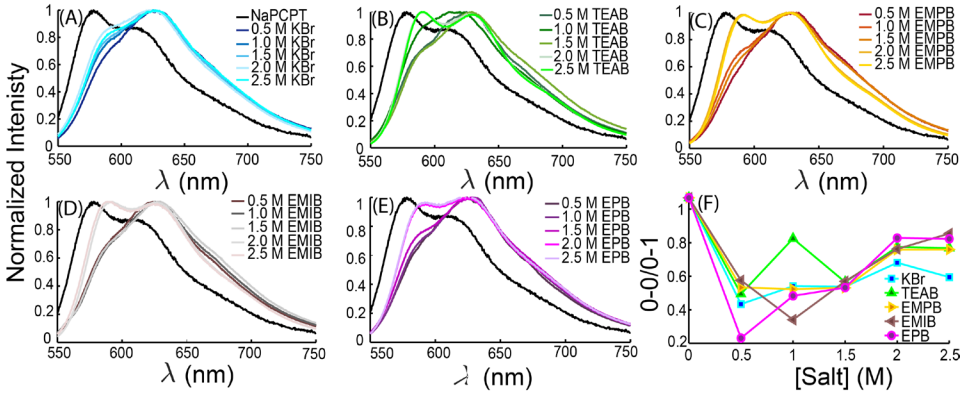

Figure AII.20: Steady state photoluminescence emission spectra (excitation 500 nm) of 1.6 mg/mL PCPT control and PFPI/PCPT complex with increasing (A) [KBr], (B) [TEAB], (C) [EMPB], (D) [EMIB], and (E) [EPB]. (F) Vibronic ratio vs. [salt] for each salt type.

Time-Resolved Photoluminescence. TRPL decay curves are shown in Figure AII.21 for the concentrated phase of EMPB, EMIB, and EPB excited at 375 nm and

emission collected at 600 nm. Similar decay curves are shown in Figure AII.22 for excitation of NaPCPT directly at 500 nm and emission collected at 600 nm for all salts. While average PL lifetimes in the presence of KBr fluctuate only slightly from that of the control, in TEAB, EMPB, and EMIB samples, lifetimes were found to increase significantly for higher (≥ 1.5 M) salt concentrations consistent with the onset of the phase transition from phase separated to a fully dissolved solution. Notably, EPB was the only salt found to decrease the average excited-state lifetime, even at high molarities.

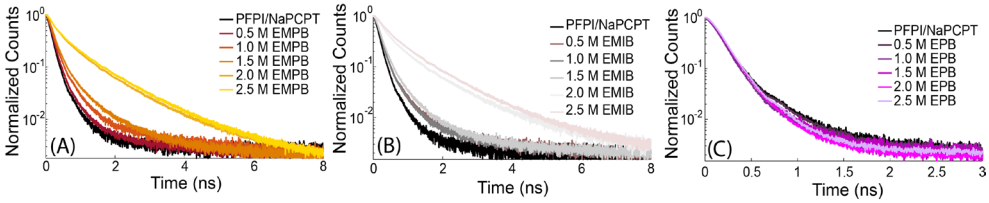

Figure AII.21: Time-Resolved PL decay curves (λ_{ex} = 375 nm, λ_{em} = 600 nm) of PFPI/PCPT complex with increasing (A) [EMPB], (B) [EMIB], and (C) [EPB].

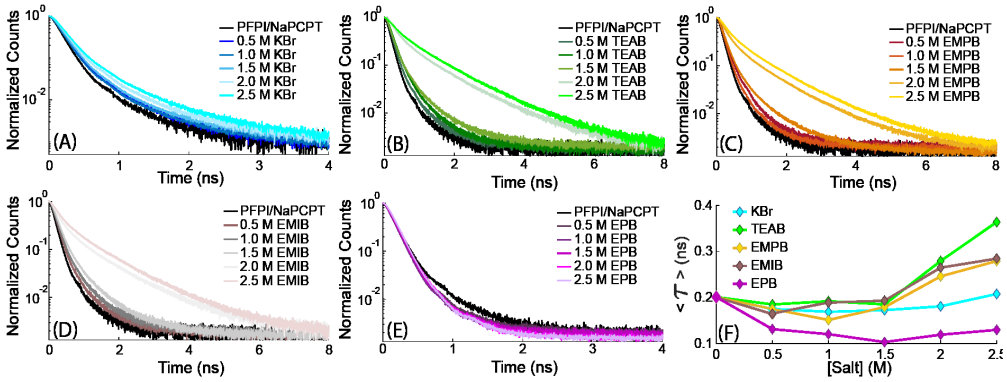

Figure AII.22: Time-Resolved Photoluminescence decay curves (excitation 500 nm, emission 600 nm) of PFPI/PCPT complex with increasing (A) [KBr], (B) [TEAB], (C) [EMPB], (D) [EMIB], and (E) [EPB]. (F) Average excited state lifetimes vs. [salt] for each salt type.

Examples of successful fits to TRPL data, the details of which are discussed in the 'Experimental Methods' section, are shown in Figure AII.23. From these fits, it

was found that the decays we're all biexponential, with the short component of the decays dominating. However, analysis of the long component parameters is insightful. Figure AII.24 shows the long component amplitude (a_2) and lifetime (τ_2) vs. [salt]. In Figure AII.24A we see that the contribution of the excited-state population to the long component of the lifetime increases significantly for higher [salt], particularly for TEAB samples.

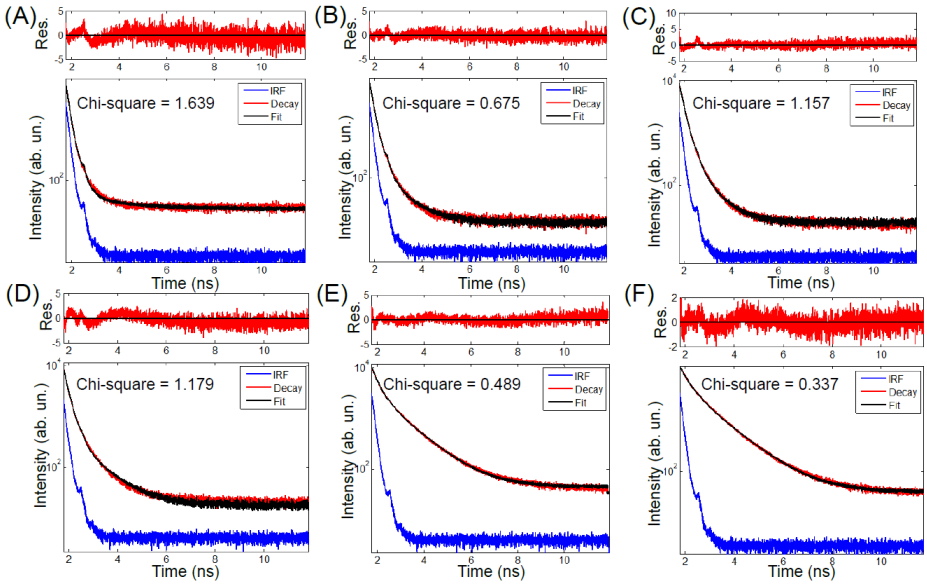

Figure AII.23: Non-linear least squares fitting minimization of (A) PFPI/PCPT, (B) PFPI/PCPT with 0.5 M TEAB, (C) PFPI/PCPT with 1.0 M TEAB, (D) PFPI/PCPT 1.5M TEAB, (E) PFPI/PCPT with 2.0 M TEAB, and (F) PFPI/PCPT 2.5 M TEAB. Goodness of fit was determined by minimizing the Chi-squared value. TR-PL decays were from excitation at 500 nm and collection of emission at 600 nm.

Time-Resolved Photoluminescence Anisotropy. Time-resolved photoluminescence anisotropy measurements of the concentrated phase were carried out (λex = 500 nm, λem = 600 nm) using TCSPC. Calculation of the time-dependent anisotropy r(t) was done using

$$r(t) = \frac{I_{VV}(t) - G I_{VH}(t)}{I_{VV}(t) + 2G I_{VH}(t)} \qquad \textbf{(AII.1)}$$

where I_{VV} and I_{VH} are the vertical-vertical and vertical-horizontal emission components, and G corrects for differences in detection of the two polarized components:

$$G = \frac{\int_0^\infty I_{VH}(t)dt}{\int_0^\infty I_{HH}(t)dt} \qquad \textbf{(AII.2)}$$

Figure AII.25 shows TRPL anisotropy for the concentrated phase of the pure CPEC and 0.5 M salt samples were Figure AII.25F shows that there is each sample gives a similar anisotropy decay. In contrast, Figure AII.26F shows a comparison between 2.5 M of each salt type, where there is obvious long-lived anisotropy for TEAB, EMPB, and EMIB samples compared to KBr and EPB.

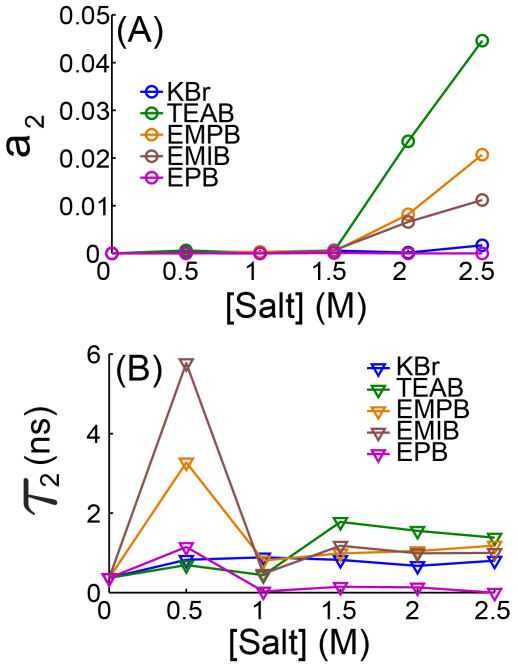

Figure AII.24: (A) Amplitude of exciton population contributing to long-time component of excited-state lifetime as a function of [salt] and type. (B) long-time component of excited-state lifetime vs [salt].

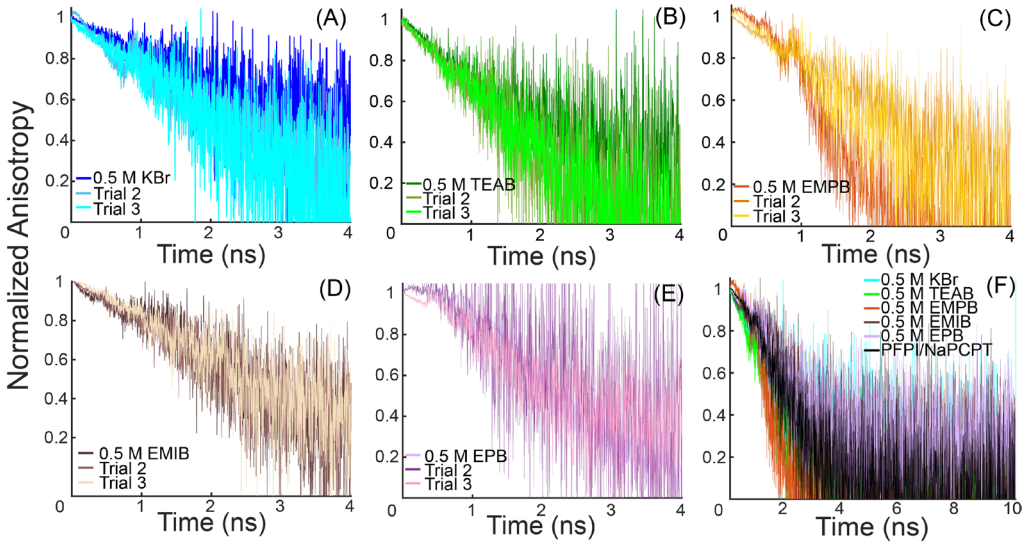

Figure AII.25: Triplicate measurements of time-resolved PL anisotropy of the concentrated phase of 0.5 M samples of (A) KBr, (B) TEAB, (C) EMPB, (D) EMIB, and (E) EPB. (F) shows a comparison between samples. Samples where excited at 500 nm and emission was collected at 600 nm.

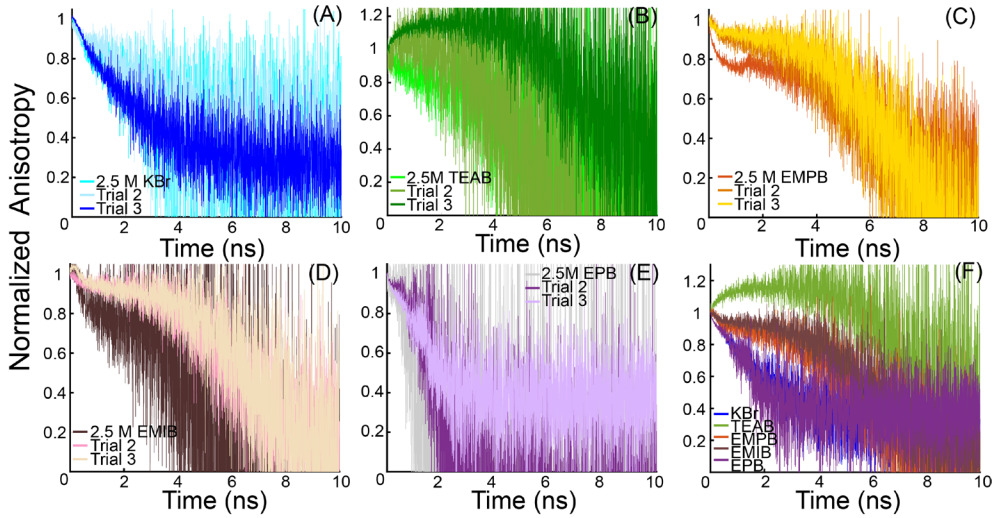

Figure AII.26: Triplicate measurements of time-resolved PL anisotropy of the concentrated phase of 2.5 M samples of (A) KBr, (B) TEAB, (C) EMPB, (D) EMIB, and (E) EPB. (F) shows a comparison between samples. Samples where excited at 500 nm and emission was collected at 600 nm.

Molecular Energy Levels. Table AII.1 lists the available HOMO, ionization potential (I_p), LUMO, and electron affinity (E_A) values for the CPEs and the pyridinium ion.[3–6] Cleanly measuring the energy levels within the complex fluid is extremely challenging due to the highly heterogeneous and multicomponent nature of the complex fluid. However, the electronic energy levels of conjugated polymers are predominantly dictated by the backbone chemical structure, while the environment acts as a perturbation. Thus, the energy levels of our polymer are expected to be quite similar to prior literature values.

Table AII.1. Molecular Energy Levels of CPEs and EPB.

Molecule	HOMO (eV)	I_p (eV)	LUMO (eV)	E_A (eV)
PFPI	-5.46[a]	6.07[d]	-2.51[b]	3.12[c]
NaPCPT	-5.11[a]	4.92[e]	-2.97[b]	2.78[c]
EPB	-7.08[≠]	~	-2.44[ǂ]	~

[a] Determined via cyclic voltammetry (CV).

[b] Estimated using HOMO and the optical energy bandgap values

[c] Estimated by adding the optical bandgap to ionization potential determined using ultraviolet photoelectron spectroscopy (UPS) measurements

[d] Determined using the incident photon energy (21.2 eV) and the onset of the HOMO.

[e] From UPS measurements.

≠ Calculated using Density Functional Theory.

ǂ Calculated using Density Functional Theory and confirmed against CV experiments.

References

(1) Johnston, A. R.; Perry, S. L.; Ayzner, A. L. Associative Phase Separation of Aqueous π-Conjugated Polyelectrolytes Couples Photophysical and Mechanical Properties. Chem. Mater. **2021**, 33 (4), 1116–1129. https://doi.org/10.1021/acs.chemmater.0c02424.

(2) Chang, L.-W.; Lytle, T. K.; Radhakrishna, M.; Madinya, J. J.; Vélez, J.; Sing, C. E.; Perry, S. L. Sequence and Entropy-Based Control of Complex Coacervates. Nat. Commun. **2017**, 8 (1), 1273. https://doi.org/10.1038/s41467-017-01249-1.

(3) Barton Cole, E. E.; Baruch, M. F.; L'Esperance, R. P.; Kelly, M. T.; Lakkaraju, P. S.; Zeitler, E. L.; Bocarsly, A. B. Substituent Effects in the Pyridinium Catalyzed Reduction of CO2 to Methanol: Further Mechanistic Insights. Top. Catal. **2015**, 58 (1), 15–22. https://doi.org/10.1007/s11244-014-0343-z.

(4) Jung, H. S.; Nguyen, T. Q. Electronic Properties of Conjugated Polyelectrolyte Thin Films. J. Am. Chem. Soc. **2008**, 130 (31), 10042–10043. https://doi.org/10.1021/ja801451e.

(5) Mai, C. K.; Zhou, H.; Zhang, Y.; Henson, Z. B.; Nguyen, T. Q.; Heeger, A. J.; Bazan, G. C. Facile Doping of Anionic Narrow-Band-Gap Conjugated Polyelectrolytes during Dialysis. Angew. Chemie - Int. Ed. **2013**, 52 (49), 12874–12878. https://doi.org/10.1002/anie.201307667.

(6) Tankov, I.; Yankova, R.; Genieva, S.; Mitkova, M.; Stratiev, D. Density Functional Theory Study on the Ionic Liquid Pyridinium Hydrogen Sulfate. J.

Mol. Struct. **2017**, 1139, 400–406.

https://doi.org/10.1016/j.molstruc.2017.03.040.

Chapter 4

Excitonically Coupled Simple Coacervates via Liquid/Liquid Phase Separation

Acknowledgements: This chapter has been submitted to the Journal of Physical Chemistry Letters as a communication with the following authorship: Anna Johnston, Gregory Pitch, Eris D. Minckler, Ivette Mora, Vitor H. Balasco Serrão, Eric A. Dailing, Alexander L. Ayzner. Anna Johnston carried out the steady-state and time-resolved spectroscopy, fluorescence lifetime imaging, data analysis, and originally crafted the manuscript. Gregory Pitch carried out the synthesis of the CPE and edited the manuscript. Eris Minckler carried out the fluorescence microscopy imaging and data analysis. Ivette Mora participated in the collection of the cryo-transmission electron microscopy (cryo-TEM) and data analysis. Vitor Balasco Serrão collected the cryo-TEM data, Eric Dailing carried out the molecular weight analysis. Alexander Ayzner edited the manuscript and oversaw the project. A big thank you to each one of them for their help.

This material is based upon work supported by the National Science Foundation under grant no. 1848069 and the ACS Petroleum Research Fund New Directions grant No. 60244-ND7, as well as by the National Science Foundation Graduate Research Fellowship under grant no. DGE-1842400. Part of this work was performed at the UCSC Life Sciences Microscopy Center (RRID:SCR_021135) with the help and guidance of Dr. Benjamin Abrams. Confocal FLIM experiments were conducted at the CRL Molecular Imaging Center, RRID:SCR_017852, supported by NIH S10OD025063. We would like to thank Holly Aaron and Feather Ives for their microscopy advice and support. The authors also acknowledge the Biomolecular Cryo-Electron Microscopy Facility at Department of Chemistry and Biochemistry of University of California – Santa Cruz (RRID:SCR_021755) for the scientific and technical assistance (NIH High-End Instrumentation program - S10OD02509). Work at the Molecular Foundry was supported by the

Office of Science, Office of Basic Energy Sciences, of the U.S. Department of Energy under Contract No. DE-AC02-05CH11231.

Abstract: Viscoelastic liquid coacervate phases that are highly enriched in non-conjugated polyelectrolytes are currently the subject of highly active research from biological and soft-materials perspectives. However, formation of a liquid, electronically active coacervate has proved highly elusive, since extended π-electron interactions strongly favor the solid state. Herein we show that a conjugated polyelectrolyte (CPE) can be rationally designed to undergo aqueous liquid/liquid phase separation to form a liquid coacervate phase. This result is significant both because it adds to the fundamental understanding of liquid/liquid phase separation, but also because it opens intriguing applications in light harvesting and beyond. We find that the semiconducting coacervate is intrinsically excitonically coupled, allowing for long-range exciton diffusion in a strongly correlated, fluctuating environment. The emergent excitonic states are comprised of both excimers and H-aggregates.

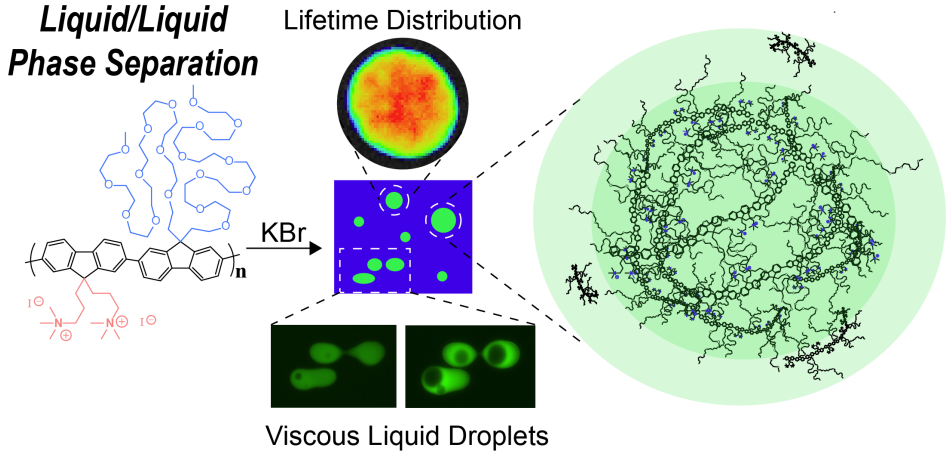

4.1 Introduction

Spontaneous separation of aqueous polyelectrolyte solutions into dilute and highly concentrated liquids is a fascinating process relevant to understanding the formation of early membrane-less organelles.[1,2] Liquid/liquid phase separation has multiple exciting applications, which stem from the attractive properties of the concentrated viscoelastic fluid phase. This highly polymer-enriched aqueous liquid phase, called a coacervate, is of interest for drug design, catalysis, biomaterials, and underwater adhesives.[3–6] Yet to date, the polyelectrolyte components of such coacervate phases have been electronically inactive.[7–13] The formation of a liquid semiconducting coacervate would open exciting new application possibilities in light-harvesting and electronically conducting soft matter. In such a crowded aqueous system, inter- and intra-chain electronic couplings between semiconducting polymer chains would support long-range exciton and charge motion. The strong fluctuations associated with a liquid state would couple to the electronic states of the system, both by influencing the ensemble of chain conformations and by direct interactions between small ions and extended π-electron states. Thus, a local trap state for an exciton in one instance may no longer be a trap in the next. At the same time, the liquid environment would allow for molecular diffusion. Such a combination is attractive from a photosynthetic perspective. We envision that a semiconducting coacervate droplet could in principle be encapsulated in a larger assembly and thereby serve as a photoactive compartment within an overarching soft artificial photosystem.

Formation of a semiconducting coacervate is also quite intriguing from fundamental considerations. The role of extended π-electron interactions on the

thermodynamics of liquid/liquid phase separation, as well as the influence of the coupling between ionic and electronic degrees of freedom on coacervate photophysics, are highly underexplored.[14-17] We expect the semiconducting coacervate to exhibit strongly correlated many-body interactions, the elucidation of which is likely to lead to the formation of novel electronic soft materials.

Typically, aqueous phase separation of electronically active conjugated polyelectrolytes (CPEs) leads to precipitants, colloidal gels, and complex fluids in which a solid-like phase persists.[14–17] To the best of our knowledge there are no examples of true semiconducting liquid coacervates. We hypothesized that an alternating co-polymer CPE composed of one ionic monomer and one highly polar nonionic monomer would have an increased probability of stabilizing a liquid coacervate phase. We reasoned that, in the limit where long-range electrostatic interactions are strongly screened, enhanced local dipolar interactions of nonionic sidechains with solvent molecules and small ions would compete with interchain π-stacking. The latter strongly favors the formation of solid phases. Thus, we synthesized a novel polyfluorene-based CPE bearing ionically charged sidechains on one monomer and oligo(ethyleneglycol) (oEG) sidechains with a substantial number of repeat units on the other (PFNG9, Scheme 4.1). We find that in the presence of high-ionic-strength potassium bromide

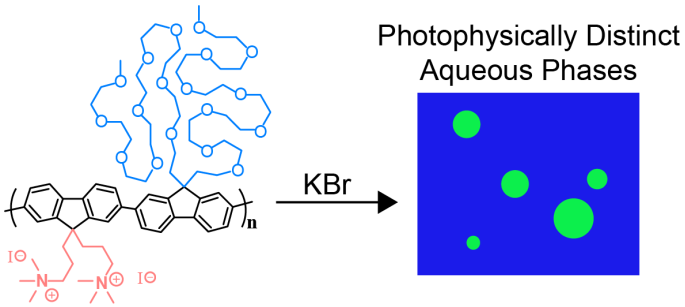

Scheme 4.1: The conjugated polyelectrolyte PFNG9 undergoes spontaneous liquid/liquid phase separation in high-ionic-strength aqueous KBr solutions.

(KBr) solutions, PFNG9 undergoes true liquid/liquid phase separation and forms spherical coacervate droplets with photophysical properties that differ substantially from the surrounding dilute solution. To the best of our knowledge, this is the first example of a semiconducting liquid coacervate.

4.2 Results and Discussion

Figure 4.1A shows the wide-field differential interference contrast (TL-DIC) light microscopy image of an aqueous sample that contains PFNG9 (4.6 mg/mL; 2.8 mM in monomer) and 5.0 M KBr. Spherical liquid droplets are seen to be dispersed through the background dilute phase – an appearance that differs drastically from all other reported CPE-based complex fluids.[14–17] Figure 4.1B shows the corresponding photoluminescence (PL) image where the sample was excited between 340-380 nm, and emission was collected between 450-490 nm. Within these illumination and emission bands, the dilute-phase PL is strongly enhanced, while

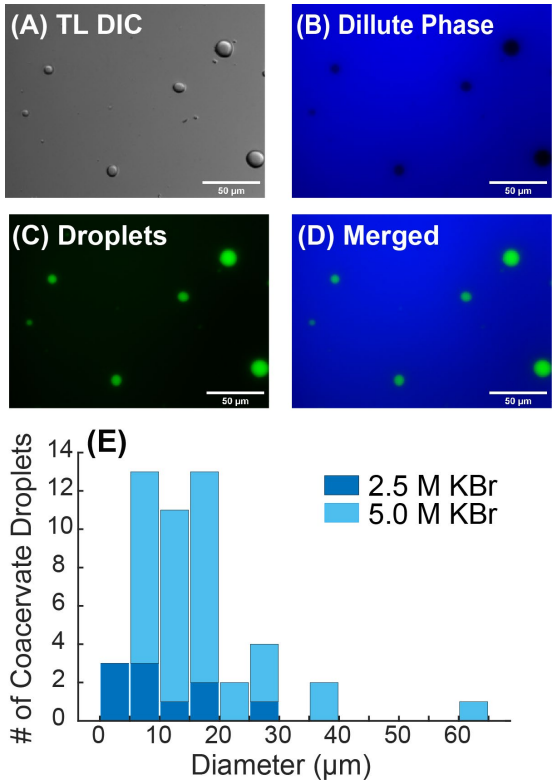

Figure 4.1: Images of CPE-based coacervate droplets. (A) TL-DIC image of the phase coexistence. (B) PL image exciting between 340-380 and collecting emission between 450-490 nm. (C) PL image exciting between 450-490 nm and collecting emission between 500-550 nm. (D) Merged PL image. (E) Comparison of the number of coacervate droplets vs. droplet diameter between 2.5 M and 5.0 M KBr samples. Distribution was collected using 5 images at each salt concentration.

droplets appear significantly darker. In contrast, illuminating the sample between 450-490 nm and collecting emission between 500-550 nm (Figure 4.1C), the dilute phase is darkened while the coacervate droplets are highly fluorescent. Clearly, the two phases are photophysically distinct from one another and the dissolved CPE in the absence of KBr (Figure AIII.13)

We observed a phase transition from more precipitant-like, fractal particle morphologies to the characteristic liquid droplet morphology conventionally associated with coacervates. Figure AIII.14 of the Supporting Information shows that this transition occurs between 2.5-5.0 M KBr with the disappearance of fractal particles at 2.5 M KBr, giving way to well-defined droplets at 5.0 M KBr (Figures AIII.14C and AIII.14F). We quantified the droplet size distribution using light microscopy at 2.5 and 5.0 M KBr, which is shown in Figure 4.1E. The number density and the observed size range of coacervate droplets are substantially larger at 5.0 M KBr. It is important to underscore that this distribution reflects droplets that could be imaged using optical microscopy. Droplets that are smaller than the diffraction limit would not be counted. In fact, we find that there are many such nanoscale and mesoscale droplets, as seen in cryogenic-transmission electron microscopy (cryo-TEM) images (Figure AIII.24 of the Supporting Information). Thus, the calculated size distributions from optical microscopy primarily reflect the micron-scale sub-population.

Figure 4.2 shows the time points of a PL microscopy video in which the flow behavior of the droplets can be observed. We find that the dynamics are quite slow,

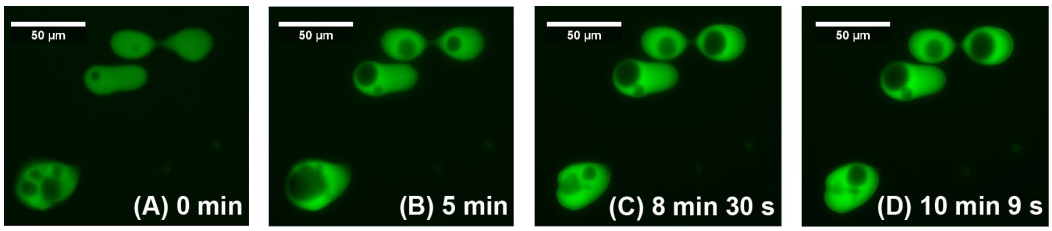

Figure 4.2: PFNG9 w/5.0 M KBr coacervate droplets imaged over 10 minutes 9 seconds.

which is consistent with the high apparent viscosity of the concentrated phase observed when handling the sample. The droplet dynamics are characteristic of a true viscous liquid as opposed to a colloidal gel.[14-17]

One of the most interesting aspects of a semiconducting coacervate is the influence of the highly correlated and strongly fluctuating environment on the ensemble of electronic states of the constituent CPE chains. To interrogate the emergent photophysical properties associated with the formation of this coacervate phase, we used a combination of steady-state and time -resolved PL spectroscopy methods. Figure 4.3A shows absorption or optical density (OD) spectra of dilute and concentrated phases, which were acquired by carefully separating the phases. Upon addition of 5.0 M KBr, the OD spectrum of the dilute phase undergoes a mild redshift relative to aqueous PFNG9 solutions without added salt. This likely reflects an increased propensity for intrachain π-stacking interactions as repulsion between ionic sidechains becomes strongly screened. In contrast to the mild redshift for the dilute solution, the OD spectrum of coacervate droplets acquires a substantial red shoulder, which implies that new electronic states form within the coacervate.

To directly compare PL spectra of the dilute solution and the coacervate droplets, we used laser-scanning confocal microscopy. Figure 4.3B shows that, when exciting at 405 nm, the dilute solution and the coacervate display a blue emission band that

decays by ~550 nm. At the same excitation wavelength, the coacervate phase gives an enhanced PL intensity on the red side of the dilute-solution PL spectrum, consistent with widefield PL microscopy images in Figure 4.1. Intriguingly, when exciting at 458 nm near the onset of red shoulder in the coacervate OD spectrum, the droplets exhibit a new, broad green emission band. We observed a similarly broad green band for the concentrated phase when physically separating the concentrated phase from the dilute phase and performing bulk PL measurements (Figure AIII.21B).

The appearance of this green band (commonly shortened to g-band) has previously been observed in a number of polyfluorene derivatives.[18–39] However, its nature continues to be controversial.[18,19,24,25,30,32–37] Initial reports suggested that it was due to the formation of

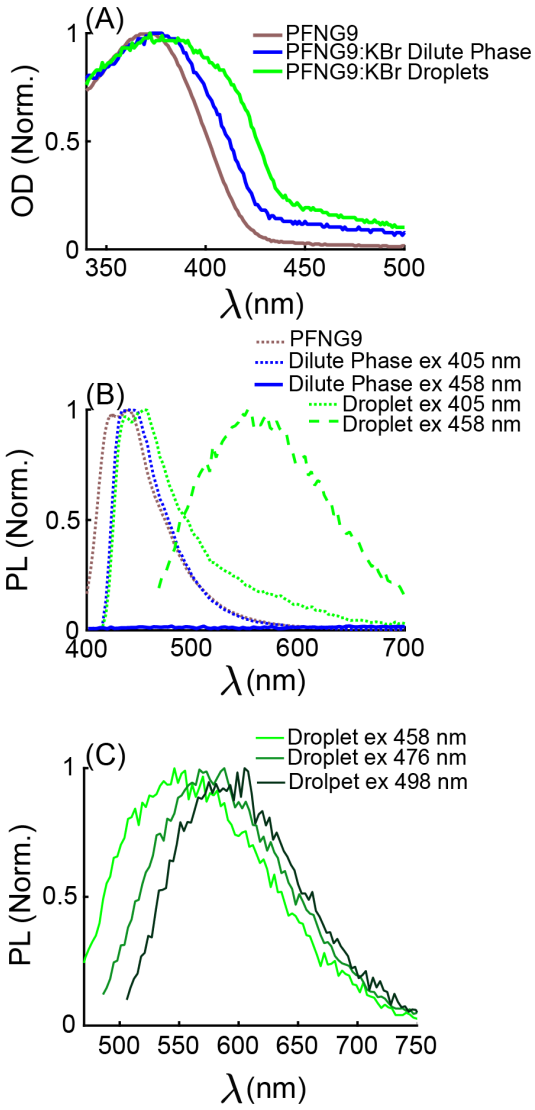

Figure 4.3: (A) Optical density (OD) and (B) photoluminescence (PL) spectra of PFNG9 compared to the separated phases of PFNG9 with 5.0 M KBr. (C) Shows no emission from the dilute phase upon excitation at 458 nm, and an excitation wavelength dependence to the droplet emission. PL shown in B and C were collected using xyλ-scan confocal microscopy and by defining regions of interest containing dilute solution or droplets from which to measure PL signal.

excimers[24,25,36,37,40,41], implying the presence of inter-chromophore interactions in the excited state. Based on early single-molecule spectroscopy measurements on (nonionic) polyfluorenes and measurements on random fluorene-co-fluorenone copolymers, others have argued that the g-band is entirely due to fluorenone defects on single chains.[31,32] However, recent measurements from more comprehensive single-molecule studies,[28,29] as well as from controlled synthesis of fluorene and fluorenone oligomers,[38] have cast serious doubt on the hypothesis that fluorenone defects on isolated polymer chains are solely responsible for the g-band. The totality of the recent work suggests that the g-band may be composed of H-aggregate exciton states as well as fluorenone-defect-based states.

We stress that PFNG9 chains in the dilute solution surrounding coacervate droplets display no g-band emission. In dilute solution, PFNG9 chains are effectively isolated. Therefore, we conclude that the g-band emission cannot be explained by fluorenone defects on single chains. To further probe the nature of the PFNG9 g-band within the coacervate, we went on to measure recovery of PL signal after light exposure to elucidate whether the coacervate was undergoing an irreversible photochemical reaction. We found the PL intensity for both the dilute solution and droplets fully recovered after ~1 and 30-s light exposure under the microscope (Figures AIII.18 and AIII.19). These results do not support the hypothesis that photodegradation by irreversible formation of fluorenone defects in the CPE backbone is leading to g-band emission. Although our results do not preclude the possibility of reversible fluorenone formation[31], we note that the bulk solution was

degassed with $Ar_{(g)}$ prior to measurements, and during image collection the coverslip was sealed with Kapton tape to minimize inward diffusion of oxygen.

What, then, is the physical origin of the g-band within the coacervate? We believe that a strong hint is provided by the evolution of the droplet PL spectrum with increasing excitation wavelength, which was collected using confocal microscopy, shown in Figure 4.3C. It is often the case that emission spectra of conjugated polymers in the solid state are independent of excitation wavelength over wide regions of the absorption spectrum. In contrast, the data in Figure 4.3C show that the structure of the g-band undergoes significant changes: The shoulder on the blue side of the spectrum disappears as the excitation wavelength goes from 458 nm to 498 nm. This suggests that different populations of distinct emitting species are excited as the excitation wavelength is increased. The presence of two emissive species is supported by the approximate decomposition of the PL spectra in Figure 4.3C into two distinct contributions with excitation wavelength-dependent amplitudes, shown in Figure AIII.23 of the Supporting Information. Our results are consistent with single-molecule measurements by Nakamura, et al., which provided evidence that the g-band of polyfluorene chains with intrachain interactions consisted of multiple emitting species.[28]

Given the inherent proximity between chains within the crowded coacervate environment and the lack of g-band emission in the dilute phase, we argue that the coacervate g-band is likely primarily composed of interchain exciton states.[42-44] The fact that only one new, relatively narrow absorption band appears within the coacervate but that two putative emissive species comprise the g-band PL spectrum is

consistent with a coexistence of excimers and H-aggregate excitons within a coacervate droplet. Evidence for H-aggregate formation is provided by the appearance of a new redshifted absorption band in the OD spectrum of the coacervate compared to the dilute phase (Figure 4.1A). In contrast, excimers result from interchromophore interactions in the excited state only and thus do not give rise to new absorption bands. Excimer states are characterized by broad and unstructured emission spectra, as the ground-state energy as a function of interchromophore separation for an excimer configuration does not correspond to a bound state.[27,40] Although the ground state of an H-aggregate is bound, unlike in an ordered thin film, in viscous droplets we expect a relatively broad range of excitonic coupling strengths. The result is a relatively broad ensemble H-aggregate spectrum where the vibronic structure is likely largely washed out. Thus, distinguishing excimers and H-aggregates based on the widths, shapes, and peak positions of their ensemble-averaged PL spectra within the coacervate is not straightforward.[43]

We note that our conclusion does not preclude the possibility that fluorenone defects also contribute to the coacervate emission spectrum. However, it must then still be the case that emission from fluorenone-based states requires an inter-chromophore excitonic coupling.[23] Thus, we conclude that the CPE coacervate is an intrinsically excitonically coupled viscoelastic liquid. This is summarized in a cartoon in Scheme 4.2.[44,45]

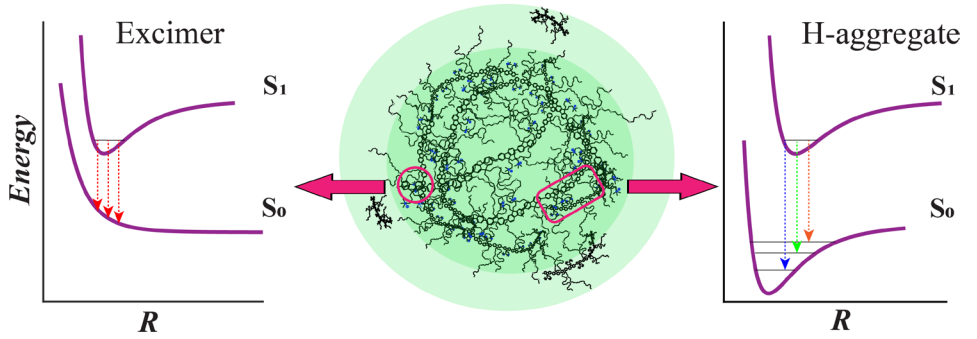

Scheme 4.2: Cartoon of a PFNG9 coacervate droplet (middle). Regions corresponding to excimer and H-aggregate exciton states are speculatively labeled as magenta domains with few or extended interchain contacts, respectively.[44,45] Illustrations of the corresponding potential energy curves as a function of the (average) inter-chromophore separation *R* are shown in the side panels.

To gain a better understanding of the coacervate photophysics, we used fluorescence lifetime imaging (FLIM) to characterize the radiative relaxation of dilute-phase and coacervate excitons. FLIM allows us to measure PL lifetimes as a function of position within the droplet. Figure 4.4A shows the heat map of PL lifetimes of a representative droplet following excitation at 445 nm while collecting emission in the 590 ± 25 nm region. The average PL lifetime ⟨τ⟩ calculated for

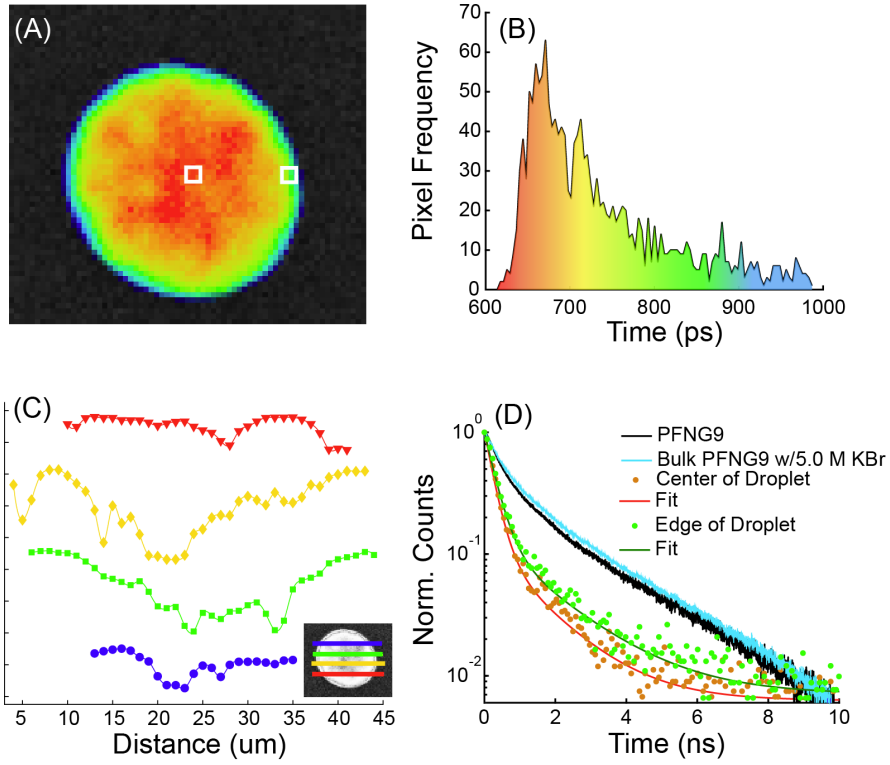

Figure 4.4: (A) Select droplet from a FLIM image, where pixel selection in the center and on the edge of the droplet are highlighted with white boxes. The grey scale image shows line cuts from which distant dependent lifetime fluctuations were pulled (see panel (C)). Excitation: 445 nm. Emission: 590 nm. (B) Histogram of PL lifetimes measured across the entire droplet. (C) shows the distance dependent fluctuations in lifetime (symbols) along with corresponding cubic spline curves (solid) taken from the line cuts shown in the grey scale image in (A). Curves have been vertically offset for clarity. (D) PL decay curves and fits associated with the selected pixels in (A). Black and light blue decays are bulk-solution TRPL. Because the quantity of dilute phase far exceeds that of the droplets, the bulk TRPL data is largely representative of the dilute-phase ⟨τ⟩, which was found to be 970 ps. The excitation/emission wavelengths are the same as in (A).

individual coacervate droplets was found to range between 560-830 ps. The PL lifetime histogram (Figure 4.4B) highlights differences in lifetime found throughout the droplet where the color-coding of the histogram matches that in the FLIM heat map. Similar images and histograms were collected for 9 additional droplets (Figure AIII.27).

The FLIM heat map shows that $\langle\tau\rangle$ is a function of position within the droplet, demonstrating that $\langle\tau\rangle$ is a fluctuating variable within the coacervate. This observation is consistent with the viscous liquid macrostate. To characterize the approximate length scale of $\langle\tau\rangle$ fluctuations, in Figure 4.4C we plot 4 linecuts through the droplet shown in Figure 4.4A. The extracted image grey value as a function of position for the different linecuts shows that relatively small fluctuations in $\langle\tau\rangle$ occur on the ~1 μm scale, while larger fluctuations are also seen on the ~10 μm scale. Differences in $\langle\tau\rangle$ must reflect differences in local structure. We speculate that the large viscosity of the droplet leads to a relatively slow interconversion between large, entangled CPE networks and relatively loosely associated domains with fewer inter-chain interactions. However, within the droplet interior, the mean fluctuation in $\langle\tau\rangle$ is not dramatic, as seen from the histogram in Figure 4.4B, suggesting relatively subtle differences in structure as a function of position.

It was commonly the case that the PL lifetime was somewhat longer near the edge of the droplets than in the center. This is shown in Figure 4.4C, which compares decays collected in the middle of the droplet to that of the near-surface region (indicated by white squares in Figure 4.4A). In going from the bulk to the surface of the droplet, the lifetime of the short component increases from 255 ps to 298 ps,

while the lifetime of the long component increases from 1367 ps to 1693 ps. The difference between bulk and surface lifetimes increases closer to the edge of the droplet, as seen from the lifetime histogram. For the regions labeled with white squares, we can quantify the change in the (intensity-weighted) contribution that each component makes to the total decay, f_i, according to $f_i = a_i\tau_i / \sum_j a_j\tau_j$, where a_i and τ_i are the amplitude and lifetime of component i, respectively. f_{short} decreases by ~8% while f_{long} increases by ~16% for the near-surface region relative to the middle. Since longer lifetimes are often associated with more extended chains, we speculate that the PFNG9 backbone undergoes a relative extension near the surface. This could allow polymer chains to maximize the number of oEG sidechains capable of orienting approximately normal to the droplet/solution interface, thereby likely lowering the surface free energy.

It is important to ask why PFNG9 forms a liquid coacervate phase while the overwhelming majority of CPEs do not. Although it is reasonable to expect that the oEG sidechains are implicated, it is not immediately clear what contribution(s) they make to the system free energy such that the liquid state becomes stabilized at high [KBr]. In our system, there is no interaction with an oppositely charged polyelectrolyte, as would occur in a complex coacervate. Therefore, in the simple PFNG9 coacervate it is likely that the interaction between the excess ions and the oEG sidechain plays a role in inducing the formation of this dense liquid phase. It is known that K^+ ions readily interact with crown ethers, which are chemically related to the oEG sidechains.[46,47] We aimed to elucidate whether the ionic strength alone determined coacervate formation independent of ion identity or whether the identity

of the cation was an important factor. We prepared similar samples using comparable concentrations of lithium bromide (LiBr), tertraethylammonium bromide (TEAB), and calcium bromide ($CaBr_2$). Liquid coacervate formation was not observed in the presence of any other salts chosen for this study (Figure AIII.15-AIII.17). We conclude that the specific K^+ – oEG interaction is likely involved in the stabilization of the coacervate phase. We reason that the large viscosity of the droplets is then a consequence of both inter-chromophore π-stacking and a large number of K^+ ions interacting with a correspondingly large number of ethylene glycol groups. The separate enthalpic and entropic contributions to the underlying free energy, including the competition between ion desolvation and sidechain interactions, remain obscured at the moment.

4.3 Conclusion

In summary, we have demonstrated that the chemical structure of a CPE can be rationally designed to undergo liquid/liquid phase separation to stabilize a semiconducting coacervate macrostate, which is of fundamental interest to coacervate physical chemistry. We find that oligo(ethyleneglycol) sidechains are critical to the simple coacervation process, which involves the interaction between ethyleneglycol units with K^+ ions. The CPE coacervate is comprised of intrinsically excitonically coupled chains with rich exciton dynamics in the presence of a fluctuating ionic environment. In addition to its fundamental significance, this observation is intriguing from an applications standpoint. The electronic connectivity within the concentrated liquid could be used to move excitons, electrons or holes through space over distances that are large compared to the monomer size. The strong coupling between

and electronic and ionic degrees of freedom can in principle be used to manipulate this quasiparticle migration. These characteristics are likely to be desirable for light harvesting, catalysis or sensing. Finally, semiconducting coacervate droplets may in principle be encapsulated in larger soft-matter assemblies, leading to the potential for compartmentalization and a significant increase in light-harvesting complexity.

4.4 References

(1) Deshpande, S.; Dekker, C. Studying Phase Separation in Confinement. Curr. Opin. Colloid Interface Sci. **2021**, 52, 101419. https://doi.org/10.1016/j.cocis.2021.101419.

(2) Ghosh, B.; Bose, R.; Tang, T. Y. D. Can Coacervation Unify Disparate Hypotheses in the Origin of Cellular Life? Curr. Opin. Colloid Interface Sci. **2021**, 52, 101415. https://doi.org/10.1016/j.cocis.2020.101415.

(3) Stewart, R. J.; Wang, C. S.; Song, I. T.; Jones, J. P. The Role of Coacervation and Phase Transitions in the Sandcastle Worm Adhesive System. Adv. Colloid Interface Sci. **2017**, 239 (1), 88–96. https://doi.org/10.1016/j.cis.2016.06.008.

(4) Saini, B.; Singh, S.; Mukherjee, T. K. Nanocatalysis under Nanoconfinement: A Metal-Free Hybrid Coacervate Nanodroplet as a Catalytic Nanoreactor for Efficient Redox and Photocatalytic Reactions. ACS Appl. Mater. Interfaces **2021**, 13 (43), 51117–51131. https://doi.org/10.1021/acsami.1c17106.

(5) Johnson, N. R.; Wang, Y. Coacervate Delivery Systems for Proteins and Small Molecule Drugs. Expert Opin. Drug Deliv. **2014**, 11 (12), 1829–1832. https://doi.org/10.1517/17425247.2014.941355.

(6) Kaur, S.; Weerasekare, G. M.; Stewart, R. J. Multiphase Adhesive Coacervates

Inspired by the Sandcastle Worm. ACS Appl. Mater. Interfaces **2011**, 3 (4), 941–944. https://doi.org/10.1021/am200082v.

(7) Keating, C. D.; Martin, N.; Santore, M. M. Editorial Overview: Coacervates and Membraneless Organelles. Curr. Opin. Colloid Interface Sci. **2021**, 56, 101527. https://doi.org/10.1016/j.cocis.2021.101527.

(8) Mountain, G. A.; Keating, C. D. Formation of Multiphase Complex Coacervates and Partitioning of Biomolecules within Them. Biomacromolecules **2020**, 21 (2), 630–640. https://doi.org/10.1021/acs.biomac.9b01354.

(9) Lu, T.; Spruijt, E. Multiphase Complex Coacervate Droplets. J. Am. Chem. Soc. **2020**, 142 (6), 2905–2914. https://doi.org/10.1021/jacs.9b11468.

(10) Keating, C. D. Aqueous Phase Separation as a Possible Route to Compartmentalization of Biological Molecules. Acc. Chem. Res. **2012**, 45 (12), 2114–2124. https://doi.org/10.1021/ar200294y.

(11) Wang, Q.; Schlenoff, J. B. The Polyelectrolyte Complex/Coacervate Continuum. Macromolecules **2014**, 47 (9), 3108–3116. https://doi.org/10.1021/ma500500q.

(12) Li, L.; Srivastava, S.; Andreev, M.; Marciel, A. B.; De Pablo, J. J.; Tirrell, M. V. Phase Behavior and Salt Partitioning in Polyelectrolyte Complex Coacervates. Macromolecules **2018**, 51 (8), 2988–2995. https://doi.org/10.1021/acs.macromol.8b00238.

(13) Sing, C. E.; Perry, S. L. Recent Progress in the Science of Complex Coacervation. Soft Matter **2020**, 16 (12), 2885–2914.

https://doi.org/10.1039/d0sm00001a.

(14) Johnston, A. R.; Perry, S. L.; Ayzner, A. L. Associative Phase Separation of Aqueous π-Conjugated Polyelectrolytes Couples Photophysical and Mechanical Properties. Chem. Mater. **2021**, 33 (4), 1116–1129. https://doi.org/10.1021/acs.chemmater.0c02424.

(15) Danielsen, S. P. O.; Nguyen, T.-Q.; Fredrickson, G. H.; Segalman, R. A. Complexation of a Conjugated Polyelectrolyte and Impact on Optoelectronic Properties. ACS Macro Lett. **2019**, 8 (1), 88–94. https://doi.org/10.1021/acsmacrolett.8b00924.

(16) Le, M. L.; Rawlings, D.; Danielsen, S. P. O.; Kennard, R. M.; Chabinyc, M. L.; Segalman, R. A. Aqueous Formulation of Concentrated Semiconductive Fluid Using Polyelectrolyte Coacervation. ACS Macro Lett. **2021**, 10 (8), 1008–1014. https://doi.org/10.1021/acsmacrolett.1c00354.

(17) Johnston, A. R.; Minckler, E. D.; Shockley, M. C. J.; Matsushima, L. N.; Perry, S. L.; Ayzner, A. Conjugated Polyeelctrolyte-Based Complex Fluids as Aqueous Exciton Transport Networks. Angew. Chemie - Int. Ed. **2022**, 134 (20), 1–12. https://doi.org/10.1002/anie.202117759.

(18) Bliznyuk, V. N.; Carter, S. A.; Scott, J. C.; Klärner, G.; Miller, R. D.; Miller, D. C. Electrical and Photoinduced Degradation of Polyfluorene Based Films and Light-Emitting Devices. Macromolecules **1999**, 32 (2), 361–369. https://doi.org/10.1021/ma9808979.

(19) List, E. J. W.; Gaal, M.; Guentner, R.; De Freitas, P. S.; Scherf, U. The Role of Keto Defect Sites for the Emission Properties of Polyfluorene-Type Materials.

Synth. Met. **2003**, 139 (3), 759–763. https://doi.org/10.1016/S0379-6779(03)00249-2.

(20) Kim, Y.; Bouffard, J.; Kooi, S. E.; Swager, T. M. Highly Emissive Conjugated Polymer Excimers. J. Am. Chem. Soc. **2005**, 127 (39), 13726–13731. https://doi.org/10.1021/ja053893+.

(21) Schwartz, B. J. Conjugated Polymers As Molecular Materials: How Chain Conformation and Film Morphology Influence Energy Transfer and Interchain Interactions. Annu. Rev. Phys. Chem. **2003**, 54 (3), 141–172. https://doi.org/10.1146/annurev.physchem.54.011002.103811.

(22) Stangl, T.; Wilhelm, P.; Schmitz, D.; Remmerssen, K.; Henzel, S.; Jester, S. S.; Höger, S.; Vogelsang, J.; Lupton, J. M. Temporal Fluctuations in Excimer-like Interactions between π-Conjugated Chromophores. J. Phys. Chem. Lett. **2015**, 6 (8), 1321–1326. https://doi.org/10.1021/acs.jpclett.5b00328.

(23) Sims, M.; Bradley, D. D. C.; Ariu, M.; Koeberg, M.; Asimakis, A.; Grell, M.; Lidzey, D. G. Understanding the Origin of the 535 Nm Emission Band in Oxidized Poly(9,9-Dioctylfluorene): The Essential Role of Inter-Chain/Inter-Segment Interactions. Adv. Funct. Mater. **2004**, 14 (8), 765–781. https://doi.org/10.1002/adfm.200305149.

(24) Klarner, G.; Davey, M. H.; Chen, W.-D.; Scott, J. C.; Miller, R. D. Colorfast Blue-Light-Emitting Random Copolymers Derived from Di-n-hexylfluorene and Anthracene. Adv. Mater. Commun. **1998**, 10 (12), 993–997.

(25) Horrocks, D.L. Brown, W. G. Solution Fluorescence Spectrum of Highly Purified FLuorene. Chem. Phys. Lett. **1970**, 5 (2), 117–119.

(26) Wu, M. W.; Conwell, E. M. Effect of Interchain Coupling on Conducting Polymer Luminescence: Excimers in Derivatives of Poly„phenylene Vinylene… M. Phys. Rev. B - Condens. Matter Mater. Phys. **1997**, 56 (16), 1–3.

(27) Förster, T. Excimers. Angew. Chemie - Int. Ed. **2014**, 8 (5), 333–343.

(28) Nakamura, T.; Sharma, D. K.; Hirata, S.; Vacha, M. Intrachain Aggregates as the Origin of Green Emission in Polyfluorene Studied on Ensemble and Single-Chain Level. J. Phys. Chem. C **2018**, 122 (15), 8137–8146. https://doi.org/10.1021/acs.jpcc.8b01767.

(29) Honmou, Y.; Hirata, S.; Komiyama, H.; Hiyoshi, J.; Kawauchi, S.; Iyoda, T.; Vacha, M. Single-Molecule Electroluminescence and Photoluminescence of Polyfluorene Unveils the Photophysics behind the Green Emission Band. Nat. Commun. **2014**, 5, 1–8. https://doi.org/10.1038/ncomms5666.

(30) Zhao, W.; Cao, T.; White, J. M. On the Origin of Green Emission in Polyfluorene Polymers: The Roles of Thermal Oxidation Degradation and Crosslinking. Adv. Funct. Mater. **2004**, 14 (8), 783–790. https://doi.org/10.1002/adfm.200305173.

(31) Becker, K.; Lupton, J. M.; Feldmann, J.; Nehls, B. S.; Galbrecht, F.; Gao, D.; Scherf, U. On-Chain Fluorenone Defect Emission from Single Polyfluorene Molecules in the Absence of Intermolecular Interactions. Adv. Funct. Mater. **2006**, 16 (3), 364–370. https://doi.org/10.1002/adfm.200500550.

(32) Lupton, J. M.; Craig, M. R.; Meijer, E. W. On-Chain Defect Emission in Electroluminescent Polyfluorenes. Appl. Phys. Lett. **2002**, 80 (24), 4489–4491.

https://doi.org/10.1063/1.1486482.

(33) Yang, X. H.; Jaiser, F.; Neher, D.; Lawson, P. V.; Brédas, J. L.; Zojer, E.; Güntner, R.; De Freitas, P. S.; Forster, M.; Scherf, U. Suppression of the Keto-Emission in Polyfluorene Light-Emitting Diodes: Experiments and Models. Adv. Funct. Mater. **2004**, 14 (11), 1097–1104. https://doi.org/10.1002/adfm.200305012.

(34) Romaner, L.; Pogantsch, A.; De Freitas, P. S.; Scherf, U.; Gaal, M.; Zojer, E.; List, E. J. W. The Origin of Green Emission in Polyfluorene-Based Conjugated Polymers: On-Chain Defect Fluorescence. Adv. Funct. Mater. **2003**, 13 (8), 597–601. https://doi.org/10.1002/adfm.200304360.

(35) Gong, X.; Iyer, P. K.; Moses, D.; Bazan, G. C.; Heeger, A. J.; Xiao, S. S. Stabilized Blue Emission from Polyfluorene-Based Light-Emitting Diodes: Elimination of Fluorenone Defects. Adv. Funct. Mater. **2003**, 13 (4), 325–330. https://doi.org/10.1002/adfm.200304279.

(36) Prieto, I.; Teetsov, J.; Fox, M. A.; Vanden Bout, D. A.; Bard, A. J. Study of Excimer Emission in Solutions of Poly(9,9-Dioctylfluorene) Using Electrogenerated Chemiluminescence. J. Phys. Chem. A **2001**, 105 (3), 520–523. https://doi.org/10.1021/jp003566i.

(37) Pei, Q.; Yang, Y. Efficient Photoluminescence and Electroluminescence from a Soluble Polyfluorene. J. Am. Chem. Soc. **1996**, 118 (31), 7416–7417. https://doi.org/10.1021/ja9615233.

(38) Bo, Y. F.; Liu, Y. Y.; Soleimaninejad, H.; Yu, M. N.; Xie, L. H.; Smith, T. A.; Ghiggino, K. P.; Huang, W. Photophysical Identification of Three Kinds of

Low-Energy Green Band Defects in Wide-Bandgap Polyfluorenes. J. Phys. Chem. A **2019**, 123 (13), 2789–2795. https://doi.org/10.1021/acs.jpca.9b00188.

(39) Conwell, E. Mean Free Time for Excimer Light Emission in Conjugated Polymers. Phys. Rev. B - Condens. Matter Mater. Phys. **1998**, 57 (22), 14200–14202. https://doi.org/10.1103/PhysRevB.57.14200.

(40) Förster, T. Excimers and Exciplexes. In the Exciplex; Gordon, M., Ware, W. R., Eds.; Academic Press, Inc., 1975.

(41) Jenekhe, S. A.; Osaheni, J. A. Excimers and Exciplexes of Conjugated Polymers. Science (80-.). **1994**, 265 (5173), 765–768.

(42) Clark, J.; Silva, C.; Friend, R. H.; Spano, F. C. Role of Intermolecular Coupling in the Photophysics of Disordered Organic Semiconductors: Aggregate Emission in Regioregular Polythiophene. Phys. Rev. Lett. **2007**, 98 (20), 1–4. https://doi.org/10.1103/PhysRevLett.98.206406.

(43) Kim, W.; Nowak-Król, A.; Hong, Y.; Schlosser, F.; Würthner, F.; Kim, D. Solvent-Modulated Charge-Transfer Resonance Enhancement in the Excimer State of a Bay-Substituted Perylene Bisimide Cyclophane. J. Phys. Chem. Lett. **2019**, 10 (8), 1919–1927. https://doi.org/10.1021/acs.jpclett.9b00357.

(44) Samanta, S.; Chaudhuri, D. Suppressing Excimers in H-Aggregates of Perylene Bisimide Folda-Dimer: Role of Dimer Conformation and Competing Assembly Pathways. J. Phys. Chem. Lett. **2017**, 8 (14), 3427–3432. https://doi.org/10.1021/acs.jpclett.7b01338.

(45) Reilly, N.; Ivanov, M.; Uhler, B.; Talipov, M.; Rathore, R.; Reid, S. A. First

Experimental Evidence for the Diverse Requirements of Excimer vs Hole Stabilization in π-Stacked Assemblies. J. Phys. Chem. Lett. **2016**, 7 (15), 3042–3045. https://doi.org/10.1021/acs.jpclett.6b01201.

(46) Haymore, B. L.; Lamb, J. D.; Izatt, R. Thermodynamic Origin. **1982**, No. Iii, 1598–1602.

(47) Steed, J. W. First- and Second-Sphere Coordination Chemistry of Alkali Metal Crown Ether Complexes. Coord. Chem. Rev. **2001**, 215 (1), 171–221. https://doi.org/10.1016/S0010-8545(01)00317-4.

Appendix III

Supporting Information for

Excitonically Coupled Simple Coacervates via Liquid/Liquid Phase Separation

III.1 Experimental

Synthetic Methods

Starting Materials and Characterization.

Reagents and materials were used as received from the following distributors. Specifically, 2,7-dibromofluorene and 4-toluenesulfonyl chloride were obtained from Oakwood Chemical. Bis(pinacolato)diboron >98% and 1,4-dioxane anhydrous 99.8% were obtained from Alfa Aesar. Nonaethylene glycol monomethyl ether >93.0% was obtained from TCI America Inc. Tetraethylammonium bromide 100% was obtained from Chem-Impex Int'l Inc. Palladium catalyst [1,1'-Bis(diphenylphosphino)ferrocene] dichloropalladium (II), dimethyl aminopropyl chloride hydrochloride 96%, sodium hydride 60% dispersed in mineral oil, and dimethylformamide anhydrous 99.8% were obtained from Sigma-Aldrich. Methyl iodide 99.5%, tetrahydrofuran HPLC grade, dichloromethane 99.5% were obtained from Spectrum Chemical. Sodium hydroxide, sodium hydroxide 50% w/w, potassium carbonate anhydrous 99.7%, triethylamine 99%, diethyl ether 99%, methanol 99.9%, acetone HPLC grade, chloroform 99.9%, ethyl acetate 99.5%, hexanes 98.5%, and potassium acetate >99% were obtained from Fisher Chemical. Dimethyl sulfoxide 99.7% was obtained from Acros Organics. Chemglass pressure tubes were used for

polymerization (48 mL - part number CG-1880-04), and quaternization (350 mL - part number CG-1880-12). $CDCl_3$ (D 99.8%) and D2O (D 99.9%) were both purchased from Cambridge Isotope Laboratories. Nuclear magnetic resonance (NMR) spectra of the monomers were collected with a Bruker Avance III HD 4 channel 500 MHz NMR, and spectra of the polymers were collected with a Bruker Avance III HD 4 channel 800 MHz NMR with a cryoprobe.

Preparation of Reagents.

Reagent TG9

Synthesis of (1-(p-tosyl)-3,6,9,12,15,18,21,24,27- nonaoxooctacosane To a clean and dried 25 mL round bottom flask placed in an ice bath, a Teflon-coated stir bar, NaOH (0.80 g, 20.0 mmol), DI H_2O (4.0 mL, 222 mmol), nonaethylene glycol monomethyl ether (G9OH, 3.00 g, 7.0 mmol), and THF (8.0 mL, 98.6 mmol) were added and allowed to react for 30 minutes. Next, PTSC (2.40 g, 12.6 mmol) was added under an atmosphere of N_2(g) and reacted for 12 hours. Upon completion, the reaction contents were dumped into 16 mL of cold DI H_2O, followed by extraction of the product with DCM (4 x 10 mL). The organic layer was washed with DI H_2O (2 x 10 mL), brine (1 x 10 mL), and subsequently dried over Na_2SO_4. The anhydrous organic layer was decanted away from the drying agent and concentrated under reduced pressure to provide the product TG9 as a colorless oil (99% yield, 4.06 g).[2] **Figure AIII.1**: TG9 ^{1}H NMR (500 MHz, $CDCl_3$): δ 7.80- 7.79 (d, 2H), 7.35- 7.33 (d, 2H), 4.16 (t, 2H), 3.68 (t, 2H), 3.65- 3.64 (m, 22H), 3.61 (m, 4H), 3.58 (s, 4H), 3.54 (s, 2H),

3.37 (s, 3H), 2.44 (s, 3H) **Figure AIII.2**: TG9 ^{13}C NMR (500 MHz, $CDCl_3$): δ 144.9, 133.2, 130.0, 128.1, 72.1, 70.9, 70.8, 70.7, 70.7, 69.4, 68.8, 68.1, 59.2, 25.8, 21.8.

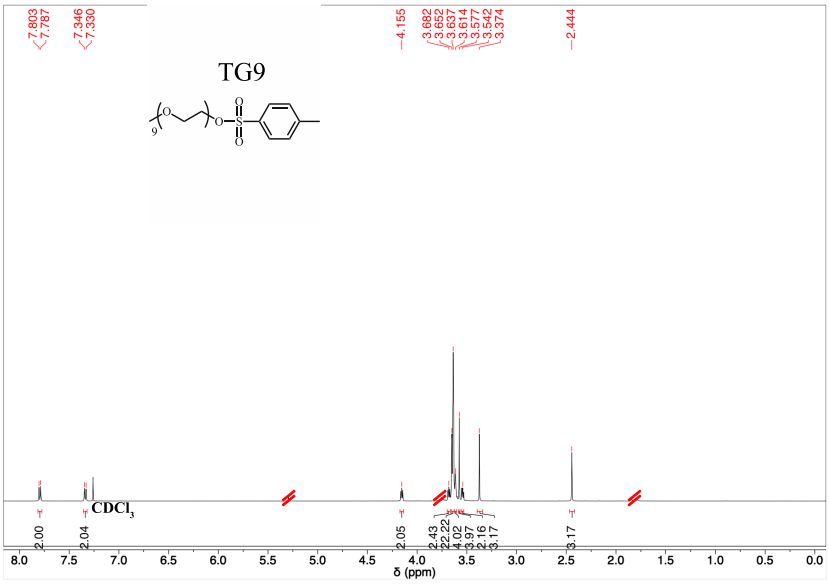

Figure AIII.1: TG9 ^{1}H NMR with trace amount of *DCM, THF,* and water.

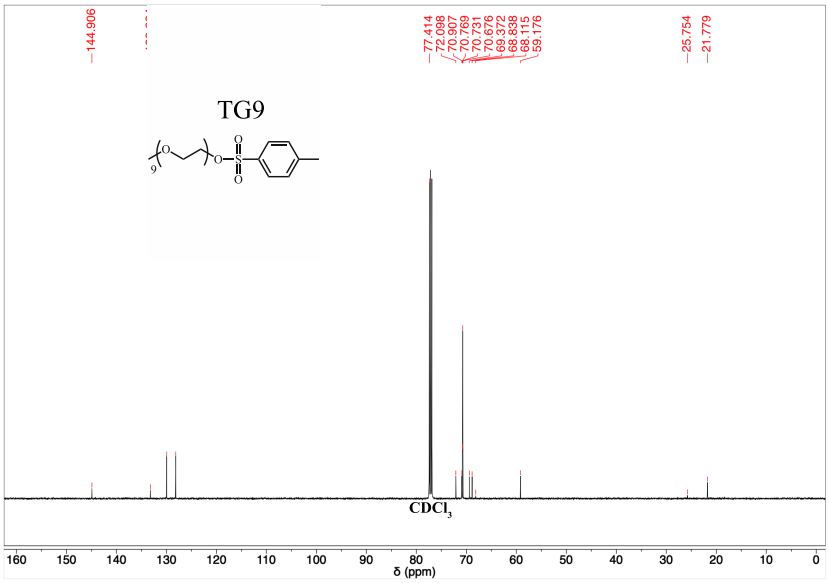

Figure AIII.2: TG9 ^{13}C NMR

Synthesis of Monomers.

Monomer FN

Synthesis of (2,7-dibromo-9,9-bis(3'-(N,N-dimethyl-amino)-propyl)-fluorene) To a clean, dried, 100 mL two neck round bottom flask, a Teflon coated stir bar, dimethyl sulfoxide (DMSO, 30.9 mL, 434.6 mmol), 2,7- dibromofluorene (F, 2 g, 6.2 mmol), tetrabutylammonium bromide (TBAB, 39.8 mg, 0.12 mmol), and 4 mL of a 50 wt. % aqueous sodium hydroxide solution (50 wt. % aq. NaOH, 4 mL, 154.3 mmol) was added under an atmosphere of nitrogen (N_2(g)). An additional aliquot of DMSO (10.5 mL, 145.1 mmol) was added to the reaction flask, followed by dimethyl aminopropyl chloride hydrochloride salt (DAPCl, 2.6 g, 16.4 mmol). The reaction was stirred and heated at 60 °C for 12 hours. Reaction progress was monitored by thin-layer chromatography (TLC). Deionized water (DI H_2O, 40 mL, 2.216 mmol) was added to

the reaction flask to dissolve precipitated salts as well as to solvate DMSO. The product (FNB) was extracted from the wet DMSO layer with diethyl ether (Et_2O, 8 x 25 mL),

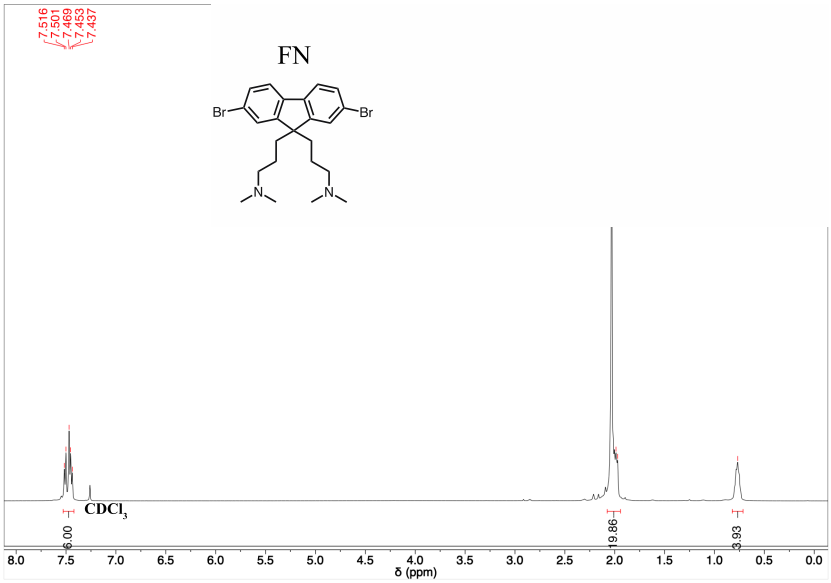

Figure AIII.3: FN ^{1}H NMR

and washed with a 10 wt. % aqueous NaOH (10 wt. % aq. NaOH, 2 x 50 mL). The organic layer was washed with DI H_2O (3 x 50 mL), followed by a brine wash (1 x 50 mL), and then dried over anhydrous sodium sulfate (Na_2SO4). The concentration of the anhydrous organic layer under reduced pressure lead to crude solid which was purified with a silica gel column (Hexanes: Ethyl Acetate: Triethylamine, 49:49:2) to obtain FN (59% yield, 1.81 g).[4,5] **Figure AIII.3**: FN ^{1}H NMR (500 MHz, $CDCl_3$): δ 7.52-7.50 (d, 2H), 7.47 (s, 2H), 7.45-7.44 (d, 2H), 2.03 (s, 12H), 1.99 (m, 8H), 0.77 (m, 4H) **Figure AIII.4**: FN ^{13}C NMR (500 MHz, $CDCl_3$): δ 152.2, 139.3, 130.6, 126.3, 121.8, 121.4, 59.7, 55.5, 45.5, 37.7, 22.2.

Monomer FNB

Synthesis of (2,7-diboryl pinacol ester-9,9-bis(3'-(N,N-dimethyl-amino)-propyl)-fluorene) To a clean, dried, 100 mL two neck round bottom flask, a Teflon coated stir bar, dimethylformamide (DMF, 39 mL, 505.8 mmol), FN (1 g, 2.0 mmol), bis(pinacolato)diboron (B_2Pin_2, 2.26 g, 8.9 mmol), potassium acetate (KOAc, 3.53 g, 17.8 mmol), [1,1'-Bis(diphenyl-phosphino)ferrocene]dichloro-palladium(II) ($Pd(dppf)Cl_2$, 0.296 g, 0.40 mmol) were added under an atmosphere of N_2(g). The contents of the reaction were stirred and heated at 80 °C for 24 hours. Reaction progress

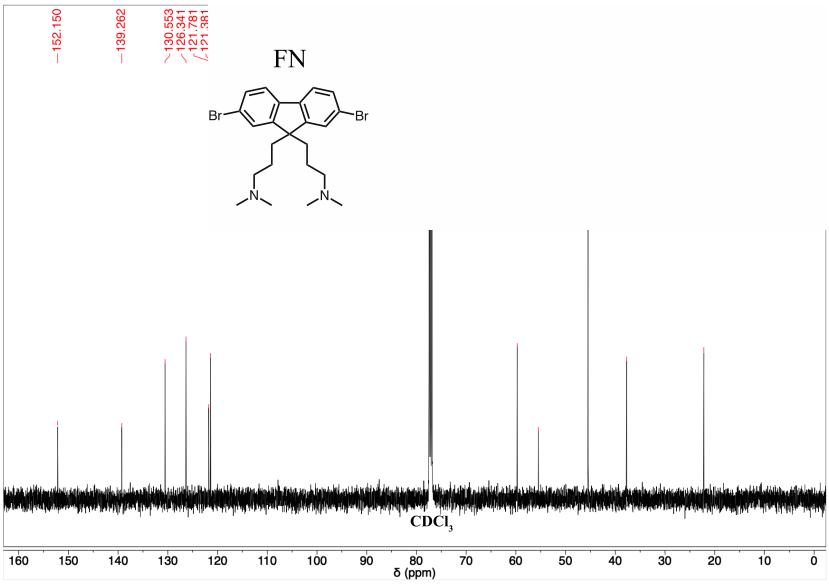

Figure AIII.4: FN ^{13}C NMR

was monitored by TLC. Upon completion, the reaction was concentrated to dryness, and the crude solid was extracted with hot HPLC-grade hexanes (7 x 100 mL). The combined hexanes layer was filtered, concentrated to dryness, reextracted with hot

hexanes, and re-concentrated to dryness. Acetone was used to extract the product from the re-dried hexanes layer and was allowed to crystallize out of the solution as an off-white solid. The FNB crystals were collected via filtration and washed with a minimal amount of cold acetone to obtain FNB (55% yield, 0.6647 mg).[4,5] **Figure AIII.5**: FNB ^{1}H NMR (500 MHz, $CDCl_3$): δ 7.80-7.78 (d, 2H), 7.78 (s, 2H), 7.71-7.70 (d, 2H), 2.06 (m, 4H), 1.99 (m, 4H), 1.98 (s, 12H), 1.37 (s, 24H), 0.75 (m, 4H) **Figure AIII.6**: FNB ^{13}C NMR (500 MHz, $CDCl_3$): δ 149.4, 144.0, 134.3, 129.1, 119.8, 84.0, 59.2, 54.7, 44.6, 37.4, 31.1, 25.1.

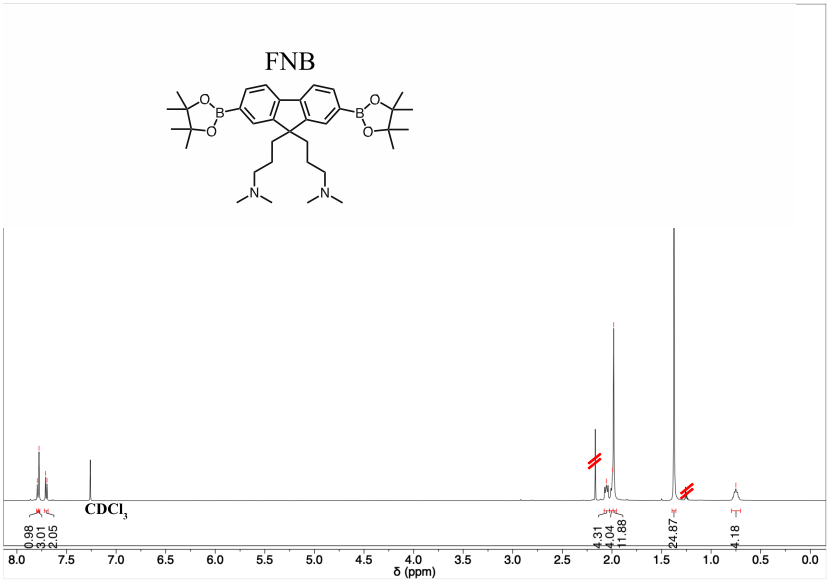

Figure AIII.5: FNB ^{1}H NMR with trace amount of acetone and hexanes.

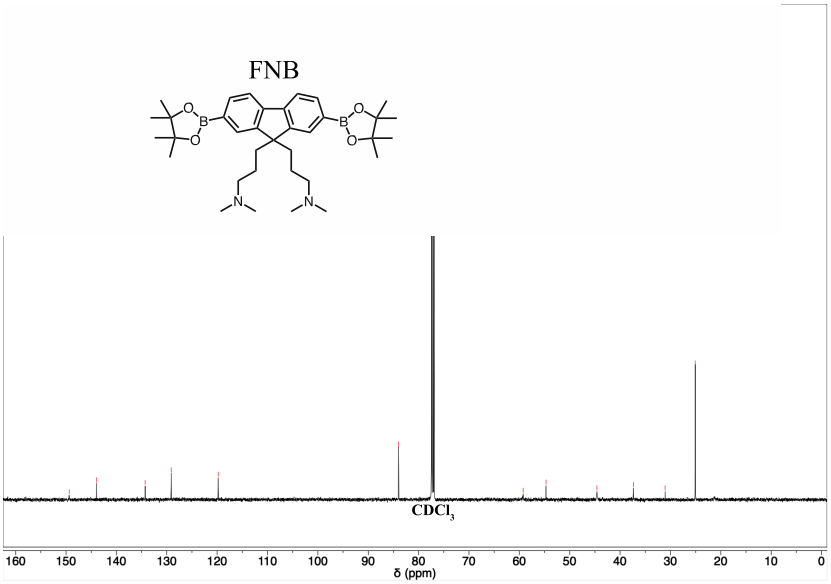

Figure AIII.6: FNB ^{13}C NMR

Monomer FG9

Synthesis of (2,7-dibromo-9,9-bis-(2-(2-(2-(2-(2-(2-(2-(2-methoxy-ethoxy) ethoxy) ethoxy) ethoxy) ethoxy) ethoxy) ethoxy) ethyl)- fluorene) To a clean and dried 50 mL round bottom flask, a Teflon coated stir bar, F (670 mg, 2.1 mmol), anhydrous DMF (12 mL, 155 mmol), and NaH in 60% w/w dispersed in mineral oil (210 mg, 5.3 mmol) were added under an inert atmosphere of N_2(g). After 30 minutes, the bright red solution was allowed to react at 60 °C for 12 hours with previously prepared TG9 (3.0 g, 5.2 mmol). After quenching the remaining NaH with DI H_2O (15 mL), the reaction was extracted with DCM (4 x 50 mL). Dried the combined organic layer over Na_2SO_4. The anhydrous organic layer was decanted away from the drying

agent. While stirring, a mixture consisting of 95% DCM with 5% Methanol (MeOH) was used to wash the product from the Na_2SO_4 slurry. The DCM: MeOH solution was

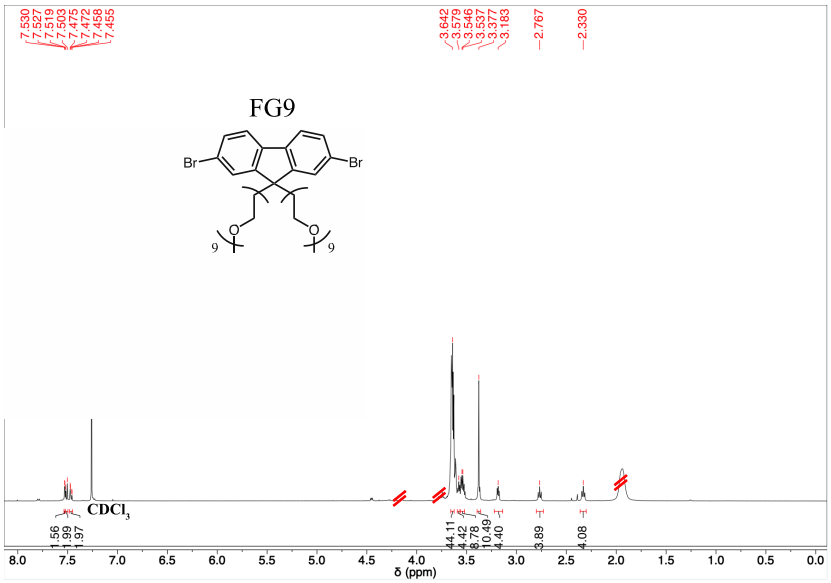

Figure AIII.7: FG9 ^{1}H NMR with trace amount of THF and EtOAc.

decanted from the Na_2SO_4, and combined with the organic layer. The organic layer was concentrated under reduced pressure to provide a semi-crude solid which was purified further via a silica gel column (Ethyl Acetate: MeOH, 90:10). Since the percentage of MeOH in the solvent used to elute the aggregated fraction of FG9 was 10%, FG9 was dissolved in chloroform ($CHCl_3$) to help precipitate out the once dissolved silica gel. The $CHCl_3$ solution was then filtered to remove the precipitate, and concentrated under reduced pressure to obtain FG9 (30.0% yield, 0.710 g).[3] **Figure AIII.7**: FG9 ^{1}H NMR (500 MHz, $CDCl_3$): δ 7.53 (d, 2H), 7.52- 7.50 (d, 2H), 7.47-7.46 (d, 2H), 3.64 (m, 44H), 3.58 (m, 4H), 3.54 (t, 8H), 3.37 (m, 10H), 3.18 (t, 4H), 2.77 (t, 4H), 2.33 (t, 4H) **Figure AIII.8**: FG9 ^{13}C NMR (500 MHz, $CDCl_3$): δ 151.0, 138.6, 130.8, 126.8, 121.7, 121.4, 72.0, 70.7, 70.7, 70.6, 70.6, 70.5, 70.1, 66.9, 60.5, 59.1, 52.0, 39.6.

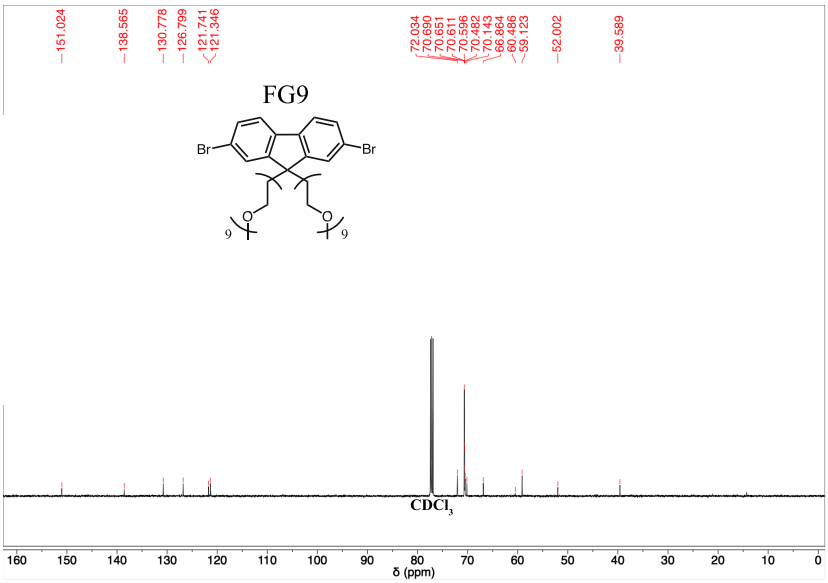

Figure AIII.8: FG9 ^{13}C NMR

Synthesis of Neutral Polymers.

Polymer nPFNG9

Polymerization of poly([9,9-bis(3'-(N,N-dimethyl-amino)-propyl)-fluorene]-alt-co-[9,9-bis-(2-(2-(2-(2-(2-(2-(2-(2-methoxy-ethoxy) ethoxy) ethoxy) ethoxy) ethoxy) ethoxy) ethoxy) ethyl)- fluorene] To a clean and dried 48 mL pressure tube, a Teflon coated stir bar, FG9 (1140 mg, 1.00 mmol), FNB (580 mg, 0.99 mmol), potassium carbonate (K_2CO_3, 1.73 g, 12.5 mmol), 1,4- Dioxane (Dioxane, 10.0 mL, 136.0 mmol), DI H_2O (6.0 mL, 332.4 mmol), and $Pd(dppf)Cl_2$ (10 mg, 0.01 mmol) were added. The reaction solution as well as the head space was flushed with $N_2(g)$. The pressure vial was capped quickly, placed into a silicon oil bath, stirred, and heated

at 100 °C for 24 hours. To stop the reaction, the stirring function was turned off, the bottom water layer was removed, and an aliquot of nPFNG9 dispersed in Dioxane was removed for further characterization. The polymer in Dioxane (1 mL) was pipetted into DI H_2O (10 mL) to induce precipitation of nPFNG9. The water was decanted from the polymer and nPFNG9 was dried via vacuum filtration.[1,6] **Figure AIII.9**: nPFNG9 ^{1}H NMR (800 MHz, $CDCl_3$): δ 7.78- 7.69 (br, 1.00 H), 3.62 (br, 3.72 H), 3.53 (br, 1.51 H), 3.42 (br, 0.35 H), 3.36 (br, 0.64 H), 3.26 (br, 0.43 H), 2.89 (br, 0.30 H), 2.56 (br, 0.32 H), 2.01 (br, 1.56 H), 0.96- 0.88 (br, 0.36 H) **Figure AIII.10**: nPFNG9 ^{13}C NMR (800 MHz, $CDCl_3$): δ 207.1, 140.8, 127.4, 120.5, 72.1, 70.7, 70.2, 67.2, 60.1, 59.2, 45.5, 38.0, 31.1, 29.8, 22.3.

A Note on the Determination of the nPFNG9 Molecular Weight

Determination of the molecular weight for the neutral precursor nPFNG9 proved to be extremely challenging. This is because such long oEG sidechains lead the polymer to be highly amphiphilic and thereby render it insoluble in many common polar and nonpolar organic solvents used in size exclusion chromatography (SEC). We attempted to perform SEC measurements in three ways: in warm THF, DMF, and hot trichlorobenzene. We found nPFNG9 to be insufficiently soluble in all three solvents, rendering measurements unreliable. However, we also synthesized nPFNG6 – the analog of nPFNG9 with nonionic sidechains containing 6 ethyleneglycol units. nPFNG6 was synthesized, purified, and isolated under identical conditions as nPFNG9. We were in fact able to perform SEC measurements for nPFNG6, obtaining a number-

average molecular weight of 39,720 g/mol and a polydispersity of 1.16. We believe that, had it been possible to measure the molecular weight of nPFNG9, a similar value as nPFNG9 would likely be obtained.

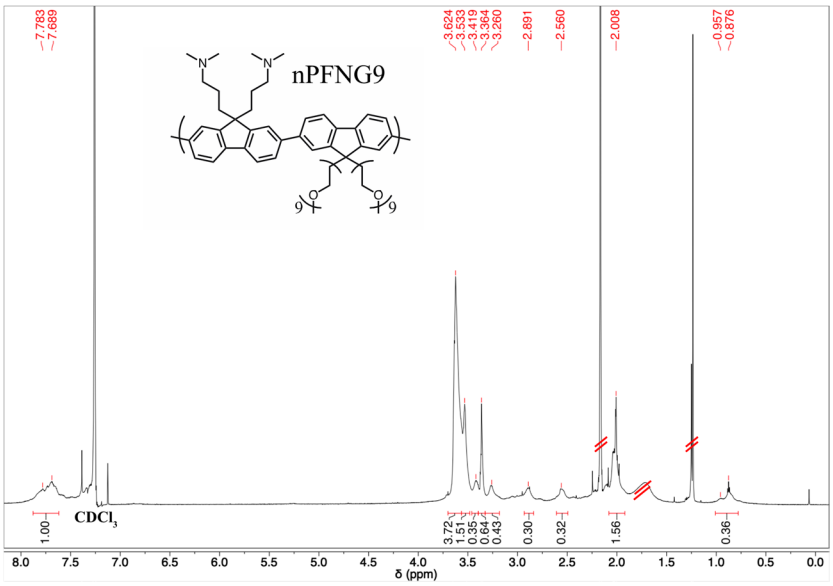

Figure AIII.9: nPFNG9 ^{1}H NMR with trace amount of acetone, water, and

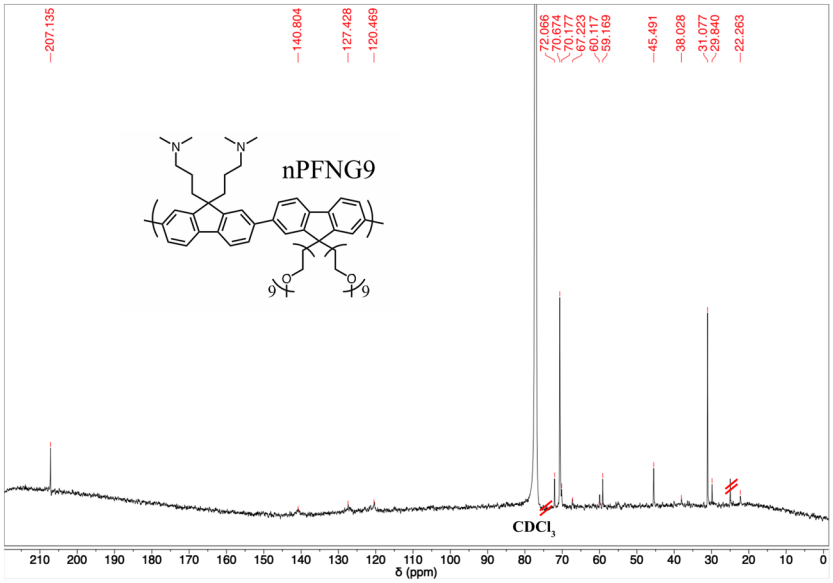

Figure AIII.10: nPFNG9 ^{13}C NMR with trace amounts of pinacol.

Synthesis of Conjugated Polyelectrolytes.

Conjugated Polyelectrolyte PFNG9

Conjugated polyelectrolyte poly([9,9-bis(3'-(N,N,N-trimethyl-ammonium)-propyl)-fluorene]-alt-co-[9,9-bis-(2-(2-(2-(2-(2-(2-(2-(2-methoxy-ethoxy) ethoxy) ethoxy) ethoxy) ethoxy) ethoxy) ethoxy) ethoxy) ethyl)- fluorene] The Dioxane containing nPFNG9 was transferred into a 350 mL pressure vessel. Then quaternization occurred via the addition of methyl iodide (MeI, 1.0 mL, 16.1 mmol) directly to the remaining dioxane layer containing nPFNG9. The cap was threaded onto the pressure vessel, heated to 80 °C for 24 hours, and allowed to cool back down to room temperature before the cap was unscrewed. An aliquot of DI H_2O (200 mL) was added

to help dissolve the precipitated polymer. The cap was threaded back onto the pressure vessel and was reheated to 80 °C for an additional 3 days. After which, the pressure vessel was cooled down to room temperature and uncapped. Once the cap was removed, the reaction contents were reheated to 80 °C to remove unreacted MeI from the reaction and reduced the volume of the reaction to 250 mL. The polymer solution was then dialyzed via a dialysis flask (10,000 MWCO) submerged in a vat of DI H_2O. The DI H_2O was replaced with fresh DI H_2O every day for 5 days. After 5 days, the dialyzed solution of PFNG9 was concentrated under reduced pressure, filtered, transferred into a 50 mL Falcon tube, and lyophilized to yield PFNG9 as a brown solid (320 mg, 24.6% yield).[1,6] **Figure AIII.11**: PFNG9 ^{1}H NMR (800 MHz, D_2O): δ 8.06-7.93 (br, 1.00 H), 3.63 (br, 2.66 H), 3.58 (br, 2.27 H), 3.34 (br, 0.67 H), 3.28 (br, 0.17 H), 3.22 (br, 0.17 H), 2.98 (br, 0.17 H), 2.80 (br, 1.65 H), 2.68 (br, 0.06 H), 2.36 (br, 0.28 H), 1.17 (br, 0.38 H) **Figure AIII.12**: PFNG9 ^{13}C NMR (800 MHz, D_2O): δ 151.2, 140.6, 139.8, 128.4, 127.1, 121.7, 120.8, 71.8, 71.0, 69.6, 67.1, 66.6, 66.3, 60.4, 58.1, 54.3, 52.6, 38.7, 35.2, 30.2, 17.7.

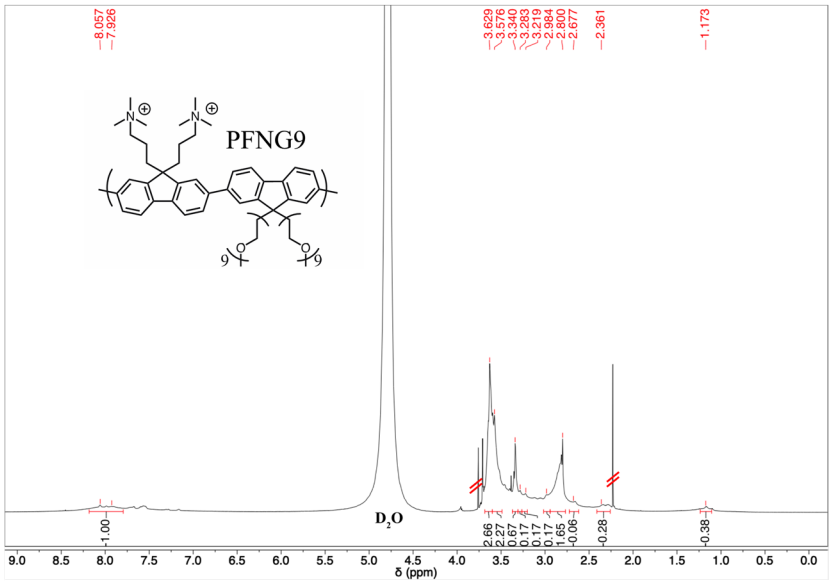

Figure S11: PFNG9 ^{1}H NMR with trace dioxane and acetone.

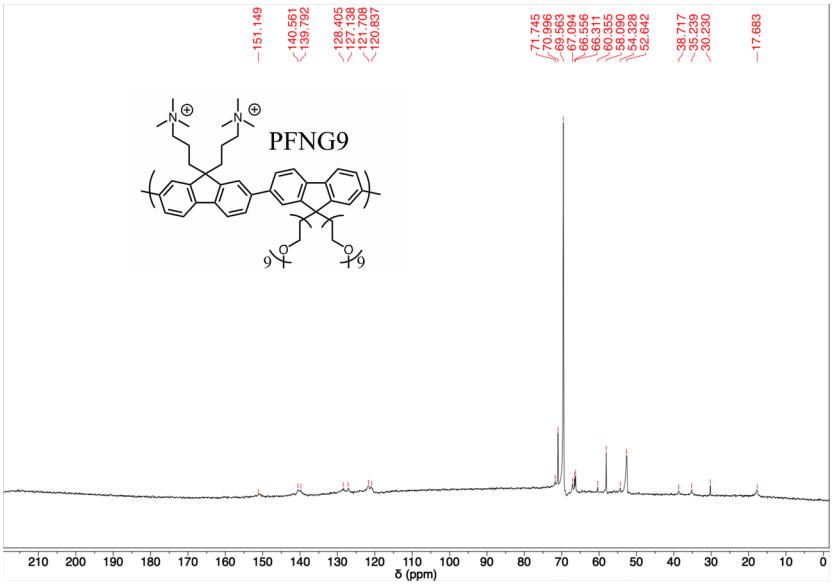

Figure S12: PFNG9 ^{13}C NMR

Sample Preparation

Potassium bromide (KBr, 99.99 % purity) was obtained from Sigma-Aldrich. Tetraethylammonium bromide (> 98.0 % purity) (TEAB) from TCI Chemicals, and calcium bromide ($CaBr_2$, extra pure) from Fisher Scientific. All chemicals were used as received. Stock solutions of 11 mg/mL PFNG9, 5.0 M KBr, 7.0 M LiBr, and 7.0 M TEAB were prepared using degassed (argon) HPLC grade water (Sigma-Aldrich). The PFNG9 stock was stirred at 70 °C for 6 hrs in a light protected vial. The salt stocks were stirred and heated at 70 °C for 15 min to guarantee all salt crystals were fully dissolved.

The PFNG9 concentration was fixed at 4.624 mg/mL for all solutions. Samples containing 5.0 M KBr were made with solid KBr; samples at 0.5 M and 2.5 M KBr were made using degassed KBr stock. The order of addition was as follows: KBr, HPLC water, PFNG9. Samples were stirred at 250 rpm at 70 °C for 6 hrs. Samples were allowed to cool to room temperature before any analysis was performed and care was taken to limit ambient light exposure. All other samples containing TEAB or $CaBr_2$ were made using degassed salt stocks in using the same prep described above.

Microscopy. Images were acquired using a Leica DM5500 B widefield microscope equipped with a Leica DCF360 monochrome camera using ∞/0.17/o, HCX PL FLUORTAR 10x/0.3 and ∞/0.17/o, HCX PL FLUORTAR 40x/0.75 objectives. When needed, a plastic scoopula was used to dislodge the coacervate phase from the

stir bar and sides of the vial. Samples were then mixed to homogenize the dilute and coacervate phases. Samples were excited using the following:

*Blue Channel (A4): excitation at 340-380 nm; emission at 450-490 nm

*Green Channel (GFP): excitation at 450-490 nm; emission at 500-550 nm

The A4 filter was chosen to select for the emission of the dilute phase and a GFP filter was used to select for the emission of the coacervate phase. Samples were also imaged using transmitted light DIC when using a 40x objective.

Five images of samples containing 2.5 M and 5.0 M KBr respectively were analyzed using the ImageJ-based software Fiji. ImageJ was used to identify the circumferences of coacervate droplets and measure their diameters (Figure X).

A Leica SP5 Confocal Microscope was used to collect PL spectra from regions of interest in an image after performing a xyλ scan, in which the excitation wavelength was fixed, and the detected emission wavelength was scanned in 5-nm increments. Images were collected using a 20x/0.75 objective at 16-bit resolution. xyλ scans were taken while exciting with 405, 458, 476, and 496 nm laser lines, and emission was detected out to 750 nm.

Steady-State Photoluminescence Spectroscopy. Steady-state PL was collected using a home-built laser system described previously.[1] Samples were excited in a front-face geometry with 375-nm light from a pulsed picosecond diode laser (BDS-SM Series, Becker & Hickl GmbH), and emission was collected between 400-700 nm using a PIXIS 100 CCD (Princeton Instruments).

Time-Resolved Photoluminescence Spectroscopy. Bulk-solution time-resolved photoluminescence (TRPL) measurements were collected using time-correlated

single photon counting. Details of the home-built laser system and experimental setup have been described previously.[7] Samples were excited at 375 nm using a pulsed picosecond diode laser (BDS-SM Series, Becker & Hickl GmbH) or at 445 nm using a pulsed supercontinuum picosecond laser (Super K EXTREME, NKT Photonics) coupled to an acousto-optic filter and an external RF driver (Super K SELECT, NKT Photonics). The excitation beam was vertically polarized, and emission was collected in a front-face geometry with the emission polarizer set to the magic angle. PL lifetimes were determined using forward convolution with the measured instrument response function taken using a scattering Ludox sample. This was done using least-squares minimization via the DecayFit MATLAB package developed by Soren Preus (Fluorescence Decay Analysis Software 1.3, FluorTools, www.fluortools.com). A sum-of-exponentials model was used for the decay.

Fluorescence lifetime imaging (FLIM) measurements were carried out using a Zeiss LSM 980 NLO confocal microscope (Becker-Hickl TCSPC FLIM). Samples were excited using a 445-nm laser line, and PL was collected using a 590/50 nm filter cube. Images were collected using a 512 x 512 pixel resolution and a 50-s collection time. Fluorescence lifetime averages and distributions were determined using the SPCImage 8.5 NG software via the maximum likelihood estimation method.

Cryo-TEM. A sample droplet of 4 μL at 4.624 mg/mL PFNG9 and 5.0 M KBr was deposited on a C-flat holey carbon-coated TEM support grid (CF-2/2-2C from Electron Microscopy Services-EMS) previously glow-discharged (PELCO easyGLOW) using 15 mA for 30 s. The sample was blotted for 2.5 s using a Vitrobot Mark IV (FEI

Company) at 22 °C and ~100% humidity and sequentially fast-plunged into liquid ethane.

The images were aquired using 1-s exposure on a 4k x 4k CETA CCD Camera coupled to a ThermoFischer Glacios cryo-TEM operating at 200 kV. Images were collected at a nominal 2Å pixel size, 73,000 x magnification, and -3.5 µM defocus. Fiji – ImageJ was used for data analysis.

III.2 Supporting Information

Optical Microscopy.

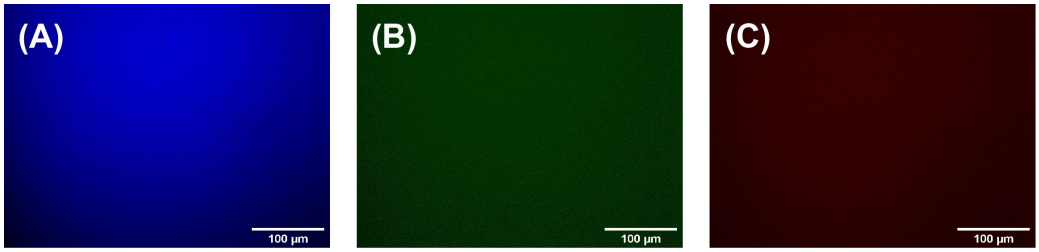

Figure AIII.13: PL microscopy images of 4.624 mg/mL PFNG9 with three different filter settings. (A) Excitation bgetween 340-380 nm and emission between 450-490 nm. (B) Excitation from 450-490 nm and emission between 500-550. (C) Excitation between 540-580 nm and emission between 540-608 nm.

Figure AIII.13 shows PL microscopy images of PFNG9 with no added salt at the fixed polymer concentration (4.624 mg/mL) used throughout this study. Images show fully dissolves solutions and a strong fluorescence signal when using the A4 excitation and emission (Figure AIII.13A) filter. Figure AIII.14 shows the progression from fractal-like particles to the formation of droplets with increasing concentration of KBr. This is accompanied by a change in the photophysics where the particles at 2.5 M fluoresce within both the blue and green channels, but the droplets formed at 5 M show a darkening in the blue channel. Figures AIII.15-AIII.17 show

microscopy images of PFNG9 with varying LiBr, tetraethylammonium bromide (TEAB), and $CaBr_2$. Figures show that PFNG9 remains fully dissolved regardless of

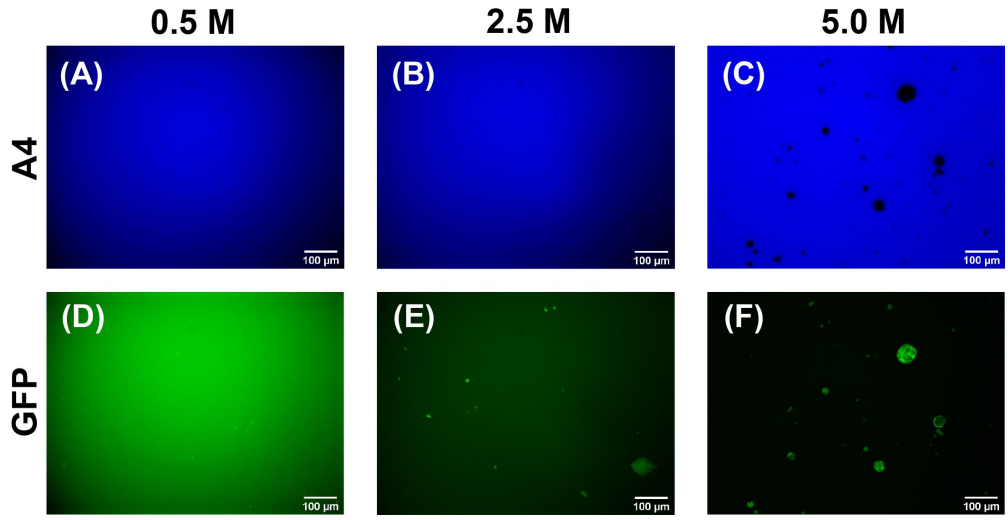

Figure AIII.14: Fluorescence Microscopy images of PNFG9 with (A and D) 0.5 M KBr, (B and E) 2.5 M KBr, and (C and F) 5.0 M KBr using two different filters. Blue channel (A-C): Ex: 340-380 nm, Em:450-490 nm. Green channel (D-F) Ex: 450-490 nm, Em: 500-550 nm.

LiBr or TEAB concentrations where the dark circular area in Figure AIII.16A is simply a trapped air bubble between the microscope slide and coverslip evident by the lack of fluorescence. Figure AIII.17 shows that PFNG9 phase separates into fractal precipitant-like particulates when exposed to $CaBr_2$, with no evidence of droplet formation occurring at the representative concentrations. Additionally, these images represent PL (ex: 450-490 nm, em: 500-550 nm) that is distinctly different from the sample found to undergo coacervation (Figure AIII.14C and AIII.14F).

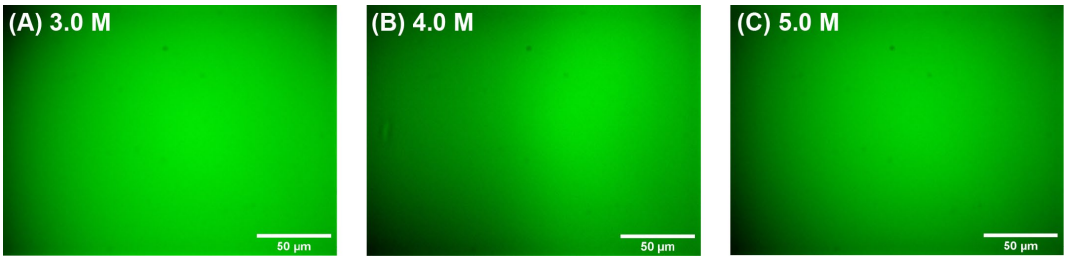

Figure S15: Fluorescence Microscopy images of PNFG9 with (A) 3.0 M LiBr, (B) 4.0 M LiBr, and 5.0 M LiBr (Ex: 450-490 nm, Em: 500-550 nm).

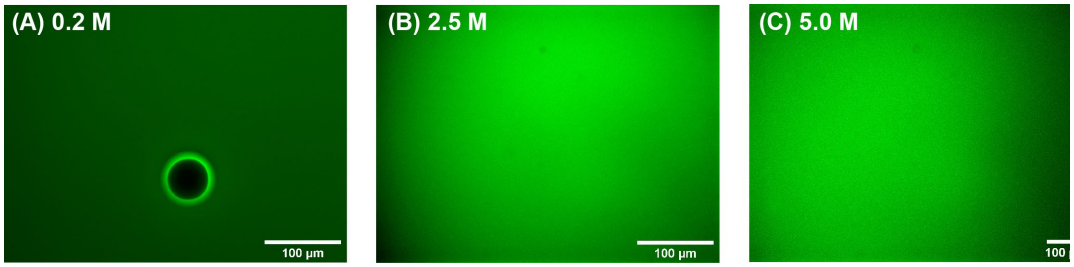

Figure AIII.16: Fluorescence Microscopy images of PNFG9 with (A) 0.2 M TEAB, (B) 2.5 M TEAB, and 5.0 M TEAB (Ex: 450-490 nm, Em: 500-550 nm) where the dark circular structure in panel A is a trapped air bubble.

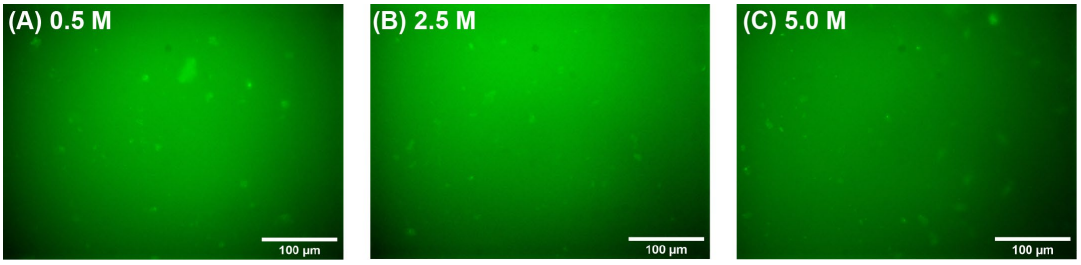

Figure AIII.17: Fluorescence Microscopy images of PNFG9 with (A) 0.5 M $CaBr_2$, (B) 2.5 M $CaBr_2$, and 5.0 M $CaBr_2$ (Ex: 450-490 nm, Em: 500-550 nm).

Figures AIII.18 and AIII.19 show fluorescence recovery of the dilute solution and droplets by comparing original PL intensity, PL intensity after a ~90-s mercury lamp exposure, and PL intensity after a 30 min dark period.

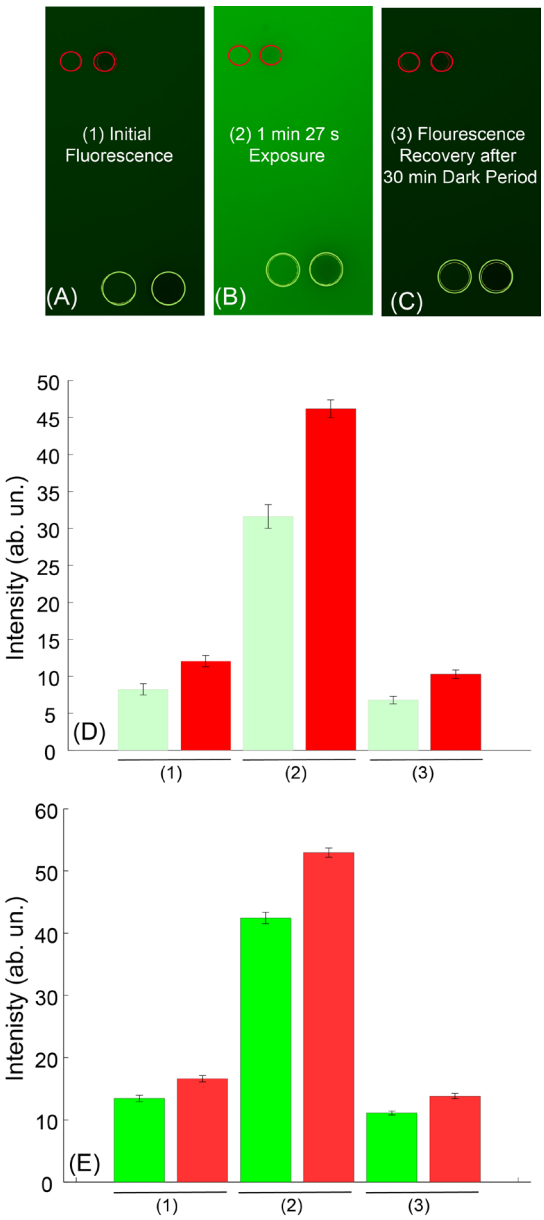

Figure AIII.18: Fluorescence intensity recovery using excitation from 340-380 nm and emission from 450-490 nm.

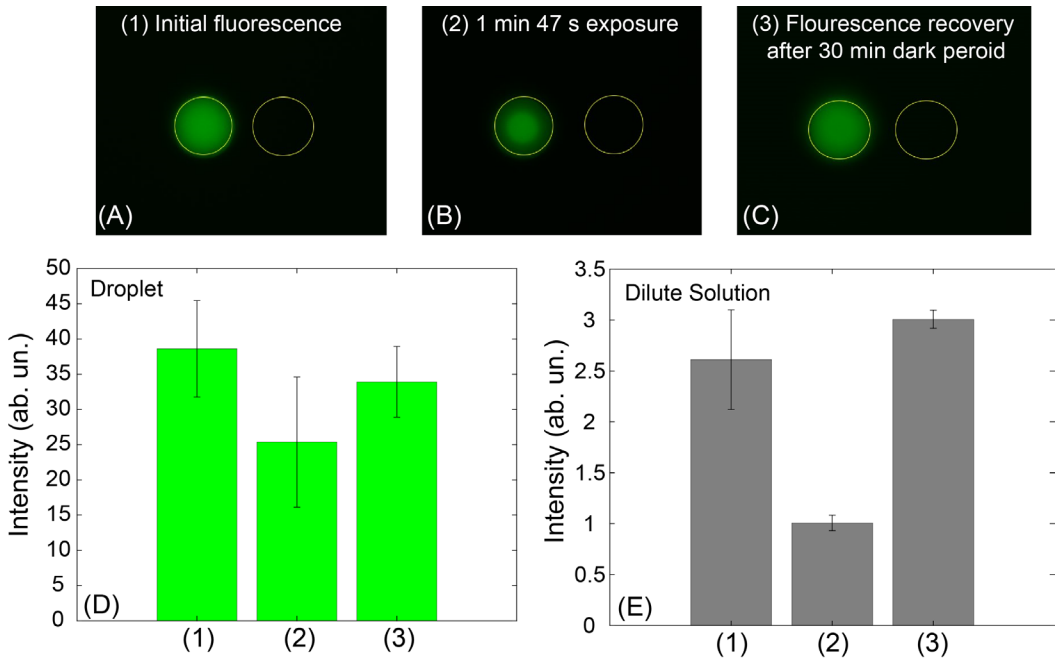

Figure AIII.19: Fluorescence intensity recovery using excitation from 450-490 nm and emission from 500-550.

Steady-State Spectroscopy.

Figure AIII.20 shows steady-state PL spectra of bulk PFNG9 solutions without added salt and with 0.5, 2.5, and 5.0 M KBr. Measurements were taken in triplicate. Dotted lines indicate averaged spectra. Figure AIII.21A shows the averaged spectra plotted together and indicates PFNG9 sampled with KBr are all redshifted relative to the no-salt control. Panel S21B shows the dilute phase and the concentrated coacervate phase PL of the PFNG9 sample with 5.0 M KBr. The dilute phase was separated from the concentrated phase by ultracentrifugation. The concentrated phase was separated from the dilute phase by carefully scraping the viscous build-up from the sides of the glass vials and stir bar with a plastic scoopula and depositing it on a standard glass microscope slide, which was then covered with a coverslip and Kapton taped to minimize evaporation. PL was then taken by exciting

the sample in a front-face geometry at a 45º angle at 375 nm. The concentrated coacervate phase was found to fluoresce more weakly compared to the dilute phase.

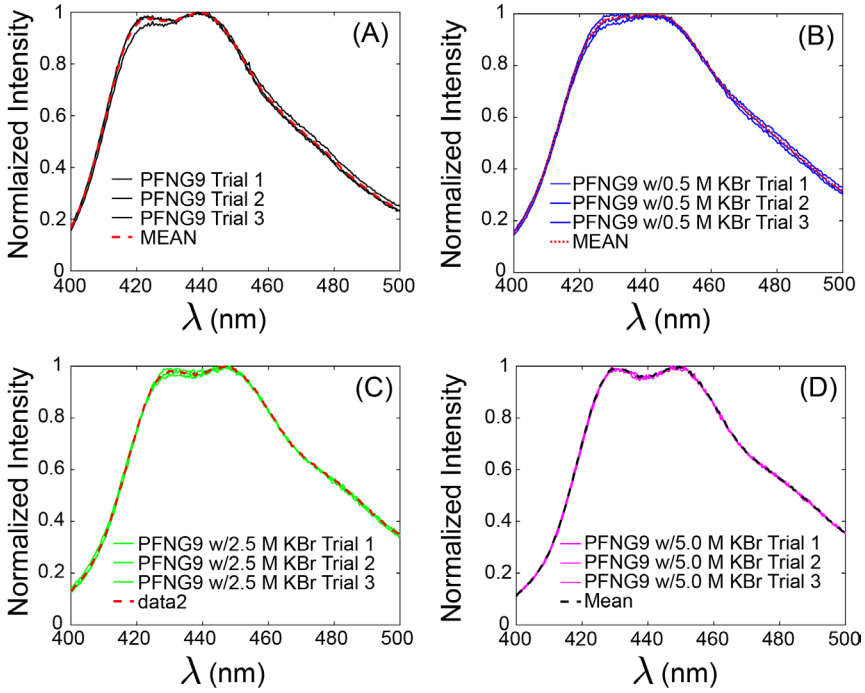

Figure AIII.20: Three trials of steady-state PL of bulk solutions (i.e., dilute and concentrated phases together) are shown along with the averaged spectrum for (A) PFNG9, and PFNG9 with (B) 0.5 M KBr, (C) 2.5 M KBr, and (D) 5.0 M KBr.

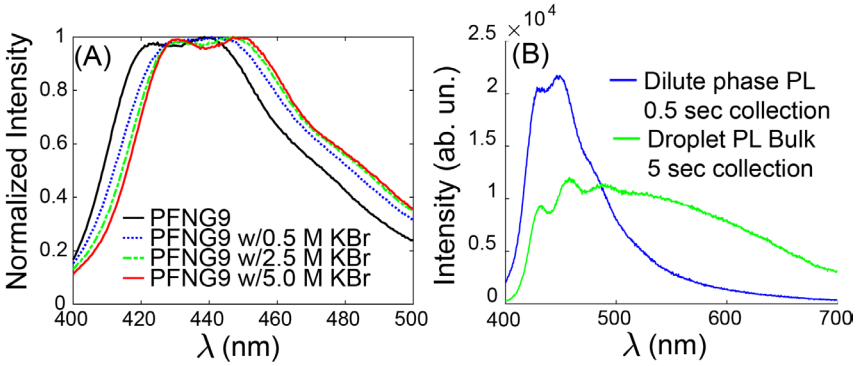

Figure AIII.21: (A) Normalized steady-state PL comparison of bulk solutions of PFNG9 without added salt and with increasing concentration of KBr. (B) PL intensity comparison between the concentrated phase of PFNG9 with 5.0 M KBr and the dilute phase. The collection times refer to how long the detector was allowed to receive emitted light from the sample during the experiment.

Figure AIII.22 shows steady-state PL collected using an xyλ scan on a confocal microscope. PL signal was collected in triplicate and the average spectra are shown as black dotted lines. The averaged spectra are then compared in Figure AIII.22D to highlight differences in PL signatures between the dilute solution and the concentrated phase, and how the droplet PL is dependent on excitation wavelength.

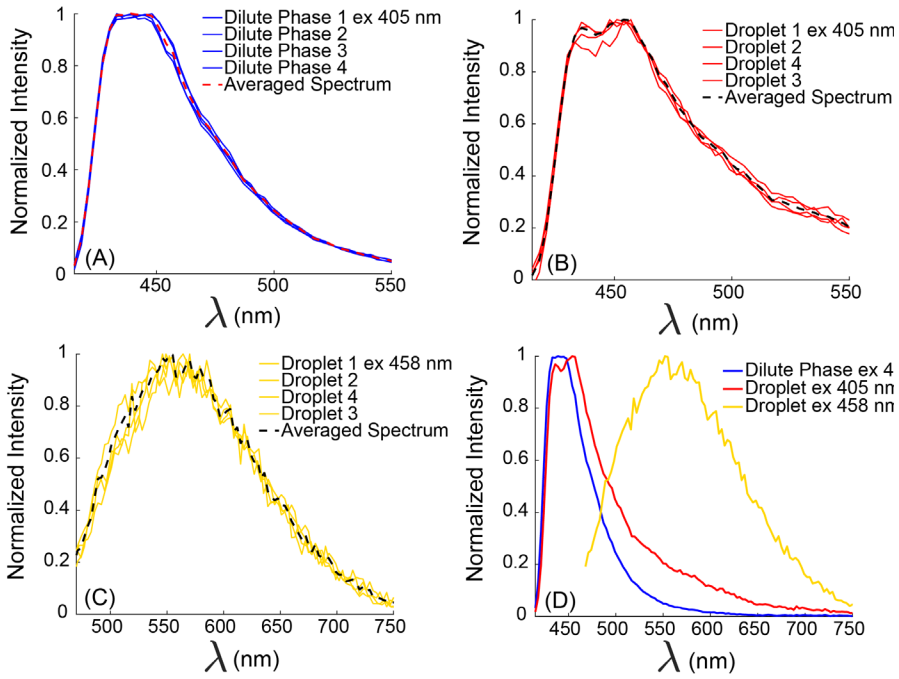

Figure AIII.22: Normalized triplicate PL measurements collected using confocal xyλ scans shown with averaged spectra for (A) the dilute phase excited at 405 nm, (B) droplets excited at 405 nm and (C) 458 nm. (D) shows averaged PL spectra of dilute phase and droplets plotted together.

Cryo-TEM.

Figure AIII.23A shows a cryo-TEM image of a coacervate droplet. The dark regions correspond to fluctuations in local KBr concentration near the onset of crystallization. The latter was confirmed by the presence of weak Bragg reflections at large scattering angles. Figure AIII.23B shows another image in which multiple droplets overlap with one another.

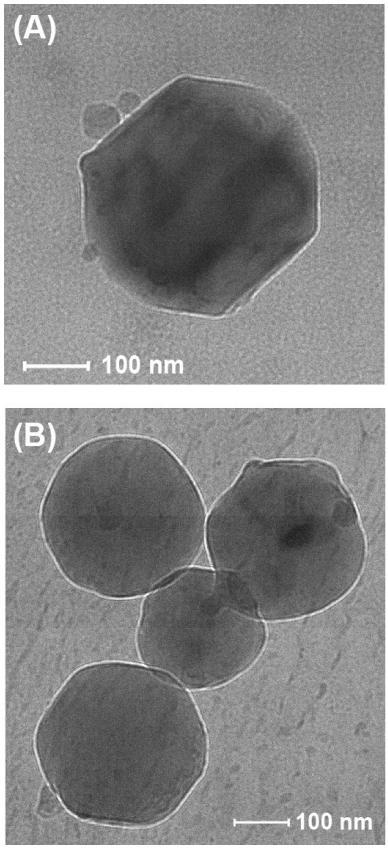

Figure AIII.23: Cryo-TEM image of coacervate droplets exhibiting inhomogeneous contrast regions within the droplet interior (A). (B) shows an image of several overlapping, mesoscale coacervate droplets.

Time-Resolved Photoluminescence Spectroscopy.

Figure AIII.24 shows TRPL decays for bulk solutions of PFNG9 with no added salt and with 0.5, 2.5, and 5.0 M KBr excited at 375 nm; emission was collected at 420 nm. Figure AIII.24A shows a slight increase in PL lifetime with increasing KBr. The short component of each lifetime and the average lifetime for each [salt] are plotted in panel S24B. Figure AIII.25 shows TRPL decays for the separated concentrated phase as described above. Samples were excited at 375 nm, and emission was collected at 420, 460, 500, and 600 nm respectively. A gradual increase in average PL lifetime is seen when collecting at redder emission wavelengths. The largest average lifetime was 1.34 ns.

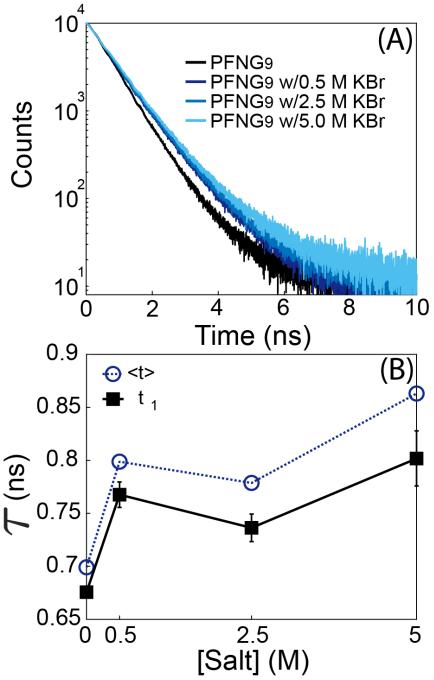

Figure AIII.24: (A)TR-PL decays found for bulk solution of PFNG9 with increasing concentrations of KBr. (B) Shows the faster component of the bi-exponential decay lifetime plotted along with <τ>.

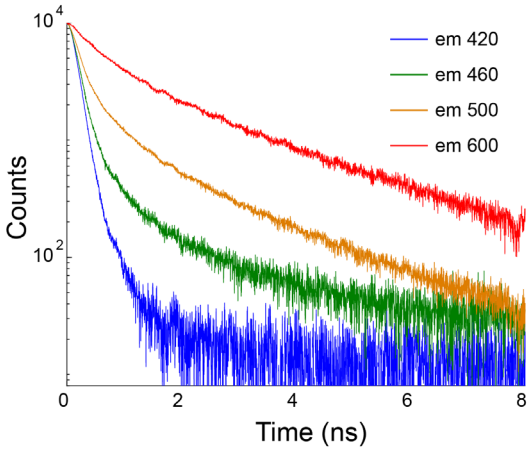

Sample	a_1	τ_1 (ns)	a_2	τ_2 (ns)	$\langle\tau\rangle$ (ns)
PFNG9 w/5.0 M KBr CP Em 420 nm	1	0.12	-	-	0.12
Em 460 nm	0.998	0.36	0.002	3.1	0.41
Em 500 nm	0.980	0.55	0.020	3.1	0.81
Em 600 nm	0.924	0.69	0.076	3.1	1.34

Figure AIII.25: TR-PL decays of the concentrated phase of PFNG9 with 5.0 M KBr where excitation was fixed at 375 nm and the wavelength of emission collected was varied.

Figure AIII.26 shows FLIM images and PL lifetime distributions for 9 droplets excited at 445 nm and emission collected at 590/50 nm.

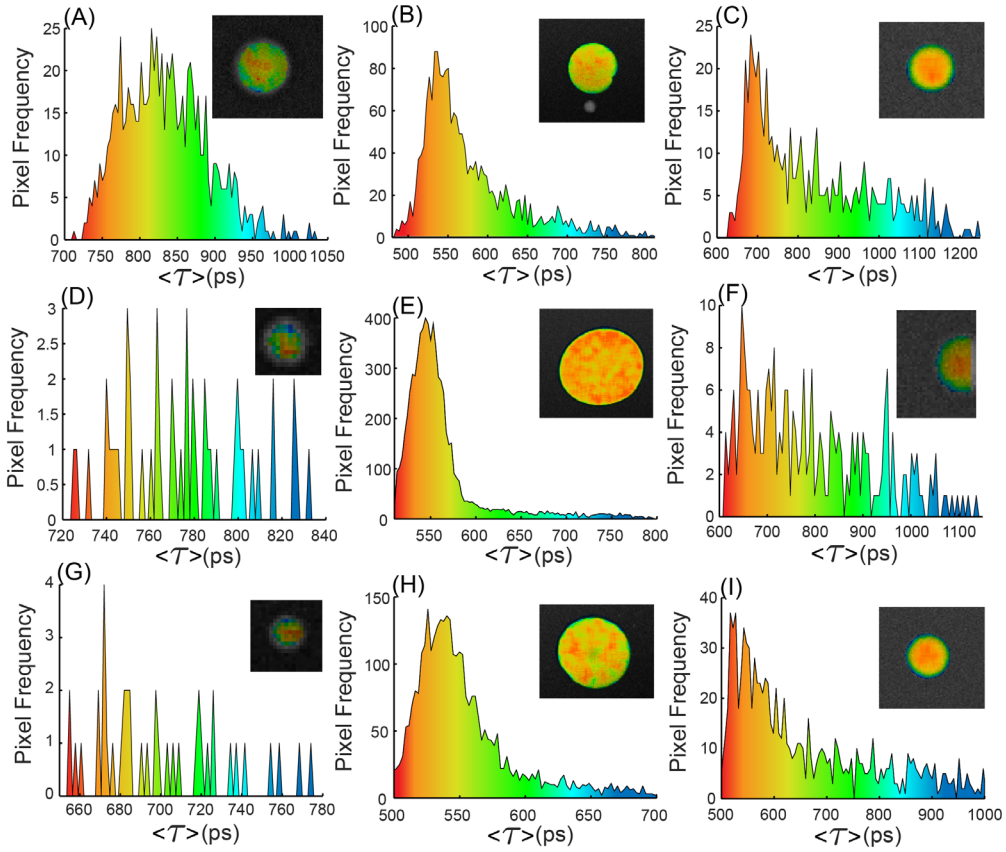

Figure AIII.26: FLIM lifetime distributions from 9 different coacervate droplets where the color coding of the PL lifetime histogram matches the colors displayed in the images. Lifetime heat maps for the corresponding droplets are shown as insets.

References

(1) Pu, K.-Y.; Wang, G.; Liu, B. Design and Synthesis of Conjugated Polyelectrolytes; John Wiley & Sons Inc., 2013.

(2) Heathcote, R.; Howell, J. A. S.; Jennings, N.; Cartlidge, D.; Cobden, L.; Coles, S.; Hursthouse, M. Gold(i)–Isocyanide and Gold(i)–Carbene Complexes as Substrates

for the Laser Decoration of Gold onto Ceramic Surfaces. Dalton T 2007, 0 (13), 1309–1315. https://doi.org/10.1039/b617347k.

(3) Meng, B.; Song, H.; Chen, X.; Xie, Z.; Liu, J.; Wang, L. Replacing Alkyl with Oligo(Ethylene Glycol) as Side Chains of Conjugated Polymers for Close π–π Stacking. Macromolecules 2015, 48 (13), 4357–4363. https://doi.org/10.1021/acs.macromol.5b00702.

(4) Wang, H.; Lu, P.; Wang, B.; Qiu, S.; Liu, M.; Hanif, M.; Cheng, G.; Liu, S.; Ma, Y. A Water-Soluble Π-Conjugated Polymer with up to 100 Mg · ML−1 Solubility. Macromol Rapid Comm 2007, 28 (16), 1645–1650. https://doi.org/10.1002/marc.200700221.

(5) Huang, F.; Wu, H.; Wang, D.; Yang, W.; Cao, Y. Novel Electroluminescent Conjugated Polyelectrolytes Based on Polyfluorene. Chem Mater 2004, 16 (4), 708–716. https://doi.org/10.1021/cm034650o.

(6) Pu, K.; Liu, B. Conjugated Polyelectrolytes as Light-Up Macromolecular Probes for Heparin Sensing. Adv Funct Mater 2009, 19 (2), 277–284. https://doi.org/10.1002/adfm.200800960.

(7) Johnston, A. R.; Perry, S. L.; Ayzner, A. L. Associative Phase Separation of Aqueous π-Conjugated Polyelectrolytes Couples Photophysical and Mechanical Properties. Chem. Mater. **2021**, 33 (4), 1116–1129. https://doi.org/10.1021/acs.chemmater.0c02424.

Chapter 5

Donor/Acceptor Complex Coacervates via Liquid/Liquid Phase Separation of Conjugated Polyelectrolytes

Acknowledgements: This chapter is a working manuscript as of August 22nd, 2022 with plans to be submitted as a communication within the next month with following authorship: Anna Johnston, Gregory Pitch, and Alexander L. Ayzner. Anna Johnston carried out all experimental work and originally crafted the manuscript. Gregory Pitch carried out the synthesis of the CPE series. Alexander Ayzner edited the manuscript and oversaw the project. A big thank you to both Greg and Alex for their help with this last investigation.

This material is based upon work supported by the National Science Foundation under grant no. 1848069 and the ACS Petroleum Research Fund New Directions grant No. 60244-ND7, as well as by the National Science Foundation Graduate Research Fellowship under grant no. DGE-1842400. Part of this work was performed at the UCSC Life Sciences Microscopy Center (RRID:SCR_021135) with the help and guidance of Dr. Benjamin Abrams. Confocal FLIM experiments were conducted at the CRL Molecular Imaging Center, RRID:SCR_017852, supported by NIH S10OD025063. We would like to thank Holly Aaron and Feather Ives for their microscopy advice and support.

Abstract: Liquid complex coacervate phases highly enriched in polyelectrolytes have gained interest in origin of life studies, and more recently in materials applications. Thus far, formation of an electronically active complex coacervate has been challenging. Strong electrostatic interaction of typical polyelectrolyte sidechains coupled with the strong π-electron interactions of conjugated systems have proved to favor the solid state. In this study, we show that a conjugated polyelectrolyte complex (CPEC) containing a copolymer with alternating ionic and oligo(ethyleneglycol)

(oEG) sidechains undergoes liquid/liquid phase separation at high ionic strength to form electronically active, liquid coacervate droplets. We believe this is the first demonstration of the formation of a liquid semiconducting complex coacervate phase containing an excited state energy donor/acceptor pair. We find that semiconducting complex coacervate is intrinsically excitonically coupled, and that electronic energy transfer occurs from donor to acceptor within the dense coacervate droplets. We observe that the K^+ – ethylene glycol interaction is key to the formation of this phase. We believe that our results have intriguing implications for optoelectronic applications and are of fundamental significance to furthering understanding of soft-matter.

5.1 Introduction

The process of liquid/liquid phase separation (LLPS) has been the subject of research across multiple domains of inquiry from the biological to the materials-centric.[1–7] Commonly, this process involves an aqueous macromolecular solution spontaneously phase-separating into a dilute solution and a viscoelastic liquid phase that is highly enriched in macromolecules. Specifically, oppositely charged polyelectrolytes often complex and undergo associative LLPS to form such concentrated viscoelastic liquid states called complex coacervates.[3,8–11] It is this highly polyelectrolyte-enriched complex coacervate phase that is the primary focus of fundamental interest in biophysics and polymer physical chemistry as well as in applications for soft materials.

Formation of complex coacervates based on electronically inactive, non-conjugated polyelectrolytes has been studied extensively. In contrast, much less is known about such systems when the backbone of the polyelectrolyte is conjugated. Formation of a fully conjugated complex coacervate is of particular interest. The highly crowded coacervate environment with substantially delocalized π-electrons would support long-range motion of both electronic excited states and electronic charge (electrons or holes). At the same time, the liquid nature of this state would allow for molecular diffusion and a local concentration of reactants. These properties are attractive from the perspectives of developing environmentally benign light-harvesting and electronic soft materials.

We have previously shown that even when only one of the two oppositely charged polyelectrolytes is conjugated, the combined system strongly favors the solid or the colloidal gel state upon aqueous phase separation.[2] No liquid coacervates were observed in the presence of either LiBr, KBr or CsBr across a large range of salt concentrations. Danielson, *et al.* observed associative phase separation using one conjugated and one non-conjugated polyelectrolyte in water/tetrahydrofuran mixtures and no added salts.[12] However, little evidence was presented for the formation of a viscoelastic **liquid** state.

We have recently shown that when two oppositely charged conjugated polyelectrolytes (CPEs) are complexed together at a 1:1 polycation/polyanion charge ratio, the concentrated phase that forms upon aqueous phase separation is a complex fluid.[2] The mechanical response of the complex fluid was dominated by the storage

modulus, showing that the concentrated phase was **not** a viscoelastic liquid. This remained true in the absence of excess salt and with substantial amounts of atomic and molecular ions. In the presence of a chemical series of molecular ions and in the limit of large ionic strength (~2.0 M excess salt), the system transitioned into the one-phase region as the complex fluid dissolved away. No liquid coacervate phase transition was observed between the solid-like complex fluid phase and the fully dissolved liquid at high salt.

We hypothesized that the reason for the difficulty of stabilizing a CPE coacervate state was primarily due to the strong propensity for extended inter-chain interactions via π-stacking, which strongly favor the solid and solid-like (complex-fluid and colloidal-gel) phases. When two CPEs are complexed near their ionic charge equivalence, the loss of net polyelectrolyte charge coupled with extensive π-stacking leads to the formation of amorphous solid domains. We reasoned that one strategy to stabilize the fully-conjugated complex coacervate state could be to modify the sidechain character of one CPE by the addition of highly polar but nonionic sidechains. We hypothesized that the enhanced dipolar interactions with solvent molecules and small ions, and the potentially additional steric hindrance, could compete with the propensity to form extended π-stacked regions.

5.2 Results and Discussion

To test our hypothesis, we synthesized a series of novel polyfluorene-based CPEs copolymers bearing charged alkylammonium sidechains on one monomer and oligo(ethyleneglycol) (oEG) sidechains with a variable number of repeat units on the other. Herein we refer to the polymers as PFNGX, where X is the length of the oEG sidechain in ethyleneglycol units per sidechain: X = 6, 9, 12 in this work, as shown in Figure 5.1. We then complexed these cationic CPEs with a common anionic CPE based on a poly(cyclopentadithiophene-*alt*-phenylene) backbone (NaPCPT). The spectral overlap between the photoluminescence (PL) spectra of the PFNGX series and the optical absorption spectrum of NaPCPT shows that the PFNGX's serve as excited-state (exciton) donors with respect to NaPCPT, which correspondingly acts as an exciton acceptor (Figure 5.1 bottom left). We find that in the presence of KBr in the high-ionic-strength limit, the PFNGX:NaPCPT solution undergoes associative LLPS to form a complex coacervate phase for all X interrogated in this work.

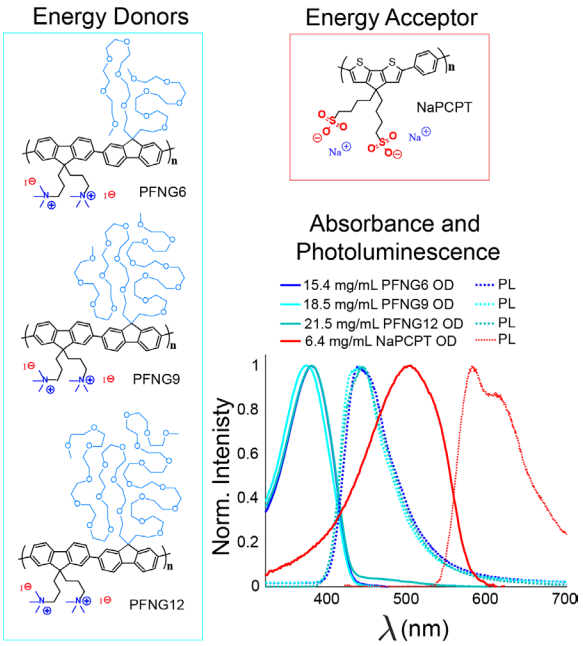

Figure 5.1: Left shows chemical structures of the energy donor CPEs PFNG6, PFNG9, and PFNG12 collectively referred to as PFNGX. Top right shows the chemical structure of the energy acceptor CPE, NaPCPT. Bottom right shows absorbance (OD) and photoluminescence (PL) of all CPEs.

We observed LLPS when [KBr] was of order 2.5 M. The number density of coacervate droplets increased substantially as [KBr] reached 5.0 M; for this reason, we focused this investigation on this salt concentration. Figure 5.2A-5.2C shows widefield microscopy images of PFNG9:NaPCPT at 5.0 M KBr using different excitation and emission wavelength bands. We found that, not only was high ionic strength necessary to observe complex coacervate formation (Figure AIV.3), but that LLPS was specific to the presence of the K^+ cation (Figure AIV.4 and AIV.5). This is consistent with our recent work on the **simple** coacervation of PFNG9 discussed in Chapter 4.

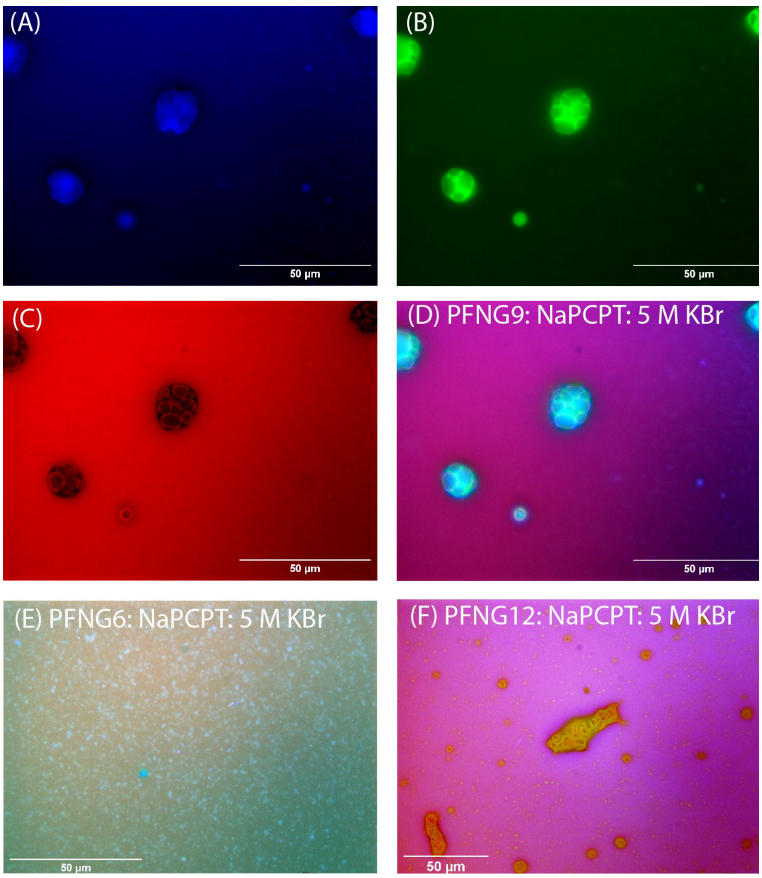

Figure 5.2: Fluorescence microscopy images of PFNG9:NaPCPT with 5 M KBr using (A) 360 ± 20 nm excitation and 470 ± 20 nm emission, (B) 470 ± 20 nm excitation and 525 ± 25 nm emission, and (C) 560 ± 30 nm excitation and 625 ± 37 nm emission. (D) shows and overlay of all fluorescence images for the PFNG9:NaPCPT complex, (E) shows an overlay for the PFNG6:NaPCPT complex, and (F) shows an overlay for the PFNG12:NaPCPT complex.

Panels 1D-F show overlayed images from all three filters for the entire PFNGX:NaPCPT series at 5.0 M KBr. We find significant differences in complex coacervate droplet size distribution and diffusion coefficient as a function of X. Diameters of droplets formed from the PFNG6:NaPCPT solution with 5.0 M KBr were found to approach the sub-micron resolution limit of the widefield microscope and were only resolvable at the highest magnification (i.e. 63x/0.6-1.4 oil objective, Figure AIV.1). These droplets were also found to have relatively low viscosity and to be highly mobile which presented difficulties during confocal imaging. Diameters of droplets and the apparent droplet viscosity of the PFNG9 and PFNG12:NaPCPT:5 M KBr complex coacervates were found to be significantly larger than with PFNG6 and comparable to one another (Figure 5.2 and AIV.5). Thus, to keep the initial investigation tractable, we focused this inquiry on the PFNG9:NaPCPT complex coacervates, with specific comparisons to the PFNG12:NaPCPT droplets where appropriate.

The PFNG9:NaPCPT and PFNG12:NaPCPT images show that that the coacervate droplets are multicompartmental, with possible dilute phase trapped between concentrated-phase regions. Although images for all excitation/emission bands for all exciton donor CPEs are shown in the Supporting Information, in Figure 5.2 we focus our attention on the individual filter settings for PFNG9. The excitation/emission settings in Figure 5.2B predominantly display PL due to PFNG9, whereas the filter characteristics used to capture the PL image in Figure 5.2C are NaPCPT-centric. It is intriguing that the droplets show regions where PFNG9 or NaPCPT PL signal is separately enhanced, suggesting an inhomogeneous spatial

distribution of the cationic and anionic CPEs within the multicompartmental droplets. For example, comparing Figure 5.2B with 5.2C shows that quasi-circular regions in the larger overarching droplets contain a shell of enhanced NaPCPT PL, whereas the connecting regions between the droplet sub-domains display enhanced PFNG9 light emission.

The structure of the compartments within the complex coacervate droplets of the PFNG9:NaPCPT samples with 5.0 M KBr are also highlighted in Figure 5.3 by images of a large droplet at three different focal planes along the lab-frame z-axis. Further evidence for the coacervate liquid state is shown by the coalescence of small droplets and Ostwald ripening of smaller droplets into larger droplets displayed in Figure 5.3D-I. These observations

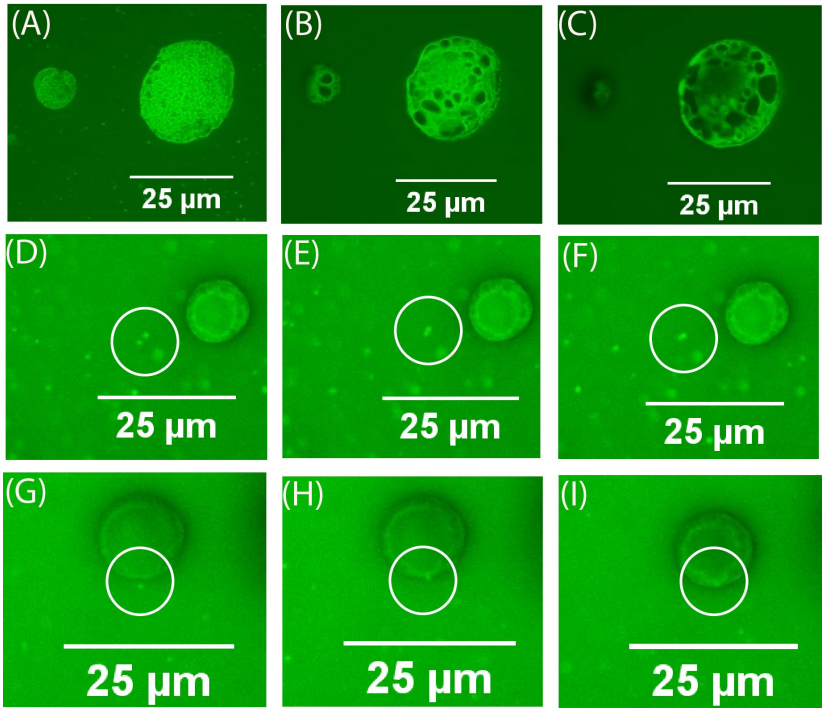

Figure 5.3: Fluorescence microscopy images of PFNG9:NaPCPT with 5.0 M KBr using 360 ± 20 nm excitation and 470 ± 20 nm emission. Panels A-C show images from three different focal planes of a Z-stack to highlight the multicompartmental structuring of the complex coacervate droplets. Panels D-F show coalescence of two small droplets. Panels G- I show Ostwald Ripening of a small droplet into a larger droplet structure.

stand in stark contrast to the microscopy of the donor/acceptor CPE complex fluid phases that we recently reported.[13]

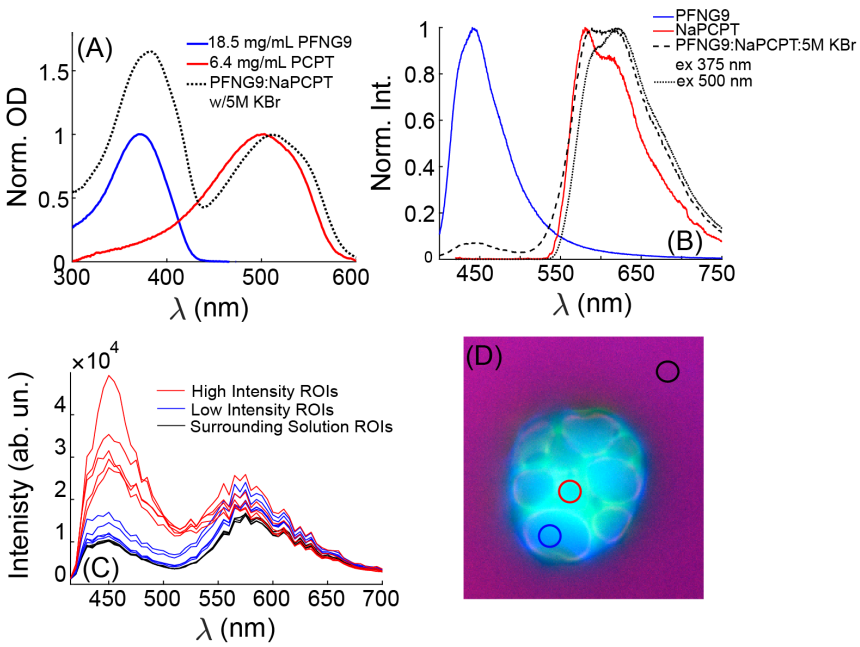

Figure 5.4: Steady state absorbance (A) and fluorescence (B) of PFNG9 and NaPCPT in isolation (blue and red curves) and complexed in a 5M KBr solution (dotted black curve). Normalization in panel A shows a spectral shift of the CPEC to lower energies. Panel B shows dramatic quenching of PFNG9, and a vibronic ratio shift for NaPCPT. (C) Differences in steady state PL spectra intensities from the highlighted ROI in panel D are shown.

To better understand the composition of the CPEC solution and the complex coacervate droplets, we used a combination of steady-state spectroscopy and confocal scanning PL microscopy. Due to the unique absorption and emission spectra of the exciton donor and acceptor CPEs, we are able probe the two polymers within the CPECs separately. Figure 5.4A shows the steady-state absorption spectra of bulk complex solutions at 5.0 M KBr, which shows distinct absorption bands for the PFNG9 and NaPCPT. Interestingly, the NaPCPT absorption spectrum is redshifted compared to NaPCPT in isolation, likely indicating a relative extension of NaPCPT chains upon complexation. Figure 5.4B shows that when preferentially exciting PFNG9 at 375 nm, the PL of this donor CPE (λ_{max} ~450

nm) is highly quenched compared to isolated PFNG9, and that the PL from the acceptor NaPCPT (λ_{max} ~600 nm) is pronounced. This was the case for the entire PFNGX:NaPCPT series at 5.0 M KBr (Figure AIV.9) and is evidence of energy transfer from PFNGX to NaPCPT occurring in bulk solution. This implies that, even when electrostatic interactions are strongly screened, the donor and acceptor CPEs are located within a Förster radius of each other.

When preferentially exciting the donor PFNG9 during the collection of widefield microscopy images, the coacervate droplets appear dark compared to the surrounding solution. However, we find that the droplets do indeed still fluoresce when exciting PFNG9 directly (Figure AIV.7). This indicates that the energy donor CPE exists in both the coacervate droplets and the supernatant phase. Additionally, fluorescence from the two longer wavelength fluorescence filters. (i.e., 470 ± 20 nm excitation and 525 ± 25 nm emission (green channel), and 560 ± 30 nm excitation and 625 ± 37 nm emission (red channel)) indicates that the acceptor CPE is also present in both phases (Figure 5.2B, 5.2C, AIV.5, and AIV.6). This, along with the absorption and emission spectra shown in Figure 5.4A and 5.4B, imply that a CPEC has formed instead of the two CPEs partitioning into separate phases. When exciting at 360 ± 20 nm and collecting emission at 470 ± 20 nm, the PL intensity from the droplets is found to increase with exposure time (Figure AIV.8). We believe this is due to the increase in thermal energy, which reduces the viscosity of the coacervate droplets. This likely allows donor and acceptor chains to separate from one another and result in a partial dissociation of the complex. Thus, PL of the donor that was originally quenched by a nearby acceptor CPE chain in these areas could then partially recover.

These observations suggest that, at such large ionic strengths, the oppositely charged CPEs are relatively weakly bound.

To gain a deeper understanding of the composition of the supernatant and complex coacervate phases, and the regions of high PL intensity, we used confocal laser scanning microscopy. Figure 5.4C shows PL from different regions of interest (ROI) of a confocal image where PFNG9:NaPCPT with 5.0 M KBr samples were excited with 405 nm light. We found the ROI with larger PL intensity corresponded with greater emission from PFNG9 (i.e. ~400-525nm). This further supports the idea of excess thermal energy leading to a partial unwinding of the complex. The low PL intensity ROI showed emission close to that of the surrounding solution, suggesting the darker regions correspond to trapped dilute phase within the coacervate droplets. A PL comparison between PFNG9:NaPCPT:5M KBr and PFNG12:NaPCPT:5M KBr PL in ROI with no intensity changes is shown in Figure 5.5. Panels A and B show droplet ROI where the dotted black line shows the averaged spectrum over many ROI. We observed an on average larger PL intensity from the exciton acceptor NaPCPT when exciting at 405 nm. This is indicating partial quenching of PFNG9 and 12 within the complex coacervate droplet. Panel B shows varying PL intensity of

PFNG12 across different ROI. This suggest the longer oEG chains may lead to more loosely associated CPECs through increased

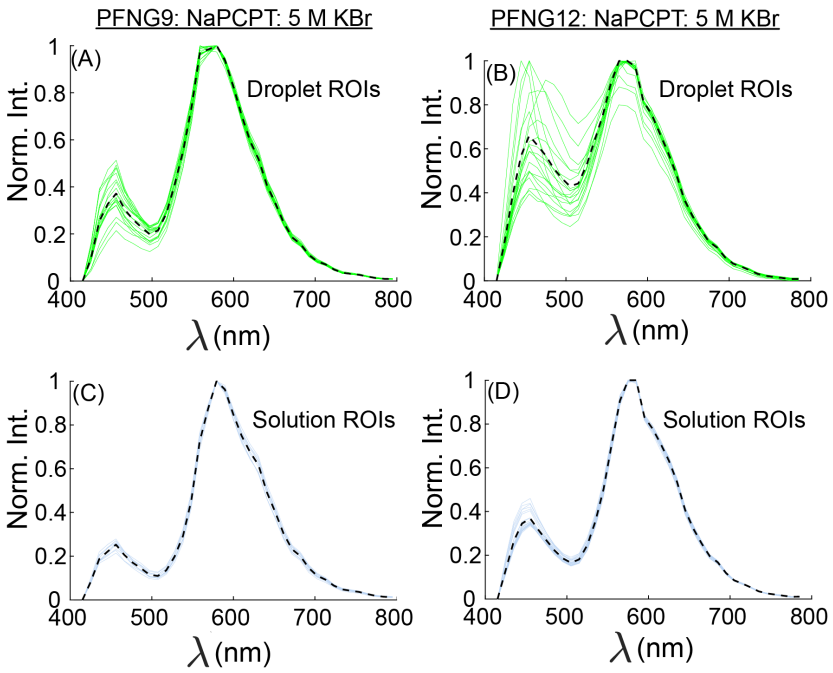

Figure 5.5: Steady-state PL of droplets (A and B) and surrounding solution (C and D) exciting at 405 nm. Panels A and C show PL from 20 ROIs of a PFNG9:NaPCPT:5M KBr solution. Panels B and C show PL from 20 ROIs of a PFNG12:NaPCPT:5M KBr solution. Dotted black lines represent averaged spectra.

steric hindrance, and increased emission from PFNG12 chains not undergoing exciton transfer to the acceptor CPE. PL from ROI associated with the surrounding solution (Figure 5.5C and 5.5D) were found to closely resemble that of the bulk solution measurements (Figure AIV.9) further confirming exciton transfer occurring in this phase and the CPEs existing in a dissolved state as a closely associated pair.

An understanding of PL lifetime is of fundamental importance to the application of new material for optoelectronic applications. To gain an understanding of PL lifetimes of the supernatant and complex coacervate phases formed in this study we used a combination Time-Resolved Photoluminescence Spectroscopy (TRPL) for bulk samples, and Fluorescence Lifetime Imaging (FLIM) techniques to

zoom in on individual droplets. Figure 5.6A shows the lifetime distribution found for PFNG9:NaPCPT:5M KBr droplets was ~560 ps. The center of the droplet was found to differ slightly from the edge of the droplet, and the lifetime of the droplet overall was found to be ~200 ps longer than that of the bulk solution (Figure 5.6B). A slight increase in PL lifetime was found for the PFNG12:NaPPCT:5M KBr sample (~620 ps, Figure AIV.12). In both cases, this was an increase in PL lifetime compared to the isolated donor CPE lifetime of 500 ps (Figure AIV.12A).

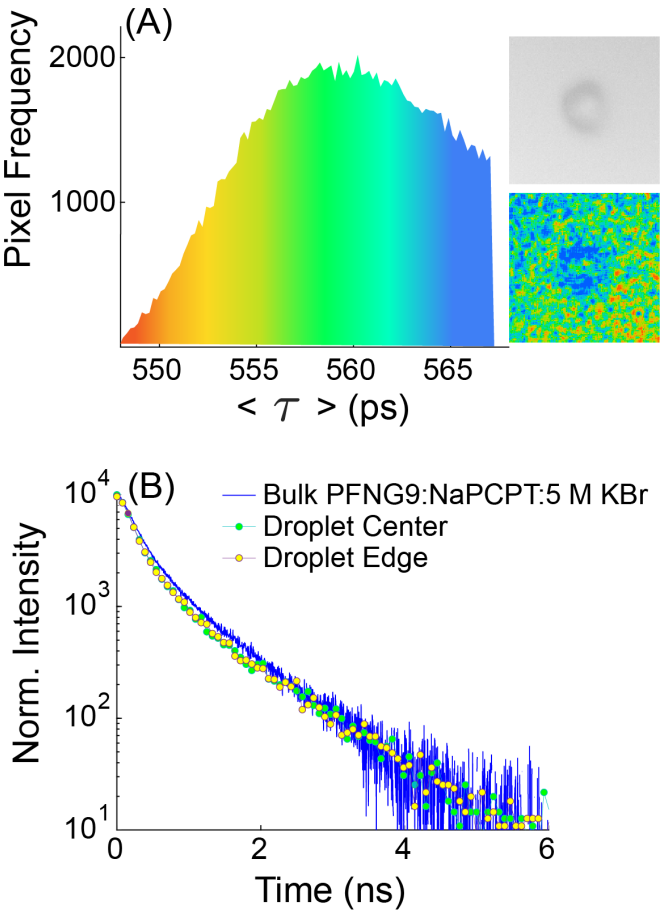

Figure 5.6: Time-resolved PL of a PFNG9:NaPCPT:5 M KBr solution is shown were (A) is the fluorescence lifetime distribution found using FLIM with the colors corresponding to the colored image on the right of the distribution. The grey-scale image shows the ROI contains a coacervate droplet. (B) TRPL decays of bulk PFNG9:NaPCPT:5 M KBr solution (τ_1= 350 ps, τ_2= 1.05 ns, <τ>= 360 ps) compared to the decays found for the droplet center (τ_1= 260 ps, τ_2= 1.01 ns, <τ>= 550 ps), the droplet edge (τ_1= 270 ps, τ_2= 1.06 ns, <τ>= 565 ps).

5.3 Conclusion

In summary, we have demonstrated the rational design of a CPE chemical structure can be utitlized to form liquid semiconducting complex coacervate droplets. As shown in Chapter 4 and here, we find the interaction between ethyleneglycol units and K^+ ions is critical in forming the coacervate phase. We find excited state energy transfer between the donor and acceptor CPEs occurs in the highly electronically coupled complex coacervate droplet phase. Addiotionally, we find that the number of ethyleneglycol units has only subtle influence on the complex coacervate photophysics. We believe this is of fundamental significance for light harvesting applications. The strong coupling between and electronic and ionic degrees of freedom can in principle be used to manipulate exciton migration within this semiconducting phase. These characteristics are likely desirable for optoelectronic applications in general or for catalysis.

5.4 References

(1) Keating, C. D. Aqueous Phase Separation as a Possible Route to Compartmentalization of Biological Molecules. *Acc. Chem. Res.* **2012**, *45* (12), 2114–2124. https://doi.org/10.1021/ar200294y.

(2) Johnston, A. R.; Perry, S. L.; Ayzner, A. L. Associative Phase Separation of Aqueous π-Conjugated Polyelectrolytes Couples Photophysical and Mechanical Properties. *Chem. Mater.* **2021**, *33* (4), 1116–1129. https://doi.org/10.1021/acs.chemmater.0c02424.

(3) Mountain, G. A.; Keating, C. D. Formation of Multiphase Complex

Coacervates and Partitioning of Biomolecules within Them. *Biomacromolecules* **2020**, *21* (2), 630–640. https://doi.org/10.1021/acs.biomac.9b01354.

(4) Drobot, B.; Iglesias-Artola, J. M.; Le Vay, K.; Mayr, V.; Kar, M.; Kreysing, M.; Mutschler, H.; Tang, T. Y. D. Compartmentalised RNA Catalysis in Membrane-Free Coacervate Protocells. *Nat. Commun.* **2018**, *9* (1), 3643. https://doi.org/10.1038/s41467-018-06072-w.

(5) Lu, T.; Spruijt, E. Multiphase Complex Coacervate Droplets. *J. Am. Chem. Soc.* **2020**, *142* (6), 2905–2914. https://doi.org/10.1021/jacs.9b11468.

(6) Chen, Y.; Yuan, M.; Zhang, Y.; Liu, S.; Yang, X.; Wang, K.; Liu, J. Construction of Coacervate-in-Coacervate Multi-Compartment Protocells for Spatial Organization of Enzymatic Reactions. *Chem. Sci.* **2020**, *11* (32), 8617–8625. https://doi.org/10.1039/d0sc03849k.

(7) Danielsen, S. P. O.; Nguyen, T.-Q.; Fredrickson, G. H.; Segalman, R. A. Complexation of a Conjugated Polyelectrolyte and Impact on Optoelectronic Properties. *ACS Macro Lett.* **2019**, *8* (1), 88–94. https://doi.org/10.1021/acsmacrolett.8b00924.

(8) Liu, Y.; Winter, H. H.; Perry, S. L. Linear Viscoelasticity of Complex Coacervates. *Adv. Colloid Interface Sci.* **2017**, *239*, 46–60. https://doi.org/10.1016/j.cis.2016.08.010.

(9) Li, L.; Srivastava, S.; Andreev, M.; Marciel, A. B.; De Pablo, J. J.; Tirrell, M.

V. Phase Behavior and Salt Partitioning in Polyelectrolyte Complex Coacervates. *Macromolecules* **2018**, *51* (8), 2988–2995. https://doi.org/10.1021/acs.macromol.8b00238.

(10) Keating, C. D.; Martin, N.; Santore, M. M. Editorial Overview: Coacervates and Membraneless Organelles. *Curr. Opin. Colloid Interface Sci.* **2021**, *56*, 101527. https://doi.org/10.1016/j.cocis.2021.101527.

(11) Johnson, N. R.; Wang, Y. Coacervate Delivery Systems for Proteins and Small Molecule Drugs. *Expert Opin. Drug Deliv.* **2014**, *11* (12), 1829–1832. https://doi.org/10.1517/17425247.2014.941355.

(12) Danielsen, S. P. O.; Nguyen, T.-Q.; Fredrickson, G. H.; Segalman, R. A. Complexation of a Conjugated Polyelectrolyte and Impact on Optoelectronic Properties. *ACS Macro Lett.* **2019**, 88–94. https://doi.org/10.1021/acsmacrolett.8b00924.

(13) Johnston, A. R.; Minckler, E. D.; Shockley, M. C. J.; Matsushima, L. N.; Perry, S. L.; Ayzner, A. Conjugated Polyeelctrolyte-Based Complex Fluids as Aqueous Exciton Transport Networks. *Angew. Chemie - Int. Ed.* **2022**, *134* (20), 1–12. https://doi.org/10.1002/anie.202117759.

Appendix IV

Supporting Information for

Donor/Acceptor Complex Coacervates via Liquid/Liquid Phase Separation of Conjugated Polyelectrolytes

IV.1. Experimental

Sample Preparation. Potassium bromide (KBr, 99.99 % purity) was obtained from Sigma-Aldrich. Tetraethylammonium bromide (> 98.0 % purity) (TEAB) from TCI Chemicals, and lithium bromide ($LiBr_2$, > 99.0 % purity) was obtained from Tokyo Chemical Industries (TCI). Poly(cyclopentadithiophene-alt-phenylene) derivative (NaPCPT) (MW=40,000 Da, PDI= 3), was obtained from 1-Material. All chemicals were used as received. Stock solutions of 100 mg/mL PFNG6/9/12 and 20mg/ml NaPCPT were prepared using degassed (argon) HPLC grade water (Sigma-Aldrich). All stocks were stirred at 70 °C for 2 hrs in a light protected vial.

The PFNG6 concentration was fixed at 15.5 mg/mL, PFNG9 was fixed at 18.5 mg/mL, PFNG12 was fixed at 21.5 mg/mL, and the NaPCPT concentration was fixed at 6.4 mg/mL. All salt containing samples were made by dissolving the appropriate amount of salt into solution, stirring at 350 rpm and heating at 70 °C for 7 hrs. Samples were allowed to cool to room temperature before any analysis was performed and care was taken to limit ambient light exposure. HPLC water used in sample prep was degassed before use with argon for a minimum of 20 minutes. Vial headspace was also degassed for a minimum of 5 minutes.

Microscopy. Images were acquired using a Leica DM5500 B widefield microscope equipped with a Leica DCF360 monochrome camera using ∞/0.17/o, HCX PL FLUORTAR 10x/0.3 and ∞/0.17/o, HCX PL FLUORTAR 40x/0.75 objectives and the following filters:

*Blue: excitation at 340-380 nm; emission at 450-490 nm

*Green: excitation at 450-490 nm; emission at 500-550 nm

*Red: excitation at 560 ± 30 nm excitation and 625 ± 37 nm emission

A Leica SP5 Confocal Microscope was used to collect PL spectra from regions of interest in an image after performing a xyλ scan, in which the excitation wavelength was fixed, and the detected emission wavelength was scanned in 5-nm increments. Images were collected using a 20x/0.75 objective at 16-bit resolution. xyλ scans were taken while exciting with 405, 514, and 594 nm laser lines, and emission was detected out to 750 nm.

Steady-State Photoluminescence Spectroscopy. Steady-state PL was collected using a home-built laser system described previously. Samples were excited in a front-face geometry with 375-nm light from a pulsed picosecond diode laser (BDS-SM Series, Becker & Hickl GmbH), and emission was collected between 400-700 nm using a PIXIS 100 CCD (Princeton Instruments).

Time-Resolved Photoluminescence Spectroscopy. Bulk-solution time-resolved photoluminescence (TRPL) measurements were collected using time-correlated single photon counting. Details of the home-built laser system and experimental setup have been described previously. Samples were excited at 375 nm using a pulsed picosecond diode laser (BDS-SM Series, Becker & Hickl GmbH) or at 500 nm using

a pulsed supercontinuum picosecond laser (Super K EXTREME, NKT Photonics) coupled to an acousto-optic filter and an external RF driver (Super K SELECT, NKT Photonics). The excitation beam was vertically polarized, and emission was collected in a front-face geometry with the emission polarizer set to the magic angle. PL lifetimes were determined using forward convolution with the measured instrument response function taken using a scattering Ludox sample. This was done using least-squares minimization via the DecayFit MATLAB package developed by Soren Preus (Fluorescence Decay Analysis Software 1.3, FluorTools, www.fluortools.com). A sum-of-exponentials model was used for the decay.

Fluorescence Lifetime Imaging (FLIM). FLIM measurements were carried out using a Zeiss LSM 980 NLO confocal microscope (Becker-Hickl TCSPC FLIM). Samples were excited using a 445-nm laser line, and PL was collected using a 590/50 nm filter cube. Images were collected using a 512 x 512 pixel resolution and a 250-s collection time. Fluorescence lifetime averages and distributions were determined using the SPCImage 8.5 NG software via the maximum likelihood estimation method.

IV.2 Supporting Information

Microscopy.

Figure AIV.1 shows widefield fluorescence microscopy images of PFNG6:NaPCPT with 5.0 M KBr. Images show sub-micron distribution of complex coacervate droplets. Absorption and emission are observed from both CPEs indicated by the different emission filters and the overlay shown in panel S1D. Figure AIV.2 shows similar images for the PFNG12:NaPCPT sample with 5.0 M KBr. Images show larger complex coacervate droplet structures with multiple compartments.

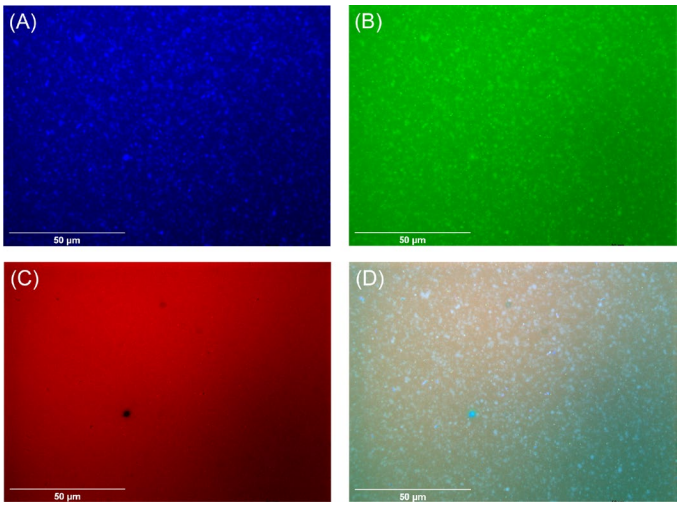

Figure AIV.1: Fluorescence microscopy images of PFNG6:NaPCPT with 5M KBr using (A) 360 ± 20 nm excitation and 470 ± 20 nm emission, (B) 470 ± 20 nm excitation and 525 ± 25 nm emission, and (C) 560 ± 30 nm excitation and 625 ± 37 nm emission. (D) shows and overlay of all fluorescence images. Images were taken using a 63x/0.6-1.4 oil objective and where contrast adjusted to highlight droplet structure.

Figure AIV.3 shows PFNG9:NaPCPT with 0.5 and 2.5 M KBr. Panel S3A shows a small amount of precipitant like structures and panel S3B shows a small number of droplets in coexistence with precipitant like structures. Figure 5.2 of the main text shows equivalent images of PFNG9:NaPCPT with 5.0 M KBr. Figure AIV.4 shows PFNG9:NaPCPT with 0.5,

2.5, and 5.0 M LiBr. Images show fully dissolved solutions with the exception of 5.0 M LiBr having small amount of precipitant like structures in coexistence with the dissolved solution. Figure AIV.5 shows PFNG9:NaPCPT with 0.5, 2.5, and 5.0 M tetraethylammonium bromide (TEAB). Images show fully dissolved solutions except for 5.0 M TEAB having very small amounts of precipitant like structures in coexistence with the dissolved solution.

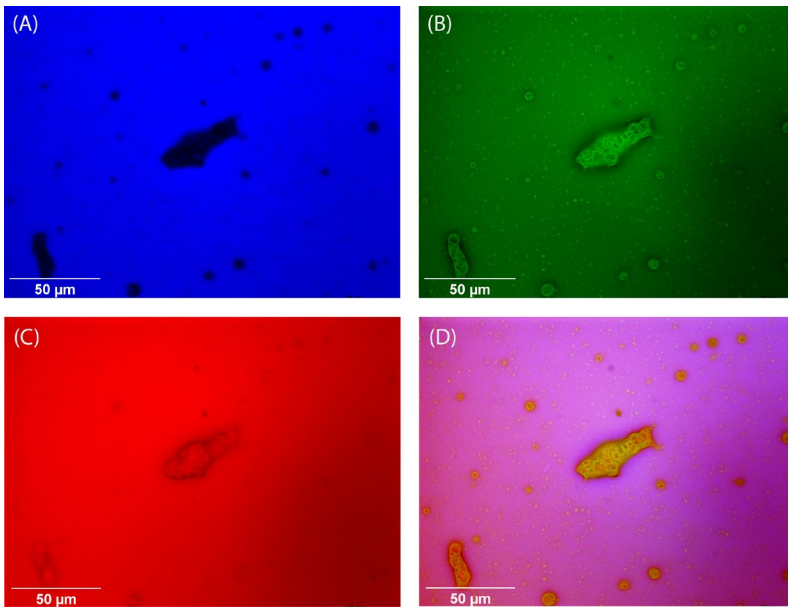

Figure AIV.2: Fluorescence microscopy images of PFNG12:NaPCPT with 5M KBr using (A) 360 ± 20 nm excitation and 470 ± 20 nm emission, (B) 470 ± 20 nm excitation and 525 ± 25 nm emission, and (C) 560 ± 30 nm excitation and 625 ± 37 nm emission. (D) shows and overlay of all fluorescence images. Images were taken using a 40x/0.75 air objective and where contrast adjusted to highlight droplet structure.

Figure AIV.6 shows confocal microscopy images of PFNG9 and PFNG12:NaPCPT with 5.0 M KBr excited at 594 nm and with emission collected out to 800 nm. These images show the existence of NaPCPT in the surrounding

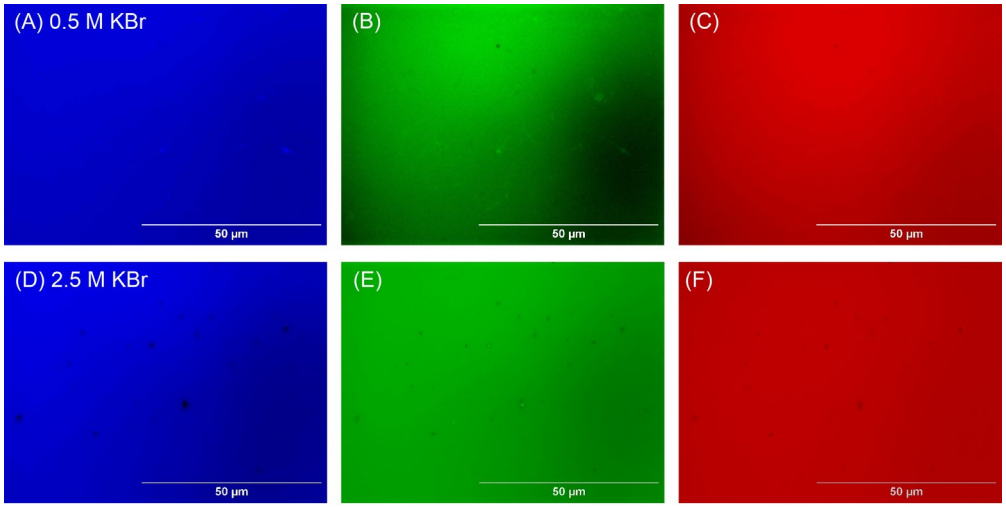

Figure AIV.3: Fluorescence microscopy images of PFNG9:NaPCPT with 0.5M KBr (top) and 2.5 M KBr (bottom) using (A & D) 360 ± 20 nm excitation and 470 ± 20 nm emission, (B & E) 470 ± 20 nm excitation and 525 ± 25 nm emission, and (C & F) 560 ± 30 nm excitation and 625 ± 37 nm emission.

solution and in the droplets. Figure AIV.7 shows widefield images of PFNG19:NaPCPT with 5.0 M KBr and an intensity comparison between the droplets and surrounding solution using different excitation and emission filters. Figure AIV.8 is showing an increase in PL intensity of PFNG9:NaPCPT with 5.0 M KBr droplets as a function of exposure time.

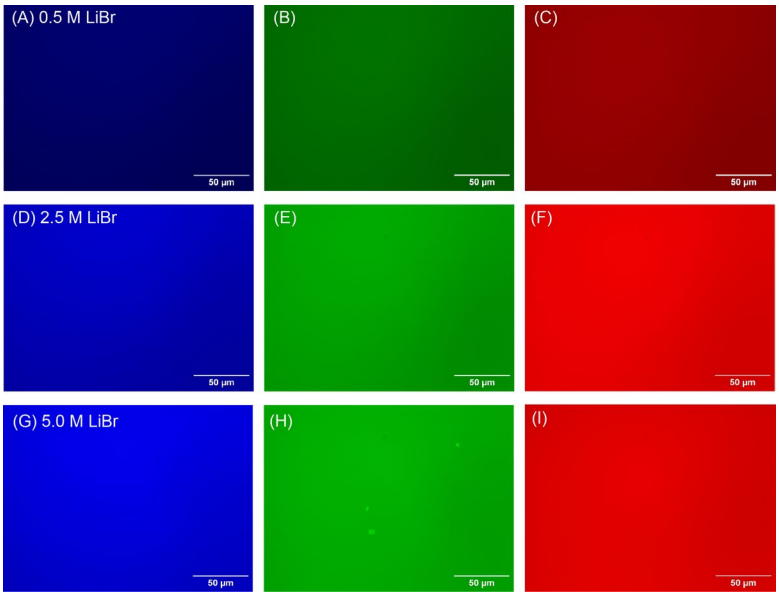

Figure AIV.4: Fluorescence microscopy images of PFNG9:NaPCPT with 0.5M LiBr (top row) and 2.5 M LiBr (second row), and 5.0 M LiBr (bottom row) using (A & D & G) 360 ± 20 nm excitation and 470 ± 20 nm emission, (B & E & H) 470 ± 20 nm excitation and 525 ± 25 nm emission, and (C & F & I) 560 ± 30 nm excitation and 625 ± 37 nm emission.

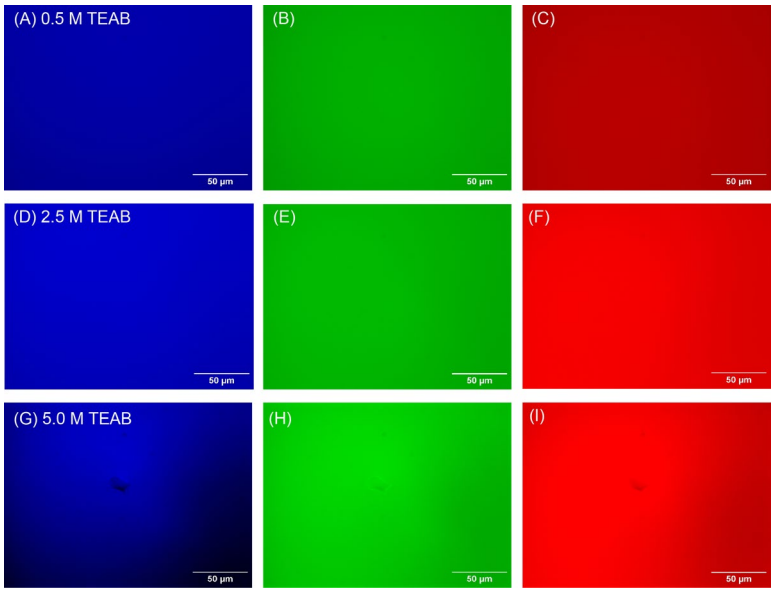

Figure AIV.5: Fluorescence microscopy images of PFNG9:NaPCPT with 0.5M TEAB (top row) and 2.5 M TEAB (second row), and 5.0 M TEAB (bottom row) using (A & D & G) 360 ± 20 nm excitation and 470 ± 20 nm emission, (B & E & H) 470 ± 20 nm excitation and 525 ± 25 nm emission, and (C & F & I) 560 ± 30 nm excitation and 625 ± 37 nm emission.

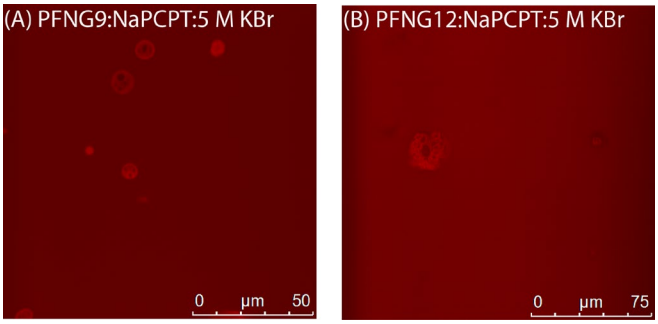

Figure AIV.6: Confocal laser scanning microscopy images of (A) PFNG9:NaPCPT:5M KBr and (B) PFNG12:NaPCPT:5M KBr where samples were excited at 594 nm and emission was collected from 604-800 nm. Based on excitation and emission wavelength choices, images show emission solely from the energy acceptor CPE NaPCPT.

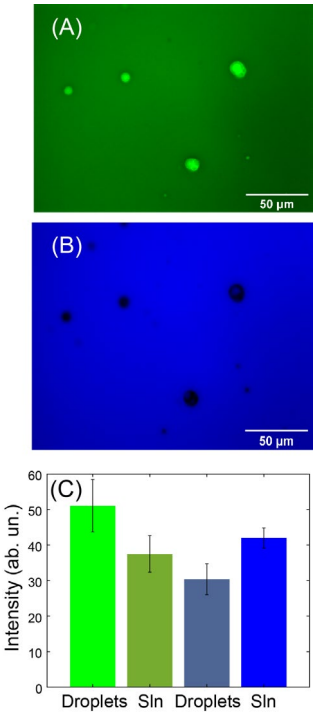

Figure AIV.7: Fluorescence microscopy images of PFNG9:NaPCPT with 5M KBr using (A) 470 ± 20 nm excitation and 525 ± 25 nm emission, and (B) 360 ± 20 nm excitation and 470 ± 20 nm emission. Panel (C) is showing the fluorescence intensity of the droplets vs. supernatant solution (sln). Images were taken using a 40x/0.75 air objective

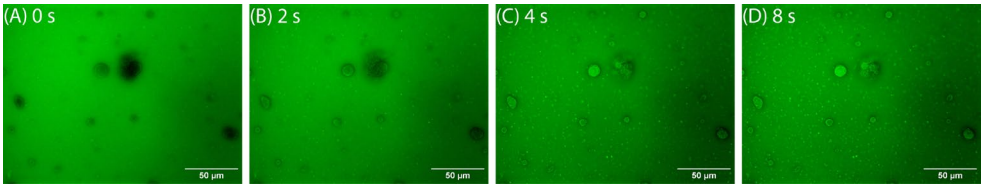

Figure AIV.8: Fluorescence microscopy images of PFNG9:NaPCPT with 5M KBr using 360 ± 20 nm excitation and 470 ± 20 nm emission and a 40x/0.75 air objective. Frames were taken from supplemental video X were panels A-D are showing fluorescence intensity increase with light exposure time over 8 seconds.

Steady-State Spectrscopy.

Figure AIV.9 shows steady state absobance of PFNG6/9/12 in panel S9A and absobance of the three CPECs in panel S9B. Panel S9C shows PL from PFNG6/9/12 alone and within the CPEC with NaPCPT. Evidence of energy transfer is shown by the decrease in PL intenisty of PFNGX and a growth in of the PL intensity of the acceptor CPE.

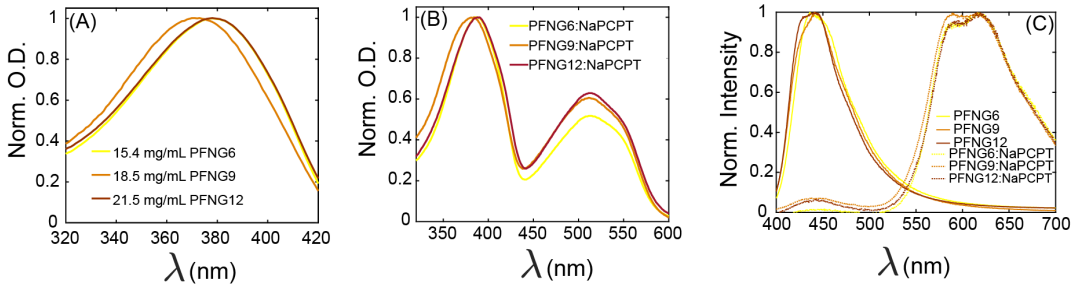

Figure AIV.9: Steady state absorbance of (A) the PFNGX series, (B) the PFNGX:NaPCPT complexes with 5 M KBr, and (C) the fluorescence of the PFNGX CPEs in isolation (left) and in complexes (right) exciting at 375 nm.

Figure AIV.10 shows steady-state PL generated form an xyλ-scan of PFNG9 andPFNG12:NaPCPT samples with 5.0 M KBr excited at 514 nm. Figures show PL from the acceptor CPE within the droplets and the surrounding solution.

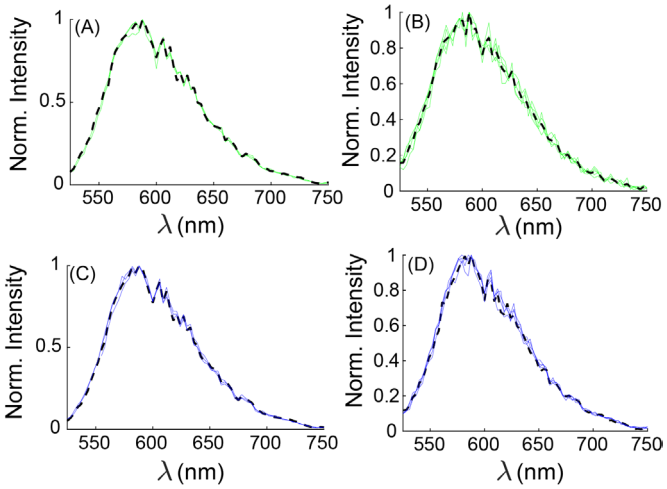

Figure AIV.10: Steady-state PL spectra of droplet ROIs (A and B) and solution ROIs (C and D) exciting at 514 nm. Panels A and C are for PFNG9:NaPCPT:5M KBr solutions and panels B and D are for PFNG12:NaPCPT:5M KBr solutions.

Time-Resolved Photoluminescence Spectroscopy and Fluorescence Lifetime Imaging.

Figure AIV.11 shows full FLIM images next to greyscale images of PFNG9 and PFNG12:NaPCPT samples with 5.0 M KBr. Figure AIV.12A shows TRPL of PFNG6/9/12 CPES on their own giving similar lifetimes of ~ 500 ps. Panel S12B shows the lifetime distribution of PFNG12:NaPCPT with 5.0 M KBr to center around ~620 ps. Panel S12C shows TRPL of bulk solution compared to different locations with in the droplet to have very little variation in lifetime.

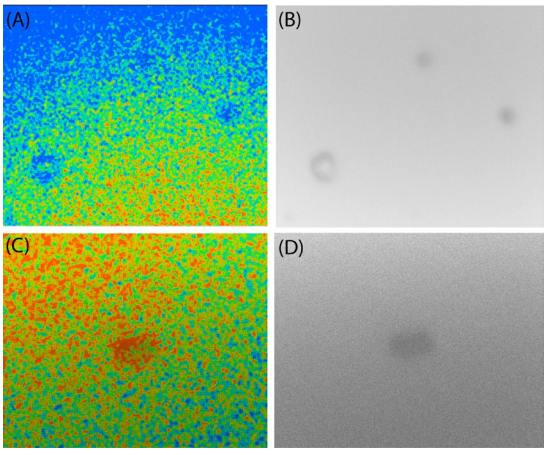

Figure AIV.11: Full FLIM images and grey-scale images of PFNG9:PCPT:5M KBr (A and B) and PFNG12:NaPCPT:5M KBr (C and D).

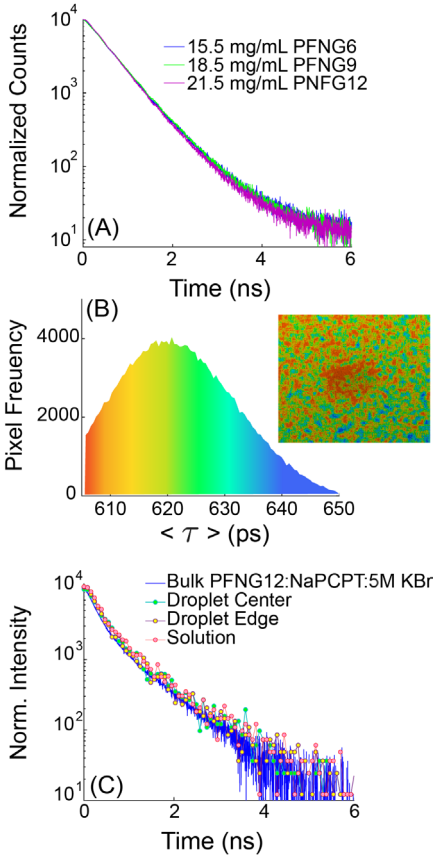

Figure AIV.12: Fluorescence lifetime decays of (A) PFNGX controls excited at 375 nm and collecting emission at 420 nm. (B) shows a FLIM lifetime distribution and image for PFNG12:NaPCPT:5M KBr solution excited at 445 nm collecting emission at 590 nm. (C) Shows bulk solution lifetime decay compared to FLIM lifetimes collected from the center and edge of the droplet and the surrounding solution.